AD-A044 298 GEORGIA INST OF TECH ATLANTA SCHOOL OF AEROSPACE ENG--ETC F/G 21/8.2
APPROXIMATE NONLINEAR ANALYSIS OF SOLID ROCKET MOTORS AND T-BUR--ETC(U)
JUL 77 E A POWELL, M S PADMANABHAN, B T ZINN F04611-75-C-0036

UNCLASSIFIED AFRPL-TR-77-48 NL

1 OF 3
ADA
044298

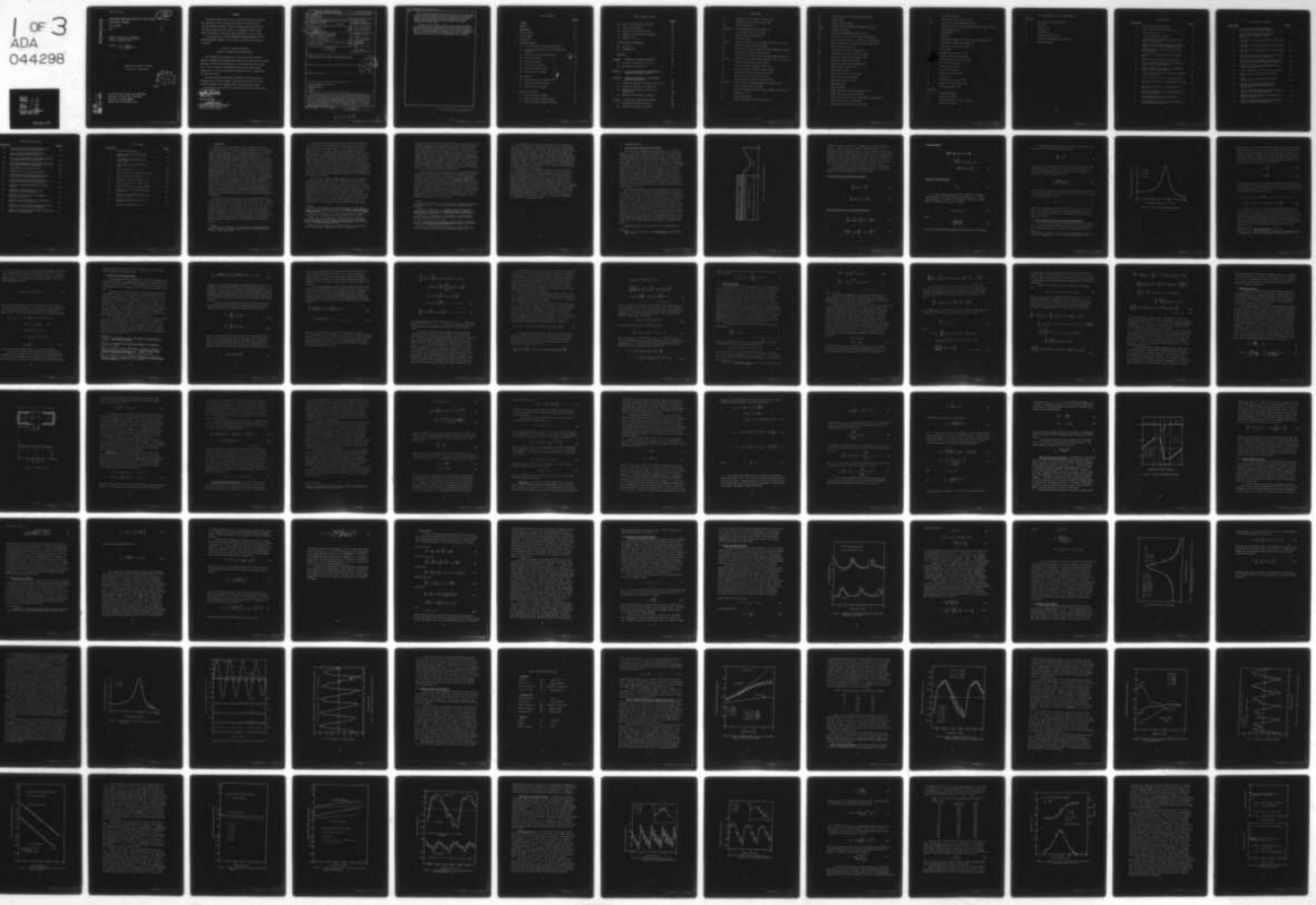

AFRPL-TR-77-48

APPROXIMATE NONLINEAR ANALYSIS OF SOLID ROCKET MOTORS AND T-BURNERS

FINAL REPORT

VOL I

GEORGIA INSTITUTE OF TECHNOLOGY
SCHOOL OF AEROSPACE ENGINEERING
ATLANTA, GEORGIA 30332

AUTHORS: E. A. POWELL
M.S. PADMANABHAN
B. T. ZINN

JULY 1977

Approved for public release;
Distribution Unlimited

AIR FORCE ROCKET PROPULSION LABORATORY
DIRECTOR OF SCIENCE AND TECHNOLOGY
AIR FORCE SYSTEMS COMMAND
EDWARDS AFB, CALIFORNIA 93523

FOREWORD

The present report consists of two volumes which describe an approximate nonlinear analysis of solid rocket motors and T-burners and the associated computer programs. Volume I contains the analytical basis for the computer programs and the results of the parametric studies, while Volume II describes the computer programs and serves as a user's manual.

The investigation is entitled APPROXIMATE NONLINEAR ANALYSIS OF SOLID ROCKET MOTORS AND T-BURNERS. The two volumes are additionally subtitled as follows:

Volume I - Analysis and Results

Volume II - Computer Program User's Manual

This investigation was sponsored by the Air Force Rocket Propulsion Laboratory, Edwards AFB, California 93523 under contract number F04611-75-C-0036 with Capt. Jack Donn as technical monitor. Program management was provided by B. T. Zinn (Co-principal Investigator) while project engineering was provided by E. A. Powell (Co-principal Investigator) and M. S. Padmanabhan (Post Doctoral Fellow).

This report has been reviewed by the information office (OI) and is releasable to the National Technical Information Service (NTIS). At NTIS, it will be available to the general public, including foreign nations.

This technical report has been reviewed and is approved for publication.

JACK J. DONN, Capt, USAF
Project Manager

FOR THE COMMANDER

WILLIAM F. MORRIS, Colonel, USAF
Chief, Technology Division

SECURITY CLASSIFICATION OF THIS PAGE *(When Data Entered)*

REPORT DOCUMENTATION PAGE

READ INSTRUCTIONS BEFORE COMPLETING FORM

1. REPORT NUMBER: AFRPL-TR-77-48	2. GOVT ACCESSION NO.
3. RECIPIENT'S CATALOG NUMBER	
4. TITLE *(and Subtitle)*: APPROXIMATE NONLINEAR ANALYSIS OF SOLID ROCKET MOTORS AND T-BURNERS. VOLUME I. Analysis and Results.	5. TYPE OF REPORT & PERIOD COVERED: Final Report. Feb 75 - Jun 77
	6. PERFORMING ORG. REPORT NUMBER
7. AUTHOR(s): E. A. Powell, M. S. Padmanabhan, B. T. Zinn	8. CONTRACT OR GRANT NUMBER(s): F04611-75-C-0036
9. PERFORMING ORGANIZATION NAME AND ADDRESS: Georgia Institute of Technology, School of Aerospace Engineering, Atlanta, Georgia 30332	10. PROGRAM ELEMENT, PROJECT, TASK AREA & WORK UNIT NUMBERS: 573010 AK
11. CONTROLLING OFFICE NAME AND ADDRESS: Air Force Rocket Propulsion Laboratory/DYS, Edwards, CA 93523	12. REPORT DATE: July 1977
	13. NUMBER OF PAGES: 194
14. MONITORING AGENCY NAME & ADDRESS *(if different from Controlling Office)*: 209p.	15. SECURITY CLASS. *(of this report)*: UNCLASSIFIED
	15a. DECLASSIFICATION/DOWNGRADING SCHEDULE

16. DISTRIBUTION STATEMENT *(of this Report)*

APPROVED FOR PUBLIC RELEASE; DISTRIBUTION UNLIMITED

17. DISTRIBUTION STATEMENT *(of the abstract entered in Block 20, if different from Report)*

18. SUPPLEMENTARY NOTES

19. KEY WORDS *(Continue on reverse side if necessary and identify by block number)*

Nonlinear Combustion Analysis
Galerkin Method
Solid Rocket Motor
T-Burner

20. ABSTRACT *(Continue on reverse side if necessary and identify by block number)*

An approximate theory based on the Galerkin method was developed to describe the nonlinear behavior of axial-mode combustion instability in solid-propellant rocket motors and T-burners. For motors with linear combustion driving and linear particle damping (gasdynamic nonlinearities only), growth rates, limiting amplitudes and waveforms were in reasonable agreement with availabie "exact" numerical solutions and experimental data. For T-burners the predicted limiting amplitudes were considerably higher than the experimentally measured values.

DD FORM 1 JAN 73 1473 EDITION OF 1 NOV 65 IS OBSOLETE

UNCLASSIFIED

SECURITY CLASSIFICATION OF THIS PAGE *(When Data Entered)*

403 914 LB

20.

To assess the importance of combustion nonlinearities, a heuristic nonlinear combustion response model was introduced into the approximate analysis. Results obtained with both the approximate model and the "exact" analysis showed that nonlinear combustion effects may be important for moderate amplitudes and may account for pulsed instabilities in some cases.

The higher Reynolds number correction to the Stokes Drag Law was also included in both the approximate and "exact" analyses. Results show that nonlinear particle effects become increasingly important as particle size and/or frequency increases. Also, particle nonlinearities may have a significant effect on optimum particle size for maximum damping and may account for pulsed instabilities in some cases.

TABLE OF CONTENTS

Table of Contents (cont'd)

NOMENCLATURE

A, B	combustion response parameters, Equation (10)
A	dimensionless cross sectional area, A^*/A^*_{ch}
A^*_{ch}	chamber reference area
$A_j(t), B_j(t)$	time-dependent amplitudes, Equations (19)
A_v	area of T-burner center vent, A^*_v/A^*_{ch}
b_j	complex axial acoustic eigenvalue
c^*	velocity of sound
$C_i(j,m)$	coefficients of linear terms in Equations (22), (23), and (25)
C_m	particle to gas mass flux ratio, $\dot{m}_p/\dot{m}_g$
c^*_p	specific heat at constant pressure of gaseous combustion products
c^*_s	specific heat of solid propellant material
c^*_v	specific heat at constant volume of gaseous combustion products
$D_i(j,m,n)$	coefficients of nonlinear terms in Equations (22), (23), and (25)
e	specific internal energy of gas, $e^*/c^*_v T^*_r$
E^*_f	activation energy of Arrhenius flame reaction
E^*_s	activation energy of Arrhenius surface reaction
f_e	equilibrium frequency of gas-particle mixture
f_g	pure gas frequency of gas-particle mixture
F_p	momentum exchange term between gas and particles
$g_j(t), h_j(t)$	slowly varying time-dependent amplitudes, Equations (38)
h	specific enthalpy of gas, $h^*/c^*_p T^*_r$
h_c	enthalpy of combustion products entering chamber from flame zone
i	imaginary unit, $\sqrt{-1}$
K	particle drag constant
k^*_g	thermal conductivity of combustion products

k_s^*	thermal conductivity of solid propellant material
L^*	chamber length
L_b^*	T-burner cup-grain length
L_{eff}	Effective plug flow length for T-burner vent, L_{eff}^*/L^*
L_v^*	T-burner vent length
$\bar{M}_e$	steady-state Mach number at nozzle entrance
$\dot{m}_g$	mass flow rate of gas per unit surface area, $\dot{m}_g^*/\rho_r^* c_r^*$
$\dot{m}_p$	mass flow rate of particles per unit surface area $\dot{m}_p^*/\rho_r^* c_r^*$
n	pressure exponent in propellant steady-state burning law
p	dimensionless pressure, p^*/p_r^*
Q_f^*	exothermic heat release in flame reaction
Q_s^*	endothermic heat release in surface reaction
r	propellant surface regression rate, $r^*/c_r^* \hat{y}_c$
R	dimensionless chamber radius, R^*/L^*
$\mathcal{R}$	combustion response function, Equation (9)
R_e	Reynolds number, Equation (80)
R_o	universal gas constant
S_c^*	cross sectional area of T-burner grain
S_{co}^*	cross sectional area of T-burner
t	dimensionless time, $t^*/(L^*/c_r^*)$
T	temperature, T^*/T_r^*
T_f^*	flame temperature
T_s^*	surface temperature of burning solid propellant
u	dimensionless axial gas velocity, u^*/c_r^*
$\bar{u}_b$	steady state velocity of gases leaving burning solid propellant
u_n	velocity of flow out of T-burner vent
u_p	dimensionless axial particle velocity, u_p^*/c_r^*

V_ℓ	vent effect parameter
x	dimensionless axial coordinate, x^*/L^*
$X_j(x)$	axial acoustic eigenfunction, Equation (20)
y	coordinate normal to regressing solid propellant surface, $y^*/L^*\hat{y}_c$
Y	complex nozzle admittance
$\hat{y}_c$	$(k_s^*/\rho_s^* c_s^* c_r^* L^*)^{1/2}$
α	growth rate
β	dimensionless T-burner total cylindrical grain length, $2L_b^*/L^*$
β_v	dimensionless T-burner vent length, L_v^*/L^*
γ	specific heat ratio for gas, c_v^*/c_p^*
μ^*	gas viscosity
ρ	dimensionless gas density, ρ^*/ρ_r^*
ρ_-^*	density of solid particle material
	dimensionless particle density, ρ_p^*/ρ_r^*
	solid propellant density
σ^*	average particle diameter
Φ	gas velocity potential
Φ_p	particle velocity potential
φ	real part of Φ
ω	dimensionless frequency, $\omega^* L^*/c_r^*$
ω_o^*	reaction rate in gas phase flame
Ω	frequency parameter, $\omega/\bar{r}^2$

Superscripts

$( )'$	perturbation quantity
$(\bar{})$	steady-state quantity
$( )^*$	dimensional quantity, complex conjugate
$(\tilde{})$	approximate solution

r,i	real and imaginary parts of a complex quantity

Subscripts

e	evaluated at the nozzle entrance
g	gas phase
p	particle phase
r	reference state
v	evaluated at T-burner vent
x,t	partial differentiation with respect to x,t
o	stagnation quantity

LIST OF FIGURES

LIST OF FIGURES (continued)

LIST OF FIGURES (continued)

LIST OF FIGURES (continued)

LIST OF TABLES

1. INTRODUCTION

Experience with solid propellant rocket motors indicates that the full-thrust operation of such motors is never completely steady. A certain degree of rough combustion (i.e., low amplitude random flow oscillations) is usually present which does not seriously affect system performance. On occasion, larger amplitude organized oscillations may develop in the combustion chamber and nozzle flow field during the ignition transient or after full thrust has been obtained[1]. Such organized oscillations are evidence of a positive feedback between the unsteady propellant combustion process and the flow field disturbance. These instabilities may be classified as either spontaneous instabilities, which originate from flow or combustion noise, or pulsed instabilities, which result from the introduction of a sufficiently large disturbance in a motor which is stable with respect to small amplitude disturbances. It is observed that, after passing through a transient period, both spontaneous and pulsed instabilities reach a limiting amplitude (or limit-cycle) at which they oscillate with a frequency that is close to the frequency of one of the chamber's acoustic modes. These limit-cycle oscillations are often characterized by nonsinusoidal pressure waveforms that have sharp peaks and flattened minima. The existence of limit-cycles, pulsed instability, and nonsinusoidal waveforms are all caused by the nonlinearities of the system.

Small amplitude combustion instability may occur without detrimental effects to the system while large amplitude oscillations may lead to increase in mean chamber pressure and burning rate, excessive heat transfer rates, and severe vibration levels. The occurrence of any one of these may result in malfunction or destruction of the rocket motor. Thus, it is important for the rocket designer to be able to estimate the limiting amplitude of the pressure oscillations as well as the conditions under which pulsed instability may occur. To do this, a theoretical approach capable of determining the nonlinear stability characteristics of solid propellant rocket motors is required.

---

[1] Dehority, G. L. and Price, E. W., "Axial Mode, Intermediate Frequency Combustion Instability in Solid Propellant Rockets," Naval Weapons Center Tech. Publ. 5654, October 1974.

Reliable theoretical approaches capable of predicting the characteristics of combustion instabilities and the conditions under which they are most likely to occur are badly needed. To be of practical use, these analyses should be conceptually simple and easily adaptable for use by engine designers. In addition, these techniques should be capable of solving combustion instability problems without exceeding memory core limitations of current computers and without requiring excessive computation time. These considerations are particularly relevant to multi-dimensional combustion instability problems. As the above requirements cannot be satisfied by any of the "exact" numerical solution techniques, (e.g., finite-difference or finite-element methods) one must resort to the use of one or more approximate solution techniques. The development of such solution techniques for the analysis of nonlinear axial combustion instabilities in solid rockets is the subject of this report.

In recent years, several nonlinear combustion instability theories have been developed. Kooker and Zinn[2,3] and Levine and Culick[4,5] used finite-difference techniques to obtain numerical solutions to the conservation equations describing the two-phase flow of gases and particles in solid rocket combustors. However, limitations on available computer core size and computational time make it impractical to use these so-called "exact" analyses in parametric studies and engine design. Hence, efforts have been undertaken in recent years to develop reliable approximate solution techniques that are free from the above-mentioned limitations. In the first known attempt at the development of such an approximate technique, Zinn,

---

[2]Kooker, D. E. and Zinn, B. T., "Numerical Solution of Axial Instabilities in Solid Propellant Rocket Motors," Proceedings of the 10th JANNAF Combustion Meeting, CPIA Publication 243, Vol. I, December 1973, pp. 389-415.

[3]Kooker, D. E. and Zinn, B. T., "Numerical Investigation of Nonlinear Axial Instabilities in Solid Rocket Motors," BRL CR 141, March 1974.

[4]Levine, J. N. and Culick, F.E.C., "Numerical Analysis of Nonlinear Longitudinal Combustion Instability in Metalized Propellant Solid Rocket Motors," Proceedings of the 9th JANNAF Combustion Meeting, CPIA Publication 231, Vol. I, December 1972, pp. 141-163.

[5]Levine, J. N. and Culick, F.E.C., "Nonlinear Analysis of Solid Rocket Combustion Instability, AFRPL-TR-74-45, Vol. I, October 1974.

Powell and Lores have used the Galerkin method in the analysis of nonlinear combustion instabilities in liquid rockets with quasi-steady nozzles experiencing longitudinal[6] and transverse[7] instabilities. Powell and Zinn[8] later extended these theories to situations in which the instabilities are three-dimensional and the rocket combustors are attached to conventional nozzles. More recently, a solution procedure utilizing the Galerkin method together with the method of averaging has been applied by Culick[9,10] in the analysis of nonlinear instabilities in solid rockets. While the above-mentioned approximate theories appear promising, more work is needed to determine their reliability and range of applicability, since these theories are limited by the assumptions upon which they are based.

The main objective of this investigation is to evaluate the usefulness of approximate nonlinear analysis techniques for predicting the stability behavior of solid rocket motors. This objective has been accomplished through a comparison of the predictions of the approximate model, based on the methodology developed by Zinn, Powell, Lores[6-8] and Culick[9,10] with the more exact analysis developed by Kooker and Zinn[2,3] and Levine and Culick[4,5]. Therefore, extensive development of nonlinear models, such as developing new theory or programming a large analysis, was not necessary. However, modifications to both the approximate and "exact" analyses were made in order to accomplish the objectives of this program. These modifications will be discussed in Sections 2 and 3 of this report.

---

[6]Lores, M. E. and Zinn, B. T., "The Prediction of Nonlinear Longitudinal Combustion Instability in Liquid Propellant Rockets," NASA CR-120904, April 1972.

[7]Zinn, B. T. and Powell, E. A., "Nonlinear Combustion Instability in Liquid Propellant Rocket Engines," Proceedings of the 13th Symposium (International) on Combustion, The Combustion Institute, 1971, pp. 491-503.

[8]Powell, E. A. and Zinn, B. T., "The Prediction of Nonlinear Three-Dimensional Combustion Instability in Liquid Rockets with Conventional Nozzles," NASA CR-121279, October 1973.

[9]Culick, F.E.C., "Nonlinear Behavior of Acoustic Waves in Combustion Chambers," Proceedings of the 10th JANNAF Combustion Meeting, CPIA Publication 243, Vol. I, December 1973, pp. 417-436.

[10]Culick, F.E.C., "Nonlinear Behavior of Acoustic Waves in Combustion Chambers," California Institute of Technology Report, April 1975.

The investigation is divided into four tasks. In the first task the influence of the gasdynamic nonlinearities, which result in mode-coupling, was assessed. For this task all processes except gasdynamical mode-coupling, were described by linear models. In the second task the approximate and "exact" analyses were extended to include the effects of nonlinear particle damping and nonlinear combustion driving. In the third task the approximate analysis was applied to determine the nonlinear stability characteristics of T-burners. Finally, the restrictions and limitations on the application of the method of averaging to the solution of solid rocket instability problems was investigated in the fourth task.

The development of the approximate analysis is given in Section 2, while the modifications to the "exact" analysis are discussed in Section 3. The results obtained during the performance of the four tasks described above are presented and discussed in Section 4. These results include an extensive parametric study to assess the importance of gasdynamic mode coupling, particle size and concentration, propellant response function, and particle and combustion nonlinearities upon growth and decay rates, frequencies, limiting amplitudes and waveforms for motors and T-burners. In many cases, the approximate solutions are compared with the corresponding "exact" solutions and with experimental data. Conclusions drawn from the results of this investigation are presented in Section 5, along with recommendations for improvement of the approximate model.

2. APPROXIMATE ANALYSIS

2.1 Basic Assumptions and Conservation Equations

The solid rocket configuration investigated herein is described in Figure 1. A full-length cylindrically-perforated solid propellant grain containing aluminum particles burns unsteadily inside a cylindrical combustor-nozzle combination. The combustion process takes place inside a thin region immediately adjacent to the propellant. The products of combustion are assumed to consist of a mixture of a single gaseous species and aluminum oxide particles which enter the engine core flow at the outer edge of the combustion zone and acquire axial velocity through interaction with the engine core flow. During instability, the interaction between the wave motion and the combustion process results in unsteady burning which provides the energy needed to sustain the instability. At the same time the interaction between the wave motion and the particles, the core flow, and the nozzle results in wave energy dissipation. Limit-cycle conditions are achieved when the wave energy addition over a cycle is balanced by the wave energy removal over a cycle.

The following assumptions are used in the development of the theoretical model: (1) the flow in the engine is one-dimensional and it consists of a single gaseous species and spherical particles that can be characterized by a single average diameter; (2) the gas phase is thermally and calorically perfect; (3) the gas phase is inviscid and non-heat conducting; (4) the thermal energy transfer between gas and particle phases is neglected; (5) the momentum exchange between the gas phase and the particles due to viscous interaction can be described by Stokes' Drag Law[11]; (6) the burning rate responds to pressure oscillations only, and it can be described by a linear burning response function; (7) the interaction of the oscillations in the combustor with the flow in the nozzle can be adequately described by using an appropriate nozzle admittance[8]; (8) the Mach number of the mean flow is small; and (9) only moderate-amplitude disturbances are considered in this analysis.

Assumptions (1), (2), (3), (7), (8) and (9) are commonly used in

---

[11] Landau, L. D. and Lifshitz, E. M., Fluid Mechanics, p. 66, Pergamon Press, 1959.

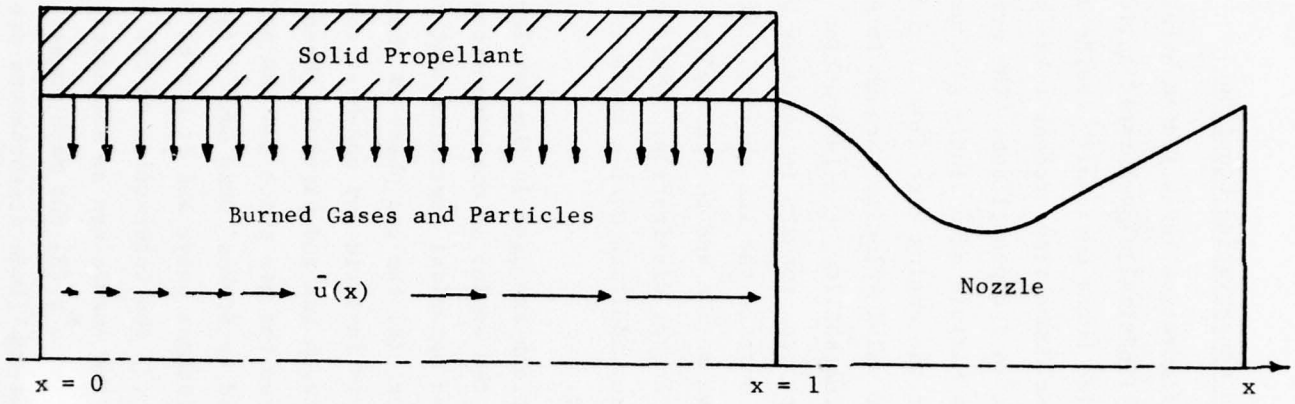

Figure 1. Solid Rocket Motor Configuration

combustion instability analyses[6-10]. Assumption (4) could be relaxed, as was done in Reference 10, at the expense of other assumptions, but it is introduced here to simplify the analysis. The use of Stokes' Law and linear combustion response (assumptions (5) and (6)) are consistent with the requirement that only the effect of gasdynamical nonlinearities is considered in the analysis of nonlinear mode-coupling (first task). The effect of particle and combustion nonlinearities upon the resulting instability are considered in the second task, and the results are presented later in the report.

Using assumptions (1) through (4) above, the system of nondimensional conservation equations that describe the unsteady behavior of the combustor two-phase flow can be expressed in the following form[3]:

Mass Conservation (gas and particulate phases)

$$\frac{\partial \rho}{\partial t} + \frac{\partial}{\partial x}(\rho u) = \frac{2\dot{m}_g}{R} \tag{1}$$

$$\frac{\partial \rho_p}{\partial t} + \frac{\partial}{\partial x}(\rho_p u_p) = \frac{2\dot{m}_p}{R} \tag{2}$$

Momentum Conservation (gas and particulate phases)

$$\rho \frac{\partial u}{\partial t} + \rho u \frac{\partial u}{\partial x} + \frac{1}{\gamma}\frac{\partial p}{\partial x} = F_p - \frac{2\dot{m}_g u}{R} \tag{3}$$

$$\rho_p \frac{\partial u_p}{\partial t} + \rho_p u_p \frac{\partial u_p}{\partial x} = -F_p - \frac{2\dot{m}_p u_p}{R} \tag{4}$$

Energy (gas phase)

$$\frac{\partial(\rho e)}{\partial t} + \frac{\partial}{\partial x}(\rho u e) + p(\gamma-1)\frac{\partial u}{\partial x}$$

$$= \frac{2\dot{m}_g \gamma h_c}{R} - \gamma(\gamma-1) F_p(u - u_p)$$

$$+ \frac{\gamma(\gamma-1)}{R}(\dot{m}_g u^2 + \dot{m}_p u_p^2) \qquad (5)$$

Equation of State (gas phase)

$$p = \rho_e \qquad (6)$$

In the above equations the quantity F_p describes the momentum exchange between the gas phase and the particulate matter. For linear particle damping, it is derived from the Stokes Drag Law for a single sphere in a steady flow; this F_p is given by

$$F_p = K\rho_p (u_p - u) \qquad (7)$$

where

$$K = \frac{18\mu^*}{\rho_m^* \sigma^{*2}} \left(\frac{L^*}{c_o^*}\right) \qquad (8)$$

The case of nonlinear particle damping is discussed later in this section.

The unsteady mass burning rate is described by the following linear response function law[12] (pressure coupling only):

$$\frac{\dot{m}_g'}{\bar{\dot{m}}_g} = \Re \frac{p'}{\bar{p}} \tag{9}$$

where $\Re$ is the complex response function that must be provided from either experimental data or an analysis of the unsteady combustion process. In this report the response function $\Re$ is taken to be the well-known, two-parameter (i.e.,A,B) expression given by[12]

$$\Re = \frac{n\ A\ B}{\lambda + \frac{A}{\lambda} - (1+A) + AB} \tag{10}$$

where A and B are related to the steady-state combustion of the propellant[3], n is the pressure exponent in the steady-state burning law and λ is a complex solution of the quadratic equation

$$\lambda^2 = \lambda - i\ \Omega \tag{11}$$

where Ω is a nondimensional frequency parameter. A typical curve of real part of the response function versus frequency parameter Ω is shown in Figure 2. Nonlinear expressions for unsteady mass burning rate are given later in this section.

2.2 Order of Magnitude Analysis and Approximate Wave Equations

To proceed with the analysis, each dependent variable is expressed as a sum of a space-dependent steady-state quantity and a perturbation which is both time and space dependent. Following the methodology introduced in

[12] Culick, F.E.C., "A Review of Calculations for Unsteady Burning of a Solid Propellant, "AIAA J., Vol. 6, No. 12, pp. 2241-2244, December, 1968.

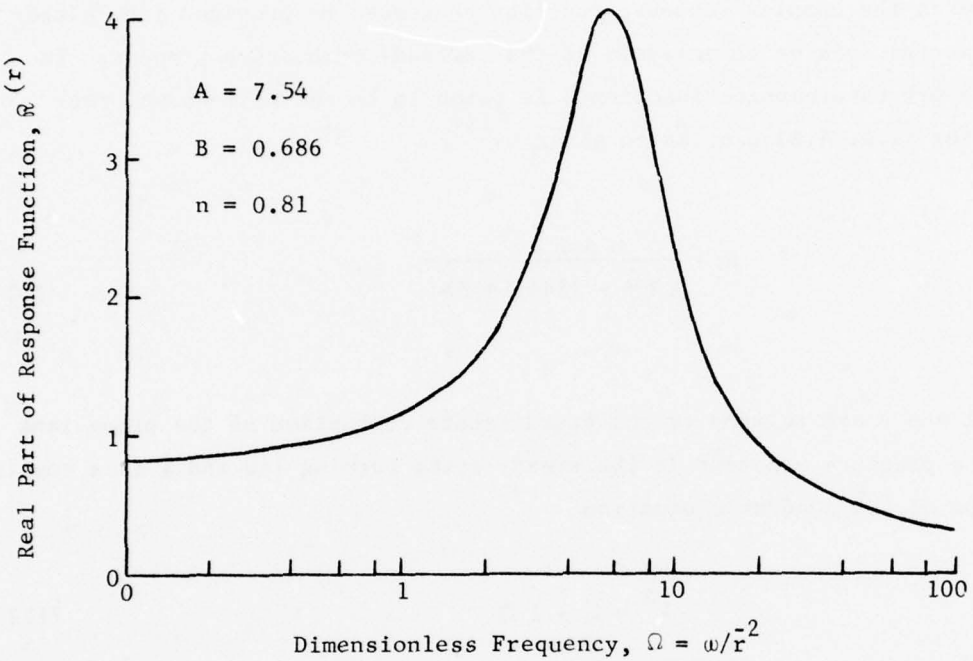

Figure 2. Typical Linear Propellant Response

References (6), (7) and (8) each perturbation quantity and the mean flow Mach number are assumed to be of $0(\epsilon)$ where ϵ is a small ordering parameter that is a measure of the wave amplitude. Substituting the assumed expressions for the dependent variables into Equations (1) through (6), neglecting all terms of order higher than ϵ^2 and subtracting out the steady-state equations result in the derivation of the desired second order perturbation equations. Introducing the velocity potentials Φ and Φ_p defined by

$$u' = \frac{\partial \Phi}{\partial x} \tag{12a}$$

$$u_p' = \frac{\partial \Phi_p}{\partial x} \tag{12b}$$

into the resulting system of second order wave equations, using the substitution principle[13,14] to eliminate variables, the system of second order equations can be combined to yield the following nonlinear wave equation describing the unsteady two-phase flow inside the motor:

$$\Phi_{xx} - \Phi_{tt} = 2\,\bar{u}\,\Phi_{xt} + (\gamma+1)\,\frac{d\bar{u}}{dx}\,\Phi_t + 2\,\Phi_x\,\Phi_{xt} + (\gamma-1)\,\Phi_t\,\Phi_{xx}$$

$$+ K\bar{\rho}_p\left[\Phi_t - (\Phi_p)_t\right] - (\gamma-1)\,\bar{\rho}_p\,\bar{u}_p\,(\Phi_p)_{xt} - \gamma\mathcal{R}h_c\,\frac{d\bar{u}}{dx}\,\Phi_t \tag{13}$$

Considering the nature of the problem under consideration, an inspection of the above equation suggests that it has the proper form. The left-hand side of the equation is the wave equation operator; the first two terms on the right-hand side describe the effects of the mean flow; the third and fourth terms describe gasdynamical nonlinearities while the fifth and sixth terms describe the gas-particle interaction; finally, the seventh term represents the "driving" provided by the unsteady combustion process.

---

[13] Lighthill, M. J., Surveys in Mechanics, p. 250, 1956.

[14] Blackstock, D. T., "Approximate Equations Governing Finite-Amplitude Sound in Thermo-Viscous Fluids", General Dynamics GD/E Report GD-1463-52, 1963.

Applying the order of magnitude analysis to the particle momentum equation yields the following equation for the particle potential, Φ_p:

$$(\Phi_p)_t + \bar{u}_p(\Phi_p)_x + \frac{1}{2}(\Phi_p)_x^2 = K(\Phi - \Phi_p) - \frac{d\bar{u}_p}{dx}\Phi_p \qquad (14)$$

A detailed derivation of Equations (13) and (14) is given in Appendix A.

In the analysis for a solid rocket motor, the head end (x=0) of the chamber is assumed to consist of a rigid wall requiring zero velocities for both the gas and particles at this location. The influence of the exhaust nozzle on the wave motion in the combustion chamber is introduced through the boundary condition at x=1, which is the location of the nozzle entrance plane. As is customary in combustion instability analyses[8], the nozzle effect is introduced through an appropriate nozzle admittance relation. Thus, the solutions to Equations (13) and (14) are required to satisfy the following boundary conditions.

$$\left.\begin{aligned} \Phi_x &= 0 \\ (\Phi_p)_x &= 0 \end{aligned}\right\} \quad x = 0 \qquad (15a)$$

$$\Phi_x + \gamma Y \Phi_t = 0 \quad x = 1 \qquad (15b)$$

where $Y = Y_r + iY_i = (u'/p')_{x=1}$ is the nozzle admittance coefficient. The boundary conditions at the ends of a T-burner are described later in this section.

By making an additional approximation, the wave equation for the gas phase (i.e., Equation (13)) and the particle potential equation (i.e., Equation

(14)) can be combined to obtain a single equation describing the gas oscillations. This approach is similar to that employed by Culick[10] in which the spatial derivatives of the particle properties are neglected in the particle momentum equation. The resulting first order linear equation for u'_p is solved analytically to obtain

$$u'_p \approx Ke^{-Kt} \int_o^t u'(x,t')e^{Kt'}\, dt' \tag{16}$$

where short-term transient effects have been neglected. This solution is substituted into the gas phase equation, eliminating the need to numerically solve an additional equation describing the particle oscillations (i.e., Equation (14)). The resulting wave equation for the gas phase then becomes:

$$\begin{aligned}\Phi_{xx} - \Phi_{tt} = {} & 2\bar{u}\,\Phi_{xt} + (\gamma+1)\frac{d\bar{u}}{dx}\Phi_t + 2\Phi_x\Phi_{xt} + (\gamma-1)\Phi_t\Phi_{xx} \\ & + K\bar{\rho}_p\Phi_t - (\gamma-1)K\bar{\rho}_p\bar{u}_p\Phi_x - K^2\bar{\rho}_p\Phi \\ & + K^3\bar{\rho}_p e^{-Kt}\int_o^t \Phi e^{Kt'}\, dt' \\ & + (\gamma-1)K^2\bar{\rho}_p\bar{u}_p e^{-Kt}\int_o^t \Phi_x e^{Kt'}\, dt' \\ & - \gamma\Re h_c \frac{d\bar{u}}{dx}\Phi_t \end{aligned} \tag{17}$$

A detailed derivation of Equation (17) is also given in Appendix A.

Most of the results presented in this report were obtained by an approximate solution of Equations (13) and (14) for which fewer assumptions were necessary. Approximate solutions of Equation (17), however, are also presented in order to determine the conditions under which solving the single

equation yields accurate results, since a considerable saving in computer time is expected by using this approach.

2.3 Application of the Galerkin Method

The approximate solutions of Equations (13) and (14) or Equation (17) are obtained by means of the Galerkin method, which is a special case of the method of weighted residuals[15,16]. Before proceeding with the application of the Galerkin method to this problem, a brief description of the method will be given.

According to the "classical" Galerkin method the dependent variables are expanded in terms of a set of functions Ψ_n that identically satisfy the imposed boundary conditions. The proper choice of the functions Ψ_n is aided by information from such sources as experimental data, the solution of a linearized version of the same problem, or from solutions of closely related problems. Each of the Ψ_n is multiplied by an arbitrary constant or function yet to be determined. These expansions are then substituted into the governing differential equations to form residuals, and the arbitrary constants (or functions) are determined by imposing the condition that the residuals of the differential equations be orthogonal to all the functions Ψ_n.

When the boundary conditions which the solution must satisfy are complicated, it is usually impossible to find a set of functions, Ψ_n, that can identically satisfy these boundary conditions. It has been shown[17,18] that when this occurs it is possible to obtain approximate solutions by properly combining the boundary residuals with the differential equations' residuals when applying the orthogonality conditions. Thus, the resulting orthogonality conditions have the following form:

---

[15] Finlayson, B. A. and Scriven, L. E., "The Method of Weighted Residuals--A Review," Applied Mechanics Reviews, Vol. 19, No. 9, September 1966, pp. 735-744.

[16] Ames, W. F., Nonlinear Partial Differential Equations in Engineering, Academic Press, 1965.

[17] Zinn, B. T. and Powell, E. A., "Application of the Galerkin Method in the Solution of Combustion Instability Problems," Proceedings of the 19th International Astronautical Congress, Vol. 3, 1970, pp. 59-73. (Also appeared in IAF Paper No. P69. Originally published in 1968.)

[18] Zinn, B. T. and Powell, E. A., "The Galerkin Method and its Use in the Solution of Combustion Instability Problems", Proceedings of the 5th ICRPG Combustion Conference, December 1968, pp. 138-144.

$$\int_V E_i \left(\tilde{\rho},\tilde{v},\tilde{p}\right) \Psi_n \, dV - \int_S B_i \left(\tilde{\rho},\tilde{v},\tilde{p}\right) \Psi_n \, dS = 0 \quad i = 1,2,3 \tag{18}$$

where E_i and B_i respectively represent the differential equation and boundary residuals. The residuals are obtained when the approximate expansions for the density, velocity vector, and pressure are substituted into the equations and boundary conditions expressing conservation of mass, momentum, and energy. The above method of solution accounts for the presence of mass, momentum, and energy sources both within the flow field and on the boundaries of the rocket combustor.

In order to obtain approximate solutions of Equations (13) and (14) by the Galerkin method, the velocity potentials are expressed as series of acoustic modes with unknown time-dependent amplitudes as shown below:

$$\tilde{\Phi} = \sum_{j=1}^{N} A_j(t) \, X_j(x) \tag{19a}$$

$$\tilde{\Phi}_p = \sum_{j=1}^{N} B_j(t) \, X_j(x) \tag{19b}$$

where N is the number of modes included in the series expansion and $X_j(x)$ are the acoustic eigenfunctions for the axial modes. For a rocket motor, the X_j's are the axial acoustic modes for the chamber with no mean flow, a rigid wall boundary condition at the head-end, and a nozzle admittance boundary condition at the other end. These functions (complex) are given by:

$$X_j(x) = \cosh\left(ib_j x\right) \tag{20}$$

where b_j are the corresponding axial acoustic eigenvalues (complex). The unknown time-dependent amplitude functions (i.e., $A_j(t)$ and $B_j(t)$) are complex functions of time. The assumed form for the chosen expansions has been guided by related work in this area and experimental evidence[1,6,7] showing that rocket instabilities usually involve the acoustic modes of the combustor.

The assumed expansions are substituted into Equations (13) and (14) and boundary condition (15b) to form the residuals $E\{\Phi,\Phi_p\}$, $E_p\{\Phi,\Phi_p\}$, and $B\{\Phi\}$; any of these residuals becomes identically zero when the assumed solutions identically satisfy the corresponding differential equations or boundary conditions. To determine the unknown time-dependent coefficients, these residuals are required to satisfy the following Galerkin orthogonality conditions[7]:

$$\int_0^1 E\left\{\tilde{\Phi},\tilde{\Phi}_p\right\} X_j^*(x)\,dx - B\left\{\tilde{\Phi}\right\} X_j^*(1) = 0 \tag{21a}$$

$$\int_0^1 E_p\left\{\tilde{\Phi},\tilde{\Phi}_p\right\} X_j^*(x)\,dx = 0 \qquad j = 1, 2, \ldots, N \tag{21b}$$

where $X^*_j(x)$ are the complex conjugates of the axial acoustic eigenfunctions in Equations (19). Performing the integrations indicated in Equation (21) results in a system of coupled second-order nonlinear ordinary differential equations describing the behavior of the time-dependent amplitudes. These equations are similar in form to those developed in References 6 through 10, and they can be expressed as follows:

$$\sum_{m=1}^{2N} \left\{ C_o(j,m) \frac{d^2 A_m}{dt^2} + C_1(j,m)\, A_m + \left[C_2(j,m) + KC_3(j,m) \right.\right.$$

$$\left. + h_c \Re_m C_4(j,m) \right] \frac{dA_m}{dt} + \sum_{m=1}^{N} \sum_{n=1}^{N} \left\{ D_1(j,m,n)\, A_m \frac{dA_n}{dt} \right.$$

$$+ D_2(j,m,n)\, A_m \frac{dA_n^*}{dt} + D_3(j,m,n)\, A_m^* \frac{dA_n}{dt}$$

$$\left.\left. + D_4(j,m,n)\, A_m^* \frac{dA_n^*}{dt} \right\} = 0 \qquad j = 1,2, \ldots N \qquad (22)$$

$$\sum_{m=1}^{2N} \left\{ C_5(j,m) \frac{dA_m}{dt} + C_6(j,m)\, A_m \right\} = 0 \qquad j = 1,2, \ldots N \qquad (23)$$

In the above equations, the $B_j(t)$ functions for $j = 1,2, \ldots N$ have been denoted by $A_j(t)$ for $j = N + 1, \ldots 2N$; there are 2N unknown time dependent functions $A_j(t)$ and 2N equations (N of Equation (22) and N of Equation (23)).

The nonlinear terms involving the complex conjugates appearing in Equation (22) arise because the wave equation (i.e., Equation (13)) must be modified for use with the assumed complex solution given by Equations (19). This modification is necessary because only the real part of the assumed solution is physically meaningful. It can easily be shown that if $\Phi = \varphi + i\,\Psi$ is a solution to Equation (13), the real part, φ, is not a solution to Equation (13). This failure of φ to satisfy Eq. (13) is due to the presence of the nonlinear terms in this equation. It can also be shown, however, that a modified wave equation can be constructed for which the real part of its solution satisfies the original wave equation (i.e., Equation (13). This modified wave equation is derived in Appendix B and is given by Equation (B-8). Thus Equation (22) was actually derived by applying the Galerkin method to Equation (B-8) rather than Equation (13).

The coefficients of the various linear and nonlinear terms appearing in Equations (22) and (23) arise from the spatial integrations indicated in Equations (21). Some of these coefficients are functions of the steady state properties $\bar{u}(x)$, $\bar{u}_p(x)$, and $\bar{\rho}_p(x)$ which are obtained by solving the steady state conservation equations. All of the coefficients involve integrals of products of two or three axial acoustic eigenfunctions with various weighting functions, integrated over the length of the chamber. Expressions for these coefficients are given in Appendix C, and the steady state solutions are presented in Appendix D.

In deriving Equation (23) by applying the Galerkin method to Equation (14), the nonlinear term $1/2(\Phi_p)_x^2$ was dropped in order to be consistent with the assumption of linear particle damping. As a result of neglecting this term, Equation (23) is a linear equation.

To determine the stability characteristics of a solid rocket motor, the form of the initial disturbance is specified and the subsequent behavior of the individual modes is determined by numerically integrating Equation (22) and (23). Once the time-dependence of the individual modes (i.e., $A_j(t)$'s) is known, the gas and particle potentials, Φ and Φ_p, are calculated from Equations (19). The pressure perturbation at any axial location within the chamber is related to the real parts of Φ and Φ_p (i.e., φ and φ_p) by the following approximate momentum equation (Appendix A):

$$p' = -\gamma \left[\varphi_t + \bar{u}(x)\, \varphi_x + \frac{1}{2}\varphi_x^2 - \frac{1}{2}\varphi_t^2 + K\bar{\rho}_p(x)(\varphi-\varphi_p) + \frac{d\bar{u}}{dx}\varphi \right] \qquad (24)$$

The Galerkin method was also used to obtain approximate solutions of Equation (17) which was derived by neglecting the spatial derivatives of the particle velocity in Equation (14). The resulting differential equations governing the behavior of the unknown amplitude functions, $A_j(t)$ is given in this case as follows:

$$\sum_{m=1}^{N} \left\{ C_o(j,m) \frac{d^2A_m}{dt^2} + C_1(j,m)\, A_m + \left[C_2(j,m) + h_c \mathcal{R}_m C_4(j,m) \right] \frac{dA_m}{dt} + \right.$$

$$+ C_3(j,m)\, e^{-Kt} \int_0^t A_m(t')e^{Kt'}\, dt' \Big\}$$

$$+ \sum_{m=1}^{N} \sum_{n=1}^{N} \Big\{ D_1(j,m,n)\, A_m \frac{dA_n}{dt} + D_2(j,m,n)\, A_m \frac{dA_n^*}{dt}$$

$$+ D_3(j,m,n)\, A_m^* \frac{dA_n}{dt} + D_4(j,m,n)\, A_m^* \frac{dA_n^*}{dt} \Big\} = 0 \qquad (25)$$

$$j = 1,2, \ldots N$$

which is a system of N equations in N unknowns. The coefficients C_0, C_1, C_2, C_3, and C_4 differ from those in Equations (22) and are given in Appendix C; the coefficients D_1, D_2, D_3, and D_4 are the same as those appearing in Equations (22). In order to handle the integral terms in Equations (25), auxiliary variables $G_m(t)$ are defined by

$$G_m(t) = e^{-Kt} \int_0^t A_m(t')e^{Kt'}\, dt' \qquad (26)$$

The $G_m(t)$'s are described by the following equations

$$\frac{dG_m}{dt} = A_m(t) - KG_m(t) \qquad m = 1,2, \ldots N \qquad (27)$$

which are obtained by differentiating Equations (26). Solutions for the $A_j(t)$'s are then obtained by numerically solving Equations (25) simultaneously with Equations (27). The pressure perturbation is then obtained from the appropriate form of the momentum equation (Appendix A):

$$p' = -\gamma \Big[\varphi_t + \bar{u}(x)\varphi_x + \frac{1}{2}\varphi_x^2 - \frac{1}{2}\varphi_t^2 + \frac{d\bar{u}}{dx}\varphi$$

$$+ K\bar{\rho}_p(x)\varphi - K^2\bar{\rho}_p(x)e^{-Kt} \int_0^t \varphi\, e^{Kt'}\, dt' \Big] \qquad (28)$$

where φ is the real part of Φ given by Equation (19a) and the integral term is given by:

$$e^{-Kt} \int_0^t \varphi e^{Kt} dt = Re \left\{ \sum_{m=1}^{N} G_m(t)\ X_m(x) \right\} \tag{29}$$

2.4. Method of Averaging

The theory presented thus far represents a two-stage simplification of the original problem. In the first stage the problem has been reduced to the solution of a pair of nonlinear, partial differential equations (i.e., Equations (13) and (14)). In the second stage the solution was expanded in a series of acoustic modes with time-dependent amplitudes and the Galerkin Method was used to replace the solution of the nonlinear partial differential equations with the solution of a system of nonlinear ordinary differential equations (i.e., Equations (22) and (23) or (25)). As demonstrated in Reference 10 a further simplification of the problem (and reduction in computation time) may be obtained by using the Method of Averaging (referred to hereafter as MOA) to reduce Equations (22) and (23) or Equations (25) into a system of first order, coupled differential equations describing the growth or decay of the unknown amplitudes $A_j(t)$. A brief description of the application of the MOA to the present problem is given below; further details are available in References 10 and 19.

To apply the MOA the governing equations must be expressed in the following form:

$$\frac{d^2A_j}{dt^2} + \omega_j^2 A_j = F_j \qquad j = 1, 2, \ldots, N \tag{30}$$

where F_j is a nonlinear function of the various A_j and $\frac{dA_j}{dt}$. According to the MOA each unknown amplitude $A_j(t)$ is expressed as

$$A_j(t) = a_j(t) \sin(\omega_j t) + b_j(t) \cos(\omega_j t) \tag{31}$$

where $a_j(t)$ and $b_j(t)$ are assumed to be slowly-varying functions of time (i.e., their fractional changes during one period are small). The functions $a_j(t)$ and $b_j(t)$ are then determined from the following first order equations

---

[19] Nayfeh, A. H., Perturbation Methods, p. 165, John Wiley & Sons, 1973.

$$\frac{da_j}{dt} = \frac{1}{\omega_j \tau_1} \int_t^{t+\tau_1} F_j \cos(\omega_j t')dt' \qquad (32a)$$

$$\frac{db_j}{dt} = -\frac{1}{\omega_j \tau_1} \int_t^{t+\tau_1} F_j \sin(\omega_j t')dt' \qquad (32b)$$

$$j = 1,2, \ldots N$$

where $\tau_1 = 2\pi/\omega_1$.

The solutions of Equations (32) require less computation time as these equations only describe the slowly-varying parts of the unknown amplitudes $A_j(t)$, as the oscillatory, rapidly-varying parts of the solutions are specified by $\sin \omega_j t$ and $\cos \omega_j t$ in Equation (31).

The MOA was first applied to Equations (22) and (23), but the resulting solutions were unstable when particles were present in the combustor flow. Thus Culick's approach[10] was adopted and the MOA was applied to Equations (25). These equations are a system of coupled differential equations to be solved for the unknown complex amplitude functions, $A_j(t)$. In order to apply the MOA to this system, they must first be separated into their real and imaginary parts. This is done by assuming that $A_j(t) = F_j(t) + iG_j(t)$, substituting into Equations (25), and separating real and imaginary parts to obtain the equivalent system of real differential equations that describe the behavior of the F_j's and G_j's. Since these equations contain twice as many unknown functions (i.e., F_j and G_j) as Equations (25) it is convenient to re-index the unknown functions and their coefficients as follows:

$$F_p(t) = B_{2p-1}(t)$$

$$G_p(t) = B_{2p}(t) \qquad (33)$$

Thus the B's with odd indices correspond to the real parts, $F_p(t)$, and the B's with even indices correspond to the imaginary parts, $G_p(t)$. The corresponding set of differential equations is of the following form:

$$\sum_{p=1}^{2N} \left\{ C_o'(j,p) \frac{d^2 B_p}{dt^2} \right\} = g_j(B_1, B_2, \cdots B_{2N}, \frac{dB_1}{dt}, \frac{dB_2}{dt}, \cdots \frac{dB_{2N}}{dt}) \quad (34)$$

$$j = 1,2,\ldots 2N$$

The above equations are coupled in the second derivatives; that is, there are two or more C_o' terms in each equation. This coupling results from the non-orthogonality of the axial eigenfunctions. In order to apply the MOA to Equations (34), they must be decoupled by transforming to the form:

$$\frac{d^2 B_j}{dt^2} = f_j\left(B_1, B_2, \cdots B_{2N}, \frac{dB_1}{dt}, \frac{dB_2}{dt}, \cdots \frac{dB_{2N}}{dt}\right) \quad (35)$$

This transformation is accomplished by a matrix inversion technique described in Appendix C. Finally Equations (35) can be written in the form:

$$\frac{d^2 B_j}{dt^2} + \omega_j^2 B_j = F_j \quad (36)$$

where

$$F_j = \omega_j^2 B_j - \sum_{m=1}^{2N} \left\{ \tilde{C}_1(j,m) B_m + \left[\tilde{C}_2(j,m) + h_c \Re_m^r \tilde{E}_1(j,m) + h_c \Re_m^i \tilde{E}_2(j,m) \right] \frac{dB_m}{dt} + \tilde{C}_3(j,m) e^{-Kt} \int_o^t B_m(t') e^{Kt'} dt' \right\}$$

$$- \sum_{m=1}^{2N} \sum_{n=1}^{2N} \tilde{D}(j,m,n) B_m \frac{dB_n}{dt} \qquad j = 1, 2, \ldots 2N \quad (37)$$

Thus Equations (25) have been transformed to the required form given by Equations (30). The real coefficients C_1, C_2, C_3, E_1, E_2, and D are derived from the complex coefficients appearing in Equation (25) during the process of separating real and imaginary parts and decoupling the second derivatives (Appendix C).

The MOA is then applied to Equations (36) and (37) by assuming that

$$B_j(t) = g_j(t) \sin(\omega_j t) + h_j(t) \cos(\omega_j t) \tag{38}$$

where the $g_j(t)$ and $h_j(t)$ are slowly-varying functions of time. In performing the integrations indicated in Equations (32) the g_j and h_j are assumed constant (the basic assumption is that g_j and h_j do not vary significantly during the interval of averaging). The resulting equations describing the time-variation of the functions g_j and h_j are given by:

$$\begin{aligned}
\frac{dg_j}{dt} = \frac{1}{2\omega_j} \Bigg\{ & \omega_j^2 h_j - \sum_{m=1}^{2N} h_m \delta_{p\ell} \left[\tilde{C}_1(j,m) + \frac{K}{K^2+\omega_m^2} \tilde{C}_3(j,m) \right] \\
& - \sum_{m=1}^{2N} \omega_m g_m \delta_{p\ell} \left[\tilde{C}_2(j,m) + h_c \Re_m^r \tilde{E}_1(j,m) + h_c \Re_m^i \tilde{E}_2(j,m) - \frac{\tilde{C}_3(j,m)}{K^2+\omega_m^2} \right] \\
& - \frac{e^{-Kt}\left(e^{-\frac{2\pi K}{\omega_1}} - 1\right)}{K^2+\omega_j^2} \left[\omega_j \sin(\omega_j t) - K \cos(\omega_j t) \right] \frac{\omega_1}{\pi} \times \\
& \times \sum_{m=1}^{2N} \frac{\tilde{C}_3(j,m)}{K^2+\omega_m^2} \left[\omega_m g_m(0) - K h_m(0) \right] \\
& - \sum_{m=1}^{2N} \sum_{n=1}^{2N} \tilde{D}(j,m,n) \left[-\frac{\omega_n}{\pi} g_m h_n \beta_2(\ell,p,q) + \frac{\omega_n}{\pi} h_m g_n \beta_1(p,q,\ell) \right] \Bigg\}
\end{aligned} \tag{39a}$$

$$\frac{dh_j}{dt} = -\frac{1}{2\omega_j}\left\{ \omega_j^2 g_j - \sum_{m=1}^{2N} g_m \delta_{p\ell}\left[\tilde{C}_1(j,m) + \frac{K}{K^2+\omega_m^2}\tilde{C}_3(j,m)\right]\right.$$

$$+ \sum_{m=1}^{2N} \omega_m h_m \delta_{p\ell}\left[\tilde{C}_2(j,m) + h_c \tilde{R}_m^r E_1(j,m) + h_c \tilde{R}_m^i E_2(j,m) - \frac{\tilde{C}_3(j,m)}{K^2+\omega_m^2}\right]$$

$$+ \frac{e^{-Kt}}{K^2+\omega_j^2}\left[e^{-\frac{2\pi K}{\omega_1}} - 1\right]\left[K\sin(\omega_j t) + \omega_j \cos(\omega_j t)\right]\frac{\omega_1}{\pi} \times$$

$$\times \sum_{m=1}^{2N} \frac{\tilde{C}_3(j,m)}{K^2+\omega_m^2}\left[\omega_m g_m(0) - K h_m(0)\right]$$

$$\left. - \sum_{m=1}^{2N}\sum_{n=1}^{2N} \tilde{D}(j,m,n)\left[\frac{\omega_n}{\pi} g_m g_n \beta_2(q,p,\ell) - \frac{\omega_n}{\pi} h_m h_n \beta_2(p,q,\ell)\right]\right\} \qquad (39b)$$

$$j = 1,2,\ldots 2N \qquad (39b)$$

In these equations $\delta_{p\ell}$ is zero for $p \neq \ell$ and unity for $p = \ell$ and β_1 and β_2 are integrals of products of three trigonometric functions as defined in Appendix C. The indices ℓ, p, q are the axial mode numbers corresponding to the indices, j, m, n respectively. This notation is necessary because two $B_j(t)$ functions are needed to describe each mode.

To obtain nonlinear solutions for a rocket motor, initial amplitudes $g_j(0)$ and $h_j(0)$ are specified and Equations (39) are integrated numerically. The resulting solutions for $g_j(t)$ and $h_j(t)$ yield the growth or decay rates of the various modes directly. To obtain the pressure waveforms Equation (38) is used to compute the corresponding $B_j(t)$ which are then combined to obtain φ. Once $\varphi(x,t)$ is known the pressure perturbation, p' , is calculated using Equation (28).

A few comments regarding computation time will now be made. Applying the Galerkin method (without using the MOA) to Equation (17) yields a set of 2N second order equations and 2N first order equations after the real and imaginary parts have been separated. This is equivalent to a set of 6N first order equations. On the basis of the number of equations alone the MOA yields only a modest decrease in computation time. The advantage of the MOA lies in the fact that the g_j and h_j functions are slowly

varying, therefore a much larger time increment can be used in performing the numerical integrations resulting in a substantial saving in computation time. In order to evaluate the accuracy of the MOA, solutions obtained by the Galerkin method (without averaging) and solutions obtained by the MOA will be compared in Section IV.

2.5 Application to Motors

The approximate analyses (Galerkin method and MOA) may be applied to a variety of motor and T-burner configurations. The application of the approximate methods to determine the nonlinear stability behavior of a motor with a full-length tubular propellant grain and a quasi-steady nozzle (Figure 1) is discussed in this subsection. The application to T-burners is covered in the next subsection.

As mentioned previously, the coefficients that appear in Equations (22) and (23), (25), and (39) are dependent upon the steady-state properties $\bar{u}(x)$, $\bar{u}_p(x)$, and $\bar{\rho}_p(x)$. Therefore, the steady-state solutions must be obtained before the approximate analysis can be applied. Although these steady-state quantities could be obtained by numerically integrating the steady-state versions of Equations (1) through (6), it is more convenient to use an approximate analytical solution for the steady-state properties. In deriving the approximate unsteady equations, it was assumed that the steady-state values of ρ, p, and h (or T) were constants (the variation in these properties is of order $\bar{M}_e^2$). To this order of approximation the steady-state gas and particle velocities, $\bar{u}(x)$ and $\bar{u}_p(x)$, are linear functions of the axial coordinate x, and the particle density $\bar{\rho}_p(x)$ is a constant. The following expressions were determined by satisfying the steady-state continuity and momentum equations with $\bar{\rho}(x) = 1$ and $d\bar{\rho}_p/dx = 0$:

$$\bar{u}(x) = \left[\frac{2\dot{\bar{m}}_g}{R}\right]x = \bar{u}_e x \tag{40}$$

$$\bar{u}_p(x) = \frac{2\bar{u}_e x}{1+\sqrt{1+\frac{8\bar{u}_e}{K}}} = \left\{\frac{2}{1+\sqrt{1+\frac{8u_e}{K}}}\right\}\bar{u}(x) \tag{41}$$

$$\bar{\rho}_p = \frac{\bar{\dot{m}}_p}{2\bar{\dot{m}}_g}\left[1+\sqrt{1+\frac{8\bar{u}_e}{K}}\right] = \left\{\frac{1+\sqrt{1+8\bar{u}_e/K}}{2}\right\}C_m \qquad (42)$$

The derivation of these equations is given in Appendix D.

In order to obtain approximate stability solutions for motors, the nozzle admittance Y must also be specified. For conventional nozzles Y is a complex number which is dependent on nozzle geometry and oscillation frequency. For short nozzles the unsteady nozzle flow is nearly quasi-steady and Y becomes a real number which is independent of frequency. The value of Y for a quasi-steady nozzle is determined by the condition that the Mach number at the nozzle entrance is a constant. Assuming small perturbations and neglecting the effect of particles yields the following expression for Y:

$$Y_r = \frac{\gamma - 1}{2\gamma}\,\bar{u}_e$$

$$Y_i = 0 \qquad (43)$$

2.6 Application to T-Burners

The approximate methods described in this section were also used to analyze the nonlinear behavior of T-burners. Since the T-burner geometry differs in several important respects from that of motors, a detailed discussion of these differences is given in this subsection.

The T-burner geometry considered in this investigation is shown in Figure 3. The T-burner consists of a cylindrical tube of length L^* with a vent of length L_v^* at the center. In the simplest configuration, propellant disks are placed at each end of the T-burner (end-burning only). For metallized propellants it is often necessary to include short tubular grains of length L_b^* at the ends in order to increase the burning propellant surface area (cup grains). The cross-sectional area of the burner is S_{co}^*, while the cross-sectional area of the cylindrical grain is S_c^*. As in the case

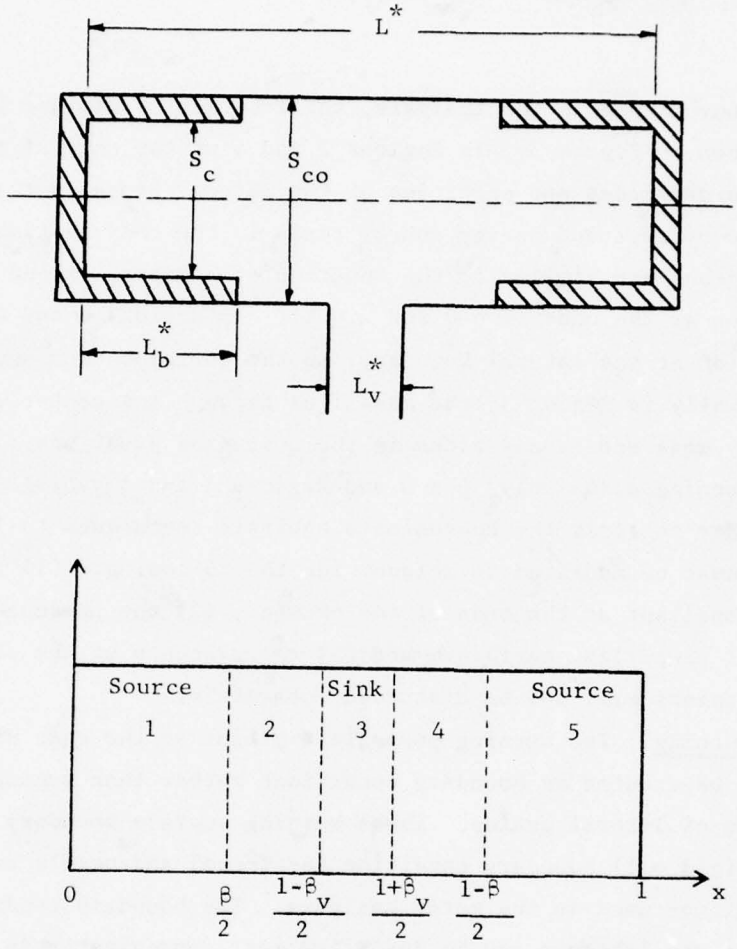

Figure 3. T-Burner Geometry

of motors, the axial variable x^* is normalized by the chamber length, thus $x = x^*/L^*$ and the dimensionless lengths of the cylindrical grains and the center vent are given by

$$\beta = 2L_b^*/L^* \quad , \quad \beta_v = L_v^*/L^* \tag{44}$$

For convenience in the analysis, the T-burner is divided into five regions as shown in Figure 3. In Regions 1 and 5 at the ends of the burner, the flux of burned gases and particles at the lateral propellant surface is represented by mass and energy source terms in the conservation equations. Thus these regions are similar to the interior of a motor, except for the boundary fluxes at the ends ($x = 0$ and $x = 1$). In Regions 2 and 4 there is no combustion at the lateral boundary, so the corresponding source terms are zero. Finally in Region 3, the mass flux through the center vent is represented by mass and energy sinks in the governing equations. For the case of end burning disks only, $\beta = 0$ and Regions 1 and 5 vanish.

In order to apply the approximate analysis techniques to T-burners, the analysis must be modified to account for the following: (1) the presence of burning propellant at the ends of the chamber, (2) the presence of partial length lateral propellant surfaces, and (3) the presence of the center vent. These points will now be discussed separately.

End Burning. The burning propellant grains at the ends of the T-burner must be treated as boundary conditions rather than source terms as in the case of lateral grains. These burning surface boundary conditions replace the rigid wall boundary condition (head-end) and nozzle admittance boundary condition used in the motor analysis. The boundary conditions at the ends of the T-burner can be described most conveniently in terms of the response function defined by Equation (9):

$$B_o = \Phi_x + \gamma \bar{u}_b (\mathcal{R} - 1)\Phi_t = 0 \qquad \text{at } x = 0$$

$$B_1 = \Phi_x - \gamma \bar{u}_b (\mathcal{R} - 1)\Phi_t = 0 \qquad \text{at } x = 1 \tag{45}$$

where $\bar{u}_b$ is the steady-state velocity of the burned gases leaving the propellant surfaces. In deriving Equation (45) from Equation (9) the assumption that

$\bar{\rho} = 1$ and $\bar{p} = 1$ was used, and p' was replaced by its first order equivalent $-\gamma\dot{\Phi}_t$. The difference in the signs for B_0 and B_1 arises because a positive pressure perturbation ($\Phi_t < 0$) yields a positive velocity perturbation at the left end ($\Phi_x > 0$) and a negative velocity perturbation at the right end ($\Phi_x < 0$). In other words, a positive flux (i.e., leaving the surface) gives positive velocities at x = 0 and negative velocities at x = 1, since the positive direction for velocities is taken to be the direction of increasing x.

In applying the Galerkin method to the T-burner, a boundary residual arises at both ends of the chamber, rather than just at one end as in the motor case. Thus the Galerkin orthogonality conditions given by Equations (21) are replaced by the following expressions:

$$\int_o^1 E\left\langle \tilde{\Phi}, \tilde{\Phi}_p \right\rangle X_j^*(x)dx + B_o\left\langle \tilde{\Phi} \right\rangle X_j^*(o) - B_1\left\langle \tilde{\Phi} \right\rangle X_j^*(1) = 0 \qquad (46a)$$

$$\int_o^1 E_p\left\langle \tilde{\Phi}, \tilde{\Phi}_p \right\rangle X_j^*(x)dx = 0 \qquad (46b)$$

$$j = 1,2,\ldots,N$$

where the E and E_p are the residuals of Equations (13) and (14) and the boundary residuals B_0 and B_1 are given by Equations (45). The eigenfunctions X_j are still given by Equation (20), but the corresponding b_j's are different from those used previously for the analysis of motors. The proper selection of the b_j's of course, should be the acoustic eigenvalues for a chamber with boundary conditions given by Equations (45). In the case of the T-burner, however, the velocities of the gases leaving the propellant surfaces are sufficiently small that these eigenvalues can be approximated by the eigenvalues for a closed-ended chamber. Thus the eigenvalues b_j are given by

$$b_j = j\pi \qquad j = 1,2,3,\ldots,N \qquad (47)$$

Partial Length Cylindrical Grains. The lateral burning surfaces are treated as source terms as was done previously for motors, but the approximate analysis has been extended to handle partial length grains. Two grain configurations are considered in this study: (1) disk grains only

and (2) cup grains (Figure 3). In the latter case flush grains ($S_{co} = S_c$) are assumed. Variable cross-sectional area has an important effect on mode shape and frequency.[20] Thus, to accommodate protruding or recessed grains, the mode shapes used in the assumed series expansion must be those given by Derr,[20] which are much more complicated than those presently used. Thus a major modification of the present analysis would be necessary to accommodate T-burners of variable cross-sectional area, which is beyond the scope of this project. Thus the approximate T-burner analysis is restricted to flush grain configurations.

In applying the Galerkin method to analyze T-burners with cup grains, the spatial integrations indicated in Equations (46) must be performed over three distinct types of regions. In the first type of region, the source terms present in the wave equation are due to lateral surface burning (Regions 1 and 5) and Equation (13) is used to obtain the residual $E(\tilde{\Phi})$. In the second type of region, the source terms are zero (Regions 2 and 4), and the residual $E(\tilde{\Phi})$ is obtained by dropping the $\frac{du}{dx}$ terms in Equations (13). The third type of region, the vent region, will be discussed later. These differences between the first two types of regions are automatically taken into account by introducing the appropriate steady-state solutions when the integrals are performed.

The steady-state solutions for Regions 1 and 2 (as well as Regions 4 and 5) were obtained from the steady-state continuity and momentum equations. In order to obtain analytical expresions for $\bar{u}(x)$, $\bar{u}_p(x)$, and $\bar{\rho}_p(x)$ a number of simplifying assumptions were made. These assumptions are consistent with the order of magnitude approximations used in deriving Equations (13) and (14). A discussion of these approximations and the derivation of the steady-state relations are given in Appendix D.

In the regions of lateral surface burning, the steady-state solutions are similar to those for motors, except for differences caused by the finite velocity at the ends of the burner. In Region 1 ($0 \leq x \leq \beta/2$) the steady-state solutions are:

---

[20] Derr, R. L., "Evaluation of a Variable Area T-Burner for Metallized Propellants," AFRPL-TR-72-97, February 1973.

$$\bar{u}(x) = \bar{u}_b\left(1 + \frac{2}{R}x\right) \tag{48}$$

$$\bar{u}_p(x) = \frac{\bar{u}_b}{1+\eta}\left\{1 + \frac{2}{R}x + \eta\left[1 + \frac{2}{R}x\right]^{-\frac{\eta+2}{\eta}}\right\} \tag{49}$$

$$\bar{\rho}_p(x) = \left\{\frac{1+\eta}{1 + \eta\left[1 + \frac{2}{R}x\right]^{-\frac{2\eta+2}{\eta}}}\right\} C_m \tag{50}$$

where $\eta = 4\bar{u}_b/RK$. For $x = 0$ these relations yield $\bar{u}(0) = \bar{u}_b$, $\bar{u}_p(0) = \bar{u}_b$, and $\bar{\rho}_p(0) = C_m$, which agree with the boundary values imposed on the steady state solutions. The gas velocity is seen to vary linearly with x with a slope given by:

$$\frac{d\bar{u}}{dx} = \frac{2\bar{u}_b}{R} \tag{51}$$

while the particle velocity approaches a linear variation with x after a short transitional distance δx. Similarly, the particle density approaches a constant value for $x > \delta x$. These asymptotic values are given as follows:

$$\bar{u}_p(x) = \frac{\bar{u}(x)}{1+\eta} \tag{52}$$

$$\bar{\rho}_p(x) = (1+\eta)C_m \tag{53}$$

For particle sizes of a few microns, η is a small positive number and the exponents appearing in Equations (49) and (50) are large, thus Equations (52) and (53) are very good approximations for all but very small values of x. In Region 5, the directions of the velocities $\bar{u}(x)$ and $\bar{u}_p(x)$ are opposite from those in Region 1, and the magnitudes of the steady-state properties are obtained from equations (48) through (50) by replacing x with 1-x. For $1 - \beta/2 \leq x \leq 1 - \delta x$ Equations (52) and (53) are also

valid, with $\bar{u}(x)$ given by:

$$\bar{u}(x) = - \bar{u}_b \left[1 + \frac{2}{R} (1-x) \right] \tag{54}$$

It should be noted that the slope $d\bar{u}/dx$ is the same in both Regions 1 and 5, since the steady-state mass fluxes at the lateral boundaries are the same in both regions.

In Regions 2 and 4 the steady state source terms vanish, and the gas velocity becomes a constant given by:

$$\bar{u}(x) = \pm \bar{u}_b (1 + \beta/R) \tag{55}$$

where the upper sign refers to Region 2 and the lower sign refers to Region 4. The magnitude of $\bar{u}(x)$ was obtained by substituting $x = \beta/2$ into Equation (48). The particle velocity in Region 2 is then given by (Appendix D):

$$\bar{u}_p(x) = \bar{u} (\beta/2) \left[1 - \frac{\eta}{1+\eta} e^{-\alpha(x-\beta/2)} \right] \tag{56}$$

where $\alpha = K/\bar{u}(\beta/2)$. For $x = \beta/2$ the exponential term is unity and Equation (56) yields $\bar{u}_p(\beta/2) = \bar{u}(\beta/2)/(1 + \eta)$ which is the velocity of the particles leaving Region 1. The exponential term decays rapidly with small increases in x to yield

$$\bar{u}_p(x) = \bar{u}(\beta /2) = \bar{u}_b(1 + \beta/R) \tag{57}$$

which is the same as the gas velocity in Region 2. The particle density quickly relaxes to the constant value given by

$$\bar{\rho}_p(x) = C_m \tag{58}$$

Again, the steady-state particle properties in Region 4 are obtained from the Region 2 properties by symmetry.

Center Vent. The effect of a subsonic exhaust vent at the center of the T-burner is modeled following the methodology of Levine and Culick.[5] Here, two effects are considered: (1) the mean flow/acoustics interaction, which vanishes in the absence of the mean flow, and (2) the acoustic radiation

through the vent, which remains finite in the absence of mean flow. For odd modes, the radiation effect is weak because the vent is located at a pressure node, but the mean flow/acoustics effect is strong due to the maximum acoustic velocity at this location. The opposite is true for even modes; the mean flow/acoustics effect is weak (velocity node) while the radiation effect is strong (pressure anti-node).

In considering the mean flow/acoustics vent effect, Levine and Culick[5] argued that the net effect is nearly zero. This result is obtained because the vent gain effect predicted by formal application of linear theory is cancelled by a vent loss due to viscous effects and the axial force exerted by the walls of the vent on the flow. Due to the possibility of a nonlinear mean flow/acoustics vent effect, however, Levine and Culick[5] retained the ability to vary the mean flow/acoustics vent effect in the nonlinear differential equations. This has also been done in the present approximate analysis.

In the vent region (Region 3 for $(1 - \beta_v)/2 \leq x \leq (1 + \beta_v/2)$), the conservation equations (i.e., Equations (1) - (5)), are modified as follows. The source terms $2\dot{m}_g/R$ and $2\dot{m}_p/R$ are replaced by ω and ω_p, respectively which are defined by:

$$\omega = - \frac{A_v}{\beta_v} u_n \tag{59}$$

$$\omega_p = - \frac{A_v}{\beta_v} \rho_p u_n \tag{60}$$

where A_v is the ratio of vent area to chamber cross-sectional area, and u_n is the dimensionless velocity of the flow out the vent. The minus sign indicates that ω and ω_p are negative for flow out of the burner (u_n positive), and it has been assumed that both gas and particles exit with the same velocity u_n. In the gas and particle momentum equations (i.e., Equations (2) and (3)) the axial velocities in the source terms arising from mean flow/acoustic interactions are multiplied by the factor $1 - V_\ell$. Setting $V_\ell = 0$ yields vent gain which corresponds to the combustion products losing their axial momentum as they exit through the vent. For $V_\ell = 1$ the combustion products retain their axial momentum and the net vent effect is zero, and $V_\ell = 2$ gives a vent loss. Using the order of magnitude analysis given in

Appendix A, the modified conservation equations are combined to yield the following nonlinear equations, valid in the vent region:

$$\Phi_{xx} - \Phi_{tt} = 2\bar{u}\Phi_{xt} + (\gamma + 1 - V_\ell)\frac{d\bar{u}}{dx}\Phi_t + 2\Phi_x\Phi_{xt} + (\gamma - 1)\Phi_t\Phi_{xx} + K\bar{\rho}_p(\Phi_t - \Phi_{p_t}) - (\gamma - 1)\bar{\rho}_p\bar{u}_p(\Phi_p)_{xt} + \omega' h_c \qquad (61)$$

$$(\Phi_p)_t + \bar{u}_p(\Phi_p)_x + \frac{1}{2}(\Phi_p)_x^2 = K(\Phi - \Phi_p) - (1 - V_\ell)\frac{d\bar{u}_p}{dx}\Phi_p \qquad (62)$$

$$p' = -\gamma\left[\varphi_t + \bar{u}\varphi_x + \frac{1}{2}\varphi_x^2 - \frac{1}{2}\varphi_t^2 + K\bar{\rho}_p(\varphi - \varphi_p) + (1 - V_\ell)\frac{d\bar{u}}{dx}\Phi\right] \qquad (63)$$

where

$$\omega' = -\frac{A_v}{\beta_v}u_n' \qquad (64)$$

The acoustic radiation vent effect is described by the term $\omega' h_c$ appearing in Equation (61). This introduces the additional unknown quantity, u_n' into the equations. Assuming plug flow in the pipe connecting the burner with the surge tank, the following transient vent equation is obtained from the unsteady, incompressible, momentum equation[5]:

$$\rho_o L_{eff} \frac{du_n}{dt} + \rho_o \frac{u_n^2}{2} = \bar{p} - p_s \tag{65}$$

In this equation, L_{eff} is the effective plug length, ρ_0 is the steady state density, P_s is the surge tank pressure (assumed constant), and P is the average pressure over the vent; that is,

$$\bar{p} = \int_{\frac{1-\beta_v}{2}}^{\frac{1+\beta_v}{2}} p(x', t)dx' \tag{66}$$

To obtain the corresponding equation for the perturbation u'_n, $u_n = \bar{u}_n + u'_n$ is introduced into Equation (65) and the steady state terms are subtracted out to give:

$$L_{eff} \frac{du'_n}{dt} + \bar{u}_n u'_n + \frac{1}{2}(u'_n)^2 = \int_{\frac{1-\beta_v}{2}}^{\frac{1+\beta_v}{2}} p'(x', t)\, dx' \tag{67}$$

where $\rho_0 = 1$ has been used. Neglecting the nonlinear term as higher order and replacing p' by its first order equivalent $-\gamma\Phi_t$ gives

$$L_{eff} \frac{du'_n}{dt} + \bar{u}_n u'_n = -\gamma \int_{\frac{1-\beta_v}{2}}^{\frac{1+\beta_v}{2}} \Phi_t(x', t)dx' \tag{68}$$

In the vent region (Region 3) the steady-state quantities are also obtained by integrating the steady-state continuity and momentum equations, where the steady-state mass source, $\bar{\omega}$, is given by:

$$\bar{\omega} = - \frac{2\bar{u}_b}{\beta_v} (1 + \beta/R) \tag{69}$$

The steady-state gas velocity is then given by:

$$\bar{u}(x) = \frac{\bar{u}_b(1+\beta/R)\ (1-2x)}{\beta_v} \tag{70}$$

for $(1 - \beta_v)/2 \leq x \leq (1 + \beta_v)/2$. This expression shows that $\bar{u}(x)$ decreases linearly from $\bar{u}_b(1 + \beta/R)$ at the left boundary of Region 3 to $-\bar{u}_b(1 + \beta/R)$ at the right boundary. The steady-state gas velocity vanishes at the center of the burner ($x = 1/2$). The particle velocity and density in the vent region are described by the following expressions (Appendix D):

$$\bar{u}_p(x) = \frac{\bar{u}_b(1+\beta/R)}{1 - \eta_v} \left\{ \frac{1 - 2x}{\beta_v} - \eta_v \left[\frac{1 - 2x}{\beta_v} \right]^q \right\} \tag{71}$$

$$\bar{\rho}_p(x) = \left\{ \frac{1 - \eta_v}{1 - \eta_v \left[\frac{1-2x}{\beta_v} \right]^{q-1}} \right\} C_m \tag{72}$$

where $q = 2/\eta_v + (V_\ell - 1)$

and $\eta_v = \frac{(4 - 2V_\ell)\bar{u}_b(1 + \beta/R)}{K\beta_v}$

These expressions are valid for $(1 - \beta_v)/2 \leq x \leq 1/2$, while the corres-

ponding values for $1/2 \leq x \leq (1 + \beta_v)/2$ are obtained from symmetry. As in Region 1 the exponent q is large for particle sizes of a few microns; thus, except in thin zones adjacent to the boundaries of Region 3, $\bar{u}_p(x)$ and $\bar{\rho}_p(x)$ are well approximated by

$$\bar{u}_p(x) = \frac{\bar{u}(x)}{1 - \eta_v} \tag{73}$$

$$\bar{\rho}_p(x) = (1 - \eta_v)C_m \tag{74}$$

which are similar to Equations (52) and (53) for Region 1. Steady-state values for a typical T-burner configuration with cup grains are shown in Figure 4.

An additional steady-state value is needed in the vent region; that is, the steady-state velocity of the flow out the vent, $\bar{u}_n$. This quantity appears in Equation (68) and is given by:

$$\bar{u}_n = \frac{2\bar{u}_b\ (1 + \beta/R)}{A_v} \tag{75}$$

Amplitude Equations for T-Burners. To summarize the solution procedures for T-burners, the application of the Galerkin method in the five regions previously discussed will now be outlined. The series expansions for $\tilde{\Phi}$ and $\tilde{\Phi}_p$ given by Equations (19) with $b_j = j\pi$ are substituted into the appropriate differential equations and boundary conditions to form the residuals $E\left\{\tilde{\Phi}, \tilde{\Phi}_p\right\}$, $E_p\left\{\tilde{\Phi}, \tilde{\Phi}_p\right\}$, $B_o(\tilde{\Phi})$, and $B_1(\tilde{\Phi})$. In Regions 1, 2, 4, and 5, Equations (13) and (14) are used to obtain E and E_p, respectively, while Equations (61) and (62) are used to obtain these residuals in Region 3. The Galerkin orthogonality conditions given by Equations (46) are then applied to obtain a system of second-order ordinary differential equations for the mode-amplitudes $A_j(t)$. The spatial integrations indicated in Equations (46) are evaluated piecewise in each of the five regions, using the appropriate residuals in each region.

The resulting system of differential equations is similar to that

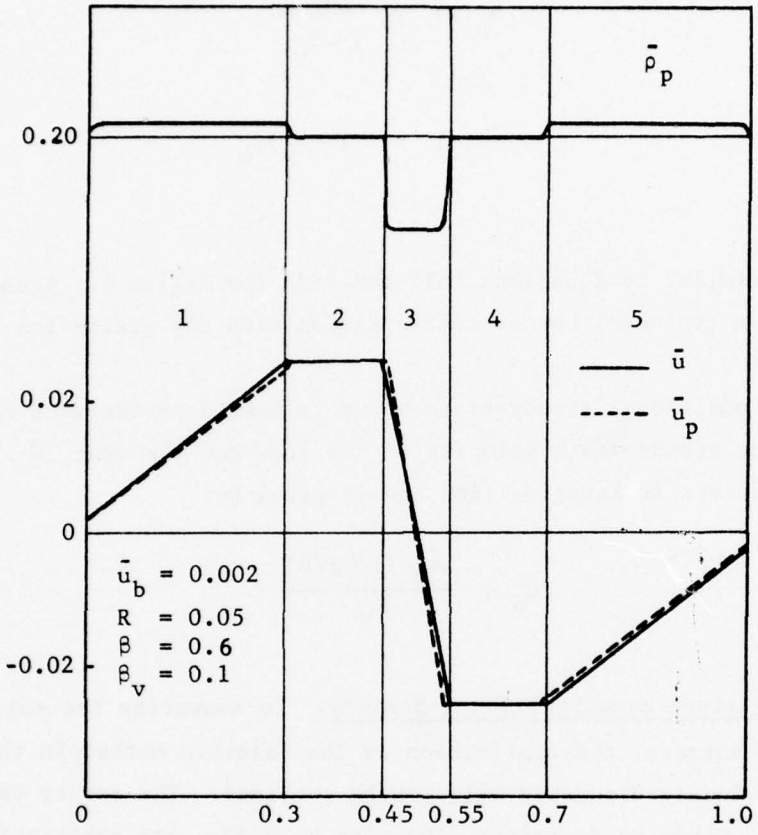

Figure 4. T-Burner Steady-State Properties

obtained for motors (i.e., Equations (22) and (23)), however, some differences should be noted. Due to the acoustic radiation term (i.e., $\omega' h_c$) appearing in Equation (61) for the vent region, additional terms of the form $C_7(j)u_n'$ appear in the T-burner mode-amplitude equations. Since u_n' is an additional unknown quantity, another equation is needed in order to obtain solutions. The required equation is supplied by substituting the series expansion for $\tilde{\Phi}$ into the unsteady flow vent equation (i.e., Equation (68)) and performing the indicated integration over the length of the vent. The resulting equation is of the form:

$$\frac{du_n'}{dt} + (\bar{u}_n/L_{eff})u_n' = -(\gamma/L_{eff}) \sum_{j=1}^{N} C_7(j) \frac{dA_j}{dt} \qquad (76)$$

where $\bar{u}_n$ is given by Equation (75). The coefficients of the linear terms in the T-burner equations also differ from the corresponding coefficients (i.e., C_1 through C_6) in the motor equations, due primarily to the differences in the steady-state properties and the presence of burning propellant disks at the ends of the burner. Expressions for the linear coefficients in the T-burner equations are given in Appendix C. The coefficients of the nonlinear terms in the T-burner equations are the same as the corresponding coefficients in the motor equations.

2.7 Nonlinear Combustion Driving

In the analysis developed in the preceding sections, the response of the burning rate to pressure oscillations was described by a linear response function (see Equations (9) through (11)). Based on intuition and studies conducted at Georgia Tech[2,3] and elsewhere[5], it is expected that as the amplitude of the oscillation grows, the true combustion response departs from the linear value predicted by Equation (9). Thus, a nonlinear expression relating the perturbations in burning rate to the gas flame pressure fluctuations is needed, if accurate stability predictions are to be obtained.

A nonlinear pressure coupled response is presently included in the "exact" analysis developed by Kooker and Zinn (in fact one of the modifications of the "exact" theory required for the study of gasdynamic non-linearities was to replace this nonlinear response with a linear one).

This nonlinear response is obtained by solving the governing equations describing the thermal wave in the solid, the surface pyrolysis reactions, and the gas phase reactions simultaneously with the conservation equations describing the unsteady flow in the chamber and nozzle. In order to use the same approach in the approximate analysis, it would be necessary to apply the Galerkin Method to obtain the behavior of the temperature in the solid propellant and the flame zone. In principle, this solution for the combustion response would have to be obtained simultaneously with the solutions of the combustor conservation equations, as was done in the "exact" analyses[2,3]. Attempts to use the Galerkin Method to obtain the nonlinear solid propellant combustion response were made during the development of the Kooker-Zinn model; however, these studies have shown that the approximate technique was unsuitable for properly predicting the nonlinear propellant response. Based upon this experience, it is expected that the same difficulties would also be encountered when attempting to incorporate the nonlinear combustion response into the present approximate analysis. Thus, in the absence of any other nonlinear models for pressure coupling, a heuristic combustion model has been used in the studies to assess the importance of modelling the nonlinear combustion response.

A number of possible expressions for describing the nonlinear burning rate could be obtained by adding various nonlinear terms to the linear burning response, such as terms proportional to $|p'|$, $(p')^2$, $|p'|(p')$, and $(p')^3$. Since the primary concern here is determining the effect of nonlinearities in the combustion response upon the nonlinear stability characteristics of a motor, rather than determining the correct form of the nonlinear combustion response, the simplest of these heuristic models was used. Thus a nonlinear combustion response was incorporated into the approximate analysis by replacing the linear response functions $\Re_m$ appearing in Equations (22) with nonlinear response functions $\Re_{NL_m}$ given by:

$$\Re_{NL_m} = \Re_m \left[1 + b_m \left| \frac{dA_m}{dt} \right| \right] \tag{77}$$

In Equation (77) $\Re_m$ is the linear response factor for the m^{th} mode, b_m is a complex constant, and $|dA_m/dt|$ is the magnitude of the complex ampli-

tude function given by

$$\left| \frac{dA_m}{dt} \right| = \sqrt{\left(\frac{dA_m^r}{dt}\right)^2 + \left(\frac{dA_m^i}{dt}\right)^2} \tag{78}$$

where the superscripts r and i denote real and imaginary parts of A_m, respectively. Since the pressure amplitude is proportional to $|dA/dt|$, the effective nonlinear response factor, $\Re_{NL}$, is a complex number whose magnitude and phase are linear functions of the amplitude of the oscillation. This expression reduces to the linear burning rate expression in the limit of small amplitude oscillations. At larger amplitudes the magnitude of the response factor will be increased or decreased from its linear value according to the value of b; also, the phase will be shifted if the imaginary part of b is nonzero. Calculated solutions obtained using this heuristic nonlinear combustion model are presented in section 4.3, where they are compared with approximate solutions obtained with the linear combustion response ($b_m = 0$) as well as with "exact" solutions obtained using the Kooker-Zinn nonlinear combustion model.

2.8 Nonlinear Particle Damping

In the preceding sections it was assumed that the viscous interaction between the particles and gas was described by the Stokes Drag Law (Equations (7) and (8)) for which the drag force is proportional to the relative velocity between the particles and gas. This linear drag law is valid for small Reynolds numbers up to about unity. For many situations encountered in solid rocket motors, however, the particle sizes and frequencies are sufficiently large that higher Reynolds numbers can occur. In these situations the Stokes law is no longer applicable and a nonlinear drag law must be used. The nonlinear particle drag effects are described by a higher order correction to the Stokes law given by[21]

---

[21] Rudinger, G., "Effective Drag Coefficients for Gas-Particle Flow in Shock Tubes," Project Squid Technical Report CAL-97-PU, March 1969.

$$F_p = K\rho_p(u - u_p)\left[1 + \frac{Re}{6}^{2/3}\right] \tag{79}$$

where Re is the Reynolds number given by

$$Re = \frac{\rho_o^* c_o^* \sigma^*}{\mu^*} \rho \left| u - u_p \right| \tag{80}$$

The straightforward, rigorous method of introducing the nonlinear particle drag law (Equation (79)) into the approximate analysis is to substitute Equation (79) for F_p where it appears in the gas and particle momentum equations (i.e., Equations (3) and (4)) and the energy equation (i.e., Equation (5)) and to follow the same order of magnitude analysis outlined in Section 2.2 and Appendix A. This procedure leads to insurmountable difficulties due to the highly nonlinear form of the drag correction term (i.e., the absolute value of the relative velocity raised to the 2/3 power). The first difficulty arises when attempting to separate the steady-state component from the equations. The relative velocity term can be written as $|\bar{u} - \bar{u}_p|^{2/3}\left|1 + (u' - u_p')/(\bar{u} - \bar{u}_p)\right|^{2/3}$, but a binomial expansion of this term is valid only if $(u' - u_p')/(\bar{u} - \bar{u}_p) << 1$. Since the relative velocity perturbation $u' - u_p'$ may often be of the same order of magnitude as the steady state relative velocity $\bar{u} - \bar{u}_p$, the binomial expansion can not be used and the steady state and perturbation quantities can not be separated. Even if this difficulty did not exist, other problems arise when attempting to combine the conservation equations to obtain the gas and particle potential equations by the procedure followed in Appendix

A. Finally, the absolute value in the drag correction terms make it impossible to separate the time and space variables when applying the Galerkin method, a crucial step needed in order to evaluate the spatial integrations involved.

Because of these difficulties in obtaining equations for the gas and particle potentials with F_p given by Equation (79), a heuristic approach is followed. It is tacitly assumed that the effect of particle drag nonlinearities can be described by the previously derived mode-amplitide equations (i.e., Equations (22) and (23)) in which the linear drag constant K is replaced by a nonlinear drag coefficient $\tilde{K}$ which is amplitude dependent. It is postulated that K has the following form:

$$\tilde{K} = K \left[1 + K_{ss} + CK_{NL} \left| A - A_p \right|^{2/3} \right] \tag{81}$$

where K is the original linear drag constant given by Equation (8), K_{ss} is a steady-state contribution to the nonlinear drag correction, K_{NL} is given by

$$K_{NL} = \frac{1}{6} \left\{ \frac{\rho_o^* \, c_o^* \, \sigma^*}{\mu^*} \right\}^{2/3} \tag{82}$$

and C is an adjustable parameter. The steady-state contribution is obtained by averaging the nonlinear drag term corresponding to the steady-state relative velocity, $\bar{u}(x) - \bar{u}_p(x)$, over the length of the motor. Since the steady-state relative velocity is proportional to x (Equations (40) and (41)), the value of K_{ss} is given by:

$$K_{ss} = \frac{1}{6} \left\{ \frac{\rho_o^* \, c_o^* \, \sigma^*}{\mu^*} \right\}^{2/3} (\bar{u}_e - \bar{u}_{p_e})^{2/3} \int_o^1 x^{2/3} dx \tag{83}$$

Evaluating the integral and using Equations (41) and (82) give

$$K_{ss} = \frac{3}{5} K_{NL} \left\{ \left[\frac{\sqrt{1 + 8\bar{u}_e/K} - 1}{1 + \sqrt{1 + 8\bar{u}_e/K}} \right] \bar{u}_e \right\}^{2/3} \tag{84}$$

The unsteady contribution to the drag correction is assumed to be proportional to the quantity $|A - A_p|^{2/3}$ where A and A_p are the complex gas and particle mode-amplitude functions for the fundamental mode (the effect of the higher modes upon this term has been neglected). The constant of proportionality for this term contains the $\sigma^{2/3}$ dependence expected from Equation (79), and the adjustable parameter accounts for the axial variation of the relative velocity perturbation $u' - u_p'$.

The heuristic nonlinear particle drag model described above has been incorporated into the approximate computer program. Calculated solutions obtained with this model are presented in Section 4.4 where they are compared with the available "exact" solutions. On the basis of these comparisons the validity of the heuristic nonlinear particle drag model is assessed.

3. EXACT ANALYSIS

The "exact" analysis developed by Kooker and Zinn,[2,3] which was used in the present investigation is based on a finite difference solution of the quasi-one-dimensional conservation equations for a solid rocket motor and nozzle combination. These equations are given as follows:

Continuity (gas)

$$\frac{\partial \rho}{\partial t} + \rho \frac{\partial u}{\partial x} + u \frac{\partial \rho}{\partial x} = \frac{2\dot{m}_g}{R} - \rho u \frac{d\ln A}{dx} \tag{85}$$

Continuity (particles)

$$\frac{\partial \rho_p}{\partial t} + \rho_p \frac{\partial u_p}{\partial x} + u_p \frac{\partial \rho_p}{\partial x} = \frac{2\dot{m}_p}{R} - \rho_p u_p \frac{d\ln A}{dx} \tag{86}$$

Momentum (gas)

$$\frac{\partial u}{\partial t} + u \frac{\partial u}{\partial x} + \frac{1}{\gamma \rho} \frac{\partial p}{\partial x} = -\left\{ K\rho_p (u - u_p) + \frac{2}{R} \dot{m}_g u \right\} / \rho \tag{87}$$

Momentum (particles)

$$\frac{\partial u_p}{\partial t} + u_p \frac{\partial u_p}{\partial x} = K(u - u_p) - \frac{2}{R} \frac{\dot{m}_p u_p}{\rho_p} \tag{88}$$

Energy (gas)

$$\frac{\partial S}{\partial t} + u \frac{\partial S}{\partial x} = \frac{\gamma(\gamma - 1)}{p} \left\{ \frac{2}{R} \left[\dot{m}_g \left(\frac{h_c - h}{\gamma - 1} \right) \right. \right. \tag{89}$$

$$\left. \left. + \frac{1}{2} \left(\dot{m}_g u^2 + \dot{m}_p u_p^2 \right) \right] + K\rho_p (u - u_p)^2 \right\}$$

where

$$S = \ln p - \gamma \ln \rho \tag{90}$$

The quantities $\dot{m}_g$ and $\dot{m}_p$ respectively represent the mass flow rates of gas and particles per unit surface area leaving the burning propellant surface. Here all mass addition due to the burning propellant occurs at the combustor

boundaries and the volume sources due to evaporation or combustion of particles are neglected. The source terms in the momentum equations result from the application of Stokes' Law to describe the particle drag and the force required to accelerate the incoming gas and particles to their local velocities. The source terms in the energy equation arise from the local addition of hot combustion products (with enthalpy h_c) entering the control volume from the flame zone and particle drag within the control volume. Including the area variation term in the continuity equation allows a quasi-one-dimensional solution for the unsteady flow in the nozzle as well as in the combustion chamber. A more complete description of the combustor model and method of numerical integration of the equations is given in Chapter II of Reference 3.

To complete the analysis, an unsteady combustion model is needed to determine the time-dependent quantities $\dot{m}_g$ and $\dot{m}_p$ which appear as mass and energy sources at the boundary of the combustor. This is done in the Kooker-Zinn model by solving the transient burning rate response to the imposed chamber pressure oscillations simultaneously with the chamber conservation equations. The combustion model used at each burning station along the propellant is based on the following four simplifying assumptions which have been employed in nearly all combustion instability studies to date:[12] (1) the unburned propellant is homogeneous and one-dimensional, (2) the conversion of the solid phase to gas is represented by a simple Arrhenius type pyrolysis law, (3) condensed phase reactions are neglected, (4) the behavior of the gas-phase flame zone is quasi-steady. Under these assumptions the problem separates into three distinct regions which are analyzed individually: (1) the nonreacting solid phase region, (2) the solid-gas interface where pyrolysis occurs, and (3) the gas-phase flame zone. The conservation equations describing the behavior of this model and their numerical solutions are discussed in Chapter III of Reference 3.

For the case of a constant area chamber, the above equations are identical to Equations (1) through (6) upon which the approximate analysis is based. Thus both the "exact" and approximate analyses are attempting to solve the same set of equations. However, the combustion response model and the treatment of the nozzle used in the original Kooker-Zinn model are different from those used in the approximate analysis. In order to facilitate comparisons with the approximate analysis, the original Kooker-

Zinn model was modified in the present study. A brief description of the required modifications is given below.

3.1 Modification for Quasi-Steady Nozzle

In the original Kooker-Zinn model the nonlinear governing equations were solved numerically throughout the entire system consisting of both the combustion chamber and the nozzle. The downstream boundary condition was imposed at an arbitrary location downstream of the nozzle throat where the flow is supersonic. The effect of the nozzle obtained from such an analysis is inherently nonlinear and would be expected to differ significantly from the nozzle effect obtained from the linear nozzle admittance boundary condition used in the approximate analysis. Therefore the "exact" analysis was modified by eliminating the nozzle form the flowfield and replacing it with a quasi-steady linear nozzle admittance condition to be satisfied at the nozzle-end of the chamber. The method of characteristics is used to obtain the boundary values at the nozzle-end in a manner similar to that used at the head-end. This modification allows the nozzle effect to be the same in both the approximate and "exact" analyses.

At the nozzle-end of the chamber, the velocity and pressure must satisfy the following relation:

$$u_e = \bar{u}_e + Y\,(p_e - \bar{p}_e) \tag{91}$$

where Y is the nozzle admittance and $\bar{u}_e$ and $\bar{p}_e$ are the corresponding steady-state quantities. For a quasi-steady nozzle (neglecting the effect of particles) the nozzle admittance Y is given by:

$$Y = \frac{\gamma-1}{2\gamma}\frac{\bar{u}_e}{\bar{p}_e} \tag{92}$$

These relations have been incorporated into the method of characteristics solution for the dependent variables at the nozzle-end boundary. The nozzle calculations are performed by a new subroutine (NOZMOC) which was added to the existing "exact" computer program.

A test case was run at this point to check out the quasi-steady nozzle modification. Pressure waveforms calculated with a conventional (i.e., nonlinear) nozzle and the quasi-steady nozzle are compared in Figure

5. Here it is seen that substituting the quasi-steady nozzle for the conventional nozzle results in an increase in the frequency of the oscillation and a decrease in the decay rate. The increased frequency results from the decrease in length over which the wave travels, and the decrease in damping results because the quasi-steady nozzle is more like a hard-wall termination than the conventional nozzle.

3.2 Linearized Burning Rate Model

The other modification of the "exact" analysis concerns the transient burning rate model. In the original "exact" analysis solutions were obtained for the thermal profiles in the solid propellant, which yield the surface temperature and regression rate at each increment of time. These profiles were coupled to the pressure oscillations in the chamber through the reaction kinetics in the flame zone and at the solid surface. These processes yielded a nonlinear response of the burning rate to the pressure oscillations.

Since the above model cannot be readily incorporated into the approximate analysis, the approximate solutions were obtained using a linear combustion response function Equation (9). In order to compare the results obtained with the approximate and "exact" theories, a linear combustion response model was incorporated into the "exact" analysis. Since the frequency and waveshape of the pressure oscillation are not known a priori, the two-parameter (A,B) form of the linearized response function (see Equation (10)) could not be introduced directly into the "exact" program. Instead, a perturbation analysis was performed on the nonlinear equations governing the response of the burning solid propellant to pressure disturbances, and the resulting higher order (i.e., nonlinear) terms were neglected. The resulting linear equations and boundary conditions are given below:

Energy Equation in Solid Propellant

$$T_t' + \bar{r} T_y' - T_{yy}' = - \bar{T}(y) r' \tag{93}$$

Surface Regression Law

$$\frac{r'}{\bar{r}} = \frac{E_s}{\bar{T}_s^2} T_s' \tag{94}$$

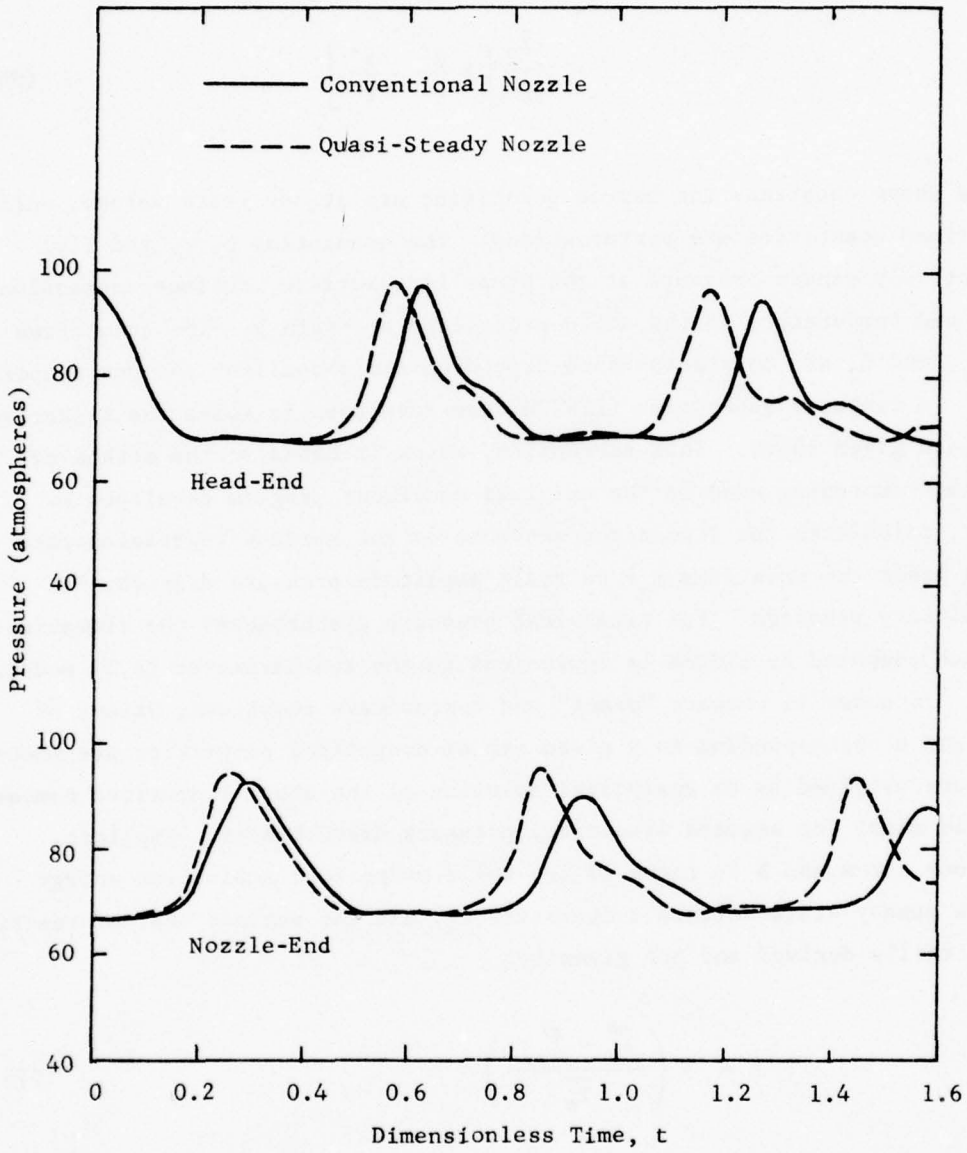

Figure 5. Comparison of Pressure Waveforms for Conventional and Quasi-Steady Nozzles

Boundary Conditions

$$T'(-y_o,t) = 0 \tag{95}$$

$$T'_y\ (o,t) = -Z_1 r' - \bar{r}\left(c_p^*/c_s^* - 1\right) T'_s + \frac{\bar{Z}_2}{\bar{r}}\left[2\,\frac{p'}{\bar{p}} - \frac{r'}{\bar{r}}\right] \tag{96}$$

In the above equations the barred quantities are steady state values, while the primed quantities are perturbations. The quantities p, r, and T(y) respectively denote pressure at the propellant surface, surface regression rate, and temperature in the solid propellant at depth y. The quantities E_s, Z_1, and Z_2 are constants which depend on the propellant and gas properties.

A computer subroutine (LINTHW) was developed to solve the linearized equations given above. This subroutine, which is based on the method of invariant imbedding used in the original nonlinear program developed by Kooker, calculates the linearized response of the surface regression rate r (and hence the mass flux $\dot{m}_g$) to small amplitude pressure disturbances of arbitrary waveform. For sinusoidal pressure disturbances the linearized response computed by LINTHW is equivalent to the two-parameter (A,B) model.

In order to compare "exact" and approximate solutions, values of A, B, and n corresponding to a given set of propellant properties are needed. These are obtained by an analytical solution of the above linearized combustion response model for assumed sinusoidal pressure disturbances. Explicit relations for A and B in terms of the solid propellant activation energy E_s^*, the steady state surface temperature T_s^*, and the surface heat of reaction Q_s^* are easily derived and are given by:

$$A = E\left(\frac{\bar{T}_s^* - \bar{T}_{cs}^*}{\bar{T}_s^*}\right) \tag{97}$$

$$B = \frac{1}{A}\left\{A + \frac{E\,Q_s^*}{c_s^*\,\bar{T}_s^*} + \frac{c_p^*}{c_s^*}\left(E\,\Lambda_o^2 + 1\right)\right\} \tag{98}$$

where

$$E = E_s^* / R_o \bar{T}_s^*$$

$$\Lambda_o^2 = \frac{Q_f^* k_g^* \bar{\omega}_o^*}{(\rho_s^* \bar{r}^* c_p^*)^2 \bar{T}_s^*}$$

$$\bar{\omega}_o^* = \omega_{con}^* \bar{p}^2 \exp (- E_f^* / R_o T_f^*)$$

In the linear analysis, the value of n cannot be obtained explicitly in terms of propellant properties but must be obtained from burning rate calculations at low frequencies. An auxiliary program which calculates the burning rate corresponding to a sinusoidal pressure input has been developed to determine the complex response factor $\Re$ by comparing the computed amplitude and phase of the burning rate perturbation with that of the pressure perturbation. This program is then used to determine the value of n, since the computed values of $\Re$ approach n as frequency approaches zero. After n is determined, values of $\Re$ are obtained for several different frequencies using both the linearized and nonlinear burning rate models. These values are compared with the response curve obtained analytically from the two-parameter linear response function described by Equations (10) and (11). An example of such a comparison is shown in Figure 6 where the close agreement obtained is an indication of the validity of both the linearized and nonlinear combustion models for small amplitude oscillations.

3.3 Nonlinear Particle Damping

In the original Kooker-Zinn "exact" model the particle drag was described by the Stokes Drag Law, which is a linear expression valid for Reynolds numbers of order unity. In order to include nonlinear particle drag effects which occur at higher Reynolds numbers (larger particle sizes and higher frequencies), the higher order correction to the Stokes Law[21] was incorporated into the "exact" analysis. Thus the drag term in the

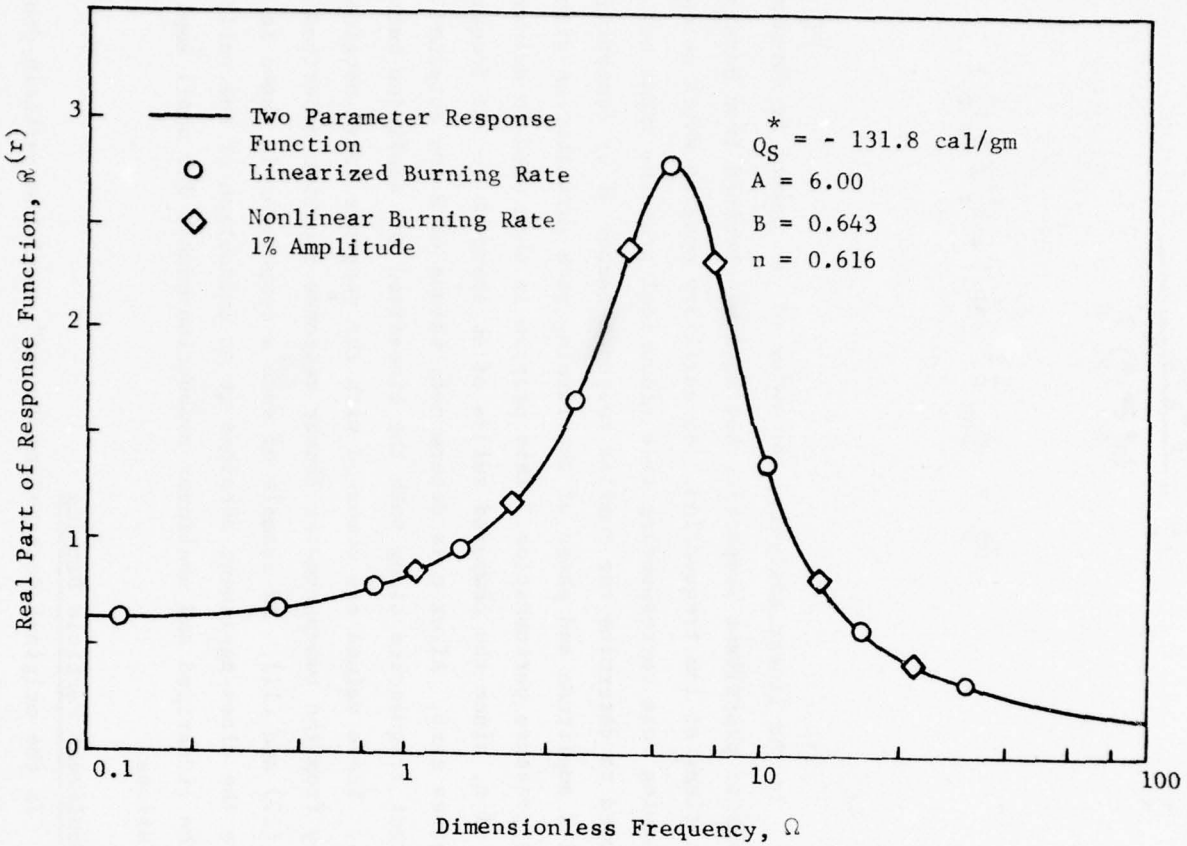

Figure 6. Comparison of Linearized and Nonlinear Combustion Models with the Two Parameter Response Function

momentum equation is given by Equations (79) and (80). A more convenient form for numerical calculations is given by

$$F_p = K\rho_p(u-u_p)\left[1 + K_{NL}\rho^{2/3}|u-u_p|^{2/3}\right] \tag{99}$$

where K_{NL} is given by Equation (82). These expressions are readily incorporated into the appropriate conservation equations (i.e., Equations (87) through (89)) by replacing the drag constant K with the variable drag coefficient $\tilde{K}$ defined by:

$$\tilde{K} = K\left[1 + K_{NL}\rho^{2/3}|u-u_p|^{2/3}\right] \tag{100}$$

The above nonlinear drag law has been incorporated into the Kooker-Zinn "exact" computer program; the linear drag law option is available by specifying $K_{NL} = 0$.

4. RESULTS AND DISCUSSION

In this section, numerical calculations of nonlinear axial mode instabilities in solid rocket motors and T-burners are presented and discussed. Most of the approximate solutions presented herein were calculated using the Galerkin method without averaging; that is, by obtaining numerical solutions of the system of second order differential equations given by Equations (22) and (23). These approximate solutions are compared with "exact" solutions obtained by the Kooker-Zinn model in many cases. The approximate solutions are also compared with Culick's approximate solutions (Method of Averaging) and Levine's "exact" solutions when available.

Most of the approximate solutions presented in this section were obtained in a parametric study to assess the importance of gasdynamic nonlinearities (mode-coupling) on the stability of solid rocket motors, a major objective of this program. In this study, the only nonlinear process considered was gasdynamical mode-coupling, while other processes such as combustion driving and particle damping were described by linear models. The following parameters were considered: (1) the number of modes used to describe the total wave, (2) the magnitude and harmonic content of the initial disturbance, (3) the characteristics of the propellant response function, (4) the oscillation frequency, and (5) the size and concentration of the aluminum oxide particles. The approximate and exact analyses are compared on the basis of the predicted growth or decay rates for the transient solutions and the final limiting amplitude and waveform. In addition, the transient behavior and relative amplitudes of the individual modes are determined.

In addition to the above parametric study approximate solutions are presented for (1) motors with a nonlinear combustion response to pressure oscillations, (2) motors with nonlinear particle damping, and (3) T-burners. Also solutions obtained using the Method of Averaging (MOA) are compared with the Galerkin method solutions for motors with and without particles. Finally approximate solutions are compared with available experimental data for both motors and T-burners.

4.1 Typical Nonlinear Solutions

Before presenting the results of the parametric studies, the applica-

tion of the approximate nonlinear analysis will be illustrated by an example.

To obtain an approximate solution for a given engine configuration and operating condition, the following must be specified: (1) the number of modes N present in the approximate series solution; (2) the structure of the initial disturbance (i.e., $A_j(0)$ and $dA_j(0)/dt$ for $j = 1, 2, \ldots 2N$); (3) the combustor and propellant grain lengths; (4) the nozzle admittance Y for each of the modes in the solution; (5) the combustion parameters A, B, and n or the values of $\Re$ for each mode; (6) the concentration and size of the aluminum oxide particles; (7) the mean flow Mach number at the nozzle entrance; (8) the steady-state temperature in the combustor and (9) the ratio of the specific heats of the gaseous phase. For the example considered here a five-mode series was employed, the initial disturbance was a pure fundamental mode (1L) oscillation of about 15% pressure amplitude, and the nozzle admittances for each of the modes were obtained by the quasi-steady nozzle relation (i.e., Equation (43)). The specific heat ratio was $\gamma = 1.2$ and the mean flow Mach number at the nozzle entrance was $\bar{M}_e = 0.10$. The response function was described by A = 7.54, B = 0.686, and n = 0.81 (Figure 7). This is the moderately strong response considered by Kooker in the "exact" analysis. Here the frequency Ω was chosen such that all of the modes lay on the descending branch of the response curve; thus, the real parts of the response function for the higher frequency modes were all smaller than the corresponding value for the fundamental (1L) mode. For such cases the series expansion in terms of the acoustic modes was expected to converge fairly rapidly, and the mode-coupling should tend to limit the amplitude. Finally, it was assumed that no particles were present in the combustor.

The approximate solutions (Galerkin method) for this case are shown in Figures 8 and 9. Figure 8 shows the relative magnitudes and transient development of the individual modes (i.e., the real parts of the functions $A_j(t)$) following the introduction of the pure 1L mode initial disturbance. It is seen that the amplitudes of the higher harmonics are much smaller than the amplitude of the fundamental mode. The transient development of the head-end pressure perturbation shown in Figure 9 was determined from the individual modes using Equations (19) and (24). The initially sinusoidal pressure waveform quickly becomes distorted due to the excitation of the higher harmonics.

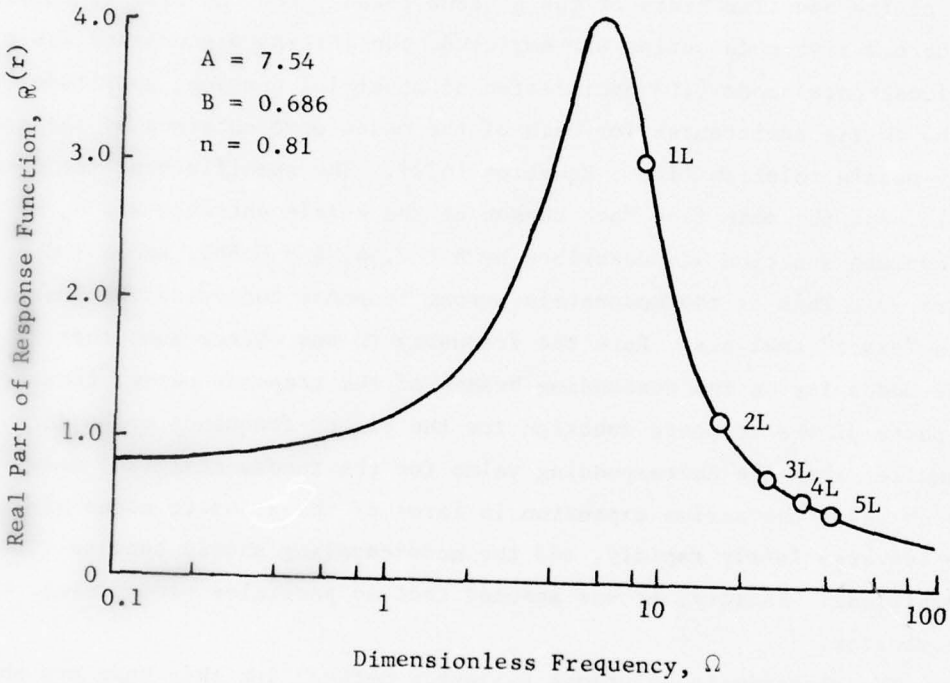

Figure 7. Moderate Response Curve with Positions of First Five Axial Modes

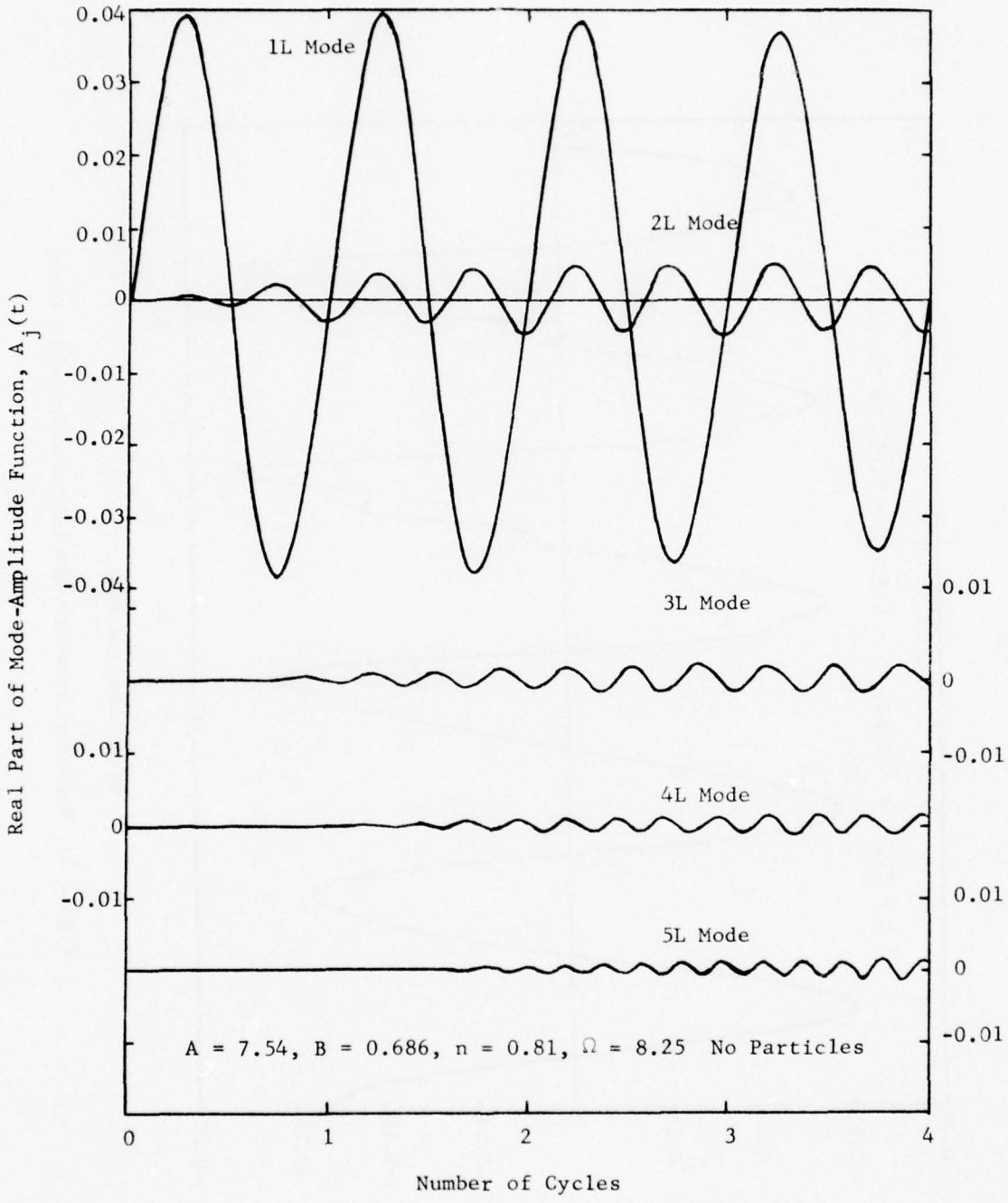

Figure 8. Amplitudes of Individual Modes for an Unstable Motor

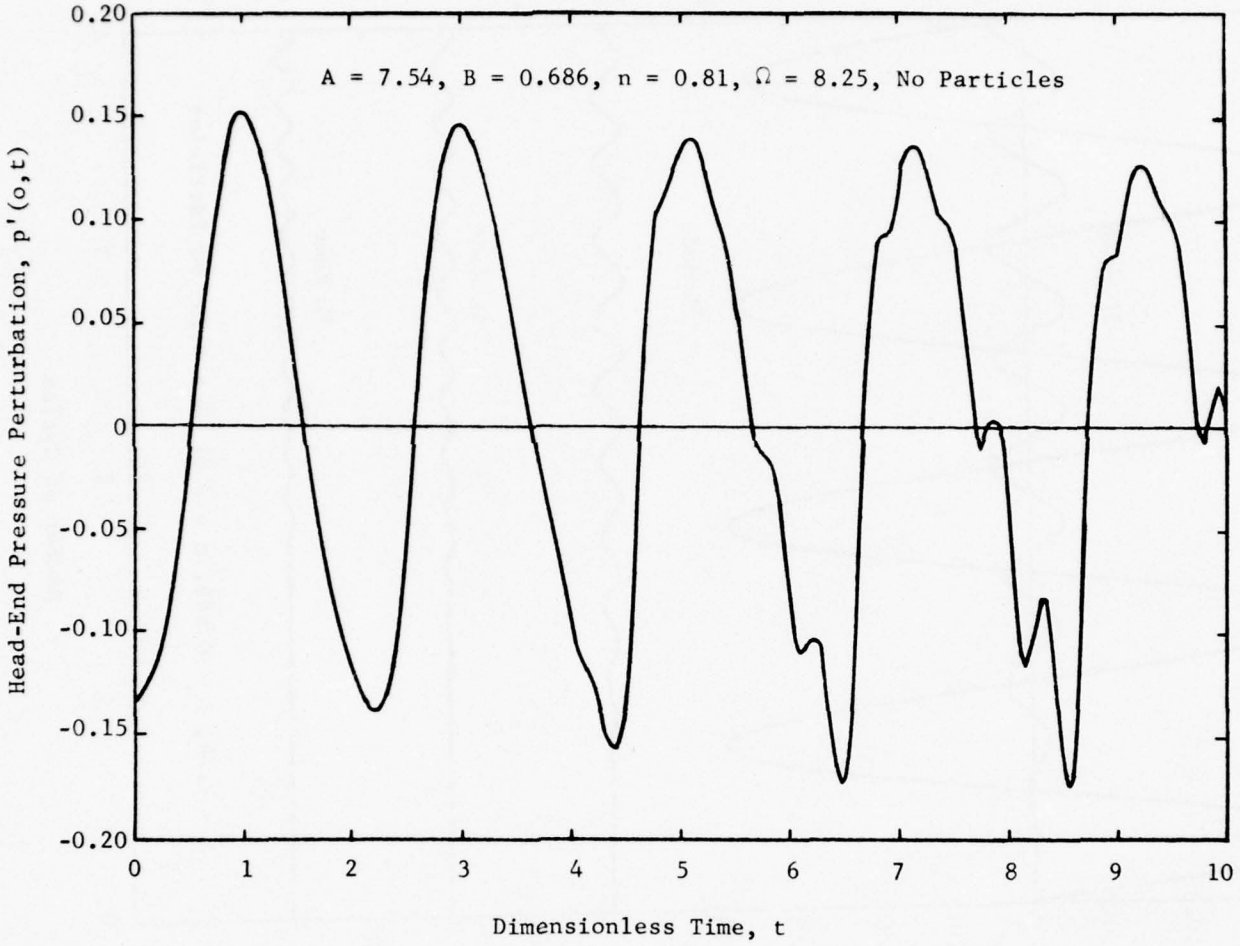

Figure 9. Head-End Pressure Waveform for Unstable Motor

It should be noted that the individual mode-amplitude functions in Figure 8 are the real parts of the $A_j(t)$'s for the gas-phase velocity potential; thus, they are the harmonic components of the velocity waveform rather than the pressure waveform. From Equations (19a) and (24) and the nearly sinusoidal shape of the $A_j(t)$'s, it is easily seen that the amplitudes of the corresponding harmonics of the pressure waveform are approximately obtained by multiplying the amplitudes of the $A_j(t)$'s by $\gamma j\omega_1$ where ω_1 is the frequency of the 1L mode. This relationship is valid for oscillations of sufficiently small amplitude that the second order terms in equation (24) are negligible. For larger oscillation amplitudes the individual pressure harmonics may be obtained by Fourier analysis of the waveform obtained by Equation (24).

4.2 Parametric Studies of Mode-Coupling

The basic set of motor parameters used in this study was based on the data given by Levine and Culick[3] which correspond to a small laboratory pulse motor. This motor has a grain length of about .597 m (1.958 ft) and an initial bore of about 50 mm (2 in). The physical properties of the propellant (ANB 3066), and its gaseous and particulate combustion products, are given in Table 1.

The data along with the endothermic heat release at the propellant surface (Q_s^*) is used as input to the Kooker-Zinn "exact" analysis, which then computes the corresponding values of A, B, and n which describe the transient propellant response. A reference state is also needed in order to evaluate some of the constants which appear in the burning rate model; in this case a surface regression rate of 1.17 cm/sec (0.459 in/sec) and a surface temperature of $800^{\circ}K$ ($1440^{\circ}R$) is assumed for a pressure of 10810 knt/m^2 (1568 psi). For most cases considered here, the mean chamber pressure is assumed equal to the above reference pressure. For this case the total flux of burned gases leaving the tubular propellant grain is 2.338 kg/sec which corresponds to a Mach number at the nozzle entrance of $\tilde{M}_e$ = 0.0780. For this combination of chamber length and steady-state temperature (T_f^*), the chamber sonic speed is 1278 m/sec (4194 ft/sec) giving a fundamental mode frequency of 1071 Hz for the pure gas (without particles)

When comparing the approximate solutions with the "exact" solutions, the values of A, B, and n computed from the above data are used as input

Table 1. ANB 3066 Propellant Data

Propellant			
density:	ρ_s^*	=	1.766 gm/cm^3
specific heat:	c_s^*	=	0.329 cal/gm-^{o}K
thermal conductivity:	k_s^*	=	1.791×10^{-4} cal/cm-sec-^{o}K
activation energy:	E_s^*	=	15,250 cal/mole
Gas-Phase Flame			
specific heat ratio:	γ	=	1.23
specific heat	c_p^*	=	0.483 cal/gm-^{o}K
thermal conductivity	k_g^*	=	1.658×10^{-4} cal/cm-sec-^{o}K
activation energy:	E_f^*	=	30,000 cal/mole
flame temperature:	T_f^*	=	3525^{o}K (6345^{o}R)
Particles			
density:	ρ_m^*	=	4.0 gm/cm^3
diameter:	σ	=	2.5 μ
particle loading:	C_m	=	0.36

to the approximate analysis. In order to completely define the values of $\Re^r$ and $\Re^i$ for each of the modes, the frequency parameters Ω_j are also needed for each mode. These are obtained from the computed frequency of the 1L mode and the steady state burning rate obtained from the "exact" analysis, and are given by:

$$\Omega_j = j\omega_1/\bar{r}^2 \qquad j = 1,2,\ldots N \tag{101}$$

The most useful parameter to vary to obtain different response functions is Q_s^* ; making Q_s^* more negative (exothermic) decreases B and yields larger values of the peak response. The frequency parameter is varied by changing the chamber length or by changing the steady state burning rate.

The results of the parametric studies will now be presented in the following order: (1) effect of number of modes in series, (2) effect of initial disturbance, (3) effect of propellant response function, (4) effect of frequency, and (5) effect of particles.

Effect of Number of Modes Used to Represent the Solution. Figures 10 and 11 show the effects of the number of modes N used to represent the approximate solutions for a case in which no particles are present. Solutions were obtained using a basic series consisting of the three lowest frequency axial modes (i.e., the first, second and third longitudinal modes). Higher harmonics were then added one at a time to the basic series and the resulting solutions were compared on the basis of wave shape and limiting amplitude. This comparison was used to determine the minimum number of modes needed to adequately describe the behavior of the unstable rocket motor with a minimum expenditure of computer time.

Figure 10 shows the development of the peak-to-peak head-end pressure amplitude with time for an initial 7% fundamental mode disturbance. The combustion parameters are A = 6.00, B = 0.590, n = 0.583 and Ω_1 = 4.907. The growth of the pressure oscillation amplitude is shown for one, three four, five, and six mode series expansions. For the one-mode series (N = 1) expansion, there is no nonlinear mode-coupling to limit the amplitude, so the oscillations grow at the linear rate of about 80 sec^{-1}. For $4 \leq N \leq 6$, increasing the number of modes decreases the predicted limit-cycle amplitude as a result of the nonlinear coupling of the fundamental mode with increasingly stable higher modes. The increased stability of

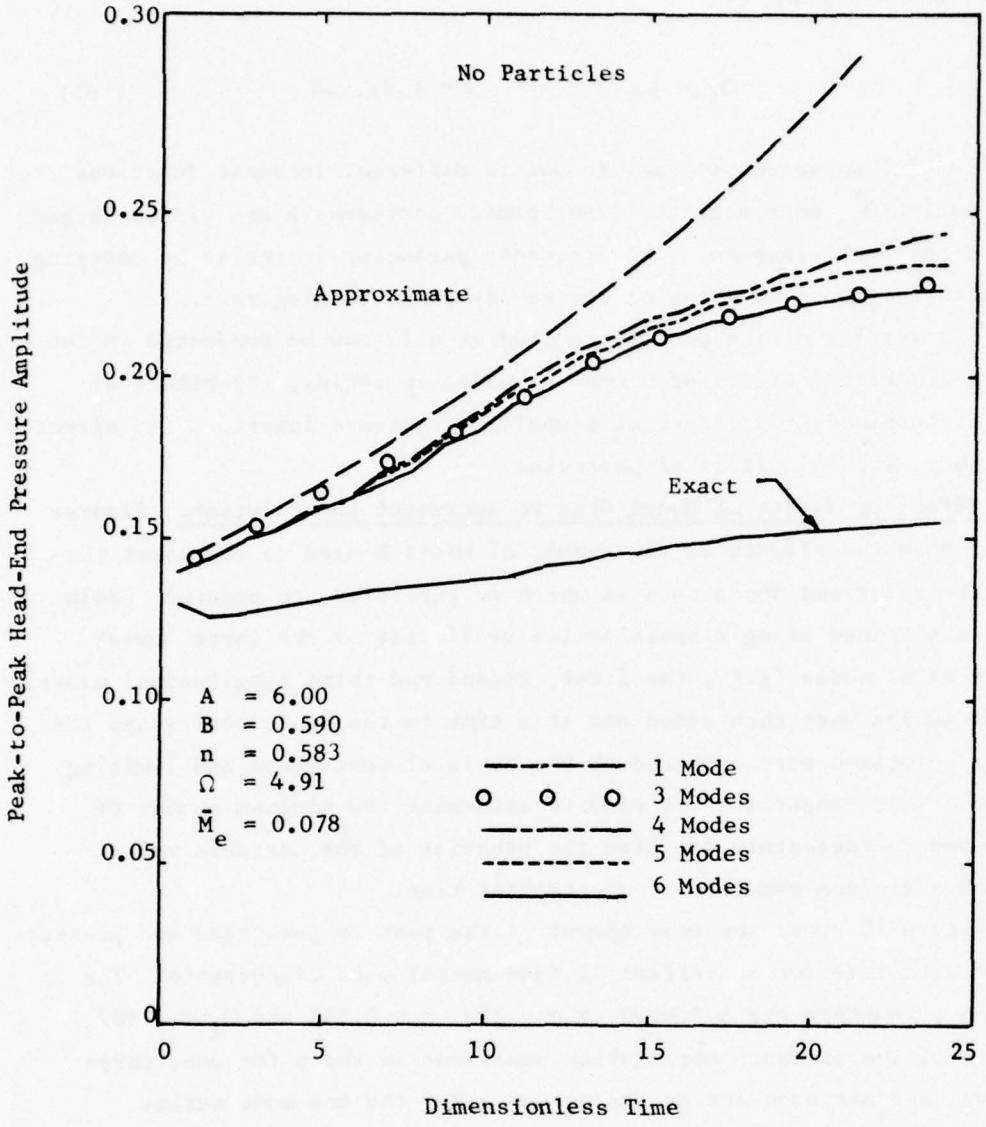

Figure 10. Effect of Number of Modes Used in the Approximate Analysis Upon Resulting Solution

these higher modes results from the decreased combustion response at higher frequencies for this case (Table 2). As the number of modes is increased, the approximate solutions also approach the "exact" solution also shown in Figure 10, but it is not clear from this figure that the approximate solutions converge to the "exact" solution in the limit of an infinite number of modes. Indeed, it appears that the approximate solutions will converge to a larger limiting amplitude than the "exact" solutions, probably due to the order of magnitude approximations made in deriving Equations (13) and (14) upon which the approximate technique is based. Also the convergence of the approximating series as $N \to \infty$ appears to occur in an irregular or oscillatory fashion, as shown by the three-mode series which yields nearly the same growth curve as the six-mode series.

Table 2. Response Functions for the First Six Axial Modes

Mode	$\Re^r$	$\Re^i$
1L	3.596	-1.221
2L	0.779	-1.407
3L	0.459	-.934
4L	0.357	-.718
5L	0.306	-.594
6L	0.273	-.512

A comparison of the pressure waveforms obtained with the four, five, and six mode expansions is shown in Figure 11. The principal effect of the higher harmonics is apparent in the secondary "wiggles" which are dependent upon the number of modes used to obtain the solution. The overall shape of the pressure waveforms (i.e., the steep rise to maximum and more gradual decline to minimum),the frequency, and the amplitude are less strongly affected by the number of modes.

Figures 10 and 11 indicate that for motors without particles, more than six modes (or possibly as few as three modes) may be necessary to adequately represent the solution. The effect of the number of modes used to describe the solution for cases in which particles are present will be discussed later in this section.

Effect of Initial Disturbance. This study was designed to determine the effect of the amplitude of the initial disturbance and its harmonic

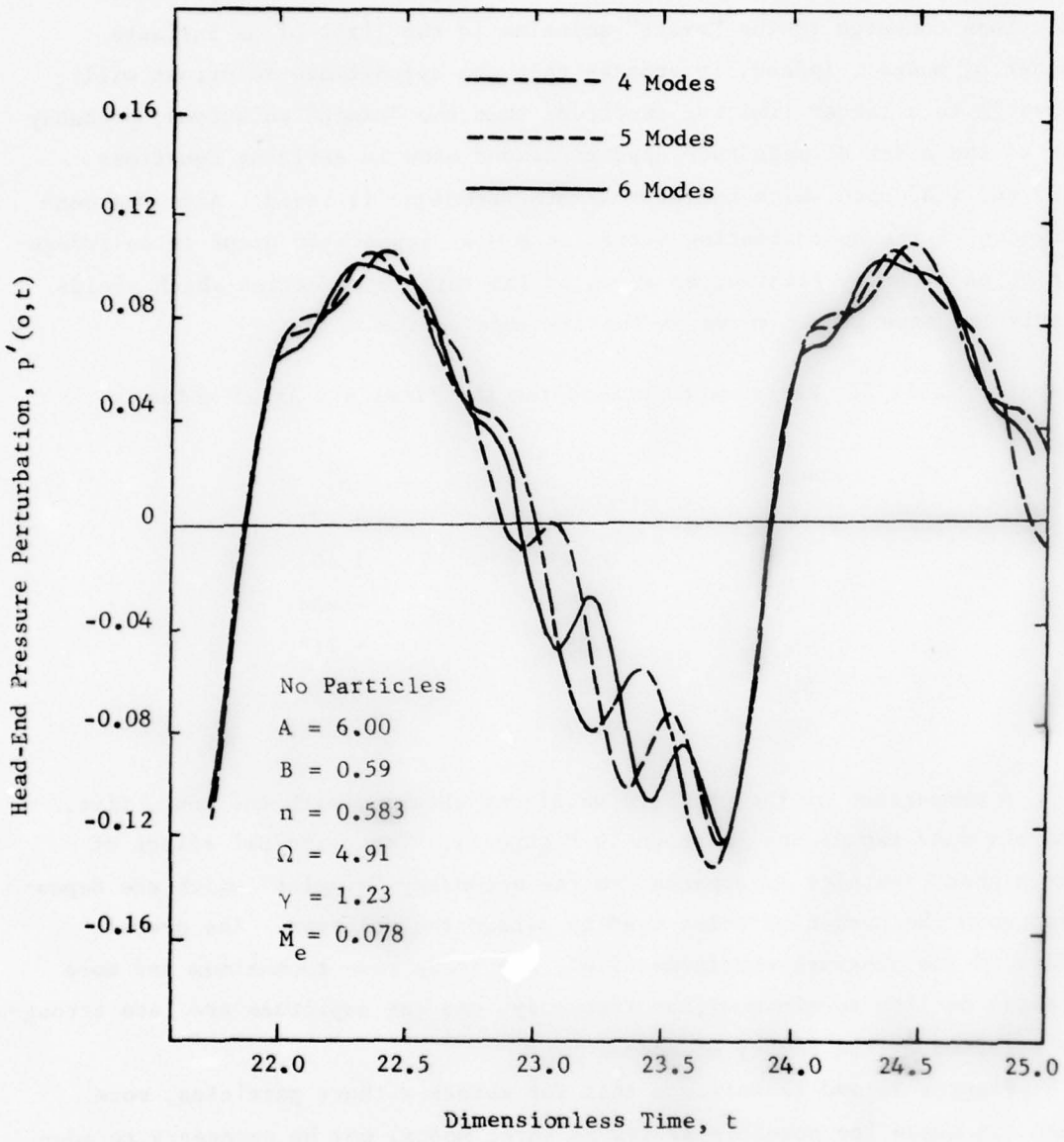

Figure 11. Effect of Number of Modes Used in the Approximate Analysis Upon Calculated Waveforms

content upon the resulting solutions. Of particular interest are cases in which growth to limit-cycle amplitude occurs. It has been shown in References (6), (7), and (8) for liquid rockets that the final limiting amplitude is independent of the form of the initial disturbance. On the other hand, results presented by Levine and Culick[5] for solid rockets indicate a significant dependence of limit-cycle amplitude upon initial disturbance amplitude for amplitudes in the range 5% - 20%. Thus additional data is needed to clarify this issue.

To determine the effect of initial disturbance amplitude upon the resulting limit-cycle solution, the case considered previously (no particles, $A = 6.00$, $B = 0.590$, $n = 0.583$, $\Omega = 4.907$) was run for initial disturbances of 3%, 7%, and 20%. Plots of head-end pressure amplitude versus time for these cases are shown in Figure 12 (using a five mode series). The 3% and 7% solutions appear to smoothly approach a limiting amplitude of 12.5% after about 36 cycles. The 20% disturbance also approaches the same limiting amplitude but in an oscillatory fashion. Although the paths are different, it appears that if the calculations are continued for a sufficiently long time, all three solutions approach the same limiting amplitude. This result is consistent with previous results [6,7,8] for liquid rockets, in which limit-cycle amplitude is independent of the initial disturbance.

For a similar case for which 2.5μ particles are present, 3% and 10% initial amplitudes yield 3.1% and 9.0% amplitude oscillations after 12 cycles. It is difficult to determine whether this indicates a true dependence of limit-cycle amplitude upon initial amplitude, or whether the approach to limit-cycle amplitude is just extremely slow. Such a slow approach to limiting amplitude is expected for cases in which the linear losses due to the mean flow, particles, and the nozzle are in nearly exact balance with the gain due to combustion driving. Such a motor is said to be operating near the point of linear neutral stability.

The effect of harmonic content of the initial disturbance was studied by introducing initial amplitudes of two or more modes simultaneously. Figure 13 shows the pressure waveform obtained for an initial disturbance composed of a combination of 1L and 2L modes for the case of no particles. Due to nonlinear coupling of modes, the amplitude of the 1L mode increases while the amplitude of the 2L mode decreases. As time progresses the waveform assumes more of a 1L mode character.

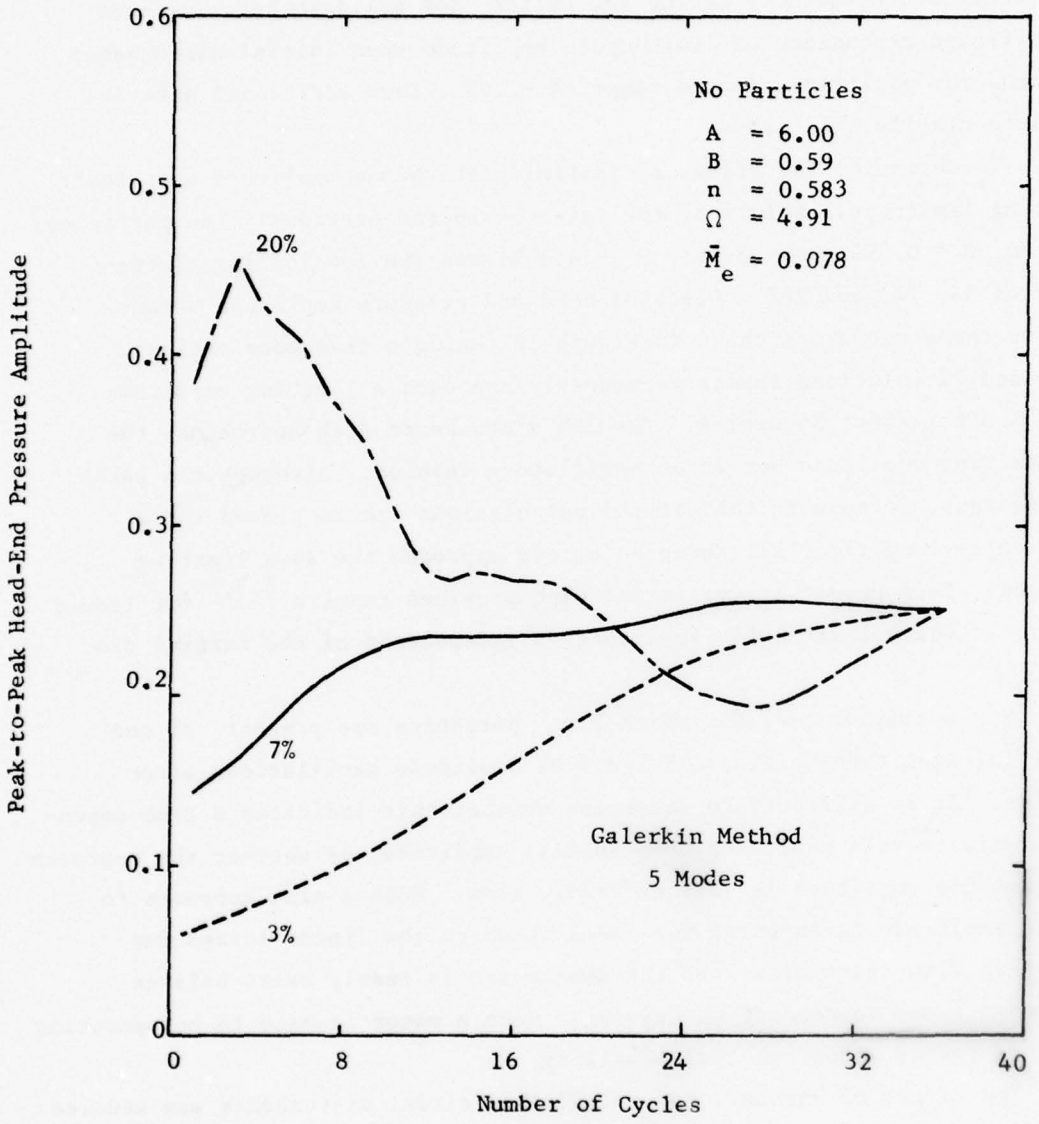

Figure 12. Effect of Initial Disturbance Amplitude Upon Approach to Limiting Amplitude

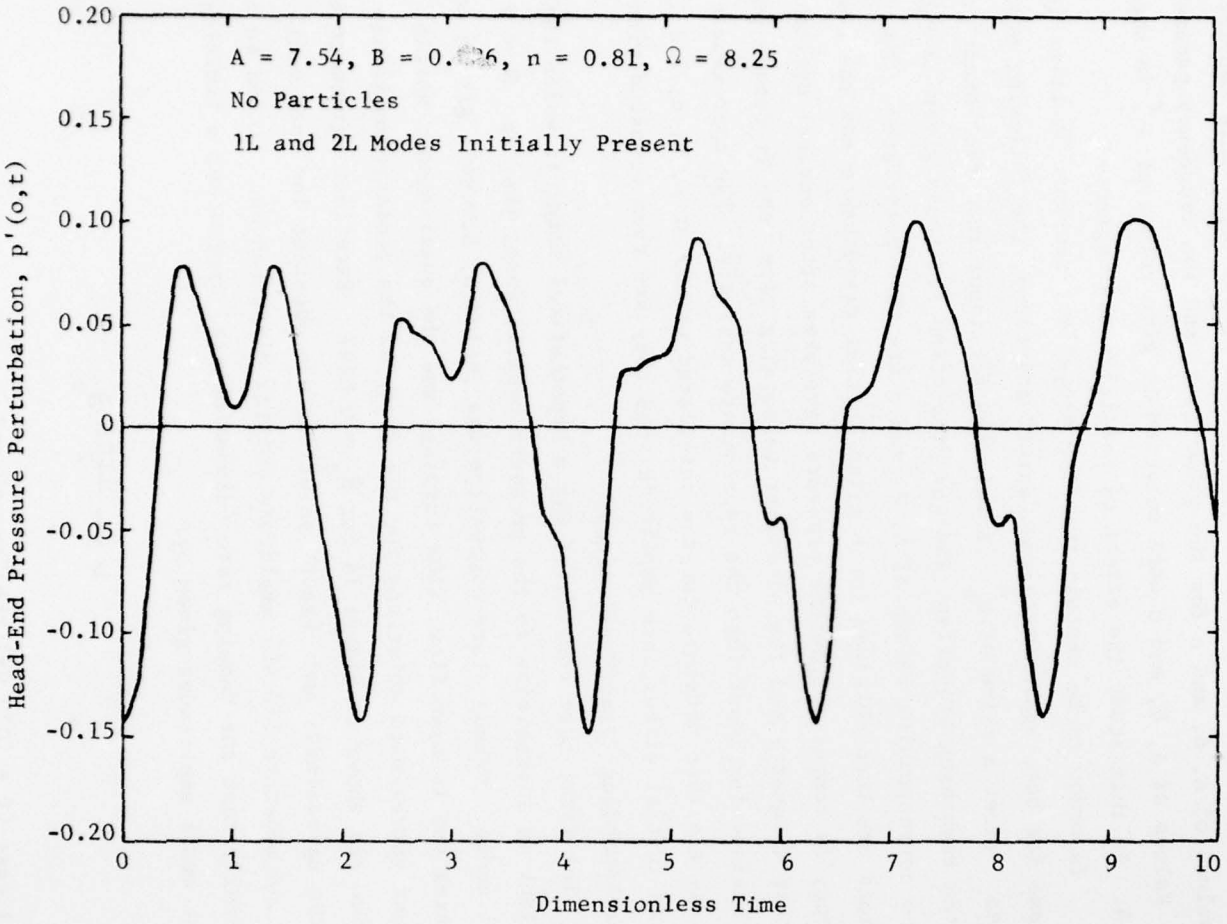

Figure 13. Effect of Harmonic Content of Initial Disturbance

Effect of Propellant Response Function. The effect of propellant response function upon the stability of solid rocket motors was investigated using both approximate and "exact" methods. The most important parameter influencing the amount of combustion driving was found to be the real part of the response function for the fundamental mode, $\Re_1^r$. This depends on the values of A, B, and n for the propellant, and the frequency parameter Ω. Values of A, B, and n were selected to give values of $\Re_1^r$ in the range 0 to 4. In this study the effect of particles was neglected.

In order to be certain that the propellant response function is the same for both approximate and "exact" solutions, the following procedure is used. First a value of Q_s^* is selected for input into the "exact" analysis; the remaining propellant and gas properties are those given in Table 1. The corresponding values of A, B, and n are then calculated. The "exact" solutions are then obtained for a given initial disturbance and the resulting frequency is computed from the pressure waveforms after several cycles. From this frequency and the steady state burning rate, the frequency parameter Ω is obtained for input into the approximate analysis. The approximate solutions are then obtained for the calculated values of A, B, n, and Ω for the same initial disturbance amplitude, and they are then compared with the corresponding "exact" solutions.

The first case considered was a hypothetical motor in which the propellant is insensitive to the pressure oscillations; that is $\Re = 0$ for all modes. Steady-state combustion was included, however, giving acoustic losses due to mean flow, flow turning, and the quasi-steady nozzle. Exact and approximate solutions for the decay of the pressure amplitude with time are shown in Figure 14 for $\bar{M}_e = 0.0847$. Excellent agreement between the approximate and "exact" solutions was obtained for both small (2.9%) and moderate (10.4%) amplitude initial disturbances. It can be shown analytically that the damping rate (dimensionless) approaches a limiting value at small amplitudes given by:

$$\alpha = -\frac{2\gamma+1}{2}\bar{M}_e \qquad (102)$$

For this case (f = 1070 Hz) the "exact" and approximate solutions both yield a damping rate of about $-308\ \text{sec}^{-1}$.

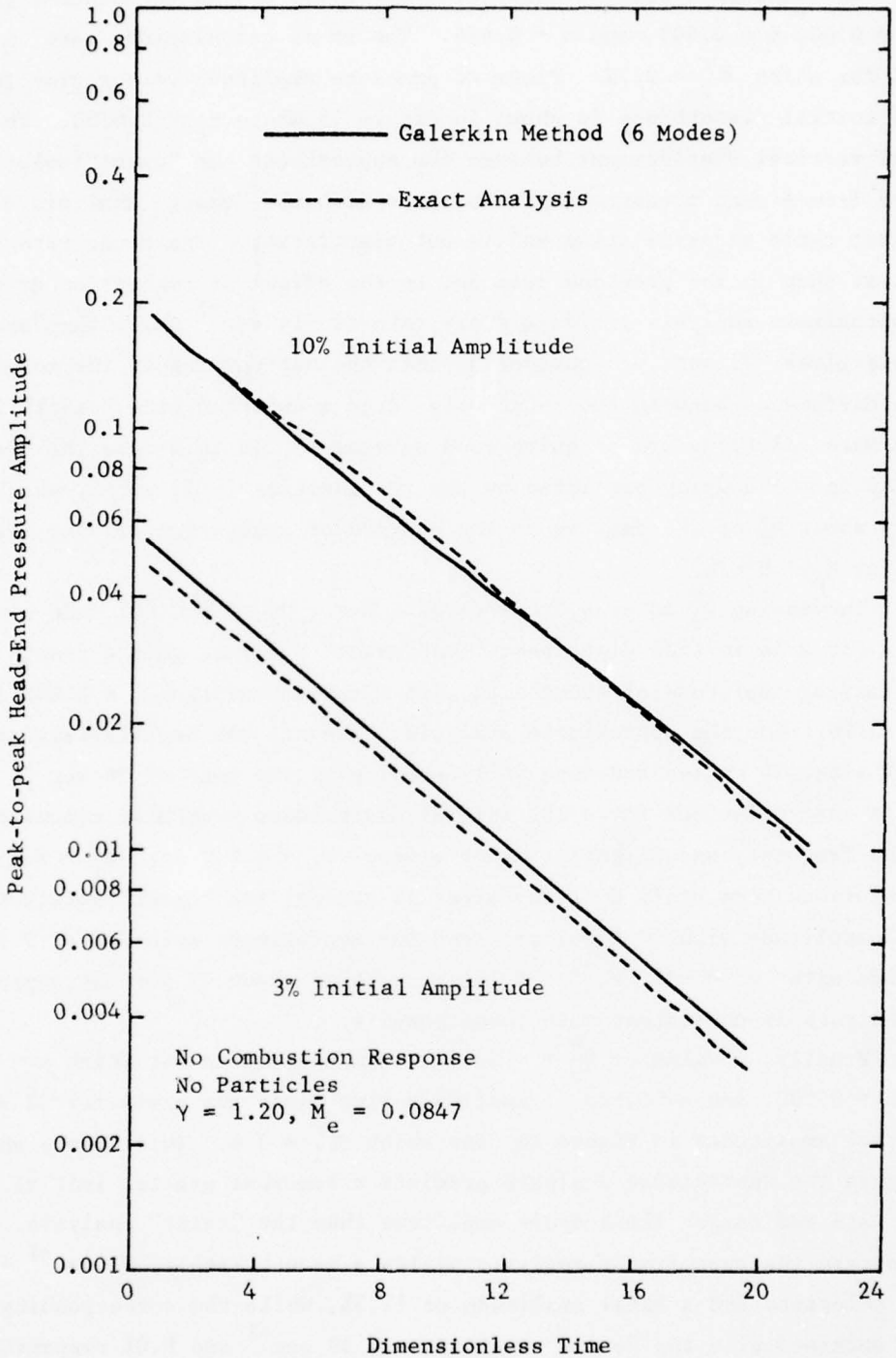

Figure 14. Decay of Oscillations Due to Mean Flow, Flow Turning, and Nozzle

In the second case, a value of $Q_s^* = -131.8$ cal/gm was assumed yielding A = 6.00, B = 0.643, and n = 0.616. The exact calculations gave $\Omega_1 = 4.91$ for which $\Re_1^r = 2.73$. Plots of pressure amplitude versus time for a 3.0% initial disturbance is shown in Figure 15 where $\bar{M}_e = 0.0780$. The initial vertical displacement between the approximate and "exact" solutions results from a mean pressure shift obtained with the "exact" analysis during the first cycle of oscillation and is not significant. The decay rate is much less than in the previous case due to the effect of combustion driving; the approximate analysis yields a decay rate of -14 sec^{-1} while the "exact" analysis gives -31 sec^{-1}. Considering that the net damping in the motor is the difference between two relatively large quantities, the "exact" and approximate solutions are in quite good agreement. In this case the discrepancy in the damping predicted by the two theories is 17 sec^{-1}, which is only about 6% of the damping in the absence of combustion driving (-288 sec^{-1} for $\bar{M}_e = 0.078$).

Increasing Q_s^* to -134.7 cal/gm gave A = 6.00, B = 0.607, and n = 0.594. For a 3% initial disturbance the "exact" analysis gave a growth to a limiting amplitude of about 2.8% with a corresponding $\Omega_1 = 4.888$ and $\Re_1^r = 3.26$. For the approximate analysis, however, the oscillations grew to 4.5% after 12 cycles and were still growing at the rate of 36 sec^{-1}. For this case solutions for a 10% initial disturbance were also calculated; here the frequency was slightly higher giving $\Omega_1 = 4.932$ and $\Re_1^r = 3.23$. Both solutions were still decaying after 12 cycles, the "exact" solution at 7.5% amplitude with $\alpha = -42$ sec^{-1} and the approximate solution at 9.5% amplitude with $\alpha = -31$ sec^{-1}. A limit cycle of about 7% for the approximate analysis is consistent with these results.

Finally, a value of $Q_s^* = -136.1$ cal/gm was chosen for which A = 6.00, B = 0.590, and n = 0.583. Amplitude-time plots are given for 3% and 7% initial amplitudes in Figure 16, for which $\Re_1^r = 3.6$. This figure shows that again the approximate analysis predicts a somewhat greater initial growth rate and larger limit-cycle amplitude than the "exact" analysis. In this case the approximate analysis yields a growth rate of 73 sec^{-1} for the 3% solutions and a final amplitude of 11.3%, while the corresponding values obtained with the "exact" analysis are 38 sec^{-1} and 8.0% respectively. The frequencies obtained are in close agreement at about 1050 Hz. Head-end and mid-chamber waveforms are shown in Figure 17 for limit-cycle con-

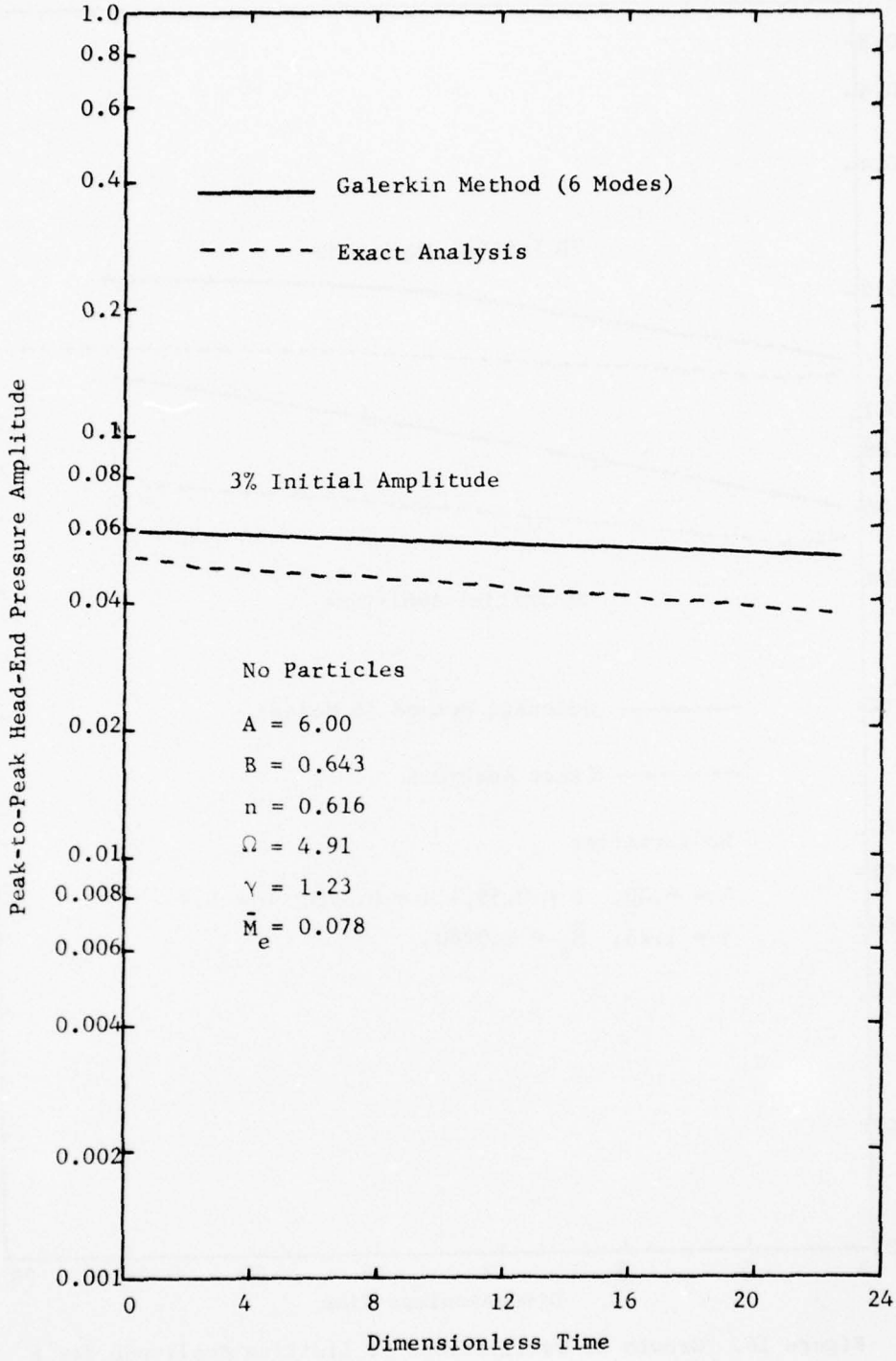

Figure 15. Decay of Oscillations in a Stable Motor Without Particles

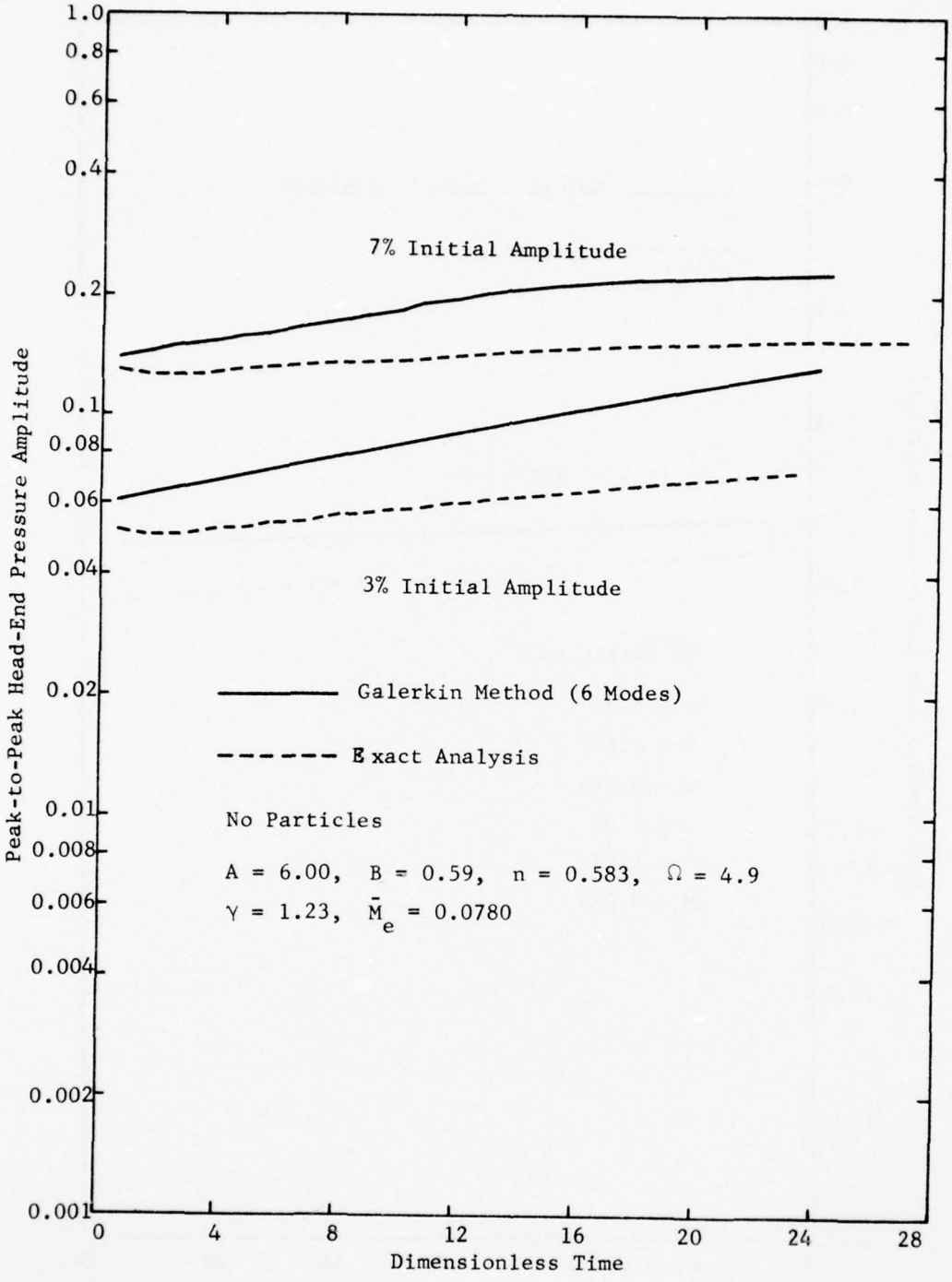

Figure 16. Growth of Oscillations to Limiting Amplitude for a Motor Without Particles

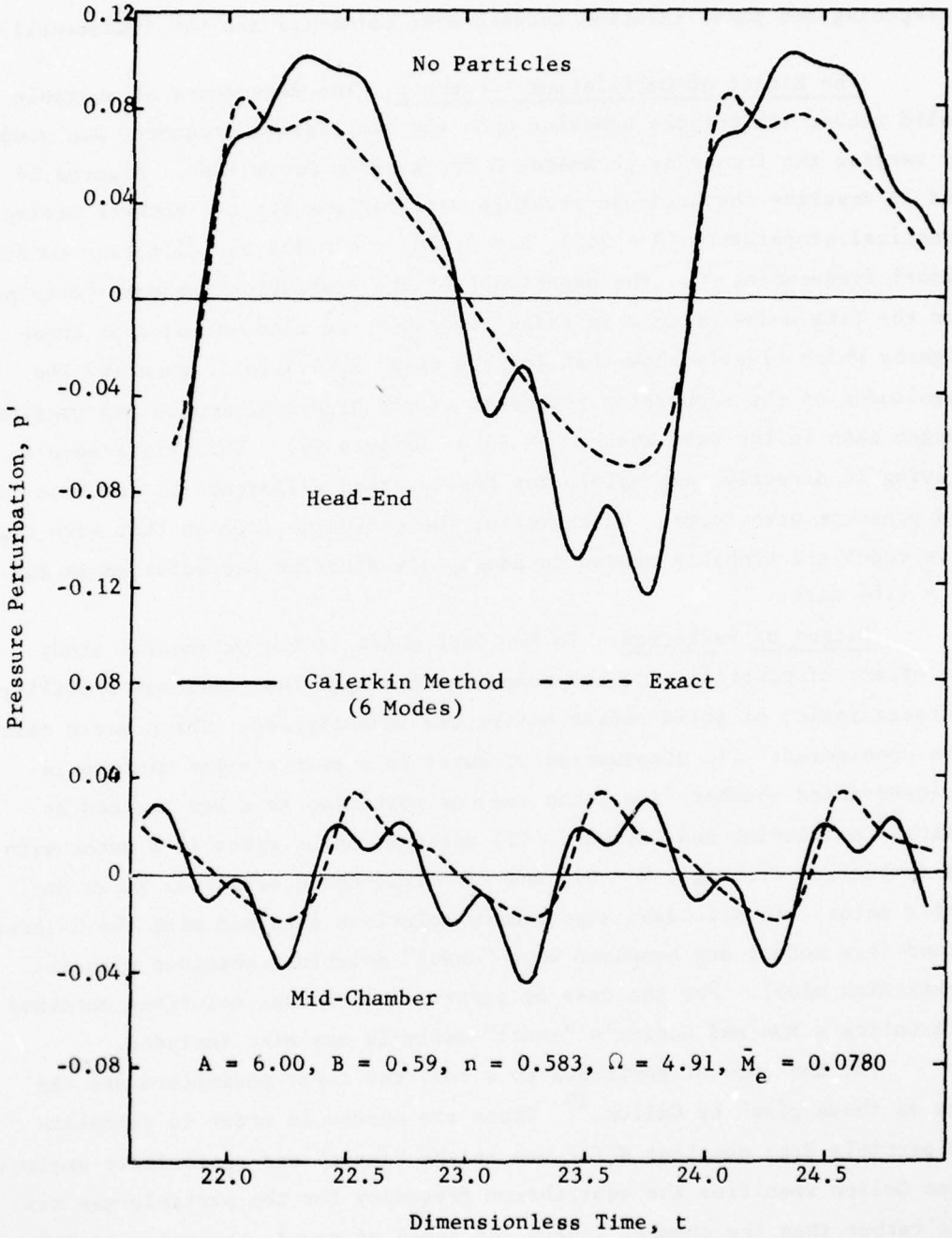

Figure 17. Pressure Waveforms at Limiting Amplitude for a Motor Without Particles

ditions (after 11 cycles of oscillation). The approximate waveforms show considerably more harmonic content than the "exact" waveforms, but the qualitative features of the waveforms are in good agreement (i.e., waveform steepening and phase relation between even harmonics and the fundamental).

The Effect of Oscillation Frequency. The dependence of unstable solid rocket limit-cycle behavior upon the oscillation frequency was studied by varying the frequency parameter Ω for a given propellant. Figures 18 and 19 describe the head-end pressure oscillations for two rockets having identical propellants (A = 7.54, B = 0.880, n = 0.85) but different nondimensional frequencies Ω. The magnitudes of the combustion response "driving" for the five modes present in these two cases are also included in these figures which clearly show that for the case $\Omega_1 = 1.64$ (Figure 18) the magnitudes of the combustion responses of the higher harmonics are considerably larger than in the case when $\Omega_1 = 10.0$ (Figure 19). This difference in driving is directly responsible for the observed difference in the head-end pressure wave forms. Furthermore, these figures suggest that more than five modes are probably needed to adequately describe the solution in the $\Omega_1 = 1.64$ case.

Effect of Particles. In the last phase of the parametric study the effect of particle size and concentration upon the nonlinear stability characteristics of solid rocket motors was investigated. Three basic cases were considered: (1) attenuation of waves in a particle-gas mixture in a closed-ended chamber (i.e., the case of particles in a box treated by Culick[10] and Levine and Culick[5]), (2) attenuation of waves in a motor without combustion driving ($\Re = 0$), and (3) limit-cycle solutions in an unstable motor. In all cases approximate solutions obtained with the Galerkin method (six modes) are compared with "exact" solutions obtained with the Kooker-Zinn model. For the case of particles in a box, solutions obtained with Culick's MOA and Levine's "exact" analysis are also included.

For the case of particles in a box, the input parameters are the same as those given by Culick.[10] These are needed in order to calculate the particle drag constant K for use in the "exact" and approximate analyses. Since Culick specifies the equilibrium frequency for the particle-gas mixture rather than the chamber length and speed of sound, the value of K for a given particle size was calculated from the following expression:

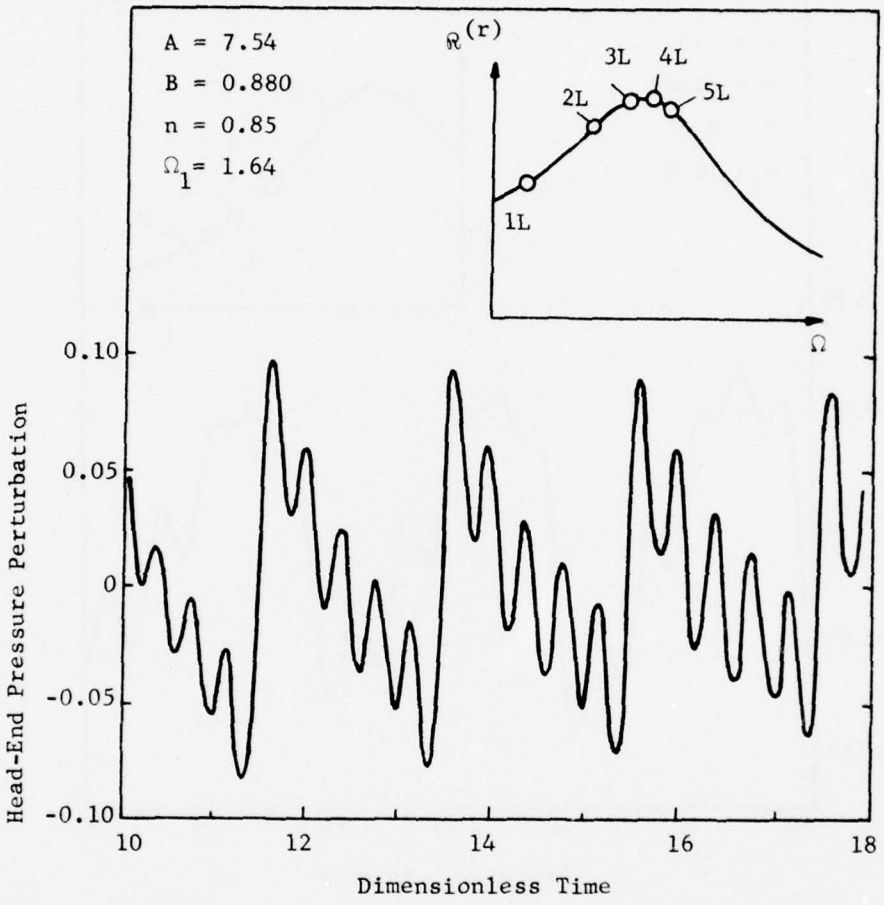

Figure 18. Pressure Waveforms for Low Frequency Oscillations in a Motor Without Particles

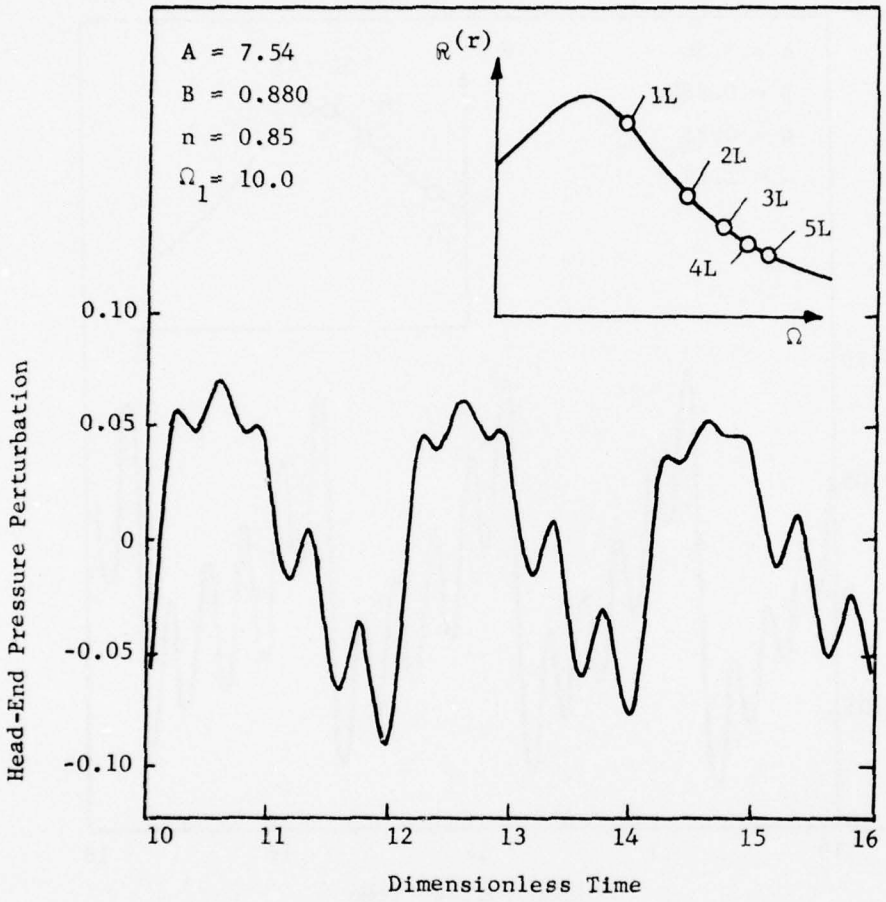

Figure 19. Pressure Waveforms for High Frequency Oscillations in a Motor Without Particles

$$K = \frac{9\mu^*}{\rho_m^* \sigma^{*2} f_g^*} \tag{103}$$

where $f_g^* = c_o^* / 2L^*$ is the frequency for the pure gas. The gas viscosity was obtained from the formula given in Reference 10:

$$\mu^* = 8.834 \times 10^{-5} \left(\frac{T}{3485} \right)^{0.66} \text{ kg/m-sec} \tag{104}$$

for $T = 3416^{o}K$ used by Culick. In the approximate analysis the ratio of specific heats $\bar{\gamma}$ for the mixture replaces γ for the gas. The value of γ depends on the specific heats of the gas and particle material and the concentration of the particles and is given by:

$$\bar{\gamma} = \gamma \left(1 + \frac{\rho_p}{\rho} \frac{C}{C_p} \right) \Bigg/ \left(1 + \gamma \frac{\rho_p}{\rho} \frac{C}{C_p} \right) \tag{105}$$

where C and C_p are the specific heats of the particles and gas respectively. Also in specifying the initial disturbance, the equilibrium frequency is needed; it is related to the pure gas frequency by:

$$f_e = f_g \sqrt{\frac{\bar{\gamma}}{\gamma \left(1 + \frac{\rho_p}{\rho} \right)}} \tag{106}$$

To evaluate the accuracy of the approximate analysis in describing the effects of linear particle damping, "exact" and approximate solutions were obtained for the case of a particle-gas mixture in a closed-ended box. Assuming an initial disturbance amplitude of 3%, values of damping and frequency

were computed for several values of the particle diameter σ. The results were calculated for a pure-gas frequency of f_g = 1071 Hz and a particle concentration of $C_m = \bar{\rho}_p/\bar{\rho} = 0.20$. The values of K corresponding to the particle sizes considered in this study are given in Table 3.

Table 3. Drag Constants for Approximate and "Exact" Models

Particle Size, σ (μ)	K (Approximate)	K′ (Exact)
2.0	46.72	160.2
2.5	29.90	102.5
3.0	20.76	71.18
4.0	11.68	40.04
6.0	5.191	17.80
8.0	2.920	10.01
9.0	2.307	7.909
10.0	1.869	6.406
15.0	.8306	2.847
20.0	.4672	1.602
25.0	.2990	1.025
30.0	.2076	.7118
40.0	.1168	.4004

The value of K′ used in the "exact" analysis differs from the value K used in the approximate analysis due to the difference in the reference state used in nondimensionalizing the "exact" equations. In the Kooker-Zinn analysis standard atmospheric conditions are used as the reference state, while the chamber stagnation conditions are used in the approximate analysis. Thus the two particle drag constants are related by

$$K' = K\,(c_o^*/c_{ref}^*) \tag{107}$$

where c_o^* and c_{ref}^* are the speeds of sound at chamber stagnation conditions and standard atmospheric conditions respectively.

Curves of decay rate and frequency as a function of particle diameter are presented in Figure 20 for particles in a box (i.e., $\bar{M}_e = 0$). The damping and frequency shift arise solely from the particle-gas interaction,

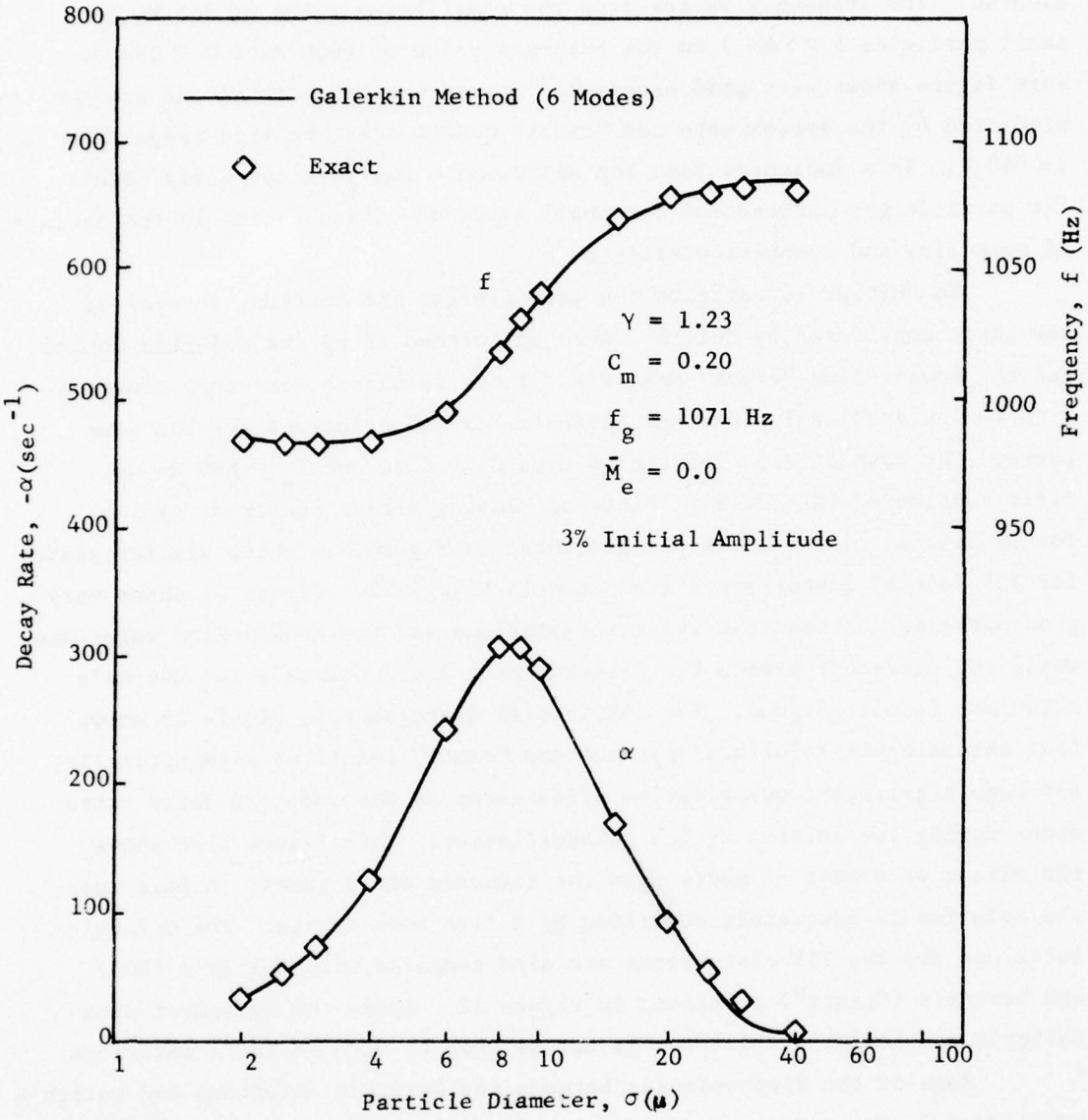

Figure 20. Effect of Particle Size on Decay Rate and Frequency For a Gas/Particle Mixture in a Box

since mean flow, combustion, and nozzle effects are absent. The damping is low for particles smaller than 2μ and for particles larger than 30 μ, and the maximum damping occurs at about 8.5μ for the frequency considered. The frequency varies from the equilibrium value of 985 Hz for small particles ($\sigma < 4\mu$) to the pure-gas value of 1080 Hz ($\sigma > 25\mu$). This figure shows very good agreement between the decay rates and frequencies predicted by the approximate and "exact" models over the size range from 2μ to 40μ. This indicates that the approximate analysis correctly models the particle-gas interaction for small amplitude disturbances in the absence of mean flow and combustion effects.

To further investigate the particle-gas interaction, several of the cases considered by Culick[10] were calculated using the Galerkin Method and the Kooker-Zinn "exact" analysis. These solutions were then compared with Culick's MOA solutions and Levine's "exact" solutions for the same cases. The case of 2.5μ particles with $C_m = 0.36$ and $f_e = 800$ Hz was first considered ($K = 32.9$). Plots of damping versus number of cycles for 3% initial disturbances are presented in Figure 21, while similar plots for 15% initial disturbances are shown in Figure 22. Figure 21 shows very good agreement between the Galerkin solutions and the Kooker-Zinn solutions, while the agreement beween the Galerkin method and Culick's and Levine's solutions is not as good. For 15% initial disturbances, Figure 22 shows that the Galerkin solutions approach the "exact" solutions asymptotically, although significant quantitative differences in the computed decay rates occur during the initial cycles of oscillation. This figure also shows the effect of number of modes upon the computed decay rates; in this case the solution is adequately described by a five-mode series. The Galerkin solutions for the 15% disturbance are also compared with Culick's (MOA) and Levine's ("exact") solutions in Figure 22. Again the agreement with Culick's and Levine's solutions is not as good as with Kooker's solutions.

Some of the discrepancies between the Galerkin solutions and Culick's MOA solutions (as well as Levine's "exact" solutions) may be due to differences in the physical models involved. For example, the Galerkin method results shown were obtained using a linear drag law to describe the particle damping, while the results of Culick and Levine were obtained using a nonlinear drag law. Furthermore, the analyses of Culick and Levine included a thermal equation for the particles, while this equation was ignored in both the Galerkin and the Kooker-Zinn analyses.

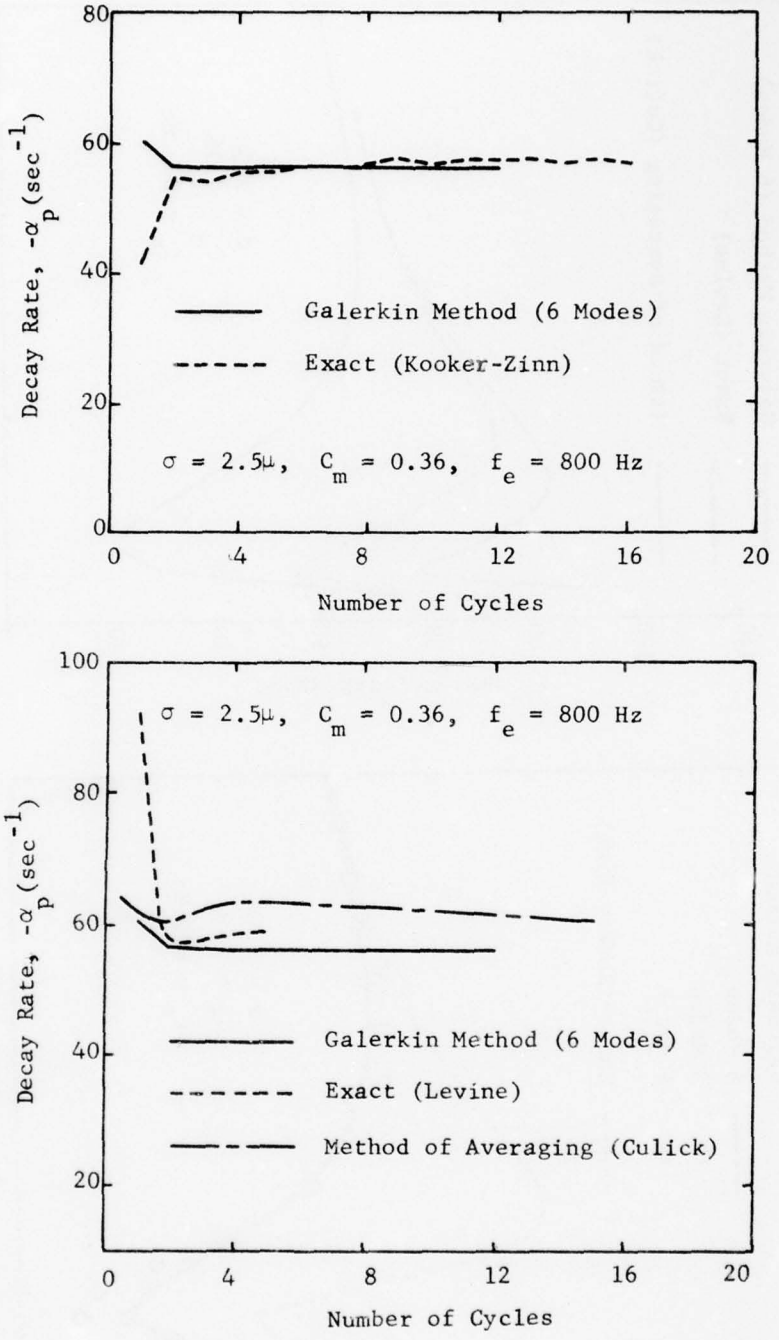

Figure 21. Decay Rates of 3% Disturbances Due to 2.5μ Particles in a Box

AD-A044 298 GEORGIA INST OF TECH ATLANTA SCHOOL OF AEROSPACE ENG--ETC F/G 21/8.2
APPROXIMATE NONLINEAR ANALYSIS OF SOLID ROCKET MOTORS AND T-BUR--ETC(U)
JUL 77 E A POWELL, M S PADMANABHAN, B T ZINN F04611-75-C-0036

UNCLASSIFIED AFRPL-TR-77-48 NL

2 OF 3
ADA
044298

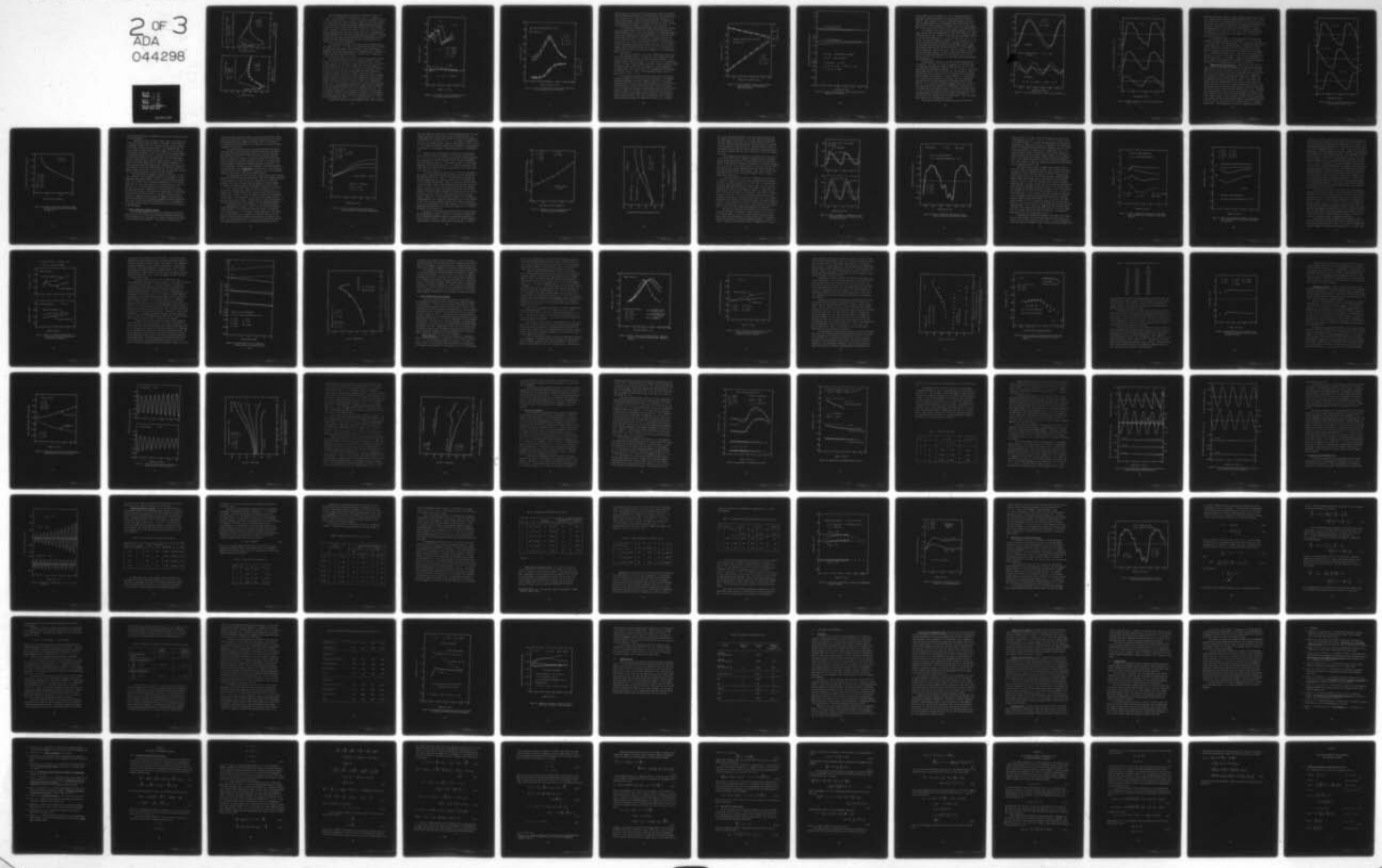

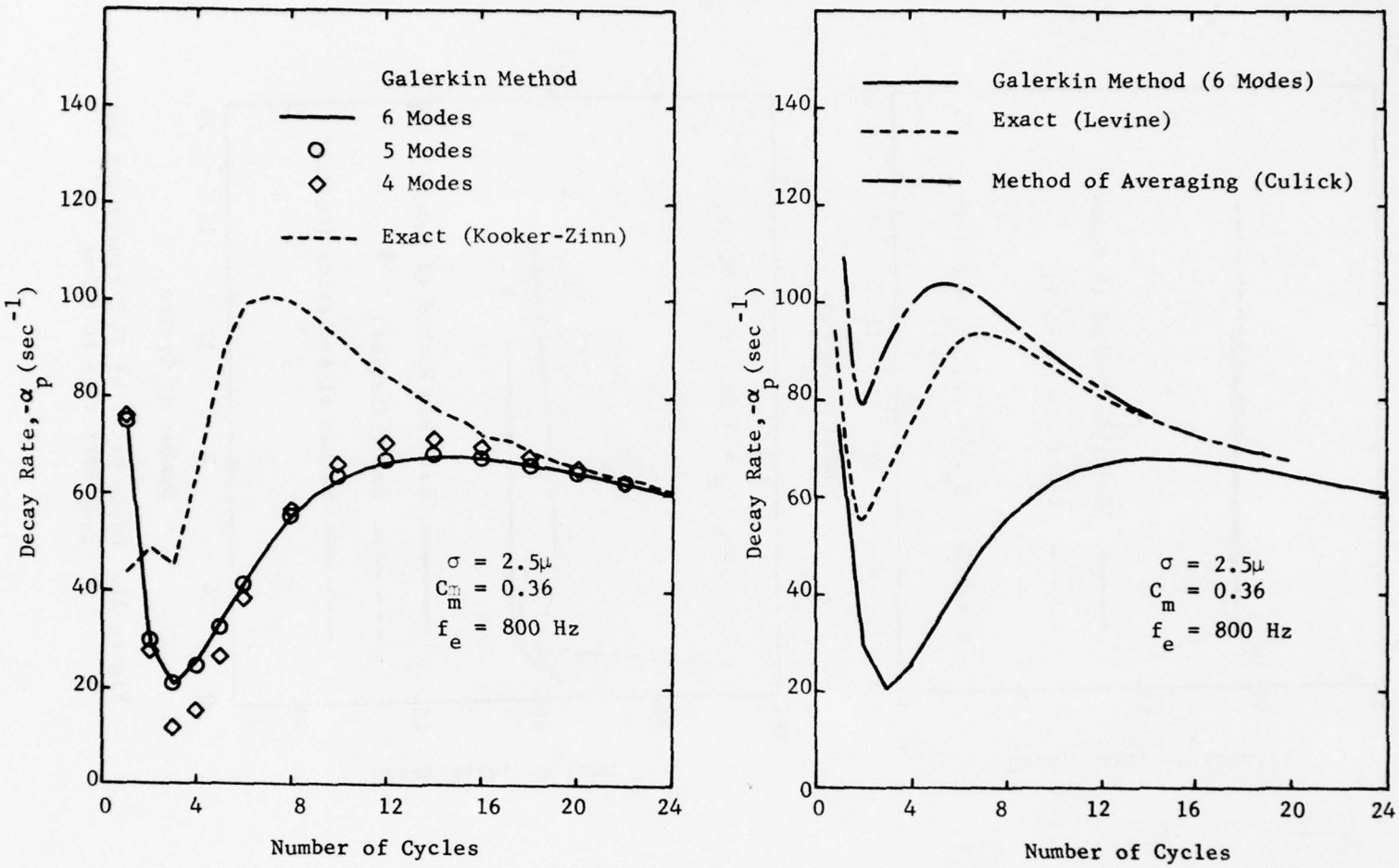

Figure 22. Decay Rates of 15% Disturbances Due to 2.5μ Particles in a Box

Two additional cases were considered for particles in a box: (1) $\sigma = 2.5\mu$, f_e = 1500 Hz (K = 17.55) and (2) $\sigma = 10\mu$, f_e = 1500 Hz (K = 1.097). For both cases C_m = 0.36 and a 15% initial disturbance was considered. Approximate and "exact" solutions for these cases are shown in Figure 23. For the 2.5μ particles the agreement between approximate and "exact" solutions at 1500 Hz is better than at 800 Hz (Figure 22), and a four-mode series is adequate to describe the solution. For the 10μ case both theories predict large variations in decay rate from cycle to cycle, and significant differences between four, five, and six mode solutions are apparent. Although for any given cycle the decay rates predicted by the approximate and "exact" analyses can differ significantly, the mean decay rates during the first 14 cycles are in fairly good agreement.

The second case considered in the study of particle damping effects was a motor for which $\Re = 0$, that is the combustion process does not respond to the pressure oscillations. Thus the effects of mean flow and nozzle damping are considered along with the particle damping effects. Calculations of decay rate and frequency were made for a motor with $\bar{M}_e = 0.0780$ and f_g = 1071 Hz for several values of σ and C_m.

The effect of particle size on the "exact" and approximate solutions for $C_m = 0.20$ is shown in Figure 24 for 3% initial disturbances. These curves are similar to those shown in Figure 20 for particles in a box, except that the damping curves are shifted upwards due to the large damping due to mean flow and nozzle effects ($\alpha = -289$ sec^{-1} in the absence of particles). The decay rate curves show that the approximate and "exact" analyses are in excellent agreement for particle diameters larger than about 15μ, and both analyses predict practically the same optimum particle size for maximum damping. For particles smaller than 15μ the approximate analysis predicts a smaller linear decay rate than the "exact" analysis with a maximum error of about 13%. This discrepancy is probably due to certain terms proportional to the particle drag constant K and the mean flow Mach number (see Appendix A) that were neglected as higher order in the approximate analysis. Since K is inversely proportional to the frequency of oscillation and the square of the particle diameter, better agreement is obtained in the high-frequency and large-particle size range. The frequencies predicted by the two models are in best agreement for small ($\sigma < 6\ \mu$) and large particles ($\sigma > 20\mu$).

It should be noted that the good agreement between "exact" and appro-

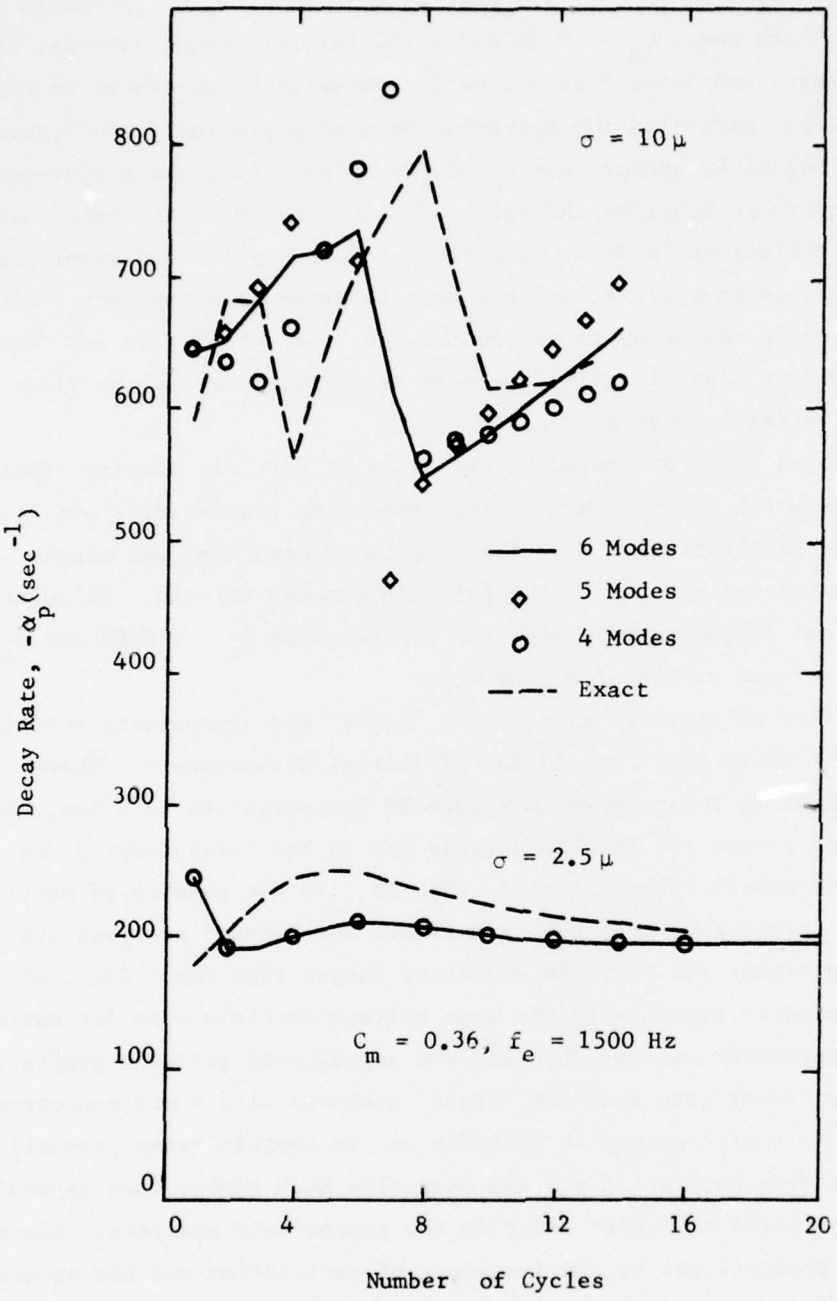

Figure 23. Decay Rates of 15% Disturbances Due to 2.5 μ and 10 μ Particles in a Box

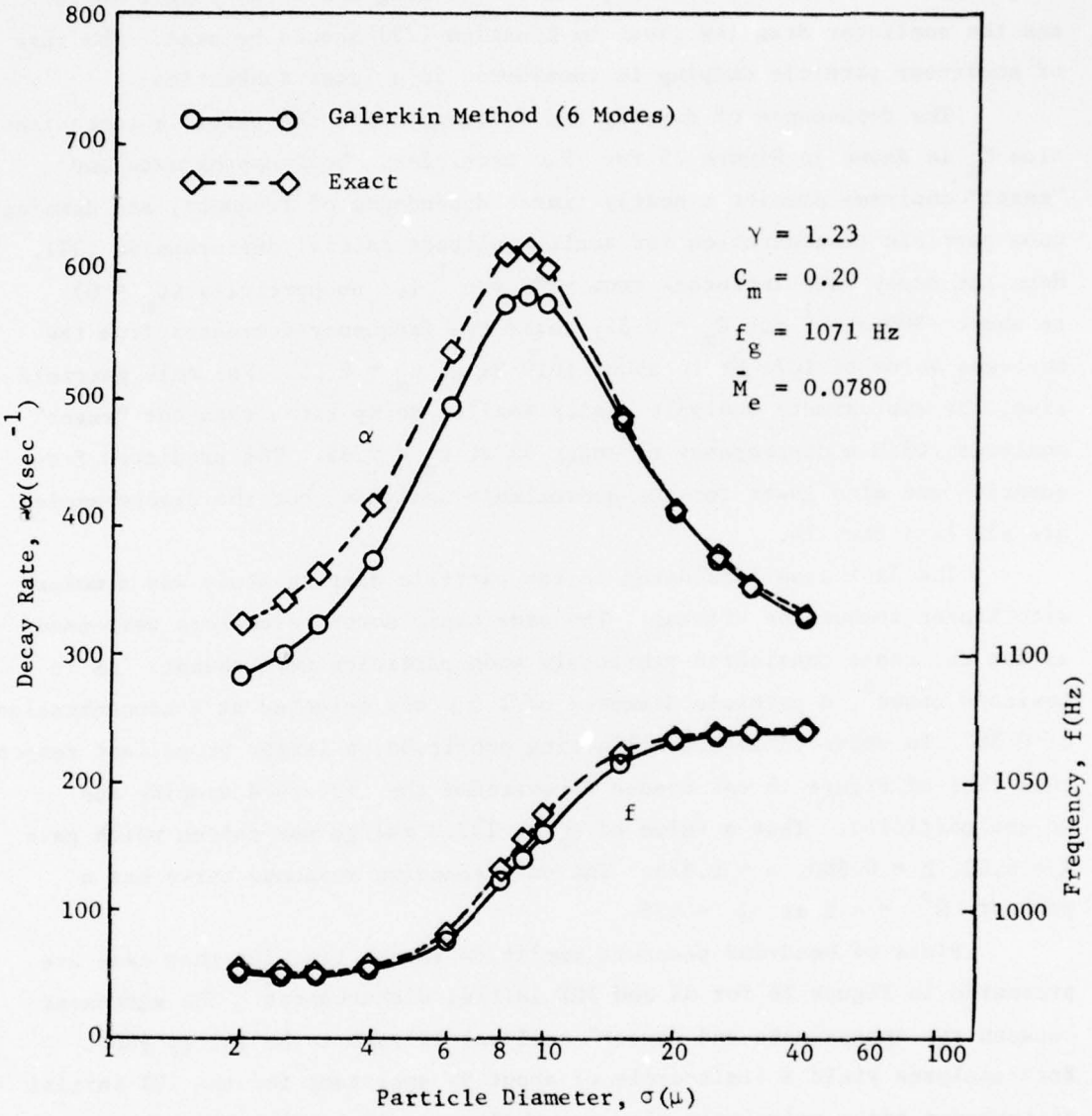

Figure 24. Effect of Particle Size on Decay Rate and Frequency for Motor Without Combustion Driving

ximate analyses for large particles has been obtained under the assumption that the particle-gas interaction is described by the Stokes Drag Law (Equations (7) and (8)). For large particle sizes and high frequencies (i.e., large Reynolds numbers), however, the Stokes Drag Law is no longer valid and the nonlinear drag law given by Equation (79) should be used. The case of nonlinear particle damping is considered in a later subsection.

The dependence of damping and frequency upon the particle concentration C_m is shown in Figure 25 for 10 μ particles. Both approximate and "exact" analyses predict a nearly linear dependence of frequency and damping upon particle concentration for small amplitude initial disturbances (3%). Here the decay rate increases from -289 sec^{-1} for no particles ($C_m = 0$) to about -800 sec^{-1} for $C_m = 0.35$, while the frequency decreases from the pure-gas value of 1071 Hz to about 1010 Hz at $C_m = 0.35$. For this particle size, the approximate analysis yields smaller decay rates than the "exact" analysis, with a discrepancy of about 5% at $C_m = 0.35$. The predicted frequencies are also lower for the approximate analysis, but the discrepancies are all less than 1%.

The last case considered in the particle damping study was a motor with linear combustion driving. The same basic motor parameters were used as for the cases considered previously when particles were absent. As in Levine's cases[5], a particle diameter of 2.5 μ was selected at a concentration of 0.36. In order to obtain a limiting amplitude, a larger propellant response than that of Figure 16 was needed to overcome the increased damping due to the particles. Thus a value of $Q_s^* = -137.0$ cal/gm was chosen which gave A = 6.00, B = 0.580, n = 0.575. The corresponding response curve has a peak of $\Re^r = 4.2$ at $\Omega = 4.5$.

Plots of head-end pressure amplitude versus time for this case are presented in Figure 26 for 3% and 10% initial disturbances. The agreement between the approximate and "exact" analyses is seen to be fairly good. Both analyses yield a limit-cycle of about 9% amplitude for the 10% initial disturbance and a relatively slow growth for the 3% initial disturbance. For the low amplitude disturbance, the approximate analysis gives the smaller growth rate, which is in contrast to the case when particles are absent (Figure 16) where the approximate analysis predicted a larger growth rate than the "exact" analysis. This result was unexpected, since the approximate analysis underestimates the damping for the case of 2.5 μ particles

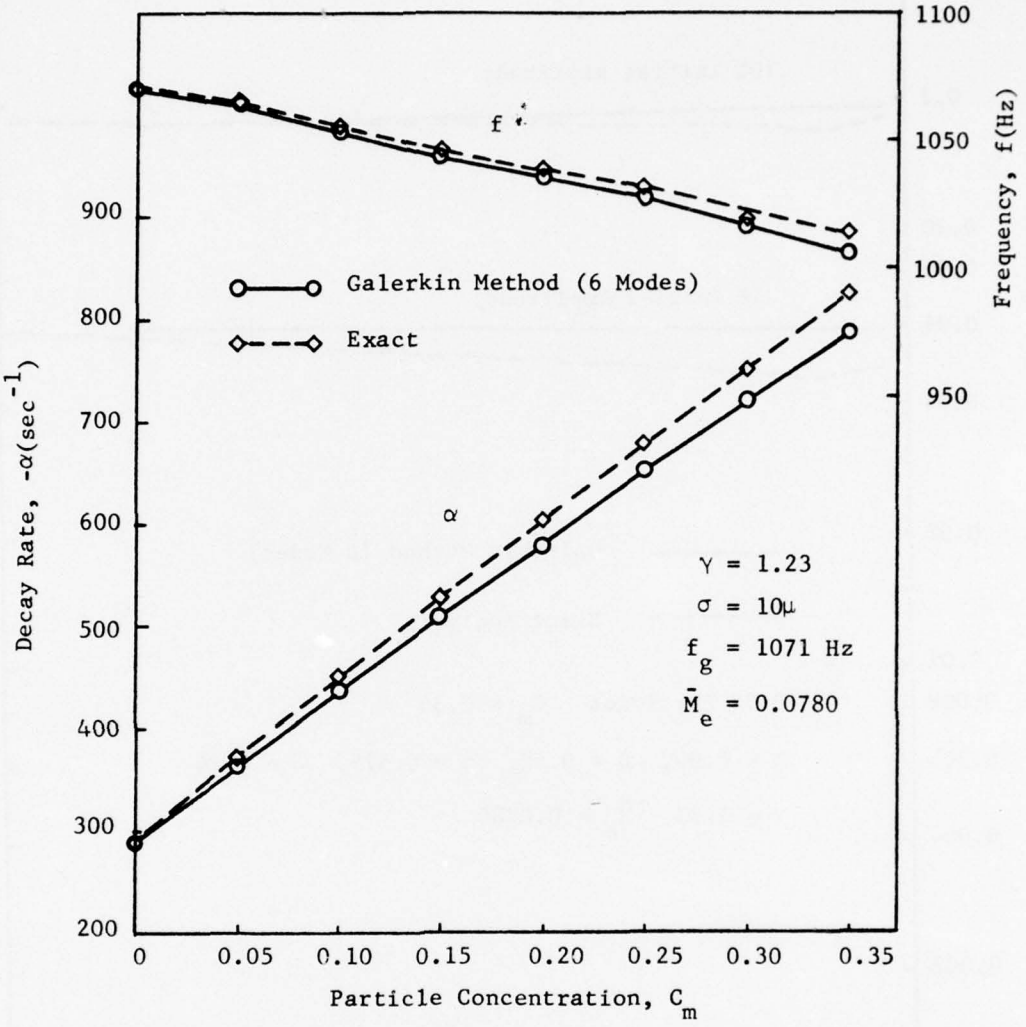

Figure 25. Effect of Particle Concentration on Decay Rate and Frequency for Motor Without Combustion Driving

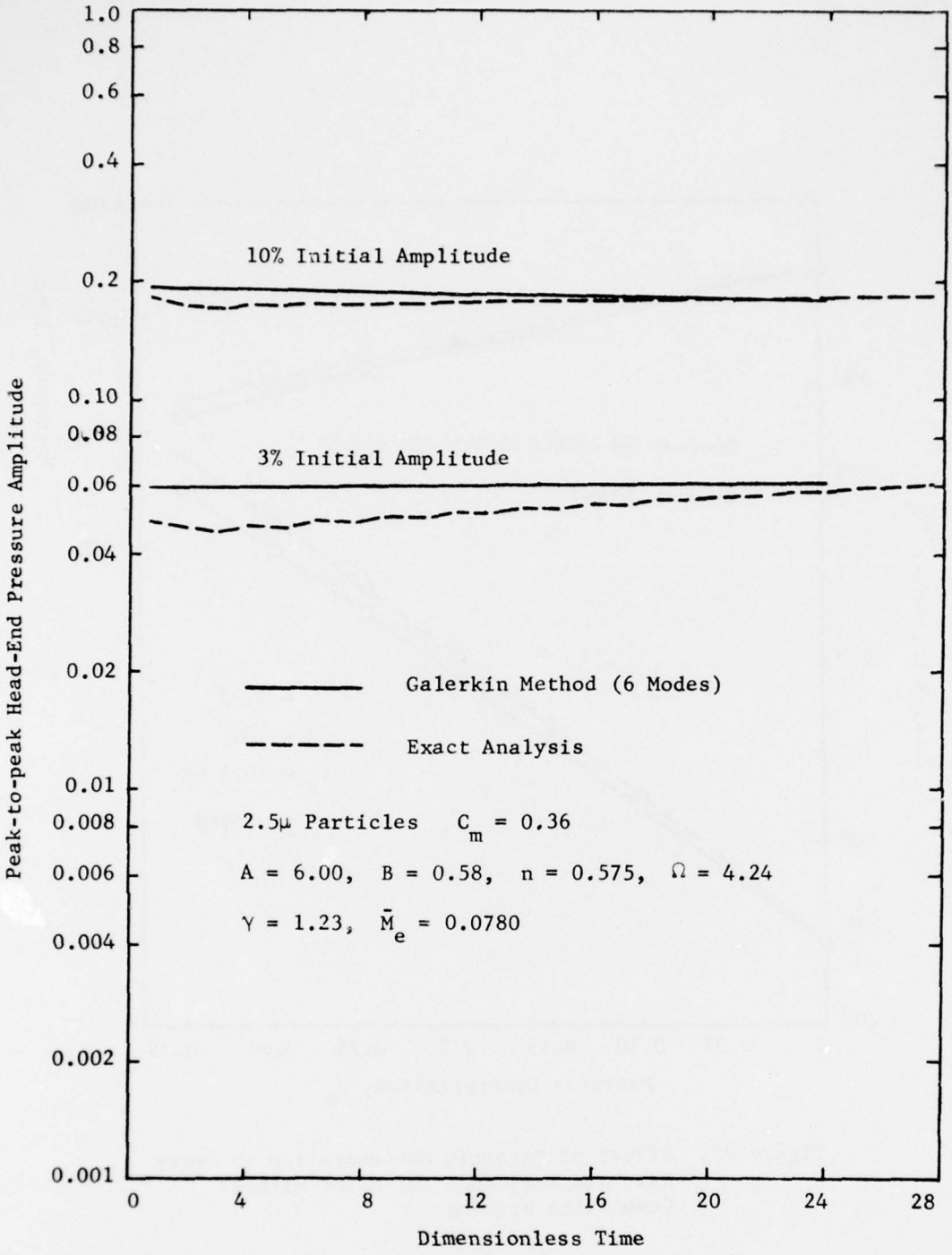

Figure 26. Growth of Oscillations to Limiting Amplitude for a Motor with 2.5μ Particles

without combustion driving (Figure 24). The corresponding head-end and mid-chamber pressure waveforms for limit-cycle conditions are shown in Figure 27. Both analyses yield nearly sinusoidal waveforms; the only evidence of higher harmonics is the steepening of the rising branch of the waveform and the double frequency oscillation at the center of the chamber. This is due to the presence of particles which suppress the higher harmonics.

The importance of using the proper frequency parameter in the approximate analysis when making comparisons with the "exact" analysis is readily illustrated by this case. From the "exact" analysis, the frequency parameter for the 10% initial amplitude is $\Omega_1 = 4.244$ for which $\Re_1^r = 4.17$. If, however, the pure-gas frequency is assumed, $\Omega_1 = 4.94$ for which $\Re_1^r = 3.78$, and the approximate analysis would predict a decaying oscillation. Thus the approximate analysis would appear to give the wrong results, because the response function was not the same in both cases. For this reason the "exact" program must always be run first to obtain the proper Ω_1 for input into the approximate program. Of course, if the calculations are being made with the approximate analysis only, the values of A, B, n, and Ω_1 must be estimated or the values of $\Re$ for the various modes may be obtained from experimental data.

Some parametric variations on the case considered above will now be considered. The effect of variations of particle size upon the limit-cycle amplitude and waveform are shown in Figure 28 for $C_m = 0.10$. Here head-end pressure waveforms are shown for $\sigma = 2.5$, 3.5, and 5μ; the corresponding amplitudes are 19.3%, 15.3%, and 8.2%. This decrease in limiting amplitude with increasing particle size is consistent with the increasing particle damping with increasing σ as shown in Figure 20. The distortion of the waveform also decreases with increasing σ due to the decreasing amplitude and the increased attenuation of the higher harmonics by the particles. For particles with diameters somewhat greater than 5μ (for the given propellant response and particle concentration), limit-cycles are not obtained and the oscillations decay. For continued increases in particle size the decay rate reaches a maximum, then declines, and limit-cycles are again obtained for large particles (σ greater than roughly 15μ). For large particles, the opposite trend is obtained, that is, limit-cycle amplitude increases with increasing particle size.

The influence of particle concentration C_m upon the limit-cycle

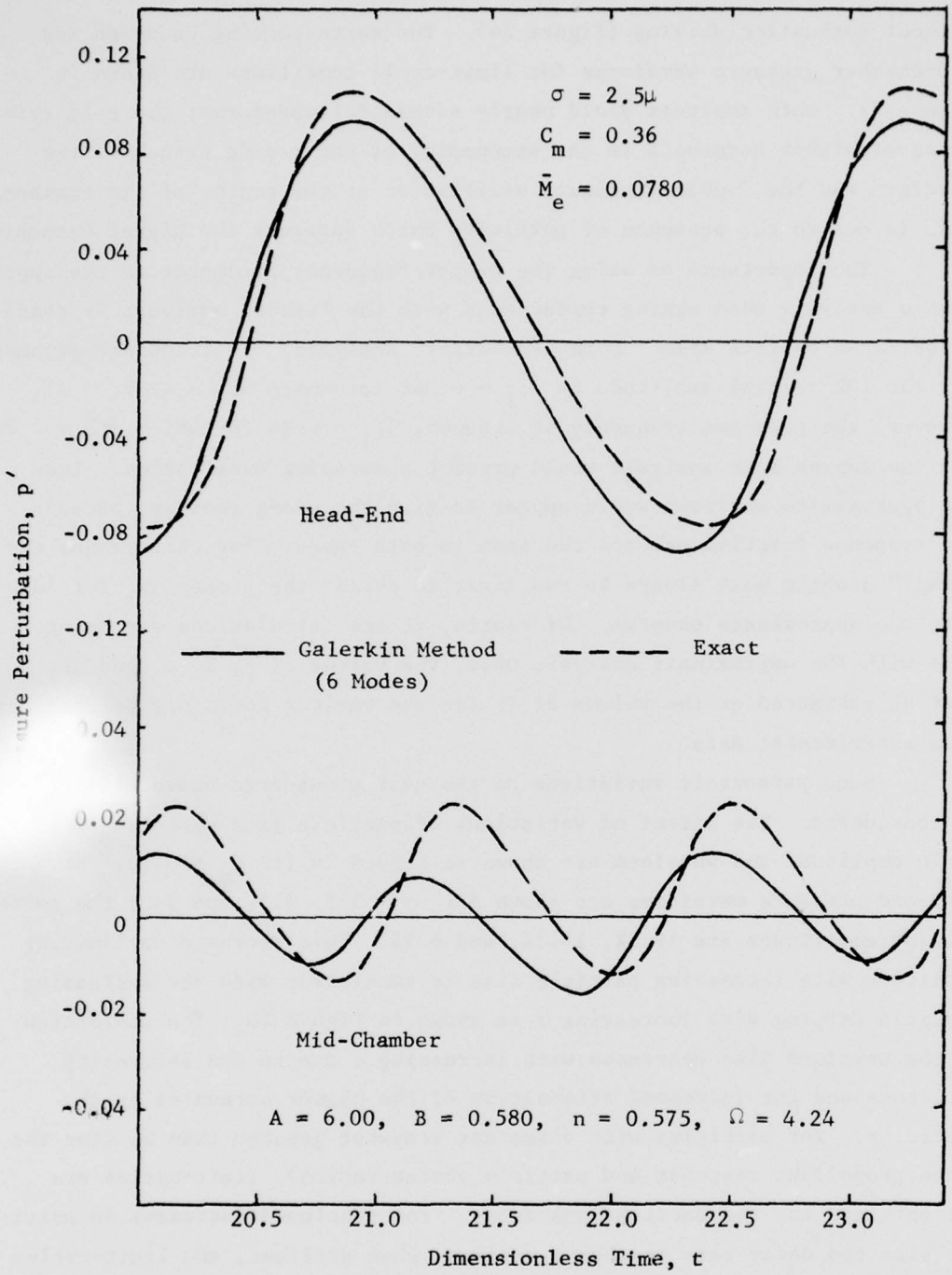

Figure 27. Pressure Waveforms for a Motor with 2.5μ Particles

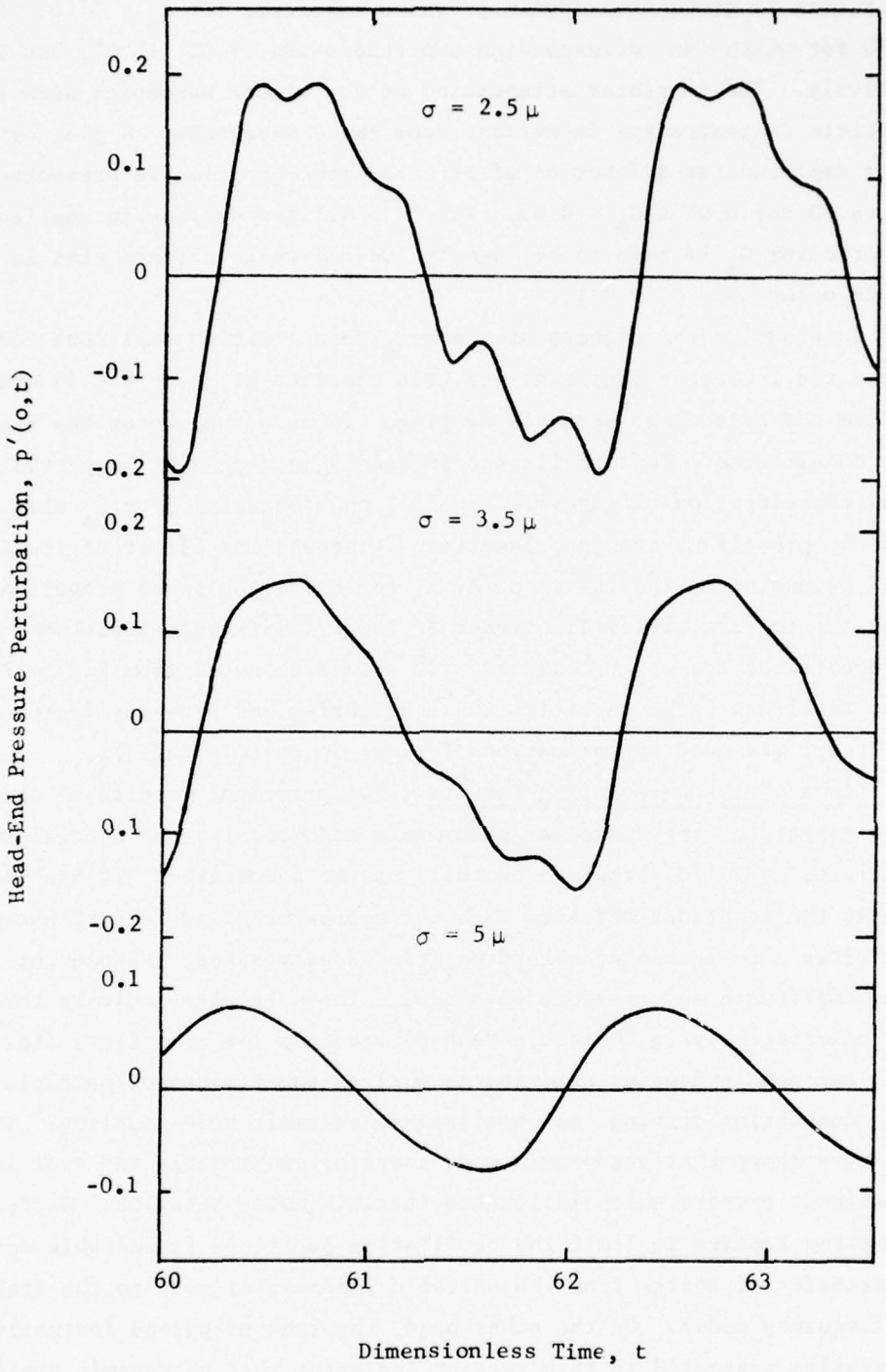

Figure 28. Effect of Particle Size on Pressure Waveforms for $C_m = 0.1$

amplitude and pressure waveform is shown in Figures 29 and 30 for 2.5μ particles. Figure 29 gives limit-cycle pressure waveforms for C_m = 0.10, 0.15, and 0.20 for which the corresponding amplitudes are 19.3%, 16.5%, and 14.3% respectively. The increased attenuation of the higher harmonics with increasing particle concentration is evident from these waveforms. A plot of limiting amplitude as a function of particle concentration is presented in Figure 30 for $0.05 \leq C_m \leq 0.03$. For $C_m > 0.1$ the decline in amplitude with increasing C_m is seen to be nearly linear, while a sharp rise in amplitude occurs for $C_m < 0.1$.

In studying the effects of σ and C_m upon limiting amplitude and waveform, the frequency parameter was held constant at $\Omega_1 = 4.2$ in order to isolate the effects of particle damping. In an actual motor the situation is more complicated. The oscillation frequency is dependent on particle size and concentration (Figures 24 and 25), thus changing σ or C_m also changes the propellant response function $\Re$ through the effect of frequency on Ω_1. Depending on the values of A, B, and n for the given propellant, allowing Ω_1 to vary will yield higher or lower limit-cycle amplitudes than would be obtained for Ω_1 = constant. It should be noted from Figure 24 that for small and large particles the equilibrium and pure-gas frequencies, respectively, are good approximations for use in calculating Ω_1.

Summary of Mode-Coupling Results. The principal results of this study to assess the importance of gasdynamic mode-coupling upon axial mode instabilities in solid rocket motors will now be summarized. It has been shown that the solutions obtained with the approximate and "exact" analyses are in fairly good agreement regarding growth/decay rates, frequencies, limiting amplitudes and pressure waveforms. These results indicate that the approximate analysis (Galerkin Method) accounts for mean flow, flow-turning, and nozzle damping effects, as well as the effects of particle damping, combustion driving, and nonlinear gasdynamic mode-coupling. These studies have shown that gasdynamic mode-coupling is probably the most important nonlinear process which influences unstable motor behavior. Gasdynamic mode-coupling appears to limit the oscillation amplitude in unstable motors by the transfer of energy from the unstable fundamental mode to the stable higher frequency modes. On the other hand, the lack of pulsed instabilities in the results presented in this section indicates that gasdynamic nonlinearities (at least to second order) can not account for pulsed or triggered instabilities. These observations on the role of gasdynamic mode-coupling

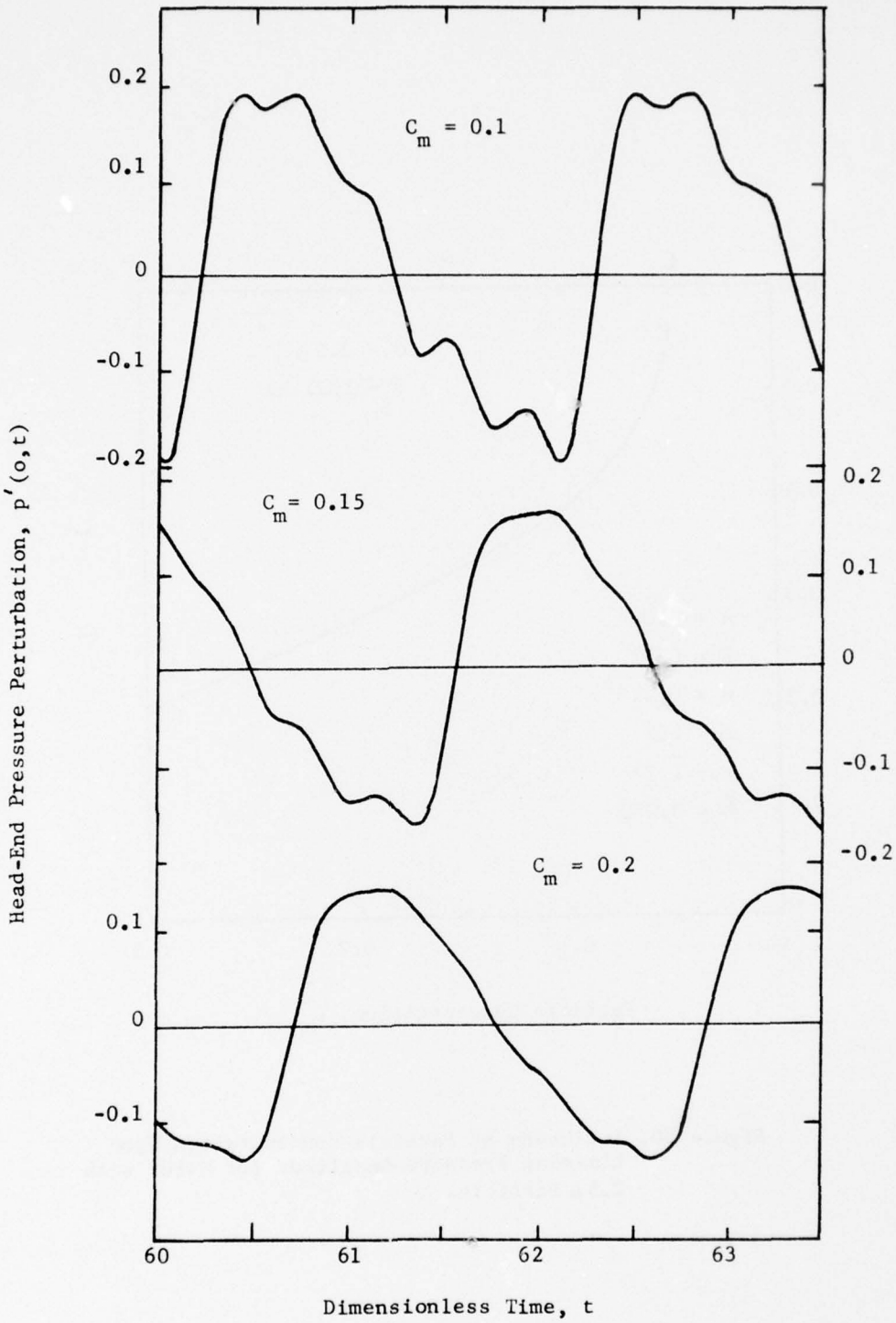

Figure 29. Effect of Particle Concentration on Pressure Waveform for $\sigma = 2.5\,\mu$

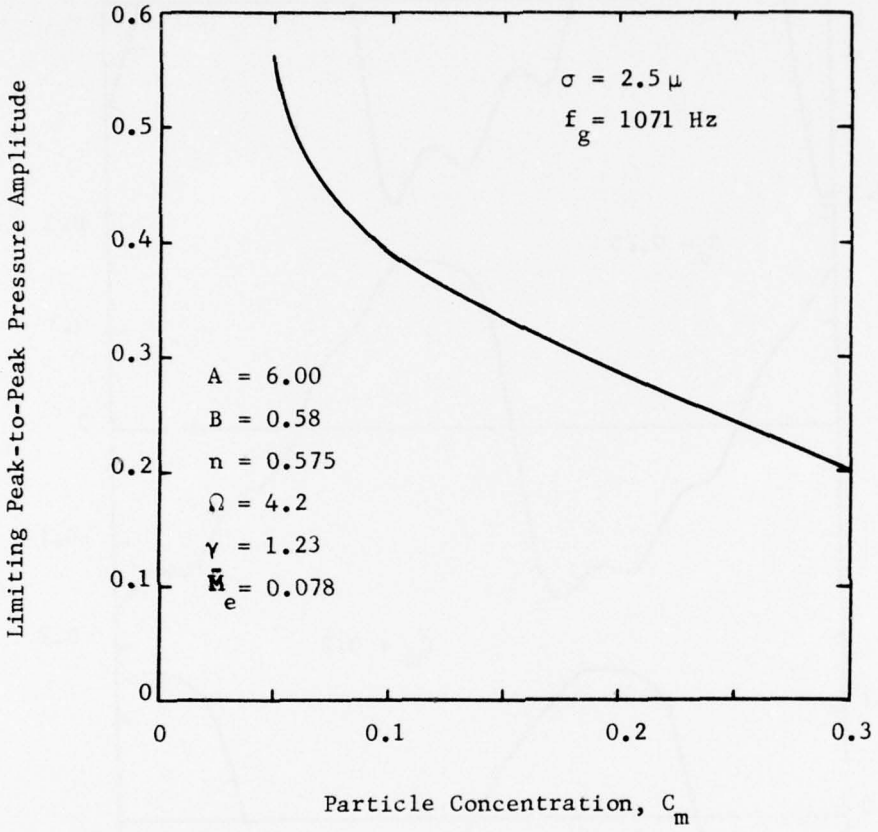

Figure 30. Influence of Particle Concentration Upon Limiting Pressure Amplitude for Motor with 2.5 μ Particles

in solid rocket motors are in agreement with the results of previous studies for liquid rockets[6,7].

Concerning the effect of number of modes upon the approximate solutions, the following results are notable. The number of modes necessary to adequately represent the solution depends upon the relative stability of the higher frequency modes with respect to the fundamental mode. For cases in which the higher modes are heavily damped, as in the case when small particles are present, a three or four mode series expansion appears to be adequate (Figures 22 and 23). For motors with large particles or for motors without particles, the higher modes are less strongly damped and six or more modes may be required (Figures 10 and 23). For cases in which the propellant response for the higher modes are comparable to or greater than the propellant response for the fundamental mode (Figure 18), the convergence of the series expansion may be so slow that an excessive number of modes are required. In the latter case, the approximate technique may require more computation time than the "exact" analysis.

Other results of the parametric studies are of interest. For the cases considered, limiting amplitude appeared to be independent of initial disturbance amplitude and harmonic content. The linear combustion response factor $\Re_1^r$ is a major factor influencing growth/decay rates and limiting amplitudes. For cases without particles, oscillations decay for $\Re_1^r < 3.3$ while for $\Re_1^r > 3.3$ limiting amplitude increases with increasing $\Re_1^r$. For cases with particles, larger values of $\Re_1^r$ are needed for instability. The oscillation frequency, determined by the chamber length and sound speed, affects the stability characteristics of the motor primarily through its influence on combustion driving and particle damping. Finally, particle size and concentration are both important parameters influencing growth and decay rates, limiting amplitudes and waveforms; there is an optimum value of the particle drag constant K (determined by particle size and frequency) for maximum damping.

4.3 Effect of Nonlinear Combustion Driving

In the studies presented so far, it was assumed that the only nonlinearity present in the solid rocket system was gasdynamic mode-coupling. In the next phase of this investigation, the effects of additional nonlinearities were included in the analysis. The effects of nonlinearities in

the pressure-coupled transient combustion process upon the stability characteristics of solid rocket motors are presented and discussed in this section. Velocity-coupled nonlinear combustion processes, which are also known to be important, were not considered in this study due to the time and economic limitations of this project.

The results presented in this section were obtained by the "exact" Kooker-Zinn model using the nonlinear combustion option and by the approximate analysis (Galerkin method) using the heuristic nonlinear combustion model described in Section 2.7. Kooker and Zinn[3] and Levine and Culick[5] have both considered the effects of combustion nonlinearities using "exact" numerical methods, and both have shown that the effect of a nonlinear combustion response is significant for amplitudes greater than about 7 - 10%. On the other hand, this study is the first attempt at incorporating burning rate nonlinearities into an approximate instability model. One of the major objectives of this study, therefore, is to assess the feasibility of modeling combustion nonlinearities using the approximate technique.

The approximate model was first used to study the basic case considered previously in the mode-coupling investigations. The linear combustion parameters for this case are A = 6.00, B = 0.59, n = 0.583; there are no particles present in the flow; and the mean flow Mach number at the nozzle entrance is 0.0780. The acoustic frequency and the steady-state burn rate yield $\Omega_1 = 4.907$. The nonlinear combustion parameter b_m appearing in the heuristic nonlinear combustion model (Equation (77)) is not known a priori. In general, b_m is a complex number which is expected to be different for each acoustic mode. In order to reduce the number of parameters to be considered in this study, it was assumed that the b_m's are all real numbers and that they are the same for all modes. Thus the effect of combustion nonlinearities was studied by varying the single parameter b in the approximate analysis.

Approximate solutions for the growth of a 7% initial disturbance to limiting amplitude are shown in Figure 31 for both linear and nonlinear combustion models. For the nonlinear combustion response, both positive (b = 0.5) and negative (b = -0.5) values of b were considered. This figure shows a significant effect of combustion nonlinearities upon the initial growth rate and limit-cycle amplitude of the pressure oscillations in the motor. For the positive value of b, both the initial growth rate and limit-cycle amplitude are greater than the corresponding values obtained with

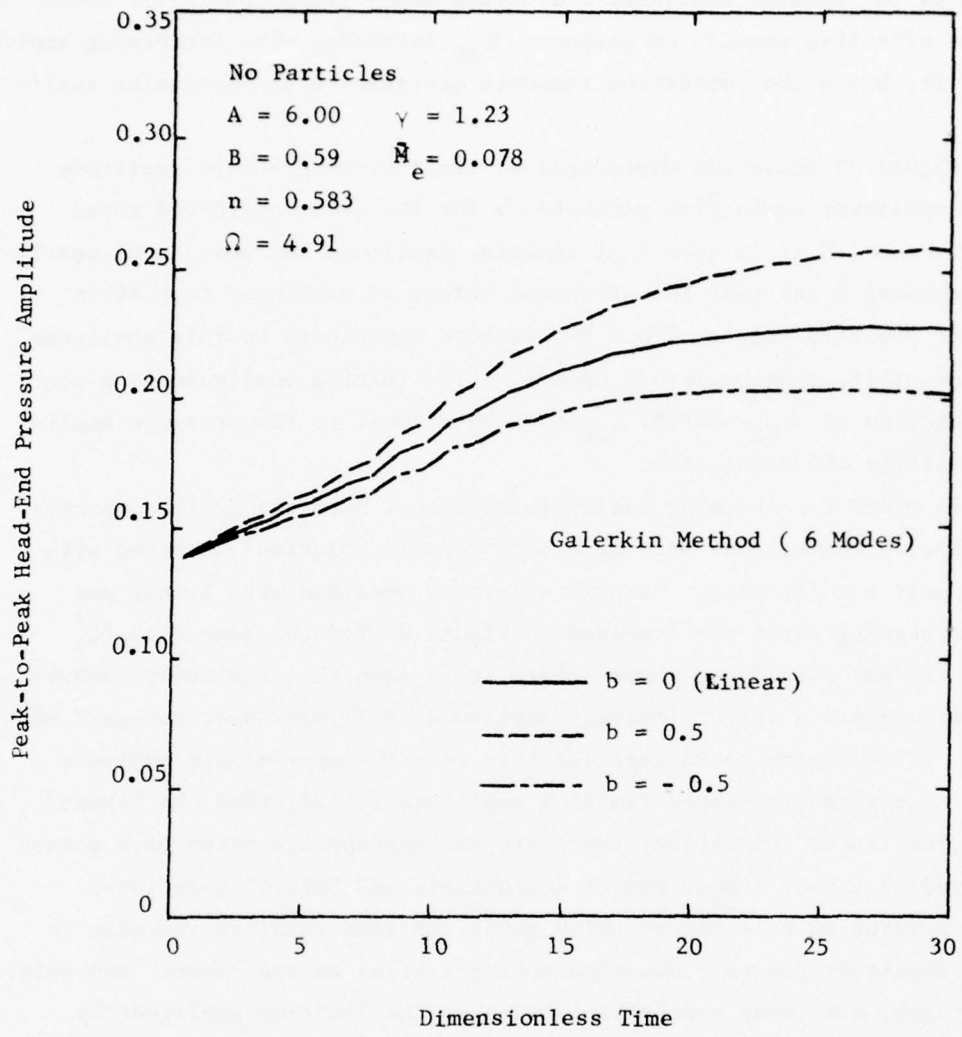

Figure 31. Effect of Combustion Nonlinearities Upon Limiting Amplitude Using the Approximate Model

the linear combustion response (b = 0), while the negative value of b yields reduced values of the initial growth rate and limiting amplitude. The limiting amplitudes obtained were as follows: 11.3% for linear combustion, 10.1% for b = -0.5, and 12.9% for b = 0.5. This behavior is expected from the form of the assumed nonlinear combustion model (Equation (77)), since for $b > 0$ the effective combustion response $\Re_{NL}$ increases with increasing amplitude and for $b < 0$ the combustion response decreases with increasing amplitude.

Figure 32 shows the dependence of limit-cycle pressure amplitude upon the nonlinear combustion parameter b for the case considered above. For $-1.0 \leq b \leq 1.0$ it is seen that limiting amplitude increases nonlinearly with increasing b and that the strongest effect of nonlinear combustion occurs for positive values of b. Two factors contribute to this nonlinear dependence of limiting amplitude upon b: (1) limiting amplitude is a nonlinear function of $\Re_{NL}$ and (2) $\Re_{NL}$ is proportional to the pressure amplitude as well as the value of b.

In order to determine realistic values of b to use in the approximate analysis, comparisons were made with "exact" solutions obtained with the nonlinear burning rate. "Exact" solutions obtained with linear and nonlinear burning rates are compared in Figure 33 for the same case (Q_s^* = -136.1 cal/gm) considered above. Here it is seen that nonlinear combustion effects yield a larger limiting amplitude (8.7% nonlinear versus 7.9% linear). It should be noted that for this case the approximate analysis yields a significantly larger limiting amplitude (11.3%) than the "exact" analysis for linear combustion, therefore the appropriate value of b cannot be obtained by direct comparison of approximate and "exact" solutions. Instead, a value of b is chosen which gives the same relative increase in limiting amplitude due to combustion nonlinearities as the "exact" analysis. For this case, nonlinear combustion increases the limiting amplitude by a factor of 1.10 according to the "exact" analysis. Thus the corresponding approximate solution should yield a limit-cycle amplitude of 12.4% corresponding to b = 0.32 (Figure 32).

The effects of a nonlinear burning rate upon the pressure and burning rate waveforms are shown in Figure 34 for the "exact" analysis, while the corresponding approximate solutions for the pressure waveforms (b = 0.32) are given in Figure 35. Figure 34 shows that a nonlinear combustion response modifies significantly the burning rate waveforms; the positive

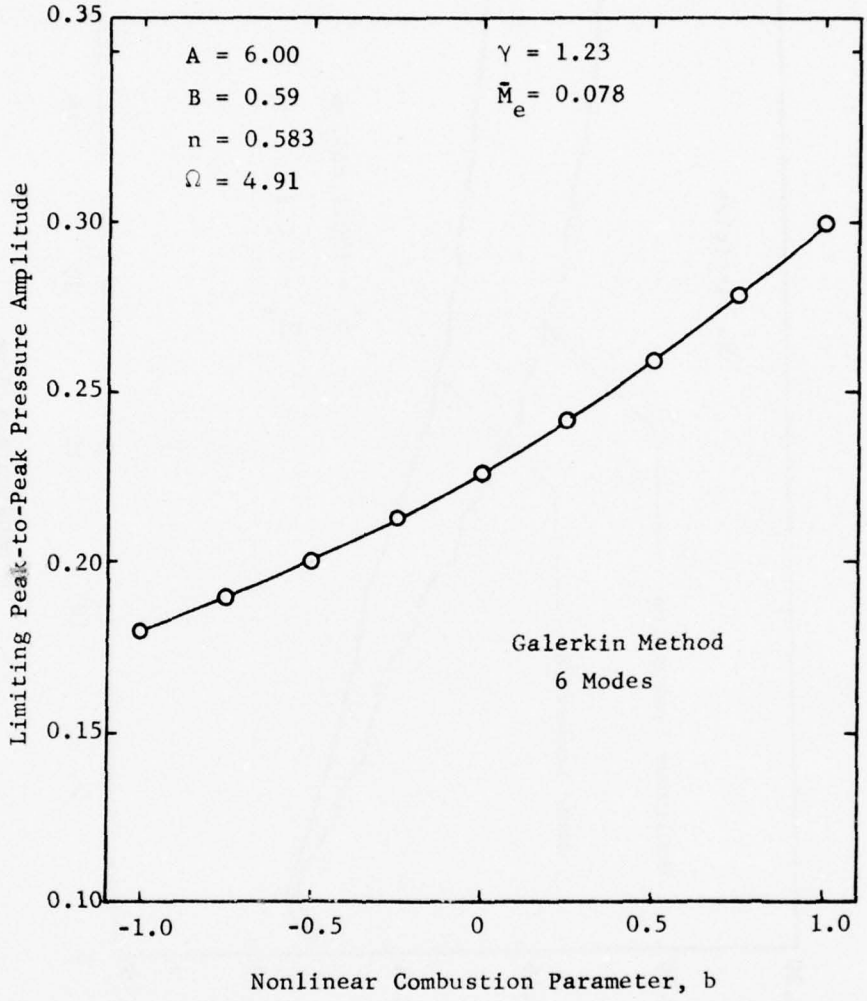

Figure 32. Dependence of Limiting Amplitude Upon Nonlinear Combustion Parameter b

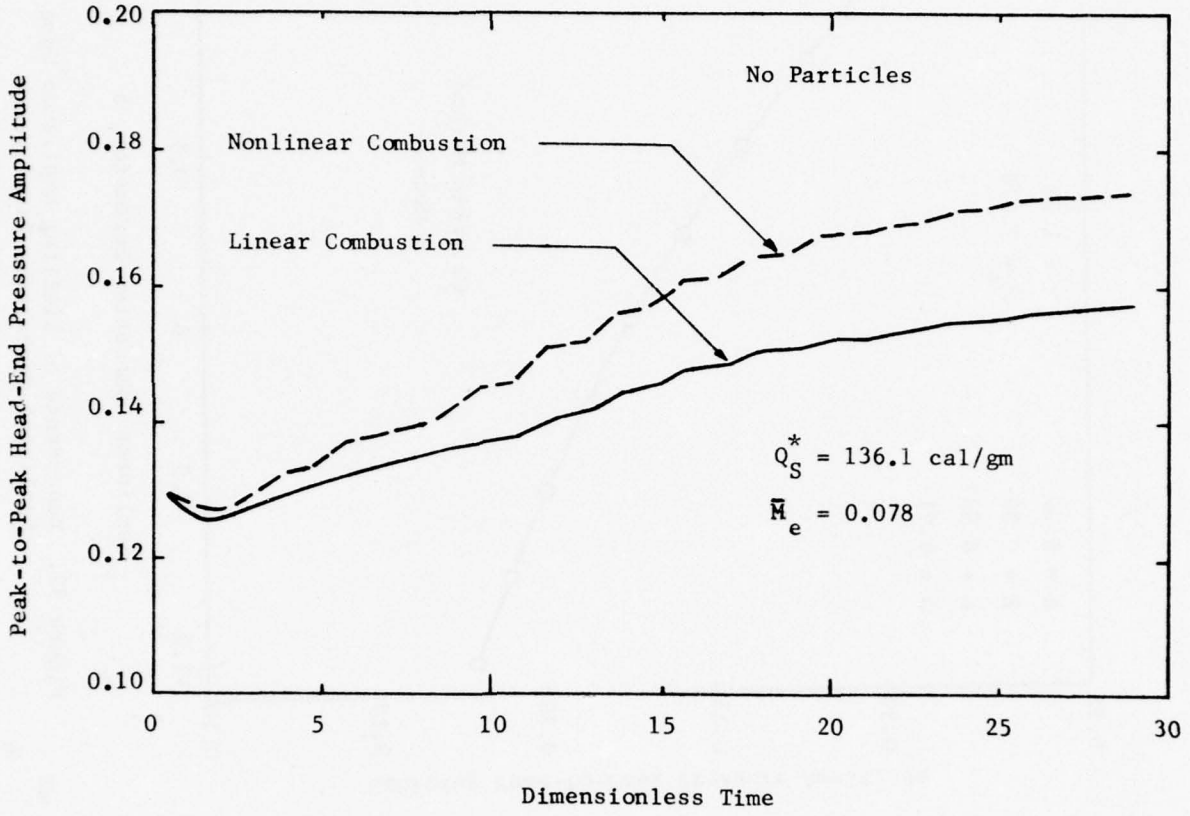

Figure 33. Effect of Combustion Nonlinearities Upon Limiting Amplitude Using the "Exact" Analysis

part of the waveform becomes steeper with higher peak burning rates and the negative part becomes flatter. On the other hand, both approximate and "exact" models predict that, for the moderate amplitudes obtained in this case, combustion nonlinearities have very little effect on the shape of the pressure wave (Figures 34 and 35). The only noticeable effect of nonlinear burning rate upon the pressure waveform is a small mean pressure shift which is obtained with the "exact" analysis but not with the approximate model.

The steepening of the burning rate waveforms and the insensitivity of the pressure wave shape to combustion nonlinearities are in agreement with previously reported "exact" solutions obtained by Levine and Culick.[5] However, Levine and Culick considered a different set of combustion parameters ($A = 6.0$, $B = 0.53$, $n = 0.3$) and included 2 μ particles in the flow, which gave a reduction in limiting amplitude from 31% to 15% when burning rate nonlinearities were included in the analysis. This trend is opposite from that obtained above, and it indicates that negative values of b may be appropriate in some cases.

To further investigate the effect of combustion nonlinearities on the stability of motors, a second case was considered which was obtained by adding 2.5 μ diameter particles ($C_m = 0.36$) to the case considered above. The linear combustion parameters ($A = 6.00$, $B = 0.59$, $n = 0.583$) and the steady-state Mach number at the nozzle entrance ($\bar{M}_e = 0.0780$) remain the same as before. The oscillation frequency, however, is lowered from 1071 Hz to 918 Hz due to the effect of the particles. This decrease in frequency results in an increase in the linear combustion response factor for the fundamental mode; that is, $\Re_1^r$ increases from 3.60 to 3.81. The increased damping due to the presence of the particles offsets the increased combustion driving to yield a system which is stable to moderate amplitude disturbances. Therefore, in the results to follow the effects of combustion nonlinearities upon the decay rate, rather than limiting amplitude, are presented.

The effect of the burning rate nonlinearities upon the decay rates for 3% and 10% initial disturbances is shown in Figure 36 as calculated by the "exact" analysis. Here the nonlinear combustion response yields larger decay rates, which reflects a decrease in the amount of combustion driving with the addition of nonlinear combustion effects. For the 3% disturbance, combustion nonlinearities increase the damping after 10 cycles

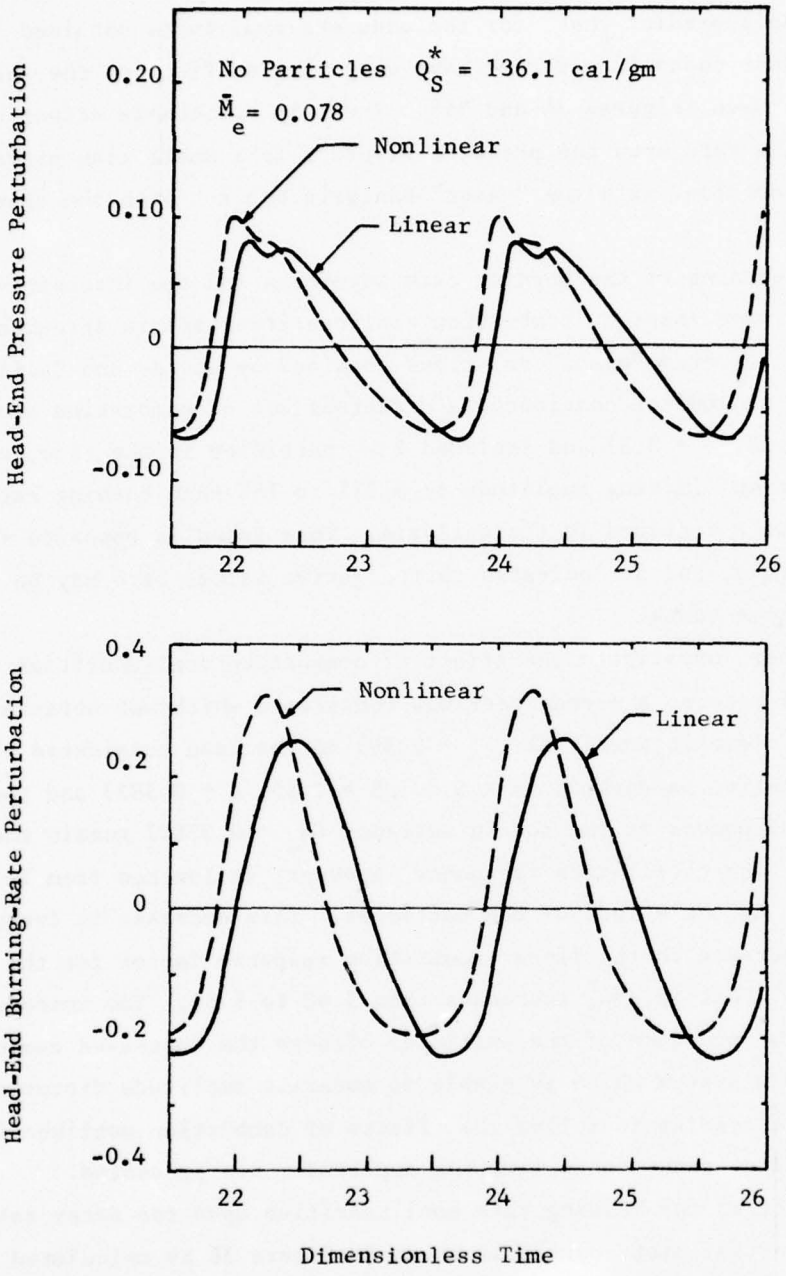

Figure 34. Effect of Combustion Nonlinearities Upon Pressure and Burning-Rate Waveforms Using the "Exact" Analysis

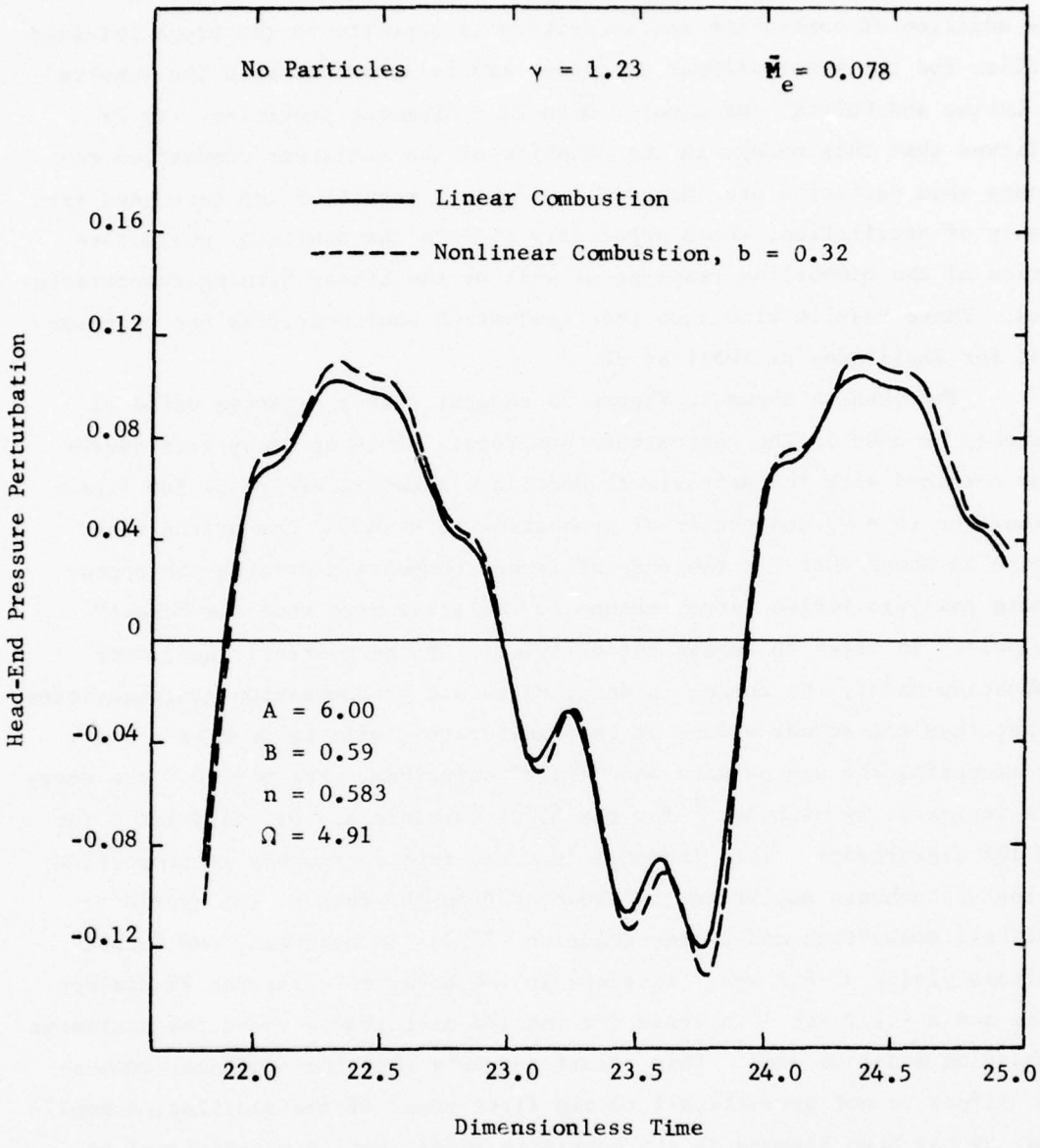

Figure 35. Effect of Combustion Nonlinearities Upon Pressure Waveform Using Approximate Analysis

from -2.8 sec^{-1} to -11.1 sec^{-1} (-8.3 sec^{-1} increase), while an increase in damping from -16.7 sec^{-1} to -28.4 sec^{-1} (-11.7 sec^{-1} increase) occurs for the 10% disturbance. This trend of decreased combustion driving with the addition of combustion nonlinearities is opposite to the trend obtained earlier for the motor without particles and in agreement with the results of Levine and Culick[5] for a motor with 2 μ - diameter particles. It is believed that this change in the behavior of the nonlinear combustion response when particles are included is simply a result of the decreased frequency of oscillation, which apparently affects the nonlinear characteristics of the combustion response as well as the linear burning characteristics. These results also show that combustion nonlinearities can be important for amplitudes as small as 3%.

The results shown in Figure 36 suggest that a negative value of b should be used in the approximate analysis. Plots of decay rate versus time obtained with the approximate model are shown in Figure 37 for linear combustion (b = 0) and nonlinear combustion (b = -0.9). Comparison with Figure 36 shows that for the case of linear combustion driving the approximate analysis yields larger values of the decay rate than the "exact" analysis. In order to assess the usefulness of the heuristic nonlinear combustion model, the change in decay rates due to combustion nonlinearities rather than the actual values of the decay rates, will be used as a basis for comparing the approximate and "exact" solutions. For b = -0.9 the decay rate increases by -4.6 sec^{-1} for the 3% disturbance and by -14.5 sec^{-1} for the 10% disturbance. This increase in decay rate is roughly in proportion to the disturbance amplitude, as expected from the form of the heuristic nonlinear combustion model (see Equation (77)). In contrast, the "exact" analysis yields a -8.3 sec^{-1} increase in the decay rate for the 3% disturbance and a -11.7 sec^{-1} increase for the 10% disturbance where the nonlinear combustion model is used. This result suggests that the nonlinear combustion effect is not proportional to the first power of the oscillation amplitude, as has been assumed in the heuristic model, but is proportional to some positive power p of the amplitude, where $p < 1$.

It was postulated above that frequency is the primary factor responsible for the differences in the nonlinear combustion characteristics observed in the two cases considered in this study. To check this hypothesis, a third case was also considered in which the motor was shortened from 0.597 m

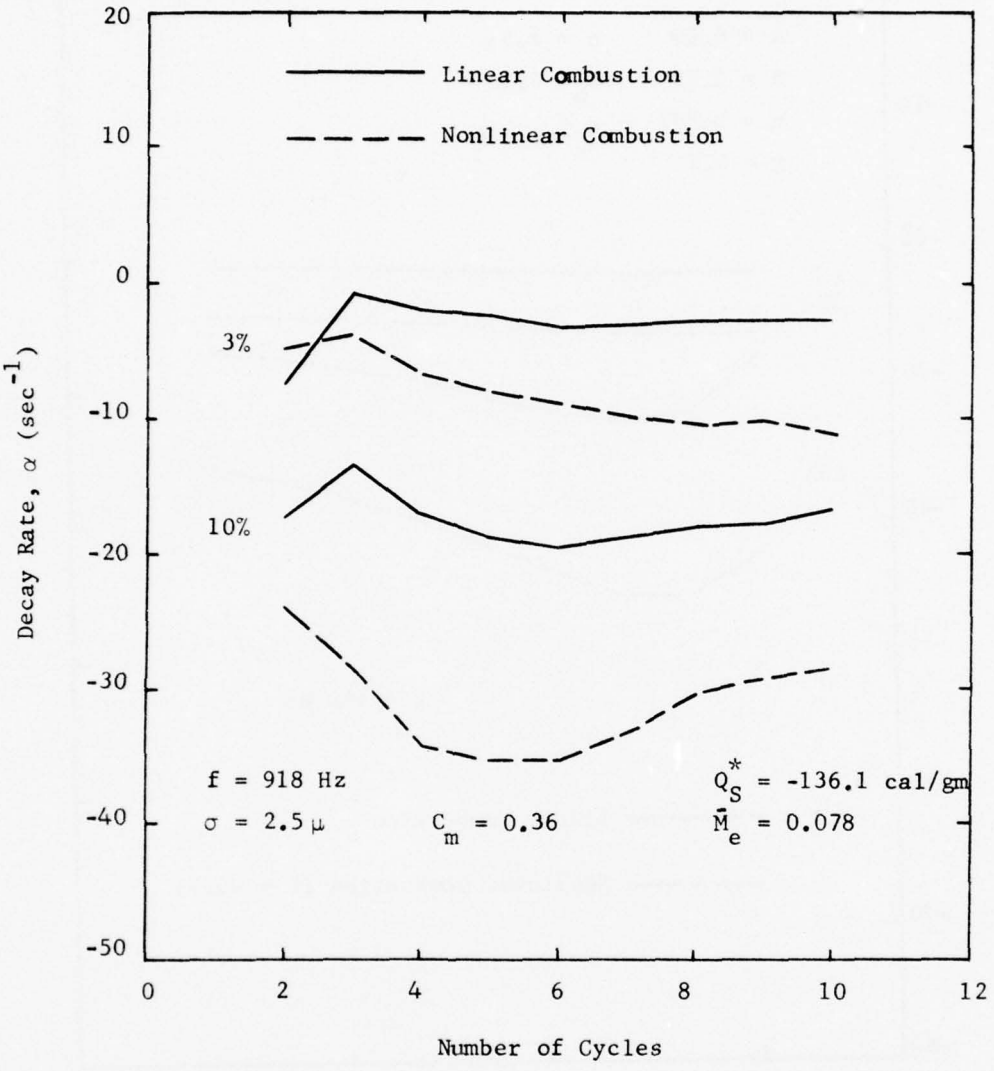

Figure 36. Effect of Combustion Nonlinearities Upon Decay Rate for Motor with 2.5 μ Particles Using "Exact" Analysis

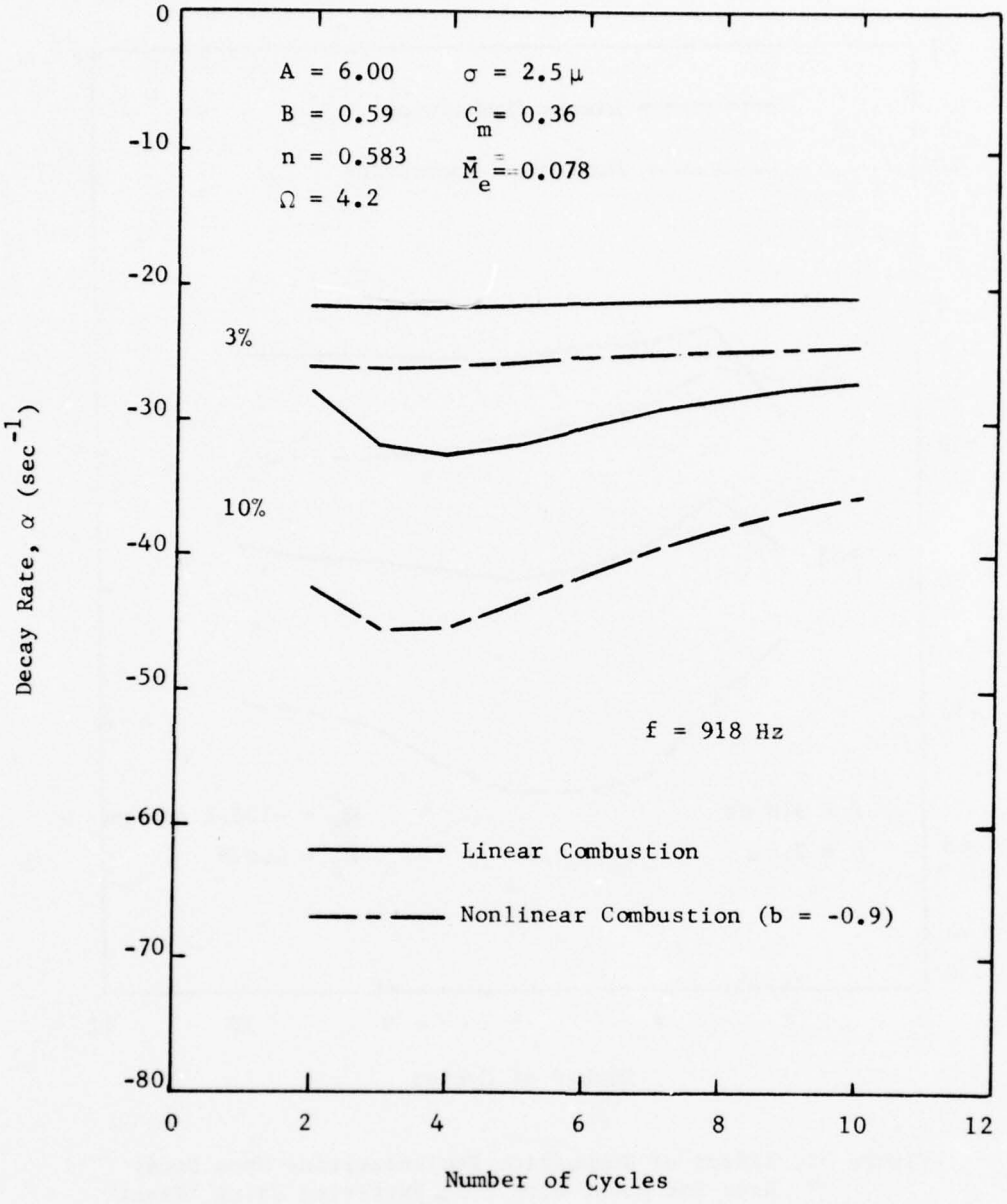

Figure 37. Effect of Combustion Nonlinearities Upon Decay Rate for Motor with 2.5 μ Particles Using Approximate Analysis

(1.958 ft) to 0.501 m (1.642 ft) for the case with 2.5μ particles. This gave an oscillation frequency of 1079 Hz which is only slightly higher than the frequency obtained in the longer motor when particles are absent. The corresponding frequency parameter was $\Omega = 5.00$ which gave a linear response factor for the fundamental mode of $\Re_1^r = 3.505$. In addition the mean flow Mach number at the nozzle entrance was reduced to 0.0654 due to the decrease in the surface area of the burning propellant. Both approximate and "exact" models were used to obtain plots of decay rate versus time for this case, which are shown in Figure 38. In the approximate calculations, the same value of b was used as in the previous case in which particles were absent (i.e., b = 0.32). In contrast to the results presented in Figure 36 and 37 for f = 918 Hz, Figure 38 shows a decrease in damping when the nonlinear combustion model is used for f = 1079 Hz. Thus combustion nonlinearities increase the amount of combustion driving in this case, which agrees with the trend obtained in the first case considered (no particles, 1071 Hz). On the basis of the "exact" solutions, it appears that a somewhat larger value of b should be used in the approximate analysis; this may be due to the slightly higher frequency obtained in this case (1079 Hz as compared to 1071 Hz obtained previously). These results indicate that the effects of combustion nonlinearities upon motor stability are strongly dependent upon the frequency of oscillation.

It has been shown in this section that for some cases combustion nonlinearities increase the amount of combustion driving as the amplitude increases. In the first case considered (f = 1071 Hz, no particles), the motor was unstable to small amplitude disturbances, and the burning rate nonlinearities led to a larger limiting amplitude of the resulting oscillations. In the third case (f = 1079 Hz, 2.5 μ particles) the motor was stable to moderate amplitude disturbances, and the increased combustion driving due to burning rate nonlinearities resulted in smaller decay rates. The latter case suggests the possibility that, if the combustion nonlinearities are sufficiently strong, larger amplitude disturbances will grow in a motor which is stable for small amplitude oscillations. Such a motor is said to be subject to pulsed or triggered instabilities.

The possibility of pulsed instability was investigated with the approximate analysis using the heuristic nonlinear combustion model. For the second case considered above (918 Hz, 2.5 μ particles), a hypothetical combustion response was considered by assuming that b = 3.0 (rather than

$A = 6.00$, $B = 0.59$, $n = 0.583$, $\Omega = 5.0$

$\sigma = 2.5\,\mu$, $C_m = 0.36$, $\bar{M}_e = 0.0654$

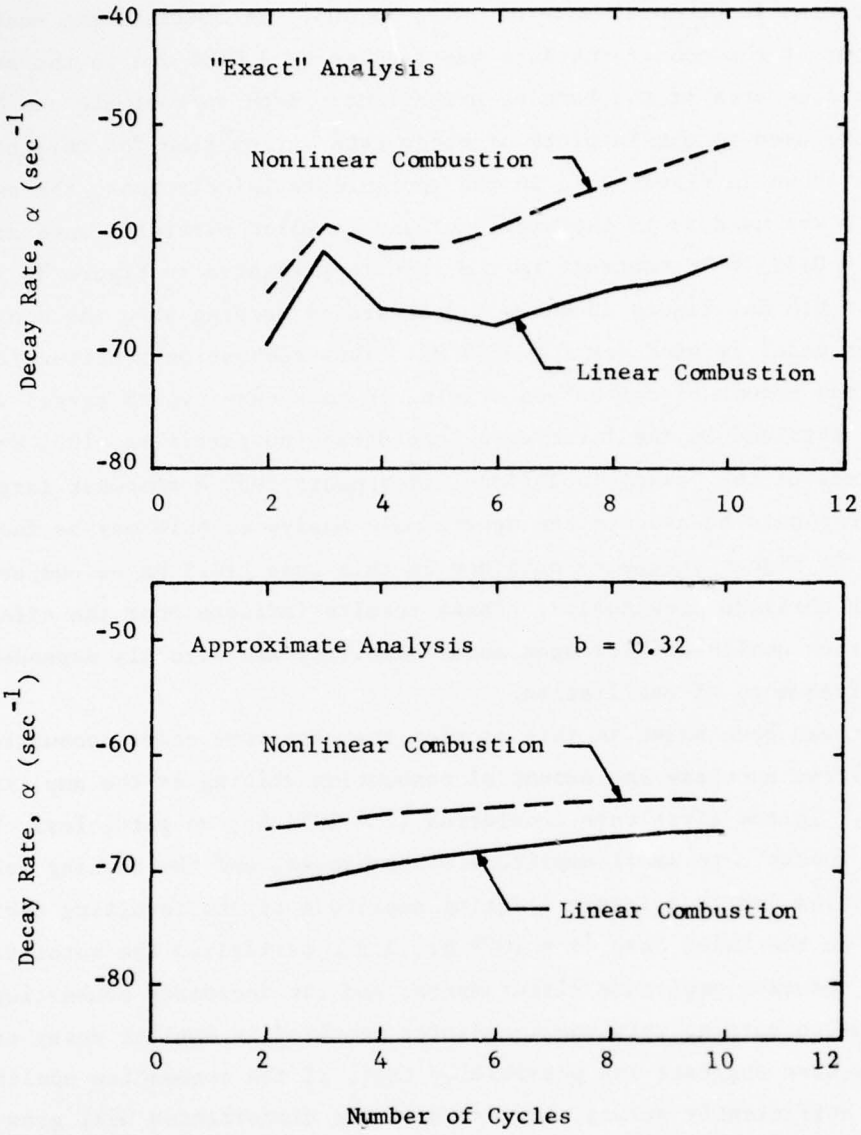

Figure 38. Effect of Combustion Nonlinearities on Decay Rate for 1079 Hz Oscillations in a Motor with 2.5 μ Particles

the negative value indicated by the "exact" model). Solutions were then generated for several different initial disturbance amplitudes using both linear and nonlinear burning rate models. The results of these computations are shown in Figure 39. For the 1% and 3% disturbances, combustion nonlinearities yield smaller decay rates as expected, while the 10% and 20% disturbances grow when the nonlinear combustion model is used. For the 20% disturbance it appears that the oscillations are approaching a limiting amplitude of about 30%. This is clearly an example of pulsed instability in a linearly stable motor.

To further explore this case, a plot of growth/decay rate, α, versus amplitude was constructed for these solutions. This graph is presented in Figure 40 which shows that α increases monotonically from negative values (decay) at small amplitudes, vanishes at about 4% amplitude, and reaches maximum positive values (growth) at about 20% amplitudes. For amplitudes larger than 20%, α falls rapidly to zero. The vanishing of α at 4% amplitude is very significant, since it indicates a threshold amplitude below which all oscillations decay and above which all oscillations grow; this amplitude is referred to as an unstable limit-cycle or triggering limit. The rapid drop in α for large amplitude oscillations indicates approach of the solution to a final limiting amplitude or stable limit cycle at which $\alpha = 0$. At this point the increased combustion driving at higher amplitudes is balanced by the increased losses due to gasdynamic mode-coupling which limits the final amplitude attained. Although this case is purely hypothetical, it illustrates the essential features of pulsed instability in actual rocket motors and demonstrates the feasibility of using the approximate nonlinear combustion model to investigate this phenomenon.

In summary, this study has shown that pressure coupled combustion nonlinearities are important in many cases; the "exact" calculations indicate that they should be included whenever the oscillation amplitudes exceed the 7 - 10% range (and sometimes for amplitudes as small as 3%). Depending on the frequency of oscillation and the various propellant properties, combustion nonlinearities may increase or decrease the combustion driving as the wave amplitude increases thereby affecting the growth/decay rates and limiting amplitudes. It has been shown that the heuristic nonlinear combustion model used in the approximate analysis accounts for many of the effects of nonlinear combustion driving, but additional information is needed

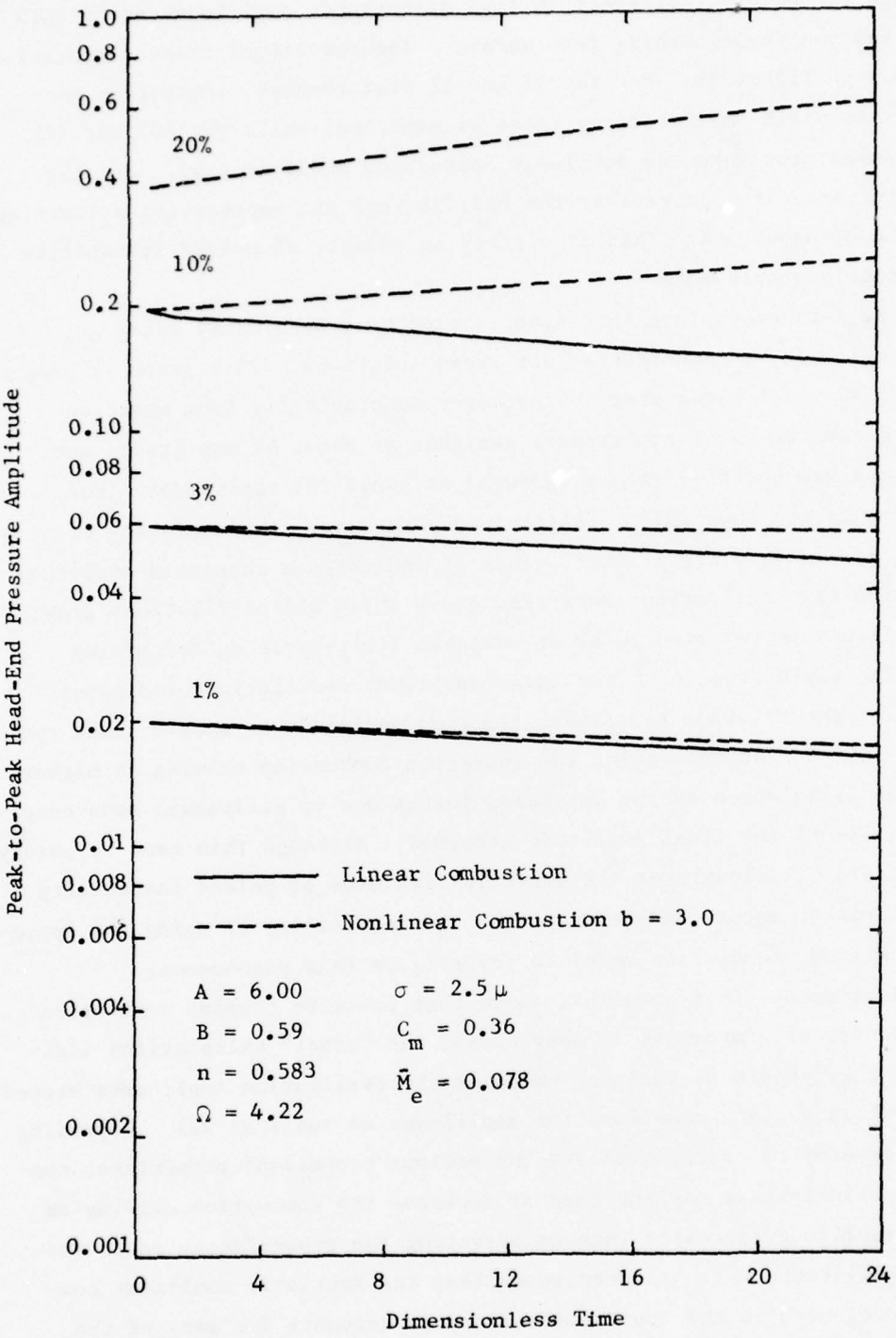

Figure 39. Pulsed Instability Due to Combustion Nonlinearities by Approximate Analysis

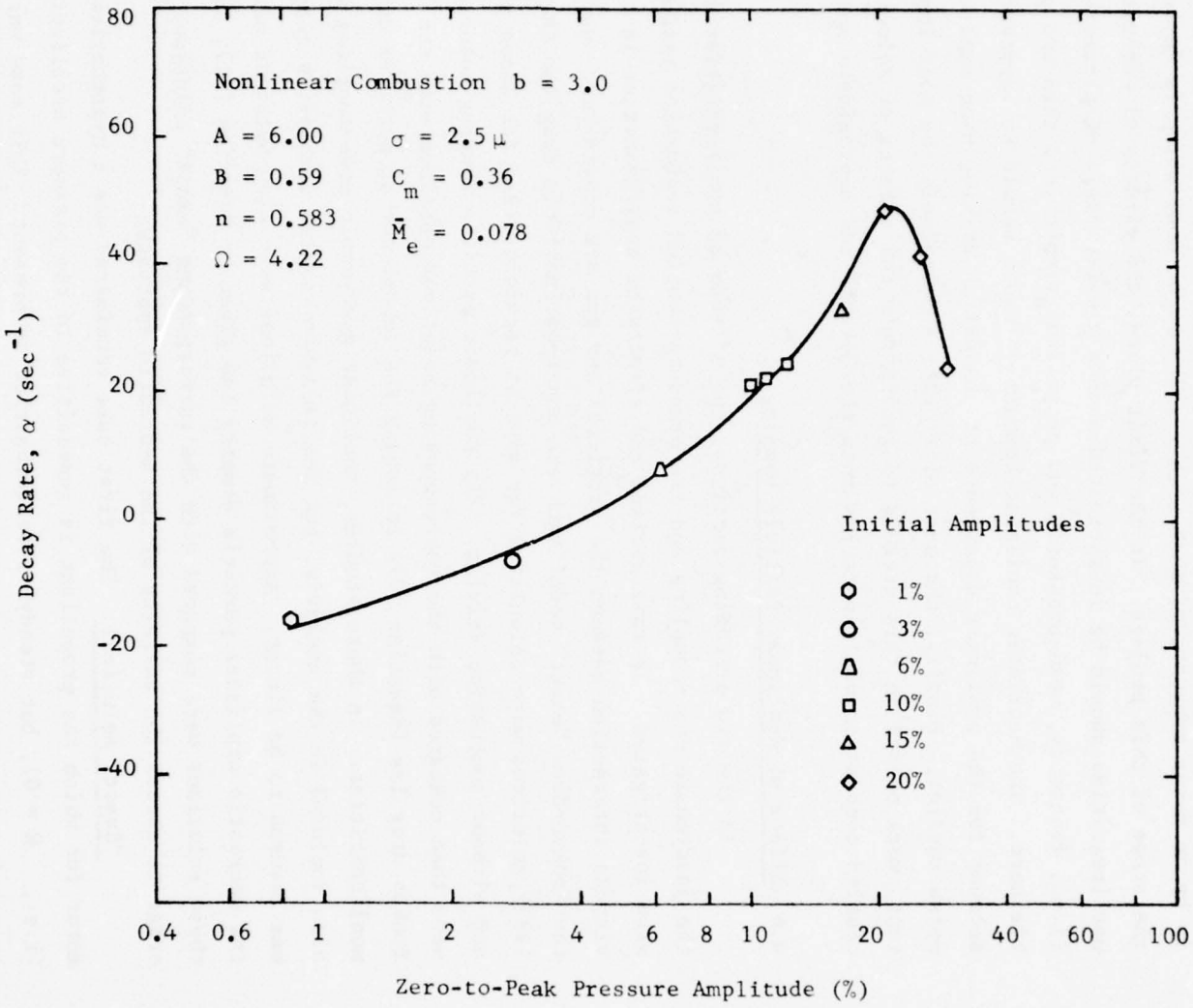

Figure 40. Decay Rate vs Amplitude for Nonlinear Combustion with b = 3.0

to determine the nonlinear combustion parameter b. Finally it has been shown that burning rate nonlinearities may be an important factor contributing to the development of pulsed instabilities, a phenomenon which is not predicted on the basis of gasdynamic nonlinearities (mode-coupling) alone.

The treatment of combustion nonlinearities presented in this section is by no means exhaustive; much work remains to be done which is beyond the scope of this project. In the first place, the effects of combustion nonlinearities should be investigated over a greater range of parameters (i.e., frequency, mean pressure, and propellant properties) than was possible here. The heuristic nonlinear combustion model should be improved to account for the nonlinear dependence of combustion driving upon amplitude noted earlier. Finally, the most difficult, and probably the most important, work needed in this area is to incorporate the effects of velocity-coupled combustion nonlinearities into the "exact" and approximate models.

4.4 Effect of Nonlinear Particle Damping

In the two preceding sections, the effects of nonlinearities in the gasdynamic mode-coupling and the pressure-coupled combustion response were investigated. In this section the effects of nonlinearities in the viscous interaction between the particles and gas are considered. Using the Kooker-Zinn "exact" model with the nonlinear particle drag law (Equation (99)), solutions were calculated for several particle sizes for cases with and without combustion driving. The nonlinear particle damping solutions were then compared with the corresponding solutions obtained with the linear Stokes drag law (Equation (7)) to assess the importance of particle damping nonlinearities. In these studies, nonlinear gasdynamic mode-coupling was also included in the analysis, but the pressure-coupled combustion response was assumed to be linear. Approximate solutions were also obtained using the heuristic nonlinear particle damping law given by Equation (81), and these solutions were compared with the corresponding "exact" solutions in order to assess the validity of the heuristic approach.

"Exact" Solutions. The first case considered was a hypothetical motor for which the propellant is insensitive to the pressure oscillations (i.e., $\Re = 0$), but steady-state combustion is present. This case was chosen in order to retain the mean flow contribution to the nonlinear particle damping, an effect which is not present in the case of a particle/gas

mixture in a closed-ended box. Using the "exact" computer program with the nonlinear particle drag option, solutions were calculated for $2.5\mu \leq \sigma \leq 40\mu$ for $C_m = 0.20$, $\bar{M}_e = 0.078$, and $f_g = 1071$ Hz. Plots of decay rate versus particle diameter for nonlinear drag (2.5% and 5% amplitude) are compared with the corresponding curve for linear drag in Figure 41.

Figure 41 shows that the dependence of decay rate upon particle size for the nonlinear drag calculations is similar to that obtained with the linear drag law; both exhibit an optimum particle size for maximum damping. However, the particle drag nonlinearities shift the peaks to larger particle sizes. For the nonlinear drag law, the maximum damping occurs at $\sigma = 13\mu$ for 2.5% amplitude and at $\sigma = 16\mu$ for 5.0% amplitude as compared to $\sigma = 8.5\mu$ for the Stokes drag law. The nonlinear particle drag effect increases as the amplitude of the oscillation increases, and it also increases with increasing particle size. Both of these effects are a consequence of the higher Reynolds numbers resulting from the increase in particle size and relative velocity. For $\sigma < 10\mu$ the decay rate decreases with increasing amplitude, while damping increases with increasing amplitude for $\sigma > 10\mu$. For $\sigma < 3\mu$ the effect of particle nonlinearities is small and can be neglected, but the nonlinear drag effects become very important for $\sigma > 15\mu$.

The next case considered was the basic set of motor parameters used in the mode-coupling study: $Q_s^* = -137.0$ cal/gm (A = 6.0, B = 0.58, n = 0.575), $\bar{M}_e = 0.078$, and $f_g = 1071$ Hz. Calculations were made for $\sigma = 2.5\mu$, 8.0μ, and 20.0μ for a particle loading of $C_m = 0.36$ using both linear and nonlinear particle drag models. The results of these calculations are shown in Figures 42, 43, and 44.

For 2.5μ particles the growth to limiting amplitude of a 10% initial disturbance is shown in Figure 42 for both linear and nonlinear drag laws. Particle nonlinearities increase the limiting amplitude from about 9.2% to about 10.5%, a modest effect. For small particles this result is expected from the small decrease in particle damping due to nonlinear drag effects at higher amplitudes (Figure 41).

For 8.0μ particles the motor is stable due to the greatly increased particle damping. To determine the effect of particle drag nonlinearities upon the decaying oscillations, decay rate was plotted as a function of amplitude (zero-to-peak) for each cycle during the decay. These plots for

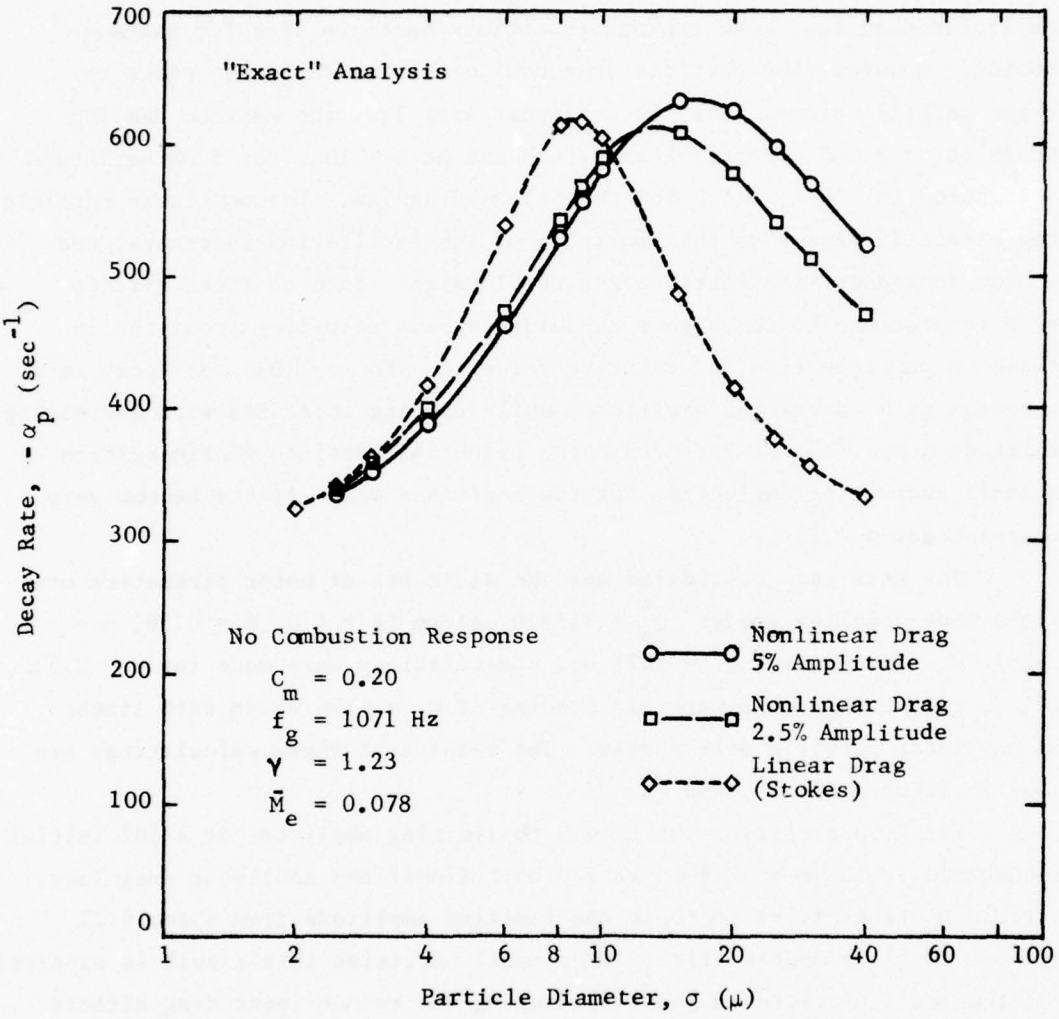

Figure 41. Effect of Particle Drag Nonlinearities Upon Decay Rates for a Hypothetical Motor Without Combustion Driving

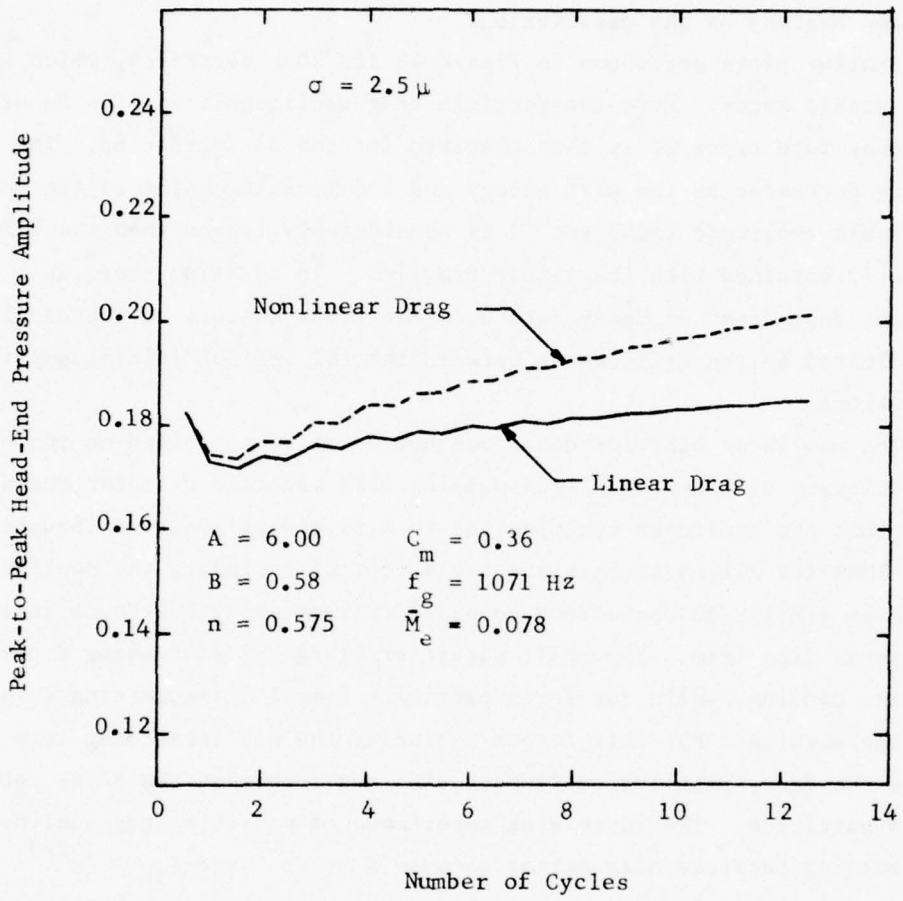

Figure 42. Effect of Particle Drag Nonlinearities Upon Limiting Amplitude for Motor With 2.5 μ Particles by "Exact" Analysis

10% and 20% initial amplitudes for nonlinear drag and for 10% initial amplitude for linear drag are shown in Figure 43. For nonlinear drag, the decay rate increases as the oscillation decays, approaching a constant value of about $-273\ \text{sec}^{-1}$ for small amplitudes. This limiting value is significantly smaller than the nearly constant value of $-323\ \text{sec}^{-1}$ obtained with the linear drag law. There is very good overlap between the nonlinear solutions for 10% and 20% initial amplitudes, indicating only a slight dependence of decay rate on the history of the oscillation.

Similar plots are shown in Figure 44 for 20 μ particles, which also yields a stable motor. Here the particle drag nonlinearities have an effect on the decay rate opposite to that observed for the 8 μ particles. The decay rate decreases as the wave decays and the limiting value of the decay rate at small amplitude ($-293\ \text{sec}^{-1}$) is considerably larger than the value ($-137\ \text{sec}^{-1}$) obtained with the linear drag law. In addition there is a significant dependence of decay rate upon the prior history of the oscillation, indicated by the differences between the 10% and 20% initial amplitude solutions.

The nonlinear behavior described above can be explained on the basis of the variation of linear particle damping with particle diameter σ and the fact that the nonlinear contribution to K is always positive (equation (100)). Thus for all particle sizes the effect of including the nonlinear drag term is similar to the effect obtained by increasing K without including the nonlinear drag term. For small particles (large K) increasing K decreases the damping, while for large particles (small K) increasing K increases the damping. For this reason including the nonlinear drag term decreases the decay rate for small particles and increases the decay rate for large particles. The increasing importance of particle drag nonlinearities with increasing particle size arises because $K \propto \sigma^{-2}$ and $K_{NL} \propto \sigma^{2/3}$. Thus for sufficiently large σ, the nonlinear contribution K_{NL} becomes larger than the linear contribution K (Table 4).

The principal factor influencing the nonlinear drag term is the absolute value of the relative velocity between particles and gas. The relative speed is composed of a steady-state part and a fluctuating part. Due to the steady-state lag of the particles relative to the gas in a motor with burning at the lateral boundary (Equation (41)), the steady-state part is significant. The steady-state contribution to the relative velocity explains the fact that the damping at vanishingly small amplitude with non-

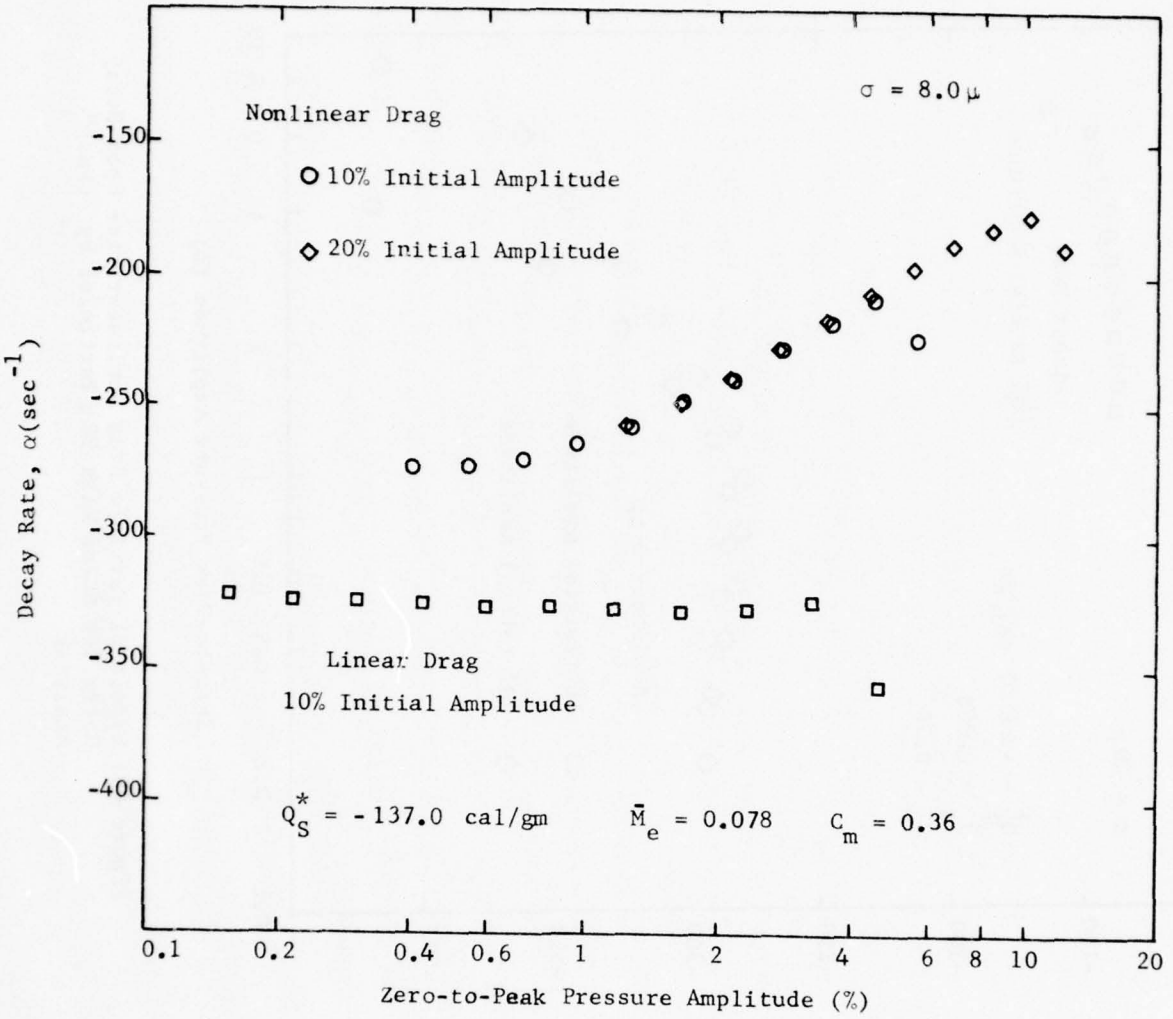

Figure 43. Effect of Particle Drag Nonlinearities Upon Decay Rates for Motor With 8 μ Particles by "Exact" Analysis

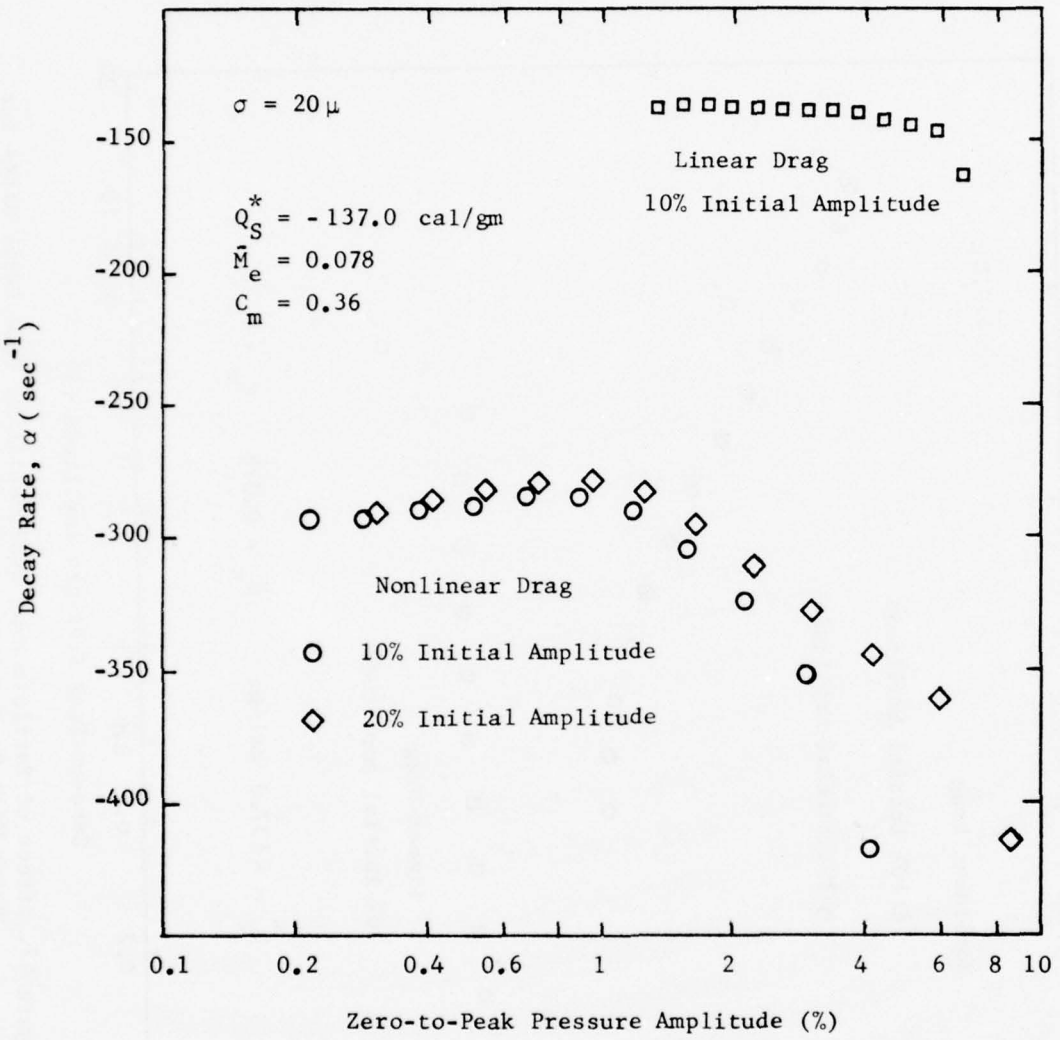

Figure 44. Effect of Particle Drag Nonlinearities Upon Decay Rates for Motor With 20 μ Particles by "Exact" Analysis

Table 4. Linear and Nonlinear Drag Constants Versus σ

σ	K	K_{NL}
2.5	102.5	0.742
3.0	71.18	0.838
4.0	40.04	1.015
6.0	17.80	1.330
8.0	10.01	1.611
10.0	6.406	1.869
15.0	2.847	2.449
20.0	1.602	2.967
25.0	1.025	3.443
30.0	0.712	3.888
40.0	0.400	4.710

linear drag differs from the corresponding damping with linear drag. Thus nonlinear particle drag is important even for infinitesimally small amplitude oscillations. The fluctuating contribution to the nonlinear drag accounts for most of the variation of decay rate with amplitude when the drag nonlinearities are taken into account.

To determine the effect of particle drag nonlinearities upon the limit-cycle amplitudes for motors with particles much larger than 2.5 μ, it was necessary to increase the combustion response and decrease the particle concentration so that instability could occur. Thus Q_s^* was increased to -139.4 cal/gm giving A = 6.00, B = 0.55 and n = 0.552, and C_m was decreased to 0.20. Results calculated with the "exact" analysis for 8.0 μ and 20 μ particles are shown in Figures 45, 46, and 47.

Figure 45 shows growth rate versus number of cycles for 3% and 10% initial disturbances for a motor with 8.0 μ particles. This case is interesting because it shows that particle drag nonlinearities, like combustion nonlinearities, may lead to pulsed instabilities. In this example 3% initial disturbances decay at a rate of roughly -25 sec^{-1}, while 10% initial disturbances grow at a rate of about 15 sec^{-1}. This behavior is a consequence of the nonlinear drag law which causes a decrease in particle damping with increasing amplitude (Figure 43) allowing the combustion process to drive oscillations for sufficiently large amplitudes.

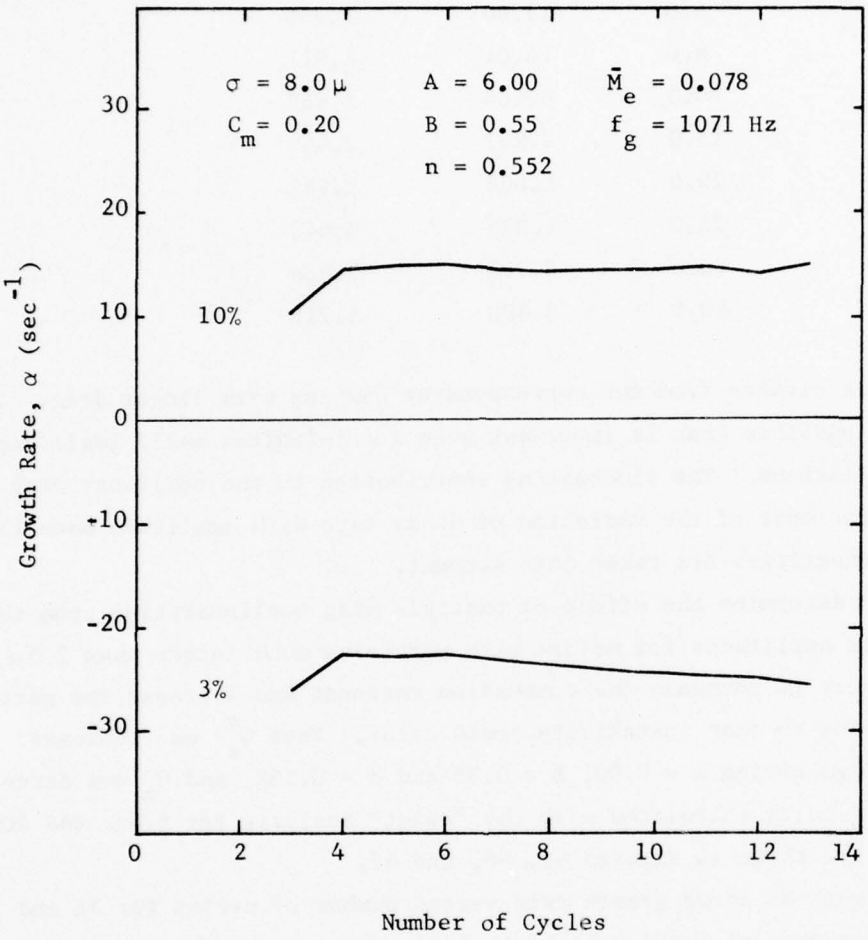

Figure 45. Pulsed Instability Due to Particle Drag Nonlinearities for Motor With 8 μ Particles by "Exact" Analysis

The particle nonlinearities have the opposite effect for 20 μ particles as shown in Figure 46. Using the linear drag law, the analysis predicts growth of oscillations to a limiting amplitude exceeding 8%. For the nonlinear drag law, the greatly increased particle damping causes the oscillations to decay to zero (or at least to a limiting amplitude less than 1.5%). The corresponding pressure waveforms for this case are presented in Figure 47, which shows the dramatic effect of particle drag nonlinearities upon the amplitude of the oscillations but little or no effect on the shape of the pressure waveform.

Approximate Solutions. In order to assess the validity of the heuristic nonlinear particle drag law described in Section 2.8, approximate solutions were obtained for 8 μ and 20 μ particles and were compared with the corresponding "exact" solutions. These results are presented as plots of decay rate versus amplitude in Figures 48 and 49 which correspond to the "exact" solution presented in Figures 43 and 44.

Figure 48 shows approximate solutions for decay rate as a function of amplitude for a motor with 8 μ particles. For nonlinear drag these curves are shown for several values of the parameter C which appears in Equation (81). For the case of C = 0 the amplitude-dependent part of the nonlinear drag vanishes and only the steady-state contribution remains. For positive values of C the decay rate increases as the amplitude of the wave decreases, which agrees with the "exact" calculations. In addition the approximate solutions agree with the "exact" solutions regarding the prediction that the particle damping at low amplitudes is smaller when the nonlinear particle drag law is used (due to the steady-state contribution to the Reynolds number).

In comparing the approximate and "exact" solutions shown in Figures 43 and 48, it should be noted that the two analyses predict different decay rates for linear particle drag (i.e., $\alpha = -323\ \text{sec}^{-1}$ for the "exact" analysis compared to $\alpha = -400\ \text{sec}^{-1}$ for the approximate analysis). Thus quantitative assessment of the validity of the postulated nonlinear drag model must be made by comparing the "exact" and approximate results on the basis of the change in decay rate due to the addition of particle drag nonlinearities rather than on the basis of the actual values of the decay rates. Therefore two quantities, $\Delta\alpha_1$ and $\Delta\alpha_2$ will be considered in comparing

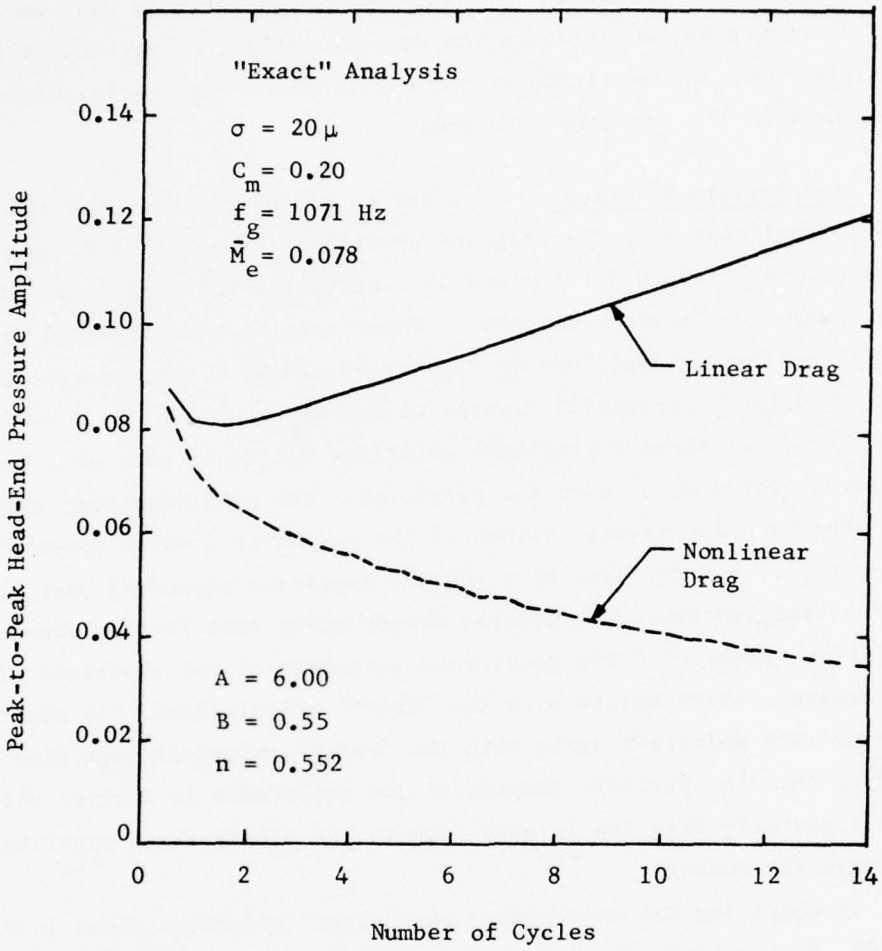

Figure 46. Strong Effect of Particle Drag Nonlinearities Upon Motor Stability for 20 μ Particles

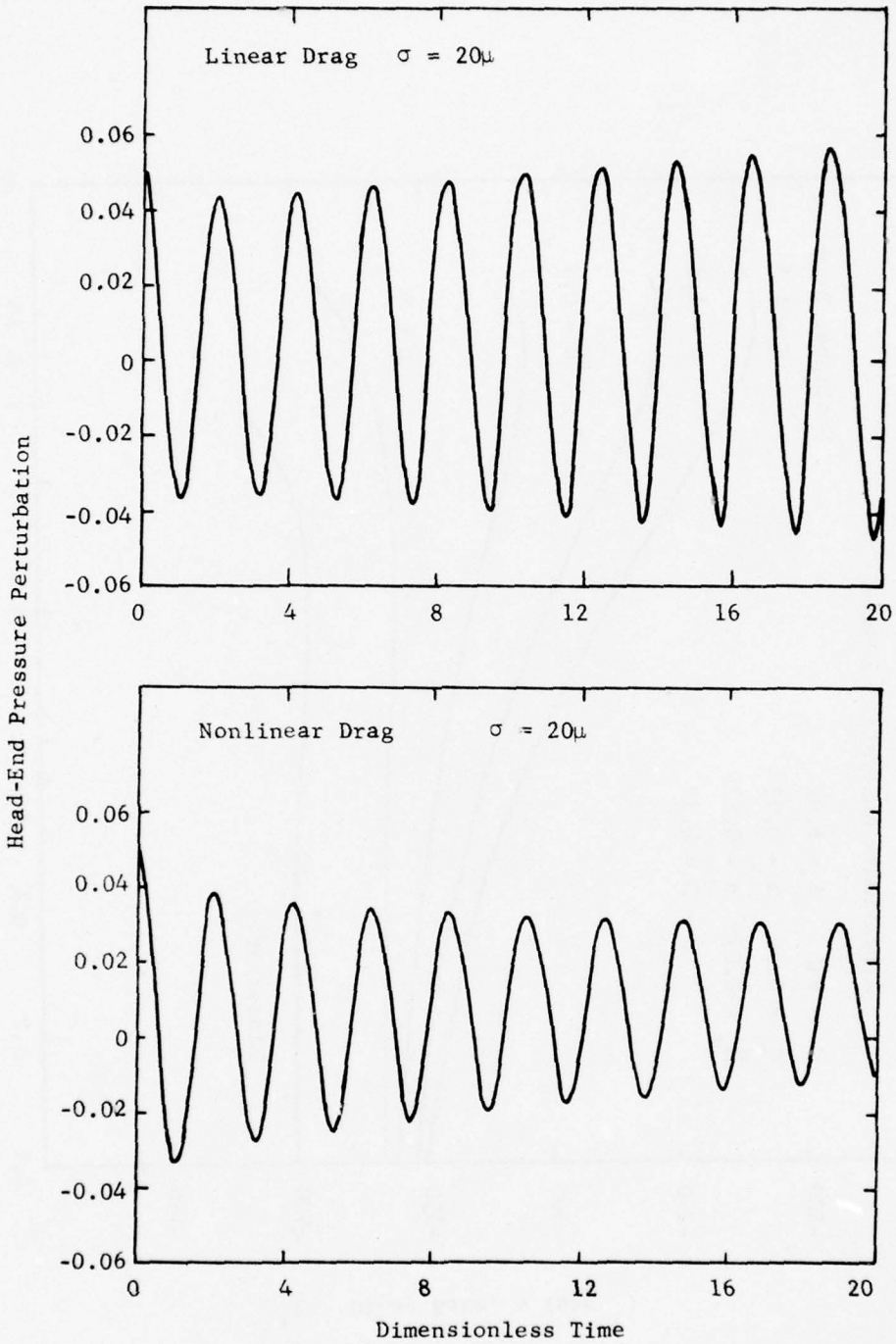

Figure 47. Effect of Particle Drag Nonlinearities on Pressure Waveforms for 20μ Particles

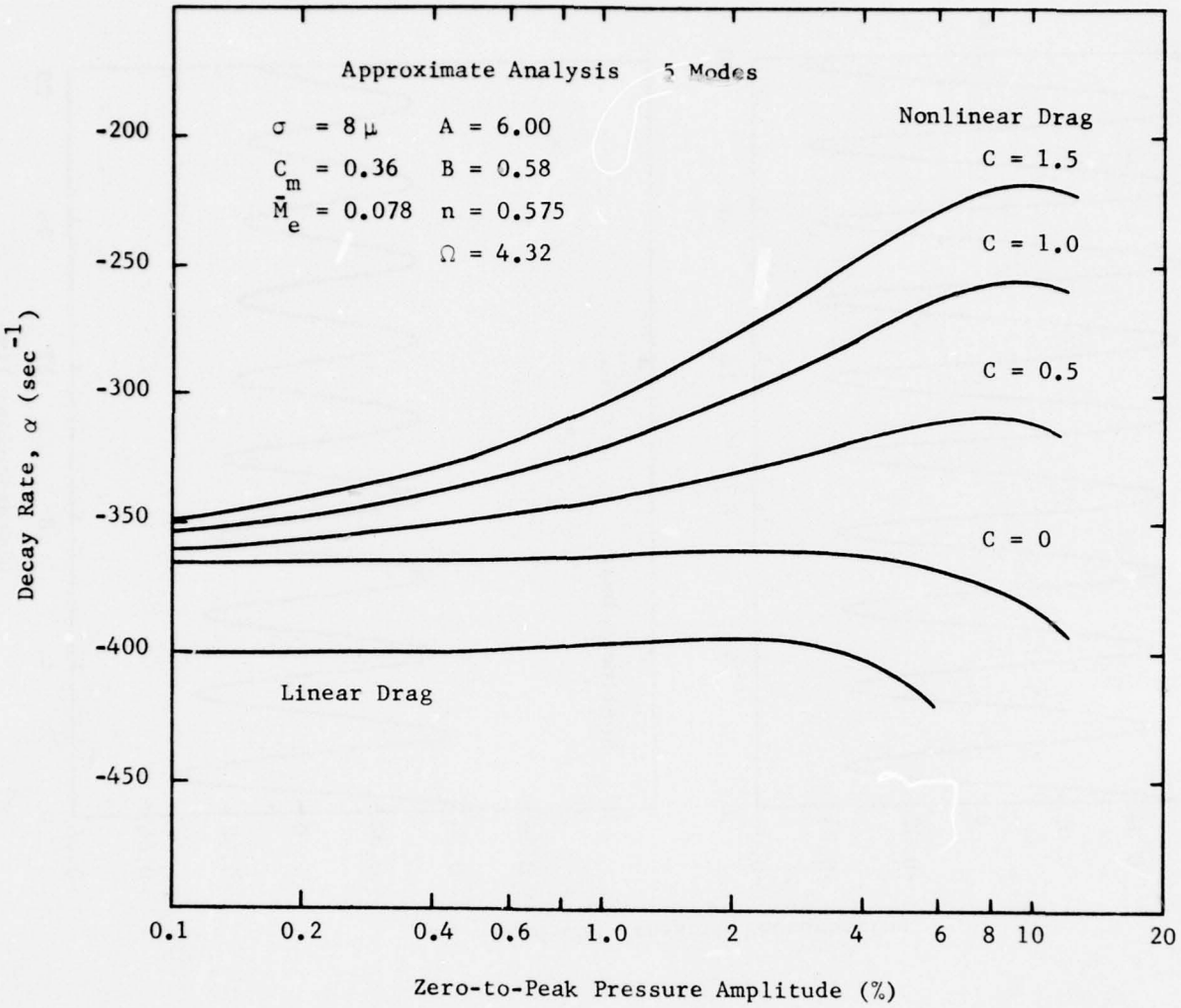

Figure 48. Decay Rate vs Amplitude for Motor With 8 μ Particles Using Approximate Nonlinear Drag Model

the approximate and "exact" solutions. The first quantity, $\Delta\alpha_1$ is the difference between the decay rate at small amplitude computed using the nonlinear drag law and the corresponding decay rate obtained using the linear drag law; thus, $\Delta\alpha_1$ = α(nonlinear drag, small amplitude) - α (linear drag). By comparing the approximate values of $\Delta\alpha_1$ with the "exact" values, the validity of the steady-state term, K_{ss}, in Equation (81) can be assessed. The second quantity, $\Delta\alpha_2$, is the difference between the decay rate at finite amplitude and the decay rate at vanishingly small amplitude as calculated using the nonlinear drag models; thus, $\Delta\alpha_2$ = α(finite amplitude) - α(small amplitude). Comparing the approximate and "exact" values of $\Delta\alpha_2$ for a given amplitude can be used to determine the proper value of the parameter C appearing in the unsteady contribution to the nonlinear particle drag (Equation (81)).

For the case of 8.0μ particles shown in Figure 48, values of $\Delta\alpha_1$ and $\Delta\alpha_2$ were calculated using both approximate and "exact" analyses. For $\Delta\alpha_1$ the approximate analysis yields 35 sec^{-1} compared to 50 sec^{-1} for the "exact" analysis. Thus the heuristic nonlinear drag model underestimates the steady-state contribution to the nonlinear drag for 8μ particles. At 4% amplitude the approximate analysis yields $\Delta\alpha_2$ = 87 sec^{-1} for C = 1 and $\Delta\alpha_2$ = 48 sec^{-1} for C = 0.5, while the "exact" analysis yields $\Delta\alpha_2$ = 63 sec^{-1}. This result indicates that a value of C = 0.7 would yield better agreement with the "exact" analysis for the case of 8μ particles.

Figure 49 shows similar decay rate versus amplitude curves obtained with the approximate analysis for a motor with 20μ particles. Again the qualitative agreement with the "exact" solutions (Figure 44) is good; the approximate solutions (C = 1), also exhibit a decreasing decay rate as the amplitude increases and a limiting decay rate at low amplitude which is considerably larger than the value obtained with the linear drag law. For this case the approximate method gave $\Delta\alpha_1$ = -205 sec^{-1} as compared to $\Delta\alpha_1$ = -156 sec^{-1} from the "exact" analysis. Thus the approximate analysis overestimates the steady-state contribution to the nonlinear drag for 20μ particles, which is opposite from the discrepancy obtained for 8μ particles. Also the amplitude dependent part of the nonlinear drag is overestimated for C = 1; at 4% amplitude the approximate analysis yielded $\Delta\alpha_2$ = -160 sec^{-1} while the "exact" analysis (10% initial amplitude) gave $\Delta\alpha_2$ = -117 sec^{-1}.

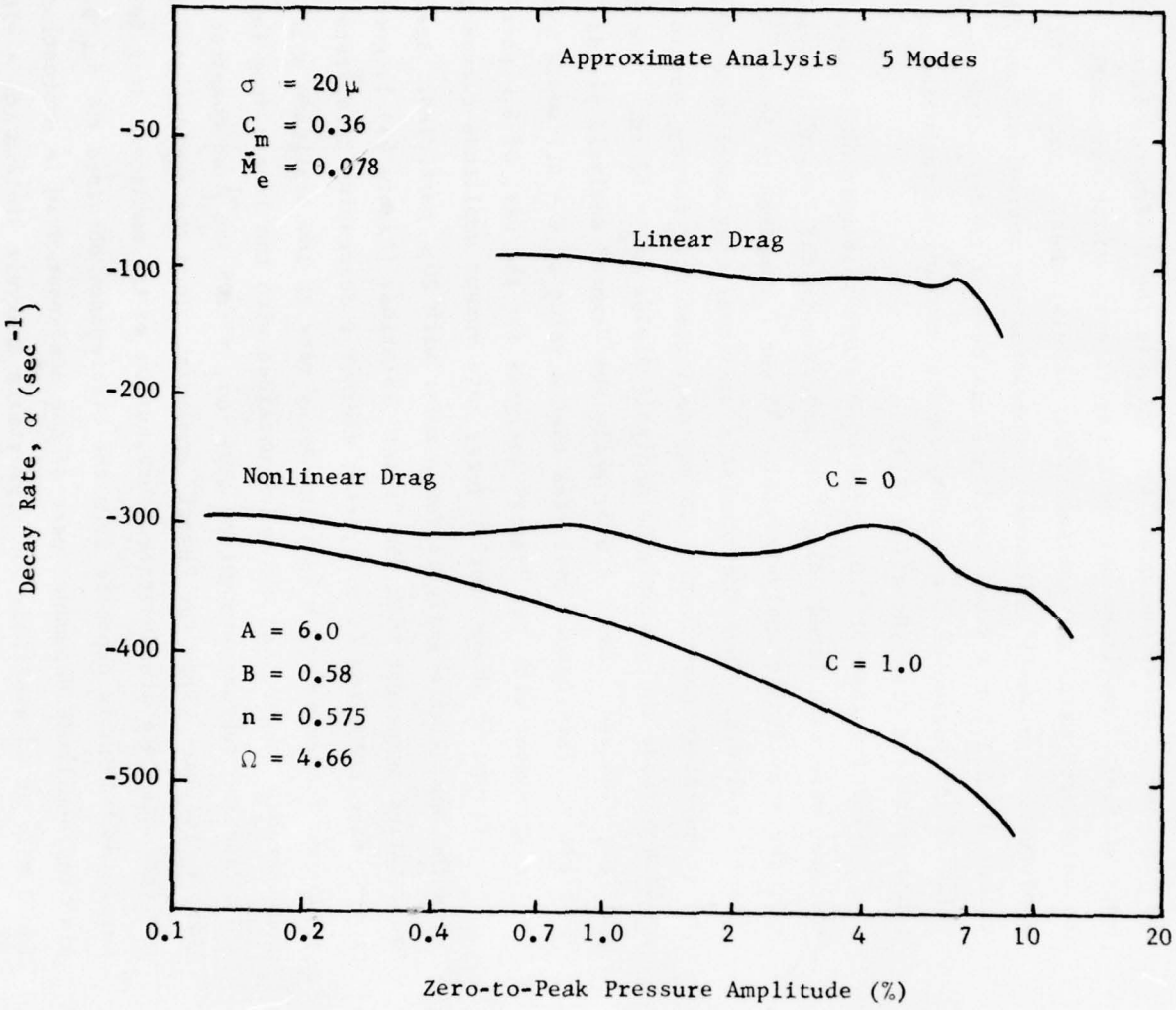

Figure 49. Decay Rate vs Amplitude for Motor With 20 μ Particles Using Approximate Nonlinear Drag Model

As in the case of 8μ particles, these results indicate that C = 0.7 will give better agreement regarding the amplitude dependence of the nonlinear particle damping.

These results presented above indicate that the heuristic nonlinear drag model used in the approximate analysis gives a reasonable qualitative description of the effects of particle drag nonlinearities on the decay rates for stable solid rocket motors. To obtain better quantitative agreement between the approximate and "exact" nonlinear particle damping solutions, a more extensive parametric study is needed to determine how the heuristic nonlinear particle drag model can be improved. Such a study was beyond the scope of this project and is recommended for future research.

4.5 Solutions for T-Burners

In this subsection the Galerkin method is used to obtain approximate solutions for a few selected T-burner configurations in order to demonstrate the applicability of the approximate analysis to T-burners. For most of the cases considered here, the length, bore, propellant properties, burning rate and combustion-product properties (gaseous and particulate) for the T-burner are assumed to be the same as those for the laboratory pulse motor considered in Section 4.2. Thus the dimensionless radius for the T-burner is R = 0.051 and the dimensionless velocity of the combustion products leaving the burning propellant surfaces is $\bar{u}_b = 0.002$. The transient combustion parameters are the same as those used for the motor solutions with particles; that is, A = 6.00, B = 0.58, and n = 0.575. The dimensionless frequency parameter is assumed to be $\Omega = 4.2$ which yields a response factor of $\Re_1^r = 4.14$. The dimensionless length of the center vent is given by $\beta_v = 0.1$, while the dimensionless plug flow length for the pipe connecting the burner with the surge tank is assumed the value $L_{eff} = 0.166$. In accordance with the theoretical limitations discussed in Section 2.6, flush grains ($S_c/S_{co} = 1.00$) are assumed for all cases considered in this study.

In obtaining the approximate T-burner solutions the following parameters were varied: (1) the length of the cylindrical grains,(2) the combustion response $\Re_1^r$, (3) the particle concentration C_m, and (4) the vent factor V_ℓ. Grain configurations considered were end-burning only ($\beta = 0$) and cup grains ($\beta = 0.1$ and 0.3). The effect of combustion

driving on the T-burner solutions was determined by comparing the growth rate for $\Re_1^r = 4.14$ with the decay rate obtained when the burning rate is insensitive to pressure oscillations ($\Re = 0$). Solutions for the case of no particles ($C_m = 0$) were also compared with those obtained for the case of 2.5μ -diameter particles with $C_m = 0.36$. The effect of the center vent was assessed by considering the case of vent gain ($V_\ell = 0$) and no vent effect ($V_\ell = 1$).

The case of end-burning (disk grains, $\beta = 0$) was considered first. Figure 50 shows growth/decay rates for 3% initial 1L-mode disturbances in end-burning T-burners for four cases: (1) no particles, $\Re = 0$, (2) no particles, $\Re_1^r = 4.14$, (3) 2.5μ particles, $\Re = 0$, and (4) 2.5μ particles, $\Re_1^r = 4.14$. In each case both linear (1L mode only) and nonlinear (5 modes) solutions are presented. For the first case, the nonlinear solutions decay at approximately the linear rate of -1.8 sec^{-1} during the first few cycles; the slight amount of damping is due to the effect of the mean flow and the center vent. Similarly the initial growth rate of the nonlinear solutions for the second case (with combustion driving) is close to the linear value of 41 sec^{-1}. In both cases the rapid rise in growth rate after seven cycles is a result of strong waveform steepening due to nonlinear gasdynamical mode-coupling (generation of higher harmonics). When 2.5 μ particles are present, the T-burner pressure oscillations decay at a nearly constant rate of -68 sec^{-1} for $\Re = 0$ (case 3) and -37 sec^{-1} for $\Re_1^r = 4.14$ (case 4) due to the increased attenuation of the higher harmonics by the particles.

In order to obtain growth of oscillations to limiting amplitude for T-burners with metallized propellants it is often necessary to increase the surface area of the burning propellant by using cup grains. This is the situation in the case selected for this study, for a cup-length of $\beta = 0.1$ is necessary to obtain spontaneous growth of oscillations when the 2.5 μ particles are present. Growth rates for cup-lengths of $\beta = 0$ (end-burning only), $\beta = 0.1$, and $\beta = 0.3$ are compared in Figure 51. For $\beta = 0.1$, the growth rate of the nonlinear solutions rapidly decreases from the linear value of 12 sec^{-1} to nearly zero, indicating approach to limiting amplitude (about 7% in this case). For $\beta = 0.3$, the initial growth rate is much larger (about 100 sec^{-1}) than for $\beta = 0.1$, but it decreases rapidly as the amplitude increases. For the latter case, the

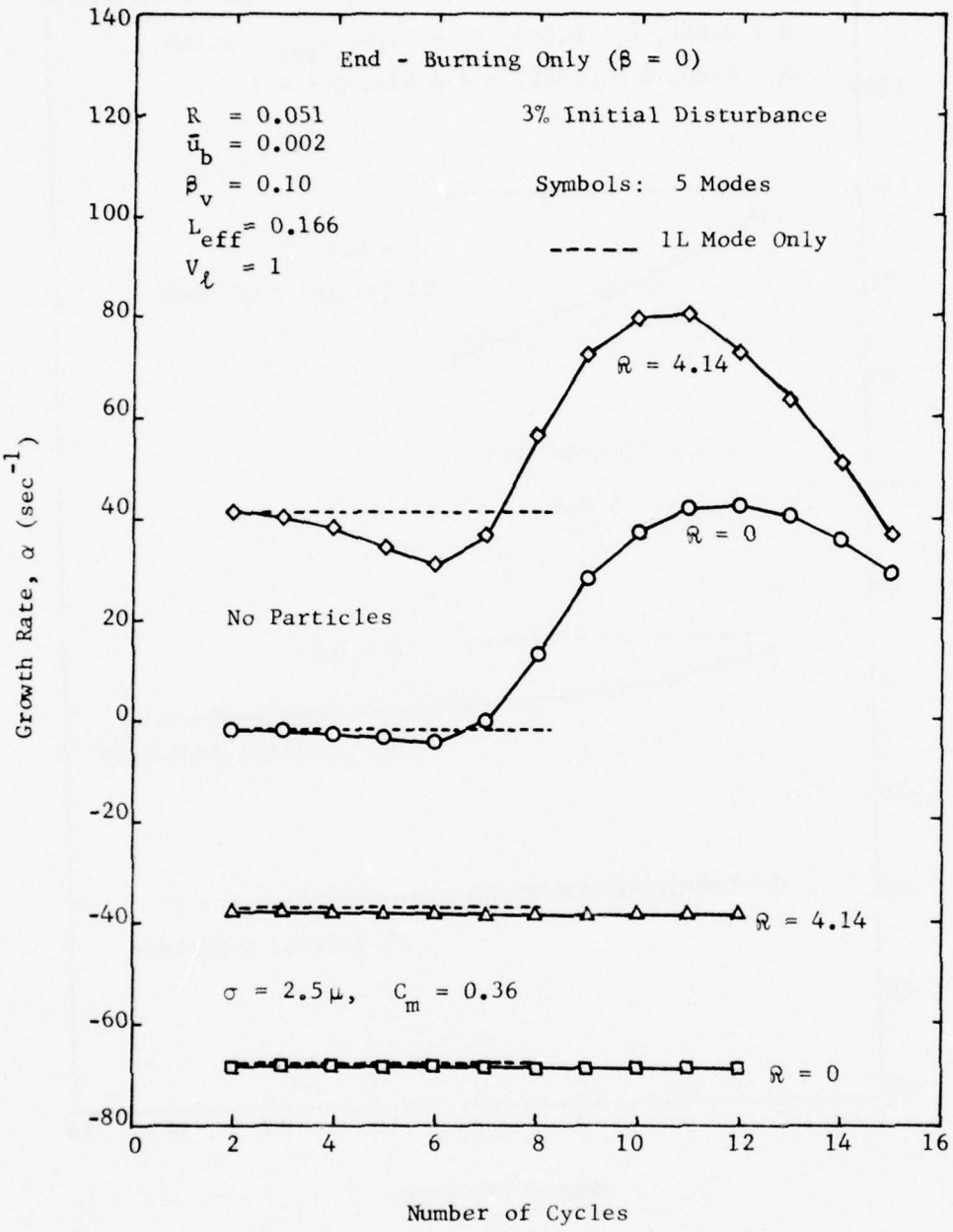

Figure 50. Growth Rates for End-Burning T-Burner

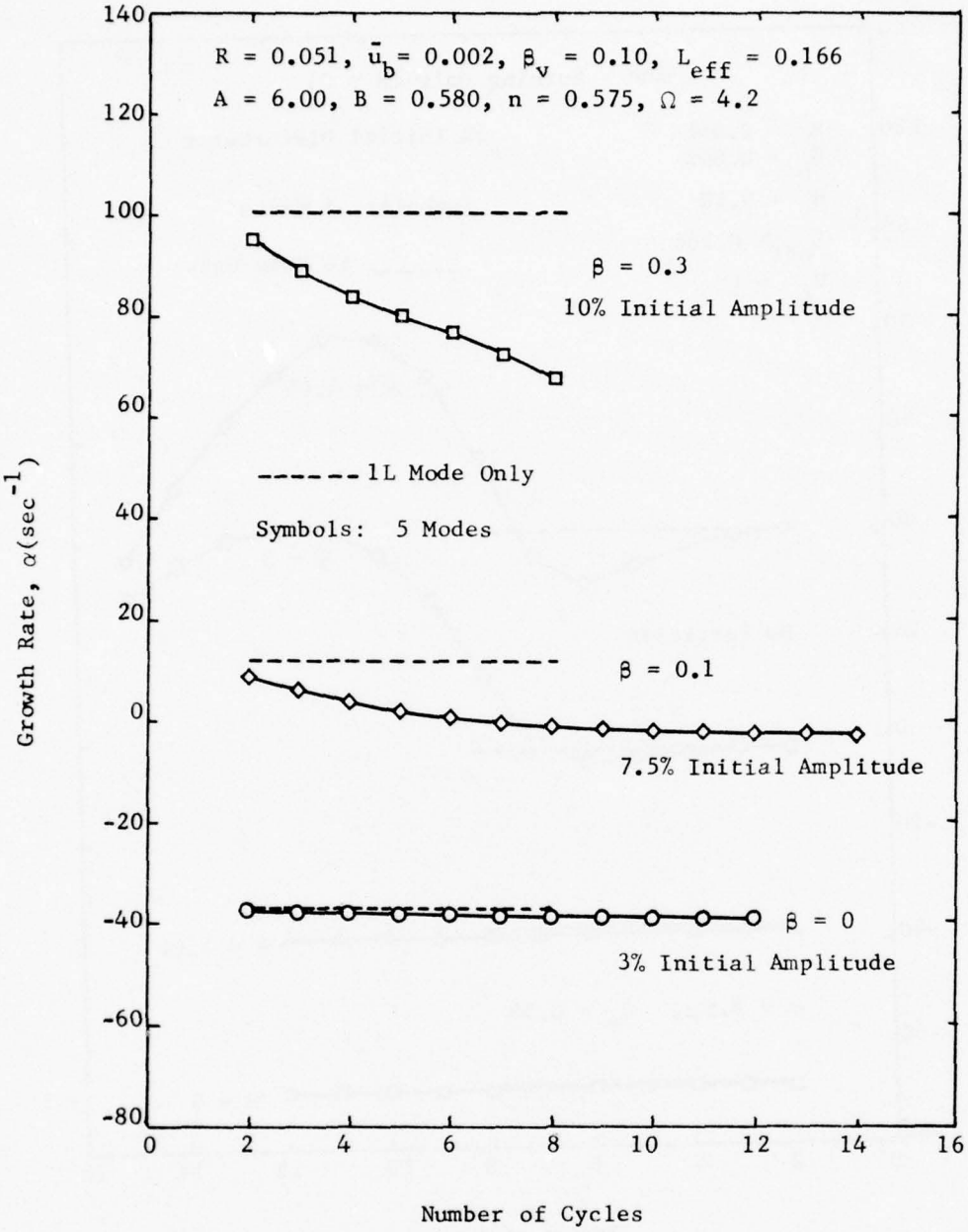

Figure 51. Growth Rates for T-Burners with Cup Grains

solution was not carried out to limiting amplitude, but it probably exceeds 20%.

The importance of the center vent for this case was determined by comparing solutions for $V_\ell = 0$ (vent gain) with the corresponding solutions for $V_\ell = 1$ (no vent effect). These comparisons were made for both end-burning and cup-grain configurations, for T-burners without combustion driving ($\Re = 0$) or particle damping. The results of these calculations are given in Table 5. The quantity $\Delta\alpha_v$ is the difference between the decay rates obtained with $V_\ell = 0$ and $V_\ell = 1$; thus, $\Delta\alpha_v$ represents the vent gain due to the mean-flow/acoustic interaction. From Table 5 it is seen that $\Delta\alpha_v$ is a rather small quantity that increases as β increases due to the resulting increase in steady-state flow velocity in the vent region. These results indicate, that, at least for the cases considered, the mean-flow/acoustic vent effect is relatively unimportant and may be neglected in the nonlinear analysis of T-burners.

Table 5. Effect of Center Vent

Case	β	α, (sec^{-1})		$\Delta\alpha_v$, (sec^{-1})
		$V_\ell = 1$	$V_\ell = 0$	
1	0.0	-1.83	-1.76	0.07
2	0.1	-22.18	-21.98	0.20
3	0.3	-59.03	-58.55	0.48

Pressure waveforms and mode-amplitude functions were obtained for two of the T-burner cases considered in this study. These results are shown in Figure 52 for an end-burning T-burner without particles and in Figure 53 for a cup grain configuration ($\beta = 0.1$) with 2.5μ - diameter particles; in both cases a five-mode series was used and the response function was $\Re_1^r = 4.14$.

In the first case (Figure 52), a 10% amplitude 1L-mode initial disturbance rapidly grows and steepens after two wave cycles as higher harmonics are generated by nonlinear gasdynamic mode-coupling. As in the case of solid rocket motors (Figure 8), the amplitude of the fundamental mode is considerably larger than the amplitudes of the higher harmonics (the response functions for the higher modes are considerably smaller than the response function for the fundamental mode). It is also seen that the amplitudes of the higher modes decrease as the axial mode number increases, except that the 5L mode has a larger amplitude than the 4L mode. The latter result is probably due to the finite number of modes (i.e., five) used in the series, and it accounts for the fifth harmonic "wiggles" apparent in the pressure waveform.

In the second case (Figure 53) when particles are present, a 7.5% amplitude 1-L mode initial disturbance is shown developing into a nearly sinusoidal limiting-amplitude pressure waveform. In contrast to the previous case the amplitudes of the higher harmonics decrease rapidly as the mode number increases; in fact it appears that the 3L, 4L and 5L modes are negligible and that a two or three mode series is adequate to represent the solution.

In order to adequately evaluate the applicability of the approximate technique to the nonlinear analysis of T-burners, the approximate T-burner solutions were compared with available "exact" solutions as well as with experimental data. Since time did not permit extension of the Kooker-Zinn "exact" analysis to analyze T-burner configurations, Levine's T-burner calculations[5] were used in these comparisons. The case selected for comparison with the "exact" analysis was for $S_b/S_{co} = 7.06$ (Table A-1 of Reference 5) for which $\beta = 0.216$ (tubular grains without end-burning disks). The combustion parameters used by Levine were A = 8.8, B = 0.67, n = 0.3, and $\Omega = 7.80$ which gave a response function of $\Re_1^r = 2.03$. The particles were characterized by an average diameter of 3.0μ and a

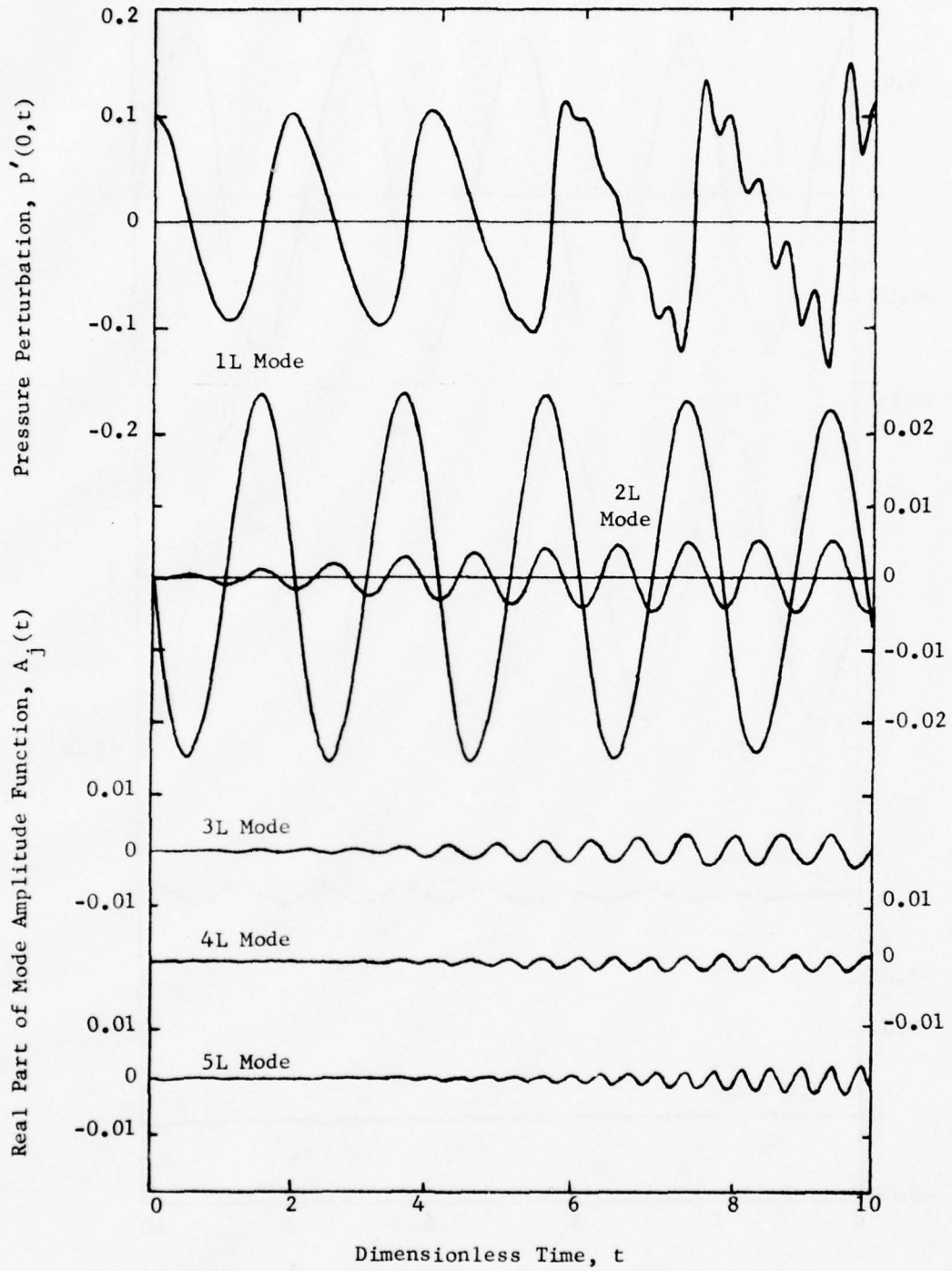

Figure 52. Pressure Waveform and Mode-Amplitude Functions for End-Burning T-Burner Without Particles

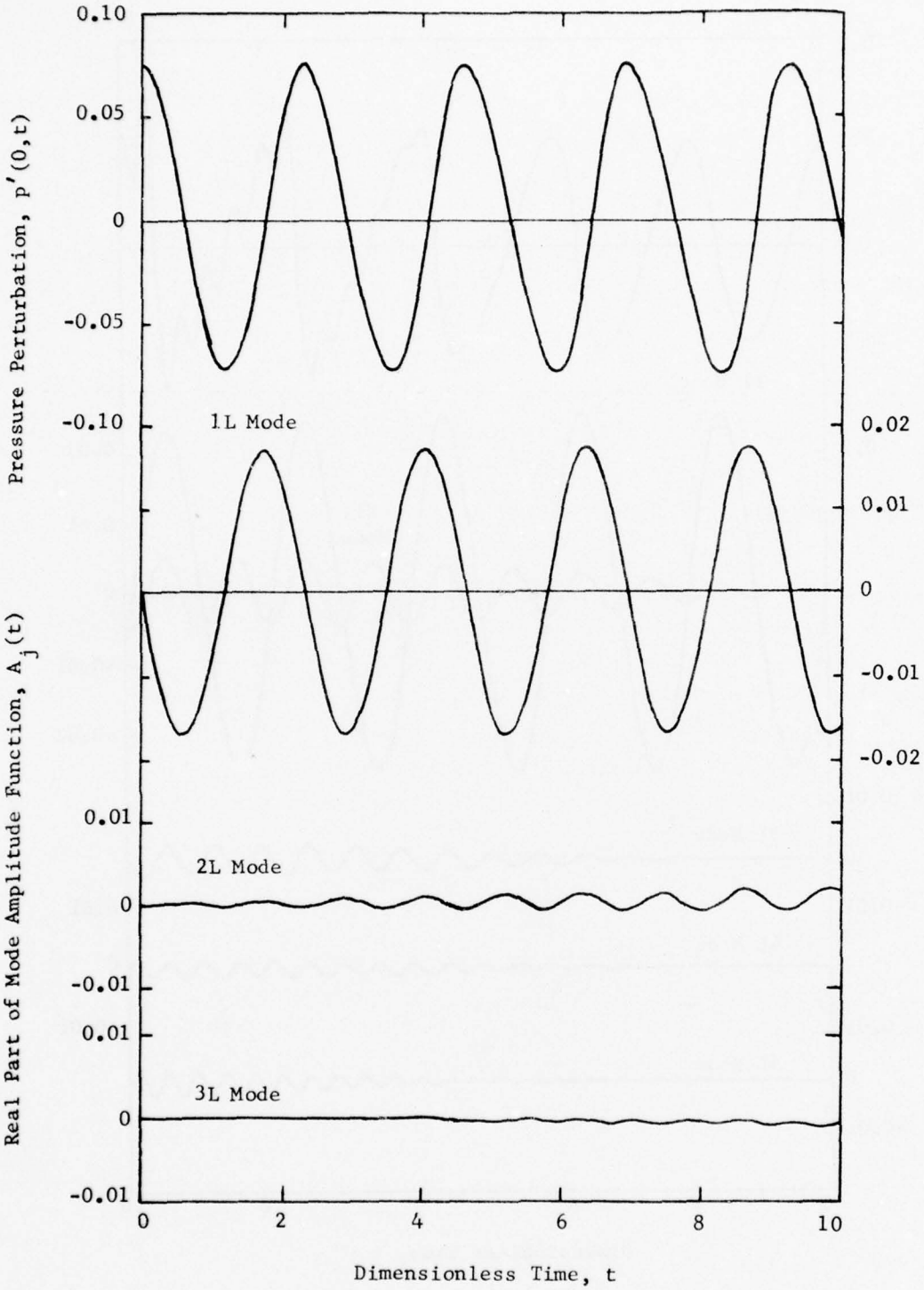

Figure 53. Pressure Waveform and Mode Amplitude Functions for Cup Grain T-Burner with 2.5 μ Particles

concentration of $C_m = 0.36$.

T-burner pressure-time histories obtained with the Galerkin method and Levine's "exact" analysis are compared in Figure 54 for 3% initial disturbances. The resulting solutions are seen to disagree regarding the initial growth rate and limiting amplitude. The approximate solutions grow very slowly as they appear to be near limiting amplitude (probably about 4%), while the "exact" solutions are still growing rapidly after 12 wave cycles (eventually reaching 37% limiting amplitude). Both solutions agree, however, regarding the nearly sinusoidal waveshape and the double frequency small amplitude oscillation at the center vent. Comparisons with experimental data for T-burners are presented in the next section.

The results presented in this subsection indicate that the Galerkin method can be used to obtain approximate solutions for growth/decay rates and limiting amplitudes for flush-grain T-burner configurations. The limited parametric study performed indicates that the approximate solutions exhibit the expected trends regarding the effect of cup-grain length, combustion response factor, particle concentration, and center vent upon the behavior of the pressure oscillations. It is difficult to draw conclusions regarding the accuracy of the approximate solutions from the limited comparison with "exact" theory given above, since Levine's model differs significantly from the present approximate model (i.e., it accounts for the thermal particle/gas interaction as well as nonlinear combustion and particle drag nonlinearities). Furthermore, the limiting amplitude predicted by the "exact" analysis is far higher than that obtained from the measured data (37% as compared to 8% for the data).[5] It is evident that much more work needs to be done to further develop and improve both the approximate and "exact" T-burner models, and that more extensive comparisons of the approximate T-burner solutions with "exact" solutions and experimental data are needed.

4.6 Comparisons With Experimental Data

In the preceding subsections, the approximate analysis has been evaluated on the basis of comparisons with available "exact" solutions for both motors and T-burners. Since the usefulness of an analytical method lies in its ability to predict observed behavior, the approximate

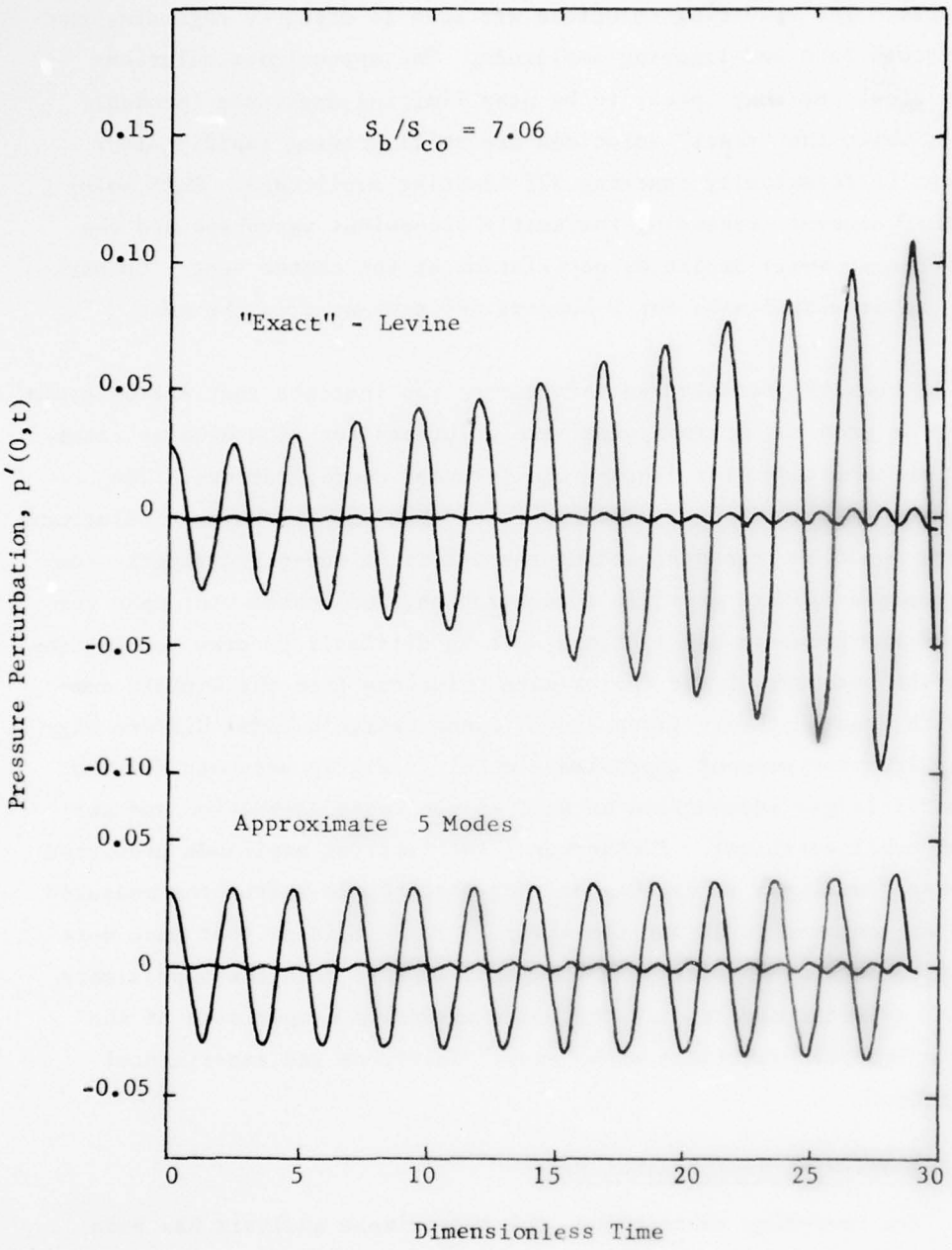

Figure 54. Comparison of Approximate and "Exact" T-Burner Solutions

solutions were also compared with available T-burner and motor test data. The results of this study are presented in this subsection.

Comparison With Motor Test Data. Due to the unavailability of any other motor test data, the experimental data considered by Levine and Culick[5] was also used in this study. This data was obtained by Aerojet several years ago for ANB 3066 propellant using a small laboratory pulse motor. This motor has a grain length of about 0.597 m (23.5 in) and an initial bore of about 50 mm (2 in); it is the same motor configuration considered previously in Sections 4.2, 4.3, and 4.4. The physical properties of the ANB 3066 propellant and its gaseous and particulate combustion products have already been given in Table 1 of Section 4.2. The motor parameters for the four cases considered by Levine and Culick[5] are given in Table 6.

Table 6. Motor Parameters for Laboratory Pulse Motor

Nominal Throat Diameter (cm)	Pulse Number	Port Area (cm^2)	Throat Area (cm^2)	$\bar{p}$ (knt/m^2)	$\bar{M}_e$	$\bar{T}_f$ (K)
1.97	1	21.5	2.83	10810	0.0782	3526
1.97	3	36.3	2.95	14800	0.0481	3556
2.20	1	24.4	3.57	8330	0.0869	3503
2.20	2	30.5	3.63	9740	0.0703	3518

The Mach number at the nozzle entrance, which is needed in the approximate analysis, was determined from the ratio of port area to throat area using the isentropic flow relations (the low flow coefficient of the nozzle was already taken into account by Levine and Culick by adjusting the throat area). The flame temperature T_f was taken from Figure 7-17

of Reference 5. For 2.0 μ particles the drag constant K was about 46.7 for all four cases.

In order to obtain approximate solutions for the test conditions given above, the transient burning rate parameters (i.e., A and B) must be estimated. Levine and Culick[5] made such estimates based on the following criteria: (1) the response function must be greater than 3 for instability, (2) the values of A and B must not result in nonlinear intrinsic instability, and (3) the corresponding values of E_s^* and Q_s^* should be reasonable. For Cases 1 and 4 this procedure was relatively straightforward, but for Cases 2 and 3 the considerable spread in mean pressure caused difficulties. For the latter two cases Levine and Culick postulated a pressure dependence of Q_s^* above and beyond that which is accounted for by the Levine-Culick nonlinear transient burning rate model. In addition to A and B, the dimensionless frequency parameter Ω was calculated using the steady-state burning rate given by

$$F = 0.813\ (P/3448)^{0.3} \tag{108}$$

where F is the surface regression rate in units of cm/sec and P is the steady-state pressure in knt/m^2. The transient burning rate parameters assumed by Levine and Culick were used as the starting point in this investigation; they are given in Table 7.

Table 7. Transient Burn Rate Parameters

Case	A	B	Ω
1	6.00	0.55	4.3
2	5.98	0.53	3.65
3	6.02	0.54	5.06
4	6.00	0.55	4.3

Approximate solutions were obtained for each of the four cases described above using the Galerkin method with a five-mode series. In each case, using Levine and Culick's estimates of A, B, and Ω along with n = 0.3, the approximate analysis predicted a decaying oscillation. Therefore the parameters A and B were varied slightly in order to increase the propellant response to the level necessary to sustain oscillations. The results of these calculations are now presented and discussed for each of these cases in the following paragraphs.

The results for Case 1 (1.97-cm throat, Pulse #1) are summarized in Table 8. The measured limiting amplitude for this case was about 3%,

Table 8. Approximate Solutions for Cases 1 and 4

B	Initial Amplitude	$\Re_1^r$	Oscillation after 12 cycles			
			Case 1		Case 4	
			Ampl. (%)	α (sec^{-1})	Ampl. (%)	α (sec^{-1})
0.550	5%	3.33	3.2	-32.1	3.1	-33.6
0.545	5%	3.66	4.3	-8.8	4.1	-12.7
0.545	2%	3.66	1.8	-5.7	1.8	-9.6
0.543	5%	3.82	5.0	1.7	4.7	-3.2
0.543	2%	3.82	2.1	5.4	2.0	0.3
0.540	5%	4.09	6.3	18.8	5.8	12.3

while the approximate analysis predicts a limiting amplitude slightly larger than 5% for B = 0.543. For comparison Levine and Culick obtained an amplitude of 4.2% with B = 0.550.

Case 4 (2.20-cm throat, Pulse #2) is considered next because the mean pressure is nearly the same as for Case 1, allowing the same values of A and B to be used (Table 7). Case 4 differs from Case 1 due to the smaller value of $\bar{M}_e$ (0.0703 as compared to 0.0782 for Case 1). Using A = 6.0 and B = 0.543 as before, the approximate analysis yielded a limiting amplitude of a little over 2% which is in excellent agreement with the measured value of slightly over 2%. For this case Levine and Culick obtained a 3% oscillation with B = 0.55. This comparison shows that the approximate analysis correctly predicts the experimentally observed trend of decreasing limiting amplitude with decreasing steady state Mach number.

The approximate solutions for Case 2 (1.97-cm throat, Pulse #3) and Case 3 (2.20-cm throat, Pulse #1) are presented in Table 9. In each case, the first set of parameters corresponds to Levine's values, which yield decaying oscillations. Since the values of Ω for these cases yield values of $\Re_1^r$ considerably below the peak value, variations of the parameter B alone are ineffective in raising $\Re_1^r$ sufficiently to drive instability. Since n is not a strong function of pressure and Ω is fairly well determined for the given chamber pressures, the only parameter left which can be varied is A. Thus the parameter A was changed (and B as well for Case 2) to yield a response factor of about 3.8. For Case 2 the second set of parameters yields a limiting amplitude of about 1.5% in good agreement with the measured value of 1-3% (modulated). For Case 3 the second set of parameters gives an amplitude in excess of 6% compared to measured values of 2-2.5%, but a slight decrease in A should give better agreement. It is difficult to assess the validity of the approximate solutions on the basis of these last two cases, since the values of the transient combustion parameters A and B used in obtaining these solutions are uncertain.

Table 9. Approximate Solutions for Cases 2 and 3

Case	A	B	Initial Amplitude	$\Re_1^r$	Oscillation after 12 cycles	
					Amplitude (%)	α (sec^{-1})
2	5.98	0.530	5%	2.74	2.5	-55.8
2	5.60	0.517	5%	3.90	4.5	-5.9
2	5.60	0.517	2%	3.90	1.9	-0.8
3	6.02	0.540	5%	2.36	1.4	-122
3	6.35	0.540	5%	3.81	5.6	19.2*
3	6.35	0.54	2%	3.81	2.3	21.6*

*Modulated

Comparison With T-Burner Test Data. The T-burner test data considered in this study are the same three cases considered by Levine and Culick[5] for comparison with the "exact" analysis. This data was selected from the ANB 3066 (3.8-cm bore) data reported in Reference 22 on the basis of two requirements: the measurements were taken near the flush grain conditions and limiting amplitudes were reported. In these cases, the T-burner length was 62.2 cm (24.5 in), the steady-state pressure was 3448 knt/m^2 (500 psi), and the propellant configuration consisted of

[22]Beckstead, M.W., et al. "Variable Area T-Burner Investigation," AFRPL TR-72-85, December 1972.

tubular propellant grains at each end of the burner without end-burning disks. The principal parameter of interest in this study was the area of the burning propellant surface which was specified by the ratio S_b/S_{co} and determined by the length of the propellant grains L_b^*. The pertinent data for the three values of S_b/S_{co} selected is given in Table 10; for all cases R = 0.0306, β_v = 0.0542, V_ℓ = 1.0 (no vent effect), and L_{eff} = 0.163. The particle diameter was assumed to be 3 μ and the particle concentration was assumed to be C_m = 0.36. Following Levine and Culick[5], the combustion response was assumed to be given by A = 8.8, B = 0.67, and n = 0.3.

Table 10. T-Burner Parameters for Comparison Study

Case	S_b/S_{co}	β	f (Hz)	$\bar{r}$ (cm/sec)	Ω_1	$\bar{u}_b$
1	1.48	0.0465	772	0.856	6.62	0.00322
2	5.58	0.1714	816	0.815	7.71	0.00307
3	7.06	0.2163	820	0.813	7.80	0.00306

Approximate solutions were obtained for the above three cases using both single-mode (1L) and five-mode series expansions. The single-mode results are presented in Table 11; they correspond to exponential growth or decay of oscillations at small amplitudes. Since the approximate analysis predicts more stable behavior than that indicated by the measured data for B = 0.67 (Levine's value), approximate solutions for B = 0.635 are also shown in Table 11 which give better agreement with the experimental data. The additional case of S_b/S_{co} = 0 (no burning, no mean flow) was also considered; for this case the approximate analysis predicted a

decay rate of -88.2 sec^{-1} as compared to a measured value of -77 sec^{-1} (extrapolated).

Table 11. Comparison of Single-Mode Solutions with Measured Data

Case	S_b/S_{co}	B = 0.670		B = 0.635		Measured
		$\Re_1^r$	α (sec^{-1})	$\Re_1^r$	α (sec^{-1})	α (sec^{-1})
1	1.48	2.15	-64.9	3.25	-47.6	-50
2	5.58	2.06	-4.9	2.83	59.9	54
3	7.06	2.03	15.1	2.75	85.0	88

Both five-mode and single-mode solutions for B = 0.635 are compared with the measured data in Figure 55, which shows plots of growth rate versus number of wave cycles for 3% amplitude initial disturbances. For S_b/S_{co} = 1.48 the approximate solutions are in very good agreement with the measured data, while reasonably good agreement is obtained for S_b/S_{co} = 5.58 and S_b/S_{co} = 7.06. The decline in growth rate for the latter two cases after six cycles indicates that the oscillations in the T-burner are approaching limiting amplitude. Figure 56 shows the continuation of the calculations for 40 cycles for these two cases, which yields limiting peak-to-peak amplitudes of about 31% for S_b/S_{co} = 5.58 and about 43% for S_b/S_{co} = 7.06, corresponding to measured values of 9.0% and 15.6% respectively.

Three significant observations regarding the applicability of the approximate T-burner analysis can be made from the comparisons presented above. First, the linear growth rates predicted by the approximate

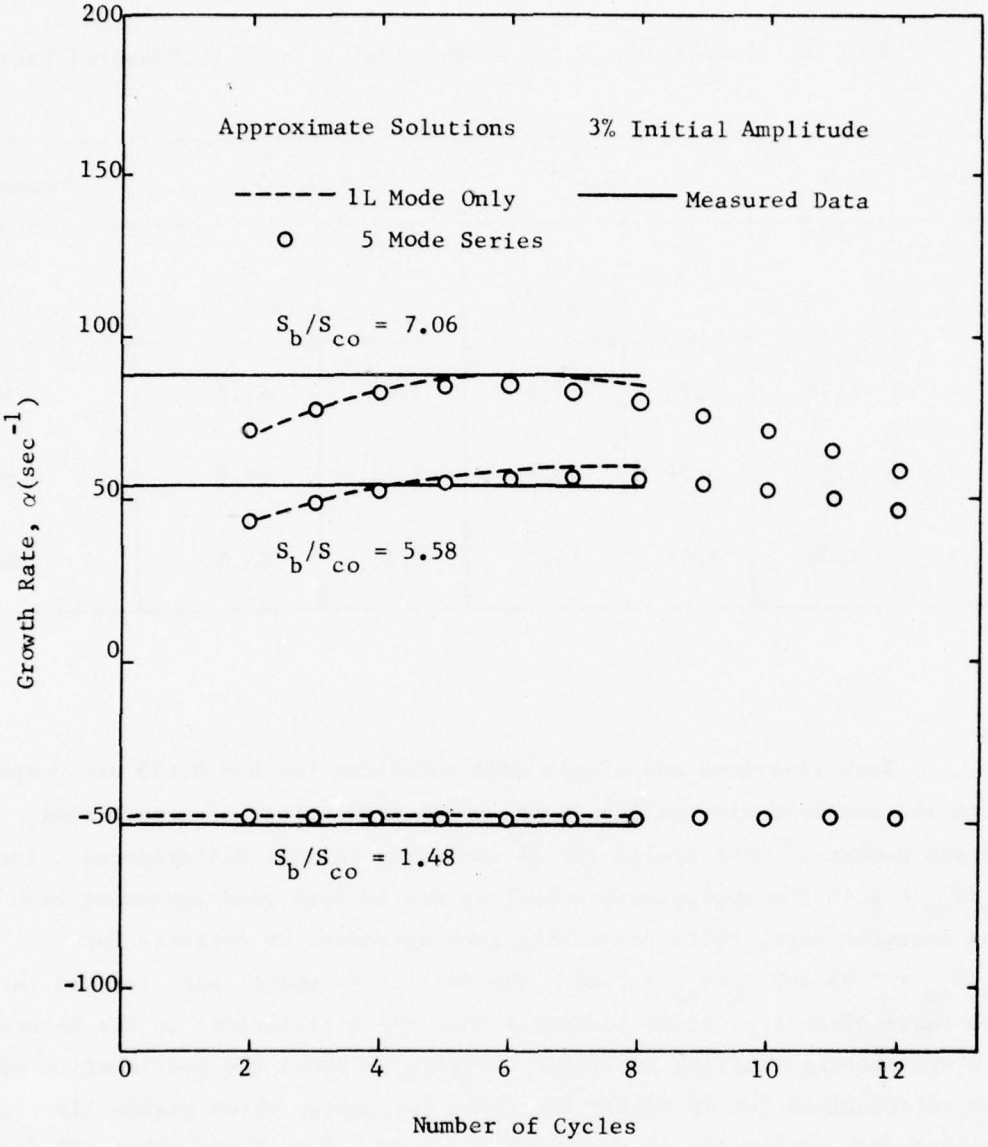

Figure 55. Comparison of Approximate Solutions with Experimental Data for T-Burners

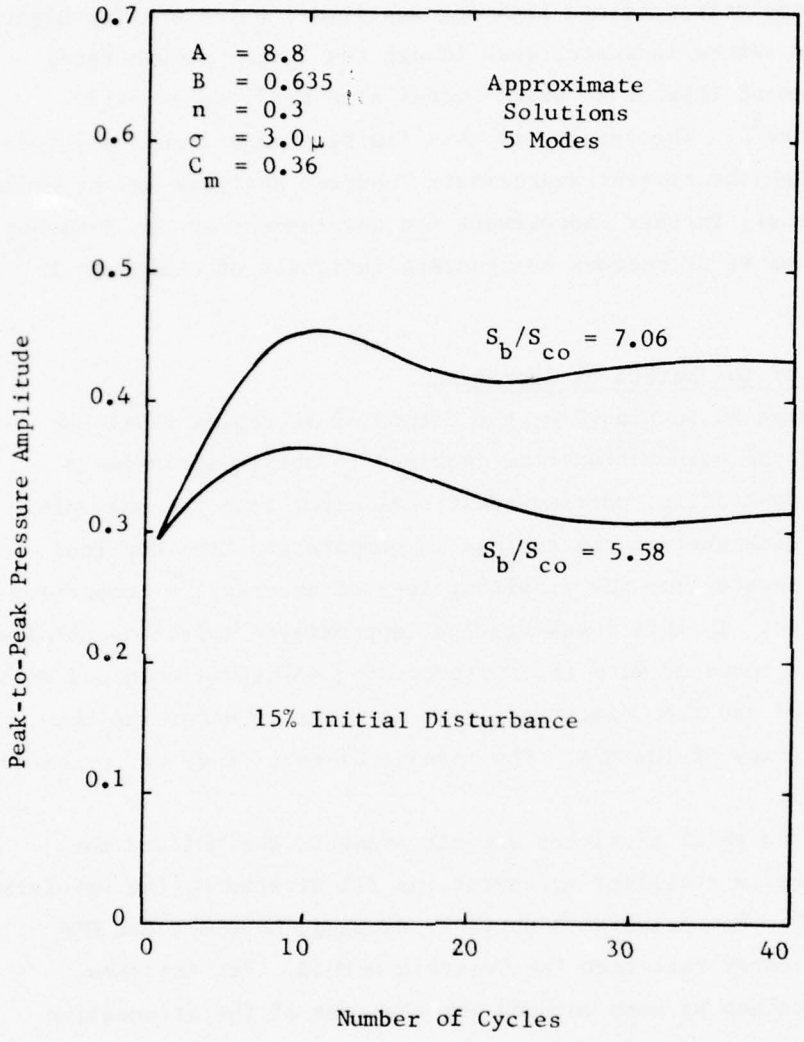

Figure 56. Approach to Limiting Amplitude for T-Burners by Approximate Analysis

T-burner analysis do not agree well with those obtained by Levine's "exact" analysis (Levine obtained good agreement with the measured data for B = 0.67). Second, for a somewhat stronger propellant response (B = 0.635) the approximate analysis agrees well with the measured data regarding the effect of S_b/S_{co} upon the linear growth rates. Finally, the approximate analysis predicts limiting amplitudes which are far higher than the measured values indicate, even though the linear growth rates are in good agreement (Levine's "exact" model also predicts excessive limiting amplitudes[5]). The results of this limited comparison study indicate that, although the present approximate T-burner analysis may be useful in predicting trends, further improvement and development of the T-burner model is needed before it becomes an accurate indicator of nonlinear T-burner behavior.

4.7 Application of the Method of Averaging

As discussed in Section 2.4, the Method of Averaging (MOA) can be used to reduce the computation time required to obtain approximate solutions at the cost of introducing additional error into the analysis. In order to determine whether the savings in computation time obtained with the MOA compensates for the resulting loss of accuracy, a comparison study was conducted. In this investigation, approximate solutions obtained using the MOA were compared with the corresponding solutions obtained with the Galerkin method and the "exact" analysis in order to determine the range of applicability of the MOA. The results of this study are presented in this subsection.

For cases in which particles are not present, the MOA and the Galerkin method are in excellent agreement, as illustrated by the waveforms shown in Figure 57. For cases with particle damping, however, the MOA predicts a larger decay rate than the Galerkin method. For instance, solutions were obtained by both methods for the case of the attenuation of 800 Hz waves in a gas-particle mixture enclosed in a box with a particle loading of $C_m = 0.36$ and a particle diameter of $2.5\,\mu$. In this case, the linear decay rate obtained using the Galerkin method was $-56\ \text{sec}^{-1}$, while the linear decay rate obtained using the MOA was found to be $-72\ \text{sec}^{-1}$.

Since previously published results by Culick[10] showed good agreement between the MOA solutions and Levine's "exact" solutions for cases

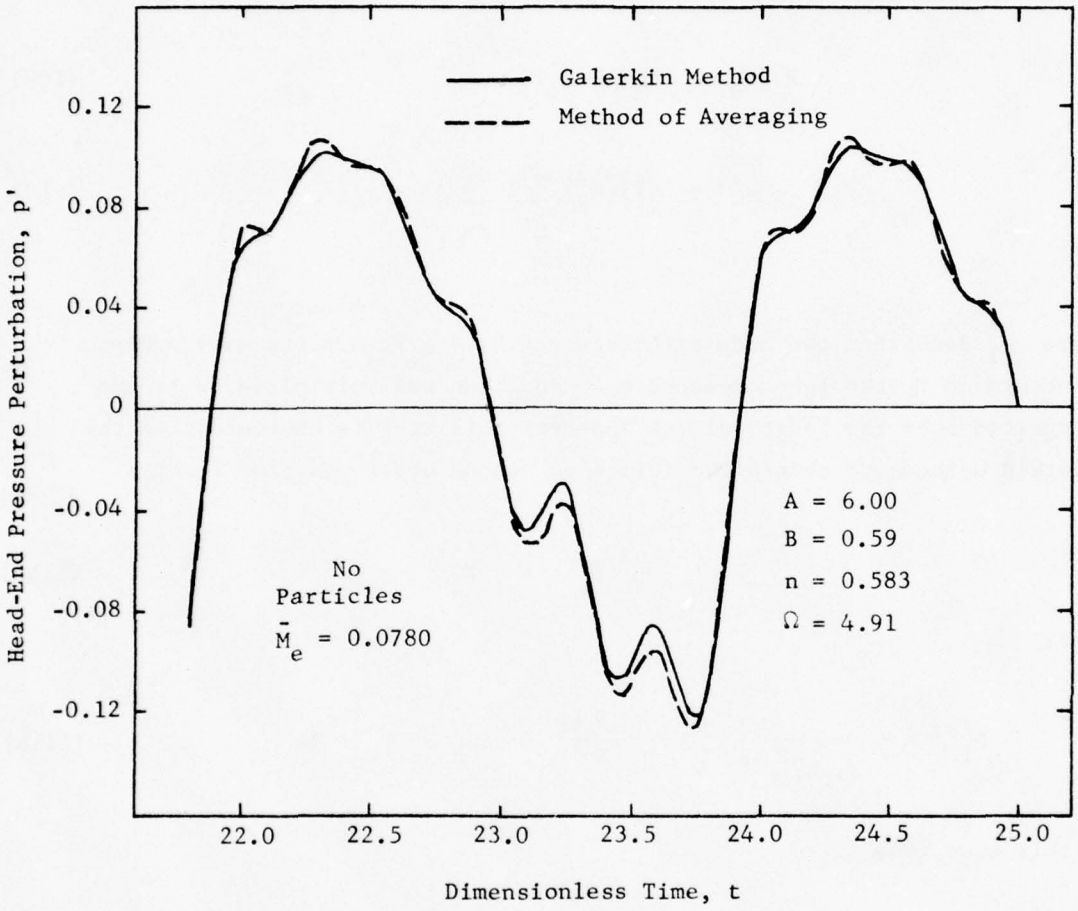

Figure 57. Waveforms for Motor Without Particles by Galerkin Method and Method of Averaging

with particle damping, Culick's equations were also examined to aid in determining the source of discrepancy. Unlike the present analysis where a wave equation for the velocity potential is derived, Culick has formulated the problem by developing an inhomogeneous wave equation for the pressure perturbation, p'. Considering a single mode expansion consisting of the 1L mode, an amplitude function $\eta_1(t)$ is defined such that

$$P'/P_o = \eta_1(t)\ \Psi_1(x) \tag{109}$$

$$u' = (1/\bar{\gamma}K_1^2)\ \frac{d\eta_1}{dt}\ \frac{d\Psi_1}{dx} \tag{110}$$

where Ψ_1 describes the mode structure and $K_1 = \omega_1/c_1$ is the wave number. To determine η_1 the inhomogeneous wave equation was multiplied by Ψ_1 and integrated over the length of the chamber (this step is equivalent to the Galerkin method) to obtain the following second order equation for η_1:

$$\frac{d^2\eta_1}{dt^2} + \omega_1^2\ \eta_1 = F_1^{(p)} \tag{111a}$$

where

$$F_1^{(p)} = \frac{\bar{\gamma}}{\rho_o E_1^2} \int_o^L \left[\delta F_p'\ \frac{d\Psi_1}{dx} + \delta u_p'\ F_p\ \Psi_1\right] dx \tag{111b}$$

In this equation,

$$F_p = \frac{\bar{\rho}_p}{\tau_d}\ (u_p' - u')$$

$$\tau_d = \frac{\rho_s \sigma^2}{18\,\mu}$$

and $\delta u_p'$ and $\delta F_p'$ are defined in Reference 10 (i.e., Equations (8.15) and

(8.13)). Using the referenced equations in Equations (111), the equation describing the behavior of η_1 becomes:

$$\frac{d^2\eta_1}{dt^2} + \omega_1^2 \eta_1 = \frac{C_m}{1+C_m} \left[\frac{d^2\eta_1}{dt^2} - \frac{1}{\tau_d} \frac{d\eta_1}{dt} + \frac{e^{-t/\tau_d}}{\tau_d^2} \int_o^t e^{t'/\tau_d} \frac{d\eta_1}{dt'} dt' \right] \quad (112)$$

Since the right-hand-side of Equation (112) contains a second derivative term, it is not in the proper form for solution by the MOA. This equation can be simplified and rewritten in the proper form in several ways. The most straightforward procedure is to bring the term $C_m/(1 + C_m)\, d^2\eta_1/dt^2$ to the left-hand-side and simplify to obtain the following expression:

$$\frac{d^2\eta_1}{dt^2} + \omega_1^2 \eta_1 = C_m \left\{ -\frac{1}{\tau_d} \frac{d\eta_1}{dt} - \omega_1^2 \eta_1 + \frac{e^{-t/\tau_d}}{\tau_d^2} \int_o^t e^{t'/\tau_d} \frac{d\eta_1}{dt'} dt' \right\} \quad (113)$$

Another way of handling Equation (112) is to use an order of magnitude argument and substitute $d^2\eta_1/dt^2 = -\omega_1^2\eta_1$ on the right-hand-side. Along with applying the MOA, this substitution has been made by Culick[10] in deriving Equations (8.23) and (8.25). With this substitution, Equation (112) becomes:

$$\frac{d^2\eta_1}{dt^2} + \omega_1^2 \eta_1 = \frac{C_m}{1+C_m} \left\{ \frac{-1}{\tau_d} \frac{d\eta_1}{dt} - \omega_1^2 \eta_1 + \frac{e^{-t/\tau_d}}{\tau_d^2} \int_o^t e^{t'/\tau_d} \frac{d\eta_1}{dt'} dt' \right\} \quad (114)$$

It is now apparent that the right-hand-side of Equation (114) differs from the right-hand-side of Equation (113) by the factor $1/(1 + C_m)$, thus it

is expected that the solutions of these two equations will differ by a similar amount.

Equations (113) and (114) respectively describe the Galerkin Equations obtained using Culick's formulation without and with the above-mentioned approximations. The MOA can now be applied to solve each of these equations. Letting

$$\eta_1(t) = g_1(t) \sin(\omega_1 t) + h_1(t) \cos(\omega_1 t)$$

where g_1 and h_1 are slowly-varying functions, and using Equations (32), equations describing the behavior of g_1 and h_1 can be derived. Thus with Culick's formulation, four sets of results were obtained for a given case: two solutions using the Galerkin method both with (Equation (114)) and without (Equation (113)) the substitution $d^2\eta_1/dt^2 = -\omega_1^2 \eta_1$ in $F_1^{(p)}$ and the two corresponding solutions obtained using the MOA.

The decay rates obtained with Culick's formulation for $\sigma = 2.5\,\mu$, $C_m = 0.36$, and $f_e = 800$ Hz are presented in Table 12 along with the decay rates obtained with the present analysis (i.e., using Equations (25) for the Galerkin solutions and Equations (39) for the MOA). In these computations the thermal energy transfer between the particles and the gas phase was ignored. For this case the "exact" calculations using the Kooker-Zinn model yield $\alpha = -57\ \text{sec}^{-1}$.

A comparison of the results presented in Table 12 leads to several observations. In every case, the MOA yields considerably higher decay rates than the Galerkin method. The substitution $d^2\eta_1/dt^2 = -\omega_1^2\eta_1$ results in a significant decrease in the computed decay rates. The solution presented in Reference 10 (i.e., with MOA and making the substitution $d^2\eta_1/dt^2 = -\omega_1^2\eta_1$ agrees well with numerical results, but the corresponding solution using the Galerkin method does not agree well. Finally, the Galerkin equations as derived by the present analysis and that of Reference 10 without the substitution $d^2\eta_1/dt^2 = -\omega_1^2\eta_1$ give good results, but in both cases the MOA leads to incorrect results.

The results reported above raise serious questions regarding the applicability of the MOA over the wide range of solid rocket operating conditions experienced in practice. The example considered above demonstrated that good results could be obtained with the MOA in a relatively

simple situation only after the approximation $d^2\eta_1 / dt^2 = -\omega_1^2\eta_1$ was introduced into the Galerkin equation while erroneous results were obtained when the MOA was applied to the "exact" Galerkin equation. At this point, in view of the absence of contrary evidence, one cannot help the feeling that at least in this example the success of the MOA was fortuitous.

Table 12. Comparison of Approximate Solutions for Particles in a Box

	Galerkin Method	Method of Averaging
Present Approximate Analysis	$-55.7\ sec^{-1}$	$-72.1\ sec^{-1}$
Analysis of Reference (10) Without the Approximation $\frac{d^2\eta_1}{dt^2} = -\omega_1^2\eta_1$	$-53.2\ sec^{-1}$	$-71.9\ sec^{-1}$
Analysis of Reference (10) With the Approximation $\frac{d^2\eta_1}{dt^2} = -\omega_1^2\eta_1$	$-42.0\ sec^{-1}$	$-52.8\ sec^{-1}$

The applicability of the MOA in the analysis of solid rocket motors cannot be judged solely on the basis of the above comparisons for particles in a box. Therefore more extensive comparisons were made for a hypothetical motor in which the propellant is insensitive to the pressure oscillations (i.e., $\Re = 0$). These calculations, therefore, include the effects of mean flow, flow turning, and nozzle damping as well as the effects of particle damping. Four particle diameters were considered, 2μ, 6μ, 10μ, and 20μ for the same motor geometry and steady-state properties considered in Section 4.2 (Figure 24). Approximate solutions were calculated using the following three techniques: (1) the Galerkin method applied to Equations (13) and (14) (i.e., numerical solution of Equations (22)

and (23)), (2) the Galerkin method applied to Equation (17) in which gas and particle equations have been combined (i.e., numerical solution of Equations (25)), and (3) the MOA applied to Equations (25) (i.e., numerical solution of Equations (39)). Decay rates and frequencies obtained with the three approximate techniques are compared with the Kooker-Zinn "exact" solutions in Table 13 for 3% initial disturbances.

Several interesting observations can be made from the data presented in Table 13. For the larger particle diameters of 10μ and 20μ (i.e., smaller values of K), all three approximate solutions are in good agreement with the "exact" solutions. On the other hand, the approximate solutions for 2μ and 6μ diameter particles (large K) differ from the "exact" solutions by various amounts. In both cases the Galerkin methods yield decay rates which are smaller than the "exact" decay rates, with Equations (25) yielding the greatest error (it was necessary to neglect the spatial derivatives of the particle velocity in order to combine the gas and particle equations). The MOA, surprisingly, yielded decay rates which were in better agreement with the "exact" decay rates than the Galerkin solutions, in spite of the fact that additional approximations were made in applying the MOA to Equations (25). Apparently the error associated with applying the MOA to Equation (25) partially compensated for the errors associated with the order of magnitude approximations and the Galerkin method used in deriving Equations (25). Since it is impossible to guarantee that this fortuitous circumstance will occur in every situation, the applicability of the MOA to more general solid rocket instability problems is still open to question.

To further investigate this question, a more realistic case was considered in which both combustion driving and particle damping were present. Thus, the three approximate solutions were compared with the "exact" solutions for the case shown in Figures 26 and 27 of Section 4.2 (i.e., $\sigma = 2.5\,\mu$, $C_m = 0.36$, $\bar{M}_e = 0.078$, $\Re_1^r = 4.17$). The results of these calculations are shown in Figures 58 and 59. Figure 58 shows growth rate versus number of wave cycles for 3% amplitude 1L mode initial disturbances, while Figure 59 shows the growth toward limiting amplitude for 10% initial disturbances. From Figure 58 it is evident that the Galerkin method (Equations (22) and (23)) underestimates the growth rate and the MOA overestimates the growth rate by about the same amount with respect to the

Table 13. Comparison of Approximate Solutions for Motor with $\mathcal{R} = 0$

Particle Size, μ	2.0	6.0	10.0	20.0
Drag Constant, K	46.72	5.191	1.869	0.4672
Damping, sec^{-1}				
Galerkin, Eqs. 22 and 23	-282	-502	-582	-408
Galerkin, Eqs. 25	-260	-488	-582	-407
M.O.A., Eqs. 39	-312	-538	-579	-408
Exact	-322	-525	-589	-411
Frequency, Hz				
Galerkin, Eqs. 22 and 23	975	989	1031	1071
Galerkin, Eqs. 25	975	987	1029	1071
M.O.A., Eqs. 39	979	1000	1041	1074
Exact	976	990	1038	1068

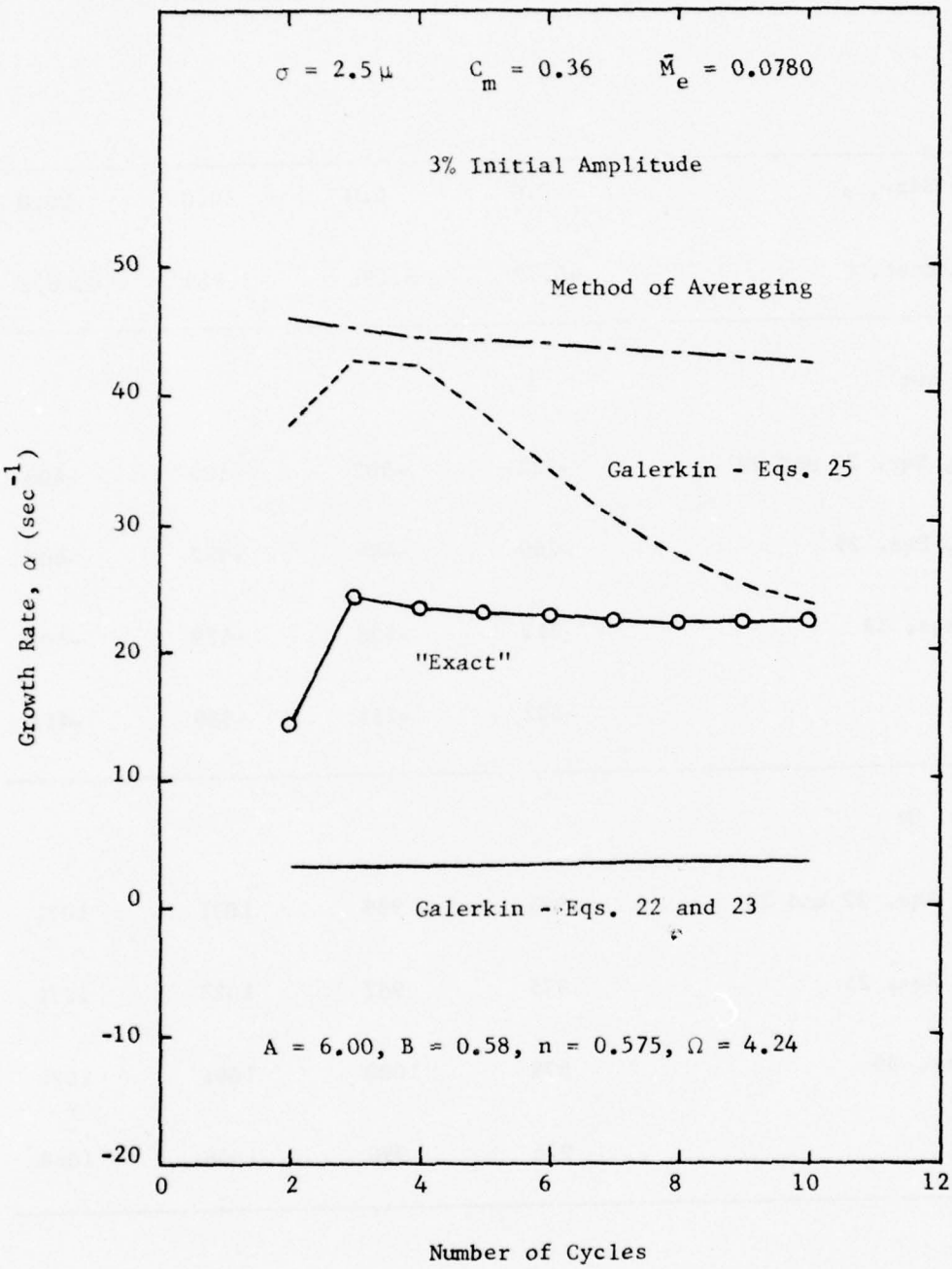

Figure 58. Comparison of Galerkin, MOA, and "Exact" Solutions for Growth Rate of Small Amplitude Disturbances

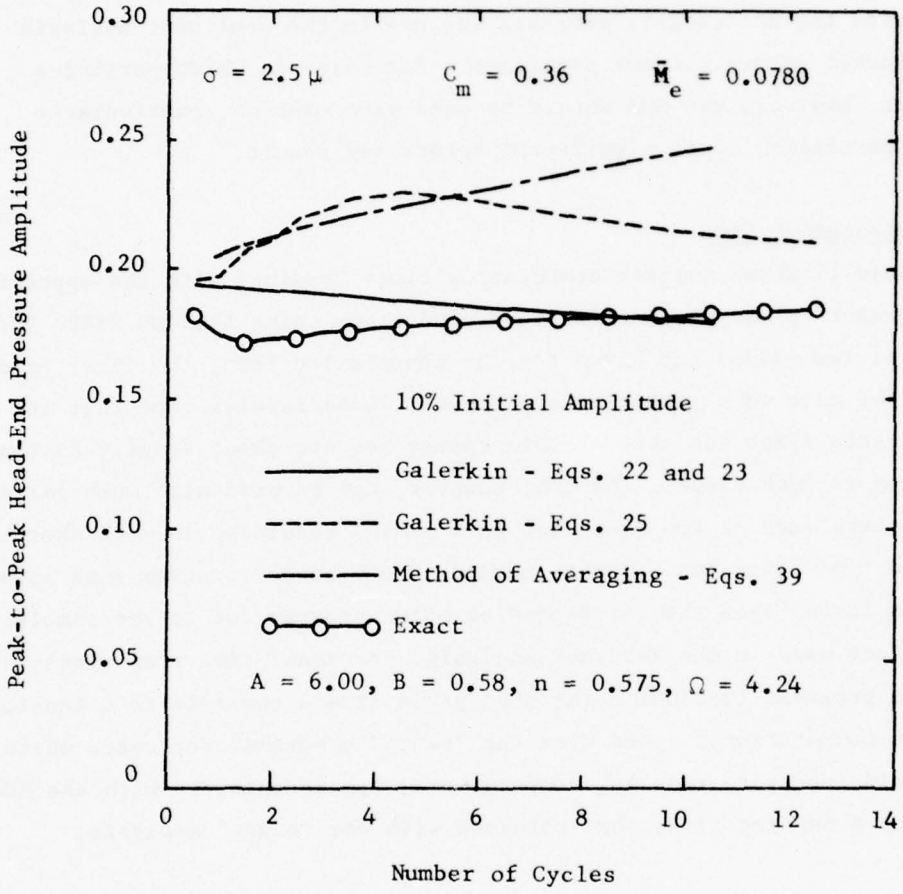

Figure 59. Comparison of Galerkin, MOA, and "Exact" Solutions for Growth to Limiting Amplitude

"exact" solution, while the Galerkin method (Equations (25)) yields growth rates between the "exact" and MOA values. Figure 59 shows that the MOA also predicts a considerably higher limiting amplitude than either the Galerkin methods or the "exact" analysis. These results show that the fortuitous agreement between the decay rates predicted by the MOA and the "exact" analysis for motors without combustion driving does not occur when combustion driving is present.

In conclusion, the considerable reduction in computation time obtained with the MOA clearly warrants its use in the nonlinear analysis of solid rocket motors without particles. For cases in which particles are present, however, the MOA should be used with caution, particularly for small particles, since significant errors may result.

4.8 Computation Time

Table 14 shows typical computation times obtained with the approximate and "exact" programs under various conditions using the CDC CYBER 70/74 computer. If two values are given for the computation time, the first value refers to the case when particles are absent. These results show that for equal time step sizes the two Galerkin approaches are about equally fast and that the MOA is much slower. The MOA, however, can be used with much larger time step sizes (one or two steps per wave cycle) resulting in much shorter computation times than the Galerkin method. The T-burner program runs about three times faster than the corresponding motor program due to the simpler eigenfunctions used in the T-burner analysis. For equal time step sizes, the approximate programs (excluding the MOA) yield from a two-fold to a ten-fold increase in computational speed over the "exact" programs. For cases where the MOA yields accurate results, computational speeds obtained with the MOA may approach a hundred times that obtained with the "exact" analysis.

Table 14. Comparison of Computation Times

Method	Number of Modes	Time Step Size	Computation Time Seconds/wave cycle
Galerkin Eqs. (22) and (23)	4	0.025	7
Galerkin Eqs. (22) and (23)	5	0.025	9-12
Galerkin Eqs. (22) and (23)	6	0.025	15-21
Galerkin Eqs. (25)	6	0.025	20
MOA	6	0.025	40
MOA	6	0.25	4
T-Burner	5	0.025	4
Exact	-	0.06	20
Exact	-	0.025	50

5. CONCLUSIONS AND RECOMMENDATIONS

5.1 Conclusions

The primary objective of this research program was to evaluate the usefulness of approximate nonlinear analysis techniques for predicting the stability characteristics of solid rocket motors and T-burners. This work involved the adaptation of a previous liquid-rocket approximate analysis for the solution of solid-rocket instability problems. This technique, which was based on the solution of an approximate wave equation by means of the Galerkin method, was also further simplified by application of the Method of Averaging (MOA). The usefulness of the approximate techniques (Galerkin and MOA) in the nonlinear stability analysis of solid rocket motors was then investigated for cases in which gasdynamic mode-coupling was the only nonlinearity considered. For this case an extensive parametric study was performed in which the approximate solutions were compared with available "exact" solutions. Later the effects of nonlinearities in the combustion driving and particle damping mechanisms were assessed using both "exact" and approximate models, which required the development of heuristic nonlinear combustion response and particle drag laws for the approximate analysis. Finally, the applicability of the approximate model to the nonlinear analysis of T-burners was determined.

The objective of this program has been reached. The predictions of the approximate techniques have been compared with the "exact" solutions for a wide variety of motor operating conditions. On the basis of the predicted growth/decay rates, frequencies, limiting amplitudes, and pressure waveforms, the Galerkin technique (without averaging) was found to be sufficiently accurate for most of the cases considered. For cases in which particle effects were important, these studies also showed that the MOA was generally less reliable than the Galerkin method. These findings were also supported by comparisons with experimental motor data. In the T-burner studies, it was found that the approximate T-burner analysis failed to accurately predict limiting amplitudes, although growth rates at low amplitudes were in fairly good agreement with measured data.

Additional conclusions reached during this investigation are summarized below in four parts: accuracy of the approximate methods, number of modes required to satisfactorily model the instability, effects of the improvements (i.e., incorporation of nonlinear burning rate and nonlinear particle drag laws into the models), and computation time.

Accuracy of the Approximate Method. The accuracy of the Galerkin method (without averaging) was found to be dependent on the case under consideration. The Galerkin method was in very good agreement with the "exact" solutions for the two simplest cases considered: (1) a motor without particle damping or combustion driving (mean flow, flow turning, and nozzle damping only) and (2) a particle-gas mixture in a closed-ended box. For a motor with particle damping but without combustion driving, the approximate analysis underestimated the damping by as much as 13% for particles smaller than 15 microns. For motors with combustion driving the approximate analysis tended to overestimate both the growth rates at low amplitudes and the limiting amplitudes for cases without particles, while these quantities were generally underestimated for cases with particles. For these cases the approximate analysis accurately predicted the expected trends regarding the effect of particle size and concentration and propellant response upon limiting amplitude. For T-burners the approximate analysis also correctly predicted the effect of various particle properties, propellant response, and cup-grain length, but for given values of these parameters the growth rates and limiting amplitudes did not agree well with the available "exact" solutions.

The accuracy of the MOA was also found to be case dependent. For small to moderate amplitude disturbances in motors without particles the MOA and Galerkin method were equally accurate. For small particles in a box, however, the MOA predicted excessive damping compared to the "exact" analysis and the Galerkin method. Although the MOA gave better agreement with the "exact" analysis than the Galerkin method for a motor with small particles but no combustion driving, the MOA did not yield accurate results for growth rates and limiting amplitudes in the same motor when combustion driving was included.

Comparison of the approximate (Galerkin) solutions with available motor test data gave reasonable agreement with the measured limiting amplitudes considering the difficulties encountered in estimating the transient combustion parameters. The approximate analysis correctly predicted the experimentally observed trend of increasing limiting amplitude with increasing steady-state Mach number. For T-burners the predicted small amplitude growth/decay rates were in good agreement with the measured values for reasonable values of the transient burning rate parameters; however, the predicted limiting amplitudes were far higher than the measured values.

Number of Modes Required. The number of modes required to adequately model the instability depended principally upon the relative stability of the higher frequency modes with respect to the fundamental mode. A three or four mode series appeared to be adequate for cases in which the higher modes were heavily damped, such as cases in which small particles are present. When the higher modes were less strongly damped, six or more modes were necessary (i.e., motors with large particles or without particles). The most unfavorable situations arose when the propellant response for the higher modes was comparable to or greater than the propellant response for the fundamental mode; here a large number of modes were required and the approximate solutions required more computer time than the "exact" solutions.

Effects of the Improvements. Results obtained with the "exact" and approximate models indicate that combustion nonlinearities should be included in the analysis of solid rocket instabilities whenever the oscillation amplitudes exceed 7-10% and sometimes for amplitudes as small as 3%. Depending upon various motor and propellant parameters, particularly frequency, combustion nonlinearities may either decrease or increase combustion driving with increasing amplitude; in the latter case pulsed instabilities may result. Although the heuristic nonlinear combustion model developed in this study accounts for the above effects, it needs to be improved to account for the nonlinear dependence of the combustion driving upon amplitude obtained with the "exact" analysis.

On the basis of the nonlinear particle damping studies, the nonlinear particle drag law should be used for the higher frequencies and larger particle sizes. Depending on the particle size, nonlinear particle drag effects may either increase or decrease particle damping with increasing amplitude; in the latter case pulsed instabilities may result. The nonlinear drag effect is important even for small amplitude disturbances due to the steady-state contribution to the relative velocity between particles and gas. Although the heuristic nonlinear particle drag model used in the approximate analysis predicts the above trends, more parametric studies are needed in order to guide further improvements of this model.

Computation Time. For equal integration time-step sizes, the Galerkin method program with a six-mode series runs about twice as fast as the "exact" program. The six-mode series requires about 20 seconds per wave cycle central processor time on the CDC CYBER 70/74 computer used in these studies. For cases

in which a four mode series is adequate, a further four-fold increase in speed can be obtained. The MOA program runs about ten times faster than the Galerkin program because a much larger time increment can be used. Due to the simpler eigenfunctions used to represent the T-burner solutions, the T-burner program runs about three times faster than the corresponding motor program.

Under the most favorable circumstances the Galerkin method may yield a ten-fold saving in computer time as compared to the "exact" analysis, while the MOA (when applicable) may yield a hundred-fold increase in computational speed over the "exact" analysis. Thus the approximate solution techniques may be used for extensive parametric studies of nonlinear solid rocket and T-burner stability behavior which would be impractical with the "exact" analytical techniques.

5.2 Recommendations

A number of investigations aimed at improving and generalizing the approximate models are recommended for future research. Some of these can be readily accomplished with only a modest expenditure of time and effort, while others will require a major research effort for their completion.

One of the basic assumptions used in the development of the present approximate and "exact" analyses was that the exchange of thermal energy between the particles and gas is negligible. Since it is known that particle thermal effects may contribute significantly to the total particle damping, they should be incorporated into the approximate and "exact" models.

The present approximate program for motors is restricted to full-length, cylindrical propellant grains. The approximate analysis should be extended to more general motor geometries such as partial length grains, gaps in grain, end-burning grains, variable port area, and arbitrary grain cross-sections. Two of these features, partial length grains and end-burning grains, have already been incorporated into the T-burner model and could easily be included in the analysis of motors.

More extensive parametric studies are needed to adequately assess the effects of nonlinear combustion driving and nonlinear particle damping upon the stability characteristics of motors and T-burners. These studies should be conducted using both the "exact" model and the approximate model. The results of these studies should then be used as a guide toward improvements of the heuristic nonlinear combustion response and particle drag laws.

In view of the limited number of comparisons with experimental data obtained during this research effort, more extensive comparisons between the approximate solutions and motor test data are badly needed. This will only be possible as more motor test data becomes available.

More studies are needed to determine the cause of the poor agreement between T-burner limiting amplitudes predicted by the approximate model and the values obtained by the "exact" analysis or from T-burner test data. This will probably involve the development of a nonlinear vent model and the inclusion of wall heat transfer effects.

It is well known that the combustion response of solid propellants depends upon both the pressure and velocity oscillations. While considerable work has been done to date on the investigation of the pressure-coupled response, relatively little work has been done on the elucidation of the velocity-coupled response. It is therefore recommended that the available information on the velocity-coupled response be used to develop analytical expressions capable of describing the velocity-coupled response of solid propellants, and that these expressions should be incorporated into the approximate and "exact" nonlinear instability models. Comparisons should then be made between the predictions of the available models, with and without the velocity-coupled response. Such comparisons should be useful in determining the role of velocity-coupled response in the behavior of unstable rockets, particularly regarding the development of pulsed instabilities.

With the completion of the above recommended improvements, the value of the approximate analysis as a useful engineering tool will be greatly enhanced.

6. REFERENCES

1. Dehority, G. L. and Price, E. W., "Axial Mode, Intermediate Frequency Combustion Instability in Solid Propellant Rockets," Naval Weapons Center Tech. Publ. 5654, October 1974.

2. Kooker, D. E. and Zinn, B. T., "Numerical Solution of Axial Instabilities in Solid Propellant Rocket Motors," Proceedings of the 10th JANNAF Combustion Meeting, CPIA Publication 243, Vol. I, December 1973, pp. 389-415.

3. Kooker, D. E. and Zinn, B. T., "Numerical Investigation of Nonlinear Axial Instabilities in Solid Rocket Motors," BRL CR 141, March 1974.

4. Levine, J. N. and Culick, F. E. C., "Numerical Analysis of Nonlinear Longitudinal Combustion Instability in Metalized Propellant Solid Rocket Motors," Proceedings of the 9th JANNAF Combustion Meeting, CPIA Publication 231, Vol. I, December 1972, pp. 141-163.

5. Levine, J. N. and Culick, F. E. C., "Nonlinear Analysis of Solid Rocket Combustion Instability, AFRPL-TR-74-45, Vol. I, October 1974.

6. Lores, M. E. and Zinn, B. T., "The Prediction of Nonlinear Longitudinal Combustion Instability in Liquid Propellant Rockets," NASA CR-120904, April 1972.

7. Zinn, B. T. and Powell, E. A., "Nonlinear Combustion Instability in Liquid Propellant Rocket Engines," Proceedings of the 13th Symposium (International) on Combustion, The Combustion Institute, 1971, pp. 491-503.

8. Powell, E. A. and Zinn, B. T., "The Prediction of Nonlinear Three-Dimensional Combustion Instability in Liquid Rockets with Conventional Nozzles," NASA CR-121279, October 1973.

9. Culick, F. E. C., "Nonlinear Behavior of Acoustic Waves in Combustion Chambers," Proceedings of the 10th JANNAF Combustion Meeting, CPIA Publication 243, Vol. I, December 1973, pp. 417-436.

10. Culick, F. E. C., "Nonlinear Behavior of Acoustic Waves in Combustion Chambers," California Institute of Technology Report, April 1975.

11. Landau, L. D. and Lifshitz, E. M., Fluid Mechanics, p. 66, Pergamon Press, 1959.

12. Culick, F. E. C., "A Review of Calculations for Unsteady Burning of a Solid Propellant," AIAA J., Vol. 6, No. 12, pp. 2241-2244, December 1968.

13. Lighthill, M. J., Surveys in Mechanics, p. 250, 1956.

14. Blackstock, D. T., "Approximate Equations Governing Finite-Amplitude Sound in Thermo-Viscous Fluids," General Dynamics GD/E Report GD-1463-52, 1963.

15. Finlayson, B. A. and Scriven, L. E., "The Method of Weighted Residuals -- A Review," Applied Mechanics Reviews, Vol. 19, No. 9, September 1966, pp. 735-744.

16. Ames, W. F., Nonlinear Partial Differential Equations in Engineering, Academic Press, 1965.

17. Zinn, B. T. and Powell, E. A., "Application of the Galerkin Method in the Solution of Combustion Instability Problems," Proceedings of the 19th International Astronautical Congress, Vol. 3, 1970, pp. 59-73. (Also appeared as IAF Paper No. P69. Originally published in 1968).

18. Zinn, B. T. and Powell, E. A., "The Galerkin Method and its Use in the Solution of Combustion Instability Problems," Proceedings of the 5th ICRPG Combustion Conference, December 1968, pp. 138-144.

19. Nayfeh, A. H., Perturbation Methods, p. 165, John Wiley & Sons, 1973.

20. Derr, R. L., "Evaluation of a Variable Area T-Burner for Metallized Propellants," AFRPL-TR-72-97, February 1973.

21. Rudinger, G., "Effective Drag Coefficients for Gas-Particle Flow in Shock Tubes," Project Squid Technical Report CAL-97-PU, March 1969.

22. Beckstead, M. W., et al. "Variable Area T-Burner Investigation," AFRPL TR-72-85, December 1972.

23. Powell, E. A., "Nonlinear Combustion Instability in Liquid Propellant Rocket Engines," Ph.D. Thesis, Georgia Institute of Technology, GITAER 70-6 (September 1970).

APPENDIX A

DERIVATION OF APPROXIMATE EQUATIONS

A-1. Derivation of Equations (13) and (14).

Under the assumption stated in Section 2, the system of nondimensional conservation equations that describe the unsteady behavior of the combustor two-phase flow are given by Equations (1) through (6). The unsteady flow in the T-burner vent region can also be described by these equations if the axial velocities in the source terms arising from the mean-flow/acoustic interactions are multiplied by the factor $1 - V_\ell$ (Section 2.6). Thus the gas and particle momentum equations become:

$$\rho \frac{\partial u}{\partial t} + \rho u \frac{\partial u}{\partial x} + \frac{1}{\gamma} \frac{\partial P}{\partial x} = - \left[K\rho_p (u-u_p) + \frac{2\dot{m}_g}{R} (1-V_\ell)u \right] \qquad (A-1)$$

$$\rho_p \frac{\partial u_p}{\partial t} + \rho_p u_p \frac{\partial u_p}{\partial x} = K\rho_p (u-u_p) - \frac{2\dot{m}_p}{R} (1-V_\ell)u_p \qquad (A-2)$$

Writing the energy equation in terms of the enthalpy, Equation (5) yields:

$$\rho \frac{\partial h}{\partial t} + (\gamma-1) \frac{\partial}{\partial t} \left[\rho \frac{u^2}{2} + \frac{\rho_p u_p^2}{2} \right] - \frac{\gamma-1}{\gamma} \frac{\partial p}{\partial t} + \rho u \frac{\partial h}{\partial x}$$

$$+ (\gamma-1) \left[\frac{\rho u^3}{2} + \rho_p \frac{u_p^3}{2} \right] = \frac{2\dot{m}_g}{R} (h_c - h) \qquad (A-3)$$

Using order of magnitude approximations, Equations (1), (2), (A-1), (A-2), and (A-3) will now be combined to obtain approximate equations governing the gas and particle velocity potentials.

Each of the dependent variables is first expressed as the sum of a steady-state quantity and a perturbation quantity, thus

$$\rho = \bar{\rho} + \rho'$$

$$\rho_p = \bar{\rho}_p + \rho_p'$$

$$u = \bar{u} + u'$$

$$u_p = \bar{u}_p + u'_p$$

$$p = \bar{p} + p'$$

$$h = \bar{h} + h' \qquad \text{(A-4)}$$

where $(\bar{\ })$ denotes a steady-state quantity and $(\ )'$ denotes a perturbation quantity. Equations (A-4) are then substituted into the conservation equations and the equation of state. Subtracting out the steady-state equations (obtained by setting the time derivatives equal to zero in the conservation equations) yields a system of equations describing the perturbation quantities. These equations are too complicated to be solved by the Galerkin method and must be further simplified by order of magnitude approximations.

It is now assumed that each perturbation quantity and the steady-state Mach number are of $O(\epsilon)$ where ϵ is a small ordering parameter that is a measure of the wave amplitude. Thus the perturbation equations are simplified by neglecting all terms of order higher than ϵ^2, which includes products of three perturbations, products of the mean flow Mach number (i.e., $\bar{u}$) and two perturbations, products of $\bar{u}^2$ and a perturbation quantity, and terms proportional to $\bar{u}^3$. As a result of the small Mach number assumption, the steady-state pressure, density, and enthalpy are nearly constant throughout the chamber, thus $\bar{\rho} = 1$, $\bar{p} = 1$, and $\bar{h} = 1$ (the error introduced by this approximation is $O(\epsilon^3)$). Furthermore the steady-state continuity equations for the gas and particles show that the steady-state source terms $\dot{\bar{m}}_g$ and $\dot{\bar{m}}_p$ are also of $O(\epsilon)$, while the linear response function (i.e., Equation (9)) indicates that for $\Re$ of O(1) the unsteady source terms $\dot{m}'_g$ and $\dot{m}'_p$ are of $O(\epsilon^2)$. Introducing these approximations into Equations (1), (2), A(-1), (A-2), and (A-3) give:

$$\frac{\partial \rho'}{\partial t} + \frac{\partial}{\partial x}\left(\rho' \bar{u} + u' + \rho' u'\right) = \frac{2\dot{m}'_g}{R} \qquad \text{(A-5)}$$

$$\frac{\partial \rho'_p}{\partial t} + \frac{\partial}{\partial x}\left(\rho'_p \bar{u}_p + \bar{\rho}_p u'_p + \rho'_p u'_p\right) = \frac{2\dot{m}'_p}{R} \qquad \text{(A-6)}$$

$$\frac{\partial u'}{\partial t} + \rho' \frac{\partial u'}{\partial t} + \bar{u} \frac{\partial u'}{\partial x} + u' \frac{d\bar{u}}{dx} + u' \frac{\partial u'}{\partial x} + \frac{1}{\gamma} \frac{\partial p'}{\partial x} =$$

$$- \left\{ K \bar{\rho}_p (u' - u_p') + K \rho_p' (\bar{u} - \bar{u}_p) + K \rho_p' (u' - u_p') \right\}$$

$$- \frac{2}{R} \dot{\bar{m}}_g (1 - V_\ell) u' \qquad \text{(A-7)}$$

$$\bar{\rho}_p \frac{\partial u_p'}{\partial t} + \rho_p' \frac{\partial u_p'}{\partial t} + \bar{\rho}_p \bar{u}_p \frac{\partial u_p'}{\partial x} + \bar{\rho}_p u_p' \frac{d\bar{u}_p}{dx} + \bar{\rho}_p u_p' \frac{\partial u_p'}{\partial x} =$$

$$+ K \bar{\rho}_p (u' - u_p') + K \rho_p' (\bar{u} - \bar{u}_p) + K \rho_p' (u' - u_p')$$

$$- \frac{2}{R} \dot{\bar{m}}_p (1 - V_\ell) u_p' \qquad \text{(A-8)}$$

$$\frac{\partial h'}{\partial t} + \rho' \frac{\partial h'}{\partial t} + (\gamma - 1) \frac{\partial}{\partial t} \left[\bar{u} u' + \frac{1}{2} (u')^2 \right] + (\gamma - 1) \frac{\partial}{\partial t} \left[\bar{\rho}_p \bar{u}_p u_p' + \frac{1}{2} \bar{\rho}_p (u_p')^2 \right]$$

$$- \frac{\gamma - 1}{\gamma} \frac{\partial p'}{\partial t} + \bar{u} \frac{\partial h'}{\partial x} + u' \frac{\partial h'}{\partial x} = \frac{2}{R} \left[- \dot{\bar{m}}_g h' + \dot{m}_g' (h_c - 1) \right] \qquad \text{(A-9)}$$

while the equation of state becomes:

$$p' = h' + \rho' + \rho' h' \qquad \text{(A-10)}$$

In order to further simplify these equations, the following velocity potentials are defined:

$$u' = \frac{\partial \Phi}{\partial x}$$

$$u_p' = \frac{\partial \Phi_p}{\partial x} \qquad \text{(A-11)}$$

Further order of magnitude considerations are also used to simplify the particle drag terms in Equations (A-7) and (A-8). Here it is assumed that the particle loading of the propellant is sufficiently low that $\bar{\rho}_p$ is $O(\epsilon)$ which implies that

ρ_p' is $O(\epsilon^2)$. Since the relative velocities $\bar{u}-\bar{u}_p$ and $u'-u_p'$ are of $O(\epsilon)$ the second and third particle drag terms on the right-hand-sides of Equations (A-7) and (A-8) are of $O(\epsilon^3)$ and can be neglected. Introducing these approximations and the velocity potentials into Equations (A-5) through (A-9) and using subscript notation for the partial derivatives gives the following second order conservation equations:

$$\rho_t' + \bar{u}\rho_x' + \rho' \frac{d\bar{u}}{dx} + \Phi_{xx} + \rho' \Phi_{xx} + \rho_x' \Phi_x = \frac{2\dot{m}_g'}{R} \tag{A-12}$$

$$(\rho_p')_t + \bar{u}_p(\rho_p')_x + \rho_p' \frac{d\bar{u}_p}{dx} + \left[\bar{\rho}_p(\Phi_p)_x\right]_x + \rho_p'(\Phi_p)_{xx} + (\rho_p')_x (\Phi_p)_x = \frac{2\dot{m}_p'}{R} \tag{A-13}$$

$$\Phi_{xt} + \rho' \Phi_{xt} + \bar{u}\Phi_{xx} + \frac{d\bar{u}}{dx}\Phi_x + \Phi_x \Phi_{xx} + \frac{1}{\gamma} p_x' = - K\bar{\rho}_p\left[\Phi_x - (\Phi_p)_x\right] - \frac{2}{R}\bar{\dot{m}}_g(1-V_\ell)\Phi_x \tag{A-14}$$

$$\bar{\rho}_p(\Phi_p)_{xt} + \bar{\rho}_p\bar{u}_p(\Phi_p)_{xx} + \bar{\rho}_p \frac{d\bar{u}_p}{dx}(\Phi_p)_x + \bar{\rho}_p(\Phi_p)_x(\Phi_p)_{xx} = K\bar{\rho}_p\left[\Phi_x - (\Phi_p)_x\right] - \frac{2}{R}\bar{\dot{m}}_p(1-V_\ell)(\Phi_p)_x \tag{A-15}$$

$$h_t' + \rho' h_t' + (\gamma-1)\left[\bar{u}\Phi_x + \frac{1}{2}\Phi_x^2 + \bar{\rho}_p\bar{u}_p(\Phi_p)_x + \frac{1}{2}\bar{\rho}_p(\Phi_p)_x^2\right]_t - \frac{\gamma-1}{\gamma} p_t' + \bar{u} h_x' + \Phi_x h_x' = \frac{2}{R}\left[-\bar{\dot{m}}_g h' + \dot{m}_g'(h_c - 1)\right] \tag{A-16}$$

In order to combine Equations (A-12) through (A-16) to obtain Equations (13) and (14), the substitution principle used by Lighthill[13] and Blackstock[14] is invoked. This principle states that any factor of a second order term may be replaced by its equivalent first order expression, because any more precise

substitution would result in the appearance of higher order terms. The substitution principle is used here to replace ρ' and h' in the second order terms with equivalent first order expressions involving Φ. The first order expressions which are needed in this analysis are as follows:

$$\begin{aligned} \rho' &= -\Phi_t \\ p' &= -\gamma\Phi_t \\ h' &= -(\gamma-1)\Phi_t \end{aligned} \tag{A-17}$$

which are derived in Reference (23). In addition the steady-state mass source $2\bar{\dot{m}}_g/R$ may be replaced by the equivalent quantity $d\bar{u}/dx$ as shown by the steady-state continuity equation. Making these substitutions into Equations (A-12), (A-14), (A-16), and (A-10) and rearranging terms yields the following expressions:

$$\rho_t' + \Phi_{xx} = \bar{u}\Phi_{xt} + \frac{d\bar{u}}{dx}\Phi_t + \Phi_t\Phi_{xx} + \Phi_x\Phi_{xt} + \frac{2\dot{m}_g'}{R} \tag{A-18}$$

$$\left[\frac{p'}{\gamma} + \Phi_t + \bar{u}\Phi_x + \frac{1}{2}\Phi_x^2 - \frac{1}{2}\Phi_t^2 + K\bar{\rho}_p(\Phi - \Phi_p) + (1-V_\ell)\frac{d\bar{u}}{dx}\Phi\right]_x = 0 \tag{A-19}$$

$$h_t' + (\gamma-1)\Phi_t\Phi_{tt} + (\gamma-1)\left[\bar{\rho}_p\bar{u}_p(\Phi_p)_x + \frac{1}{2}\bar{\rho}_p(\Phi_p)_x^2\right]_t - \frac{\gamma-1}{\gamma}p_t' = (\gamma-1)\frac{d\bar{u}}{dx}\Phi_t + \frac{2\dot{m}_g'}{R}(h_c-1) \tag{A-20}$$

$$h' = p' - \rho' - (\gamma-1)\Phi_t^2 \tag{A-21}$$

---

[23] Powell, E. A., "Nonlinear Combustion Instability in Liquid Propellant Rocket Engines," Ph.D. Thesis, Georgia Institute of Technology, GITAER 70-6 (September 1970).

Equations (A-18) through (A-21) will now be combined to obtain a nonlinear wave equation for the gas velocity potential. Substituting Equation (A-21) into (A-20) and collecting terms, the energy equation becomes:

$$\frac{1}{\gamma} p'_t - \rho'_t - (\gamma-1)\Phi_t\Phi_{tt} - (\gamma-1)\frac{d\bar{u}}{dx}\Phi_t =$$

$$\frac{2\dot{m}'_g}{R}(h_c-1) - (\gamma-1)\left[\bar{\rho}_p\bar{u}_p(\Phi_p)_x + \frac{1}{2}\bar{\rho}_p(\Phi_p)_x^2\right]_t \qquad \text{(A-22)}$$

The gas momentum equation (i.e., Equation (A-19)) is integrated with respect to x (the constant of integration must be zero according to the argument given in Reference (22)) to give:

$$p' = -\gamma\left[\Phi_t + \bar{u}\Phi_x + \frac{1}{2}\Phi_x^2 - \frac{1}{2}\Phi_t^2 + K\bar{\rho}_p(\Phi - \Phi_p) + (1-V_\ell)\frac{d\bar{u}}{dx}\Phi\right] \qquad \text{(A-23)}$$

which is also Equation (63) of Section 2.6. Setting $V_\ell = 0$ gives the corresponding equation for motors; that is, Equation (24) of Section 2.3. To proceed with the derivation of Equation (13), Equation (A-23) is differentiated with respect to t and the resulting expression is substituted for $(1/\gamma)p'_t$ in Equation (A-22). Furthermore the continuity equation (i.e. Equation (A-18)) is substituted for ρ'_t in Equation (A-22). Combining terms, neglecting the nonlinear particle term in Equation (A-22), and using the first order relation, $\Phi_{tt} = \Phi_{xx}$, yields

$$\Phi_{xx} - \Phi_{tt} = 2\bar{u}\Phi_{xt} + (\gamma + 1 - V_\ell)\frac{d\bar{u}}{dx}\Phi_t$$

$$+ 2\Phi_x\Phi_{xt} + (\gamma-1)\Phi_t\Phi_{xx}$$

$$+ K\bar{\rho}_p(\Phi_t - \Phi_{p_t}) - (\gamma-1)\bar{\rho}_p\bar{u}_p(\Phi_p)_{xt} + \frac{2\dot{m}'_g}{R}h_c \qquad \text{(A-24)}$$

If $2\dot{m}'_g/R$ is replaced by ω', Equation (A-24) becomes Equation (61) of Section 2.6 which describes the unsteady flow in the T-burner vent region. For motors the source term in Equation (A-24) is related to the pressure perturbation through the linear response function (i.e., Equation (9)). Substituting Equation (9) into the source term and using $2\bar{\dot{m}}_g/R = d\bar{u}/dx$ and the first order re-

lation $p' = -\gamma\Phi_t$ yields:

$$\frac{2\dot{m}'}{R}\frac{g}{}h_c = -\gamma\Re h_c \frac{d\bar{u}}{dx}\Phi_t \qquad \text{(A-25)}$$

Substituting Equation (A-25) into Equation (A-24) and setting $V_\ell = 0$ yields Equation (13) of Section 2.2.

The particle potential equation (i.e., Equation (14)) is readily derived from the particle momentum equation (i.e., Equation (A-15)). Using the steady-state particle continuity equation to replace $2\bar{m}_p/R$ with $\bar{\rho}_p d\bar{u}_p/dx$ in Equation (A-15), dividing by $\bar{\rho}_p$, and rearranging terms gives:

$$\frac{\partial}{\partial x}\left[(\Phi_p)_t + \bar{u}_p(\Phi_p)_x + \frac{1}{2}(\Phi_p)_x^2 - K(\Phi - \Phi_p) + (1-V_\ell)\frac{d\bar{u}_p}{dx}\Phi_p\right] = 0 \qquad \text{(A-26)}$$

where $d\bar{u}_p/dx$ is assumed to be constant (the resulting error is of $O(\epsilon^3)$). As in the case of the gas momentum equation (i.e., Equation (A-19)) Equation (A-26) can be integrated with respect to x (the same argument holds regarding the constant of integration). Performing this integration and rearranging terms gives the desired particle potential equation:

$$(\Phi_p)_t + \bar{u}_p(\Phi_p)_x + \frac{1}{2}(\Phi_p)_x^2 = K(\Phi - \Phi_p) - (1 - V_\ell)\frac{d\bar{u}_p}{dx}\Phi_p \qquad \text{(A-27)}$$

which is the same as Equation (62) of Section 2.6. Setting $V_\ell = 0$ gives Equation (14) of Section 2.2.

A-2. Derivation of Equation (17).

The basic assumption used in deriving Equation (17) is that the terms involving the spatial derivatives of the particle velocity (both steady-state and perturbation) are negligible compared to the remaining terms in the particle momentum equation. Neglecting these terms as well as those involving ρ_p' (since ρ_p' is $O(\epsilon^2)$) in Equation (A-8) yields:

$$\frac{du_p'}{dt} + Ku_p' = Ku' \qquad \text{(A-28)}$$

Using the integrating factor e^{Kt} and the initial condition $u_p'(0) = u_{p_o}'$, the solution to Equation (A-28) is

$$u_p' = Ke^{-Kt}\int_0^t e^{Kt'}u'\,dt' + u_{p_o}'e^{-Kt} \qquad \text{(A-29)}$$

Since the second term decays rapidly as time increases, it can be neglected to give:

$$u_p'(t) = Ke^{-Kt}\int_0^t u' e^{Kt'} dt' \tag{A-30}$$

Introducing the velocity potentials given by Equations (A-11), Equation (A-30) becomes:

$$\frac{\partial \Phi_p}{\partial x} = Ke^{-Kt}\int_0^t \frac{\partial \Phi}{\partial x} e^{Kt'} dt' \tag{A-31}$$

To derive Equation (17) the analytical solution for Φ_p given by Equation (A-31) is substituted into the second order gas momentum equation (i.e., Equation (A-19)) with $V_\ell = 0$ to obtain:

$$\frac{\partial}{\partial x}\left[\frac{p'}{\gamma} + \Phi_t + \bar{u}\Phi_x + \frac{1}{2}\Phi_x^2 - \frac{1}{2}\Phi_t^2 + K\bar{\rho}_p\Phi + \frac{d\bar{u}}{dx}\Phi\right]$$

$$- K\bar{\rho}_p\left[Ke^{-Kt}\int_0^t \frac{\partial \Phi}{\partial x} e^{Kt'} dt'\right] = 0 \tag{A-32}$$

while interchanging the order of differentiation and integration in the last term gives:

$$\frac{\partial}{\partial x}\left[\frac{p'}{\gamma} + \Phi_t + \bar{u}\Phi_x + \frac{1}{2}\Phi_x^2 - \frac{1}{2}\Phi_t^2 + \frac{d\bar{u}}{dx}\Phi + K\bar{\rho}_p\Phi\right.$$

$$\left. - K^2\bar{\rho}_p e^{-Kt}\int_0^t \Phi e^{Kt'} dt'\right] = 0 \tag{A-33}$$

Integrating with respect to x and rearranging terms gives:

$$p' = -\gamma\left[\Phi_t + \bar{u}\Phi_x + \frac{1}{2}\Phi_x^2 - \frac{1}{2}\Phi_t^2 + \frac{d\bar{u}}{dx}\Phi + K\bar{\rho}_p\Phi\right.$$

$$\left. - K^2\bar{\rho}_p e^{-Kt}\int_0^t \Phi e^{Kt'} dt'\right] \tag{A-34}$$

which is the same as Equation (28) in Section 2.3.

Next, Equation (A-31) is substituted into the energy equation (i.e., Equation (A-22)) and the nonlinear particle term is neglected to obtain:

$$\frac{1}{\gamma} p_t' - \rho_t' - (\gamma-1)\,\Phi_t\Phi_{tt} - (\gamma-1)\,\frac{d\bar{u}}{dx}\,\Phi_t =$$

$$\frac{2\dot{m}_g'}{R}(h_c - 1) - (\gamma - 1)\,\frac{\partial}{\partial t}\left[\bar{\rho}_p\bar{u}_p K e^{-Kt}\int_o^t \Phi_x e^{Kt'}dt'\right]$$

(A-35)

As in the previous derivation for Equation (A-24), the momentum equation (i.e., Equation (A-34)) is differentiated with respect to time, which yields:

$$\frac{1}{\gamma} p_t' = -\left\{\Phi_{tt} + \bar{u}\Phi_{xt} + \Phi_x\Phi_{xt} - \Phi_t\Phi_{tt} + \frac{d\bar{u}}{dx}\Phi_t + K\bar{\rho}_p\Phi_t\right.$$

$$\left. - K^2\bar{\rho}_p\Phi + K^3\bar{\rho}_p e^{-Kt}\int_o^t \Phi e^{Kt'}dt'\right\} \qquad \text{(A-36)}$$

Substituting Equation (A-36) for $(1/\gamma)p_t'$ and Equation (A-18) for ρ_t' in Equation (A-35), combining terms, and using the first order relation, $\Phi_{tt} = \Phi_{xx}$, gives the desired equation:

$$\Phi_{xx} - \Phi_{tt} = 2\bar{u}\Phi_{xt} + (\gamma+1)\,\frac{d\bar{u}}{dx}\Phi_t + 2\Phi_x\Phi_{xt} + (\gamma-1)\Phi_t\Phi_{xx}$$

$$+ K\bar{\rho}_p\Phi_t - (\gamma-1)\,K\bar{\rho}_p\bar{u}_p\Phi_x - K^2\bar{\rho}_p\Phi$$

$$+ K^3\bar{\rho}_p e^{-Kt}\int_o^t \Phi e^{Kt'}dt'$$

$$+ (\gamma-1)\,K^2\bar{\rho}_p\bar{u}_p e^{-Kt}\int_o^t \Phi_x e^{Kt'}dt'$$

$$+ \frac{2\dot{m}_g'}{R} h_c \qquad \text{(A-37)}$$

Finally replacing $2\dot{m}_g'/R$ with Equation (A-25) yields Equation (17) of Section 2.2.

APPENDIX B

USE OF COMPLEX VARIABLES IN THE SOLUTION OF NONLINEAR DIFFERENTIAL EQUATIONS

It is often convenient to use complex variables in the solution of the linear equations which arise in acoustics, combustion instability and related fields. In this case the solution is expressed in complex form, and the real part represents the physically meaningful solution. However, care must be used when applying this technique in the solution of nonlinear equations. The difficulties that are encountered in applying the complex variable technique to nonlinear problems will be illustrated by analyzing the following simplified example. Consider the nonlinear wave equation given by:

$$\Phi_{xx} - \Phi_{tt} = \Phi\Phi_t \tag{B-1}$$

A complex solution of Equation (B-1) of the form $\Phi = \varphi + i\Psi$ would be useful only if its real part, φ, satisfies Equation (B-1), which would be the case if the equation were linear. However, straightforward substitution of $\Phi = \varphi + i\Psi$ into Equation (B-1) and separating its real and imaginary parts yields the following equation for φ:

$$\varphi_{xx} - \varphi_{tt} = \varphi\varphi_t - \Psi\Psi_t \tag{B-2}$$

indicating that the real part, φ, does not satisfy Equation (B-1) because of the extra term, $-\Psi\Psi_t$, appearing on the right hand side. In order to eliminate this extra term, the form of the original differential equation (i.e., Equation (B-1) must be modified.

Since Equation (B-1) supposedly describes some physical phenomenon, and since only the real part of the complex solution is physically meaningful, then the nonlinear term $\Phi\Phi_t$ should really be expressed as the product $\mathrm{Re}(\Phi) \times \mathrm{Re}(\Phi_t)$ which is equivalent to $(\Phi\Phi_t + \Phi\Phi_t^* + \Phi^*\Phi_t + \Phi^*\Phi_t^*)/4$. Substituting this expression into Equation (B-1) yields:

$$\Phi_{xx} - \Phi_{tt} = \left[\Phi\Phi_t + \Phi\Phi_t^* + \Phi^*\Phi_t + \Phi^*\Phi_t^*\right]/4 \tag{B-3}$$

Substituting $\Phi = \varphi + i\Psi$ into Equation (B-3) and separating its real and imaginary parts yield:

$$\varphi_{xx} - \varphi_{tt} = \varphi\varphi_t$$

$$\Psi_{xx} - \Psi_{tt} = 0 \tag{B-4}$$

which shows that the real part of the solution of Equation (B-3) satisfies the desired equation (i.e., Equation (B-1)) and the imaginary part satisfies a homogeneous linear wave equation. This technique was applied to the solution of nonlinear combustion instability problems (i.e., to Equation (13)), and the resulting modified wave equation was solved using the Galerkin Method. Due to the approximate nature of the Galerkin Method, however, the resulting solution contained an error term which grew without limit. Consequently, the above procedure had to be modified in order to obtain satisfactory solutions of Equation (13) using the Galerkin Method.

An alternate technique is to modify Equation (B-1) such that both the real and imaginary parts satisfy the original equation. This can be done by replacing terms of the form $\Phi\Phi_t$ with $\mathrm{Re}(\Phi)\mathrm{Re}(\Phi_t) + i\mathrm{Im}(\Phi)\mathrm{Im}(\Phi_t)$; using the relations:

$$\mathrm{Re}(\Phi)\mathrm{Re}(\Phi_t) = \left(\frac{\Phi + \Phi^*}{2}\right)\left(\frac{\Phi_t + \Phi_t^*}{2}\right) = \left[\Phi\Phi_t + \Phi\Phi_t^* + \Phi^*\Phi_t + \Phi^*\Phi_t^*\right]/4$$

$$i\mathrm{Im}(\Phi)\mathrm{Im}(\Phi_t) = -i\left(\frac{\Phi - \Phi^*}{2}\right)\left(\frac{\Phi_t - \Phi_t^*}{2}\right) = -\left[\Phi\Phi_t - \Phi\Phi_t^* - \Phi^*\Phi_t + \Phi^*\Phi_t^*\right]/4 \tag{B-5}$$

in Equation (B-1) gives:

$$\Phi_{xx} - \Phi_{tt} = \left[(1 - i)(\Phi\Phi_t + \Phi^*\Phi_t^*) + (1 + i)(\Phi\Phi_t^* + \Phi^*\Phi_t)\right]/4 \tag{B-6}$$

Substituting $\Phi = \varphi + i\Psi$ into Equation (B-6) and separating into its real and imaginary parts gives:

$$\varphi_{xx} - \varphi_{tt} = \varphi\varphi_t$$

$$\Psi_{xx} - \Psi_{tt} = \Psi\Psi_t \tag{B-7}$$

which shows that both φ and Ψ satisfy Equation (B-1). Applying this method to the solution of Equation (13) yields the following modified wave equation:

$$\Phi_{xx} - \Phi_{tt} = 2\bar{u}\Phi_{xt} + (\gamma+1)\frac{d\bar{u}}{dx}\Phi_t - \gamma\Re h_c \frac{d\bar{u}}{dx}\Phi_t$$

$$+ K\bar{\rho}_p \left[\Phi_t - (\Phi_p)_t\right] - (\gamma-1)\bar{\rho}_p\bar{u}_p(\Phi_p)_{xt}$$

$$+ \frac{1-i}{2}\left[\Phi_x\Phi_{xt} + \Phi^*_x\Phi^*_{xt}\right] + \frac{1+i}{2}\left[\Phi_x\Phi^*_{xt} + \Phi^*_x\Phi_{xt}\right]$$

$$+ \frac{(\gamma-1)}{4}\left\{(1-i)\left[\Phi_t\Phi_{xx} + \Phi^*_t\Phi^*_{xx}\right] + (1+i)\left[\Phi_t\Phi^*_{xx} + \Phi^*_t\Phi_{xx}\right]\right\} \qquad \text{(B-8)}$$

Application of the Galerkin Method to Equation (B-8) yields Equations (22) of Section 2.3

APPENDIX C

COEFFICIENTS APPEARING IN THE APPROXIMATE MODE AMPLITUDE EQUATIONS

C-1. Coefficients Appearing in Equations (22) and (23).

The coefficients of the linear terms in Equations (22) are:

$$C_o(j,m) = \int_o^1 X_m X_j^* \, dx \qquad \text{for } 1 \le m \le N \tag{C-1}$$

$$C_o(j,m) = 0 \qquad \text{for } N+1 \le m \le 2N$$

$$C_1(j,m) = -\int_o^1 \frac{d^2X_m}{dx^2} X_j^* \, dx + \frac{dX_m}{dx}(1)X_j^*(1) \qquad \text{for } 1 \le m \le N \tag{C-2}$$

$$C_1(j,m) = 0 \qquad \text{for } N+1 \le m \le 2N$$

$$C_2(j,m) = 2\int_o^1 \bar{u}(x) \frac{dX_m}{dx} X_j^* \, dx + (\gamma+1) \int_o^1 \frac{d\bar{u}}{dx} X_m X_j^* \, dx + \gamma Y X_m(1) X_j^*(1) \qquad \text{for } 1 \le m \le N \tag{C-3}$$

$$C_2(j,m) = -(\gamma-1)\bar{\rho}_p \int_o^1 \bar{u}_p(x) \frac{dX_m}{dx} X_j^* \, dx \qquad \text{for } N+1 \le m \le 2N$$

$$C_3(j,m) = \bar{\rho}_p \int_o^1 X_m X_j^* \, dx \qquad \text{for } 1 \le m \le N \tag{C-4}$$

$$C_3(j,m) = -\bar{\rho}_p \int_o^1 X_m X_j^* \, dx \qquad \text{for } N+1 \le m \le 2N$$

AD-A044 298 GEORGIA INST OF TECH ATLANTA SCHOOL OF AEROSPACE ENG--ETC F/G 21/8.2
APPROXIMATE NONLINEAR ANALYSIS OF SOLID ROCKET MOTORS AND T-BUR--ETC(U)
JUL 77 E A POWELL, M S PADMANABHAN, B T ZINN F04611-75-C-0036

UNCLASSIFIED AFRPL-TR-77-48 NL

3 OF 3
ADA
044298

END
DATE
FILMED
10-77
DDC

$$C_4(j,m) = -\gamma \int_0^1 \frac{d\bar{u}}{dx} X_m X_j^* \, dx \qquad \text{for } 1 \le m \le N$$

$$C_4(j,m) = 0 \qquad \text{for } N+1 \le m \le 2N \qquad \text{(C-5)}$$

The coefficients of the linear terms in Equations (23) are:

$$C_5(j,m) = 0 \qquad \text{for } 1 \le m \le N$$

$$C_5(j,m) = \int_0^1 X_m X_j^* \, dx \qquad \text{for } N+1 \le m \le 2N \qquad \text{(C-6)}$$

$$C_6(j,m) = -K \int_0^1 X_m X_j^* \, dx \qquad \text{for } 1 \le m \le N$$

$$C_6(j,m) = \int_0^1 \bar{u}_p(x) \frac{dX_m}{dx} X_j^* \, dx + \int_0^1 \frac{d\bar{u}_p}{dx} X_m X_j^* \, dx \qquad \text{(C-7)}$$

$$+ K \int_0^1 X_m X_j^* \, dx \qquad \text{for } N+1 \le m \le 2N$$

The coefficients of the nonlinear terms in Equations (22) are given below for $1 \le j \le N$, $1 \le m \le N$, and $1 \le n \le N$. For all other values of j, m, and n, $D_1 = D_2 = D_3 = D_4 = 0$.

$$D_1(j,m,n) = \frac{1-i}{2} \int_0^1 \frac{dX_m}{dx} \frac{dX_n}{dx} X_j^* \, dx$$

$$+ \frac{(\gamma-1)(1-i)}{4} \int_0^1 \frac{d^2X_m}{dx^2} X_n X_j^* \, dx \qquad \text{(C-8)}$$

$$D_2(j,m,n) = \frac{1+i}{2} \int_0^1 \frac{dX_m}{dx} \frac{dX_n^*}{dx} X_j^* \, dx$$

$$+ \frac{(\gamma-1)(1+i)}{4} \int_0^1 \frac{d^2X_m}{dx^2} X_n^* X_j^* \, dx \qquad \text{(C-9)}$$

$$D_3(j,m,n) = \frac{1+i}{2}\int_0^1 \frac{dX_m^*}{dx}\,\frac{dX_n}{dx}\,X_j^*\,dx$$

$$+ \frac{(\gamma-1)(1+i)}{4}\int_0^1 \frac{d^2X_m^*}{dx^2}\,X_n\,X_j^*\,dx \qquad \text{(C-10)}$$

$$D_4(j,m,n) = \frac{1-i}{2}\int_0^1 \frac{dX_m^*}{dx}\,\frac{dX_n^*}{dx}\,X_j^*\,dx$$

$$+ \frac{(\gamma-1)(1-i)}{4}\int_0^1 \frac{d^2X_m^*}{dx^2}\,X_n^*\,X_j^*\,dx \qquad \text{(C-11)}$$

In the integrals appearing in the coefficients given above, the eigenfunctions $X_j(x)$ are defined by Equation (20) and $X_j^*(x)$ denotes their complex conjugates.

C-2. Coefficients Appearing in Equations (25).

The linear coefficients in Equations (25) are given below for $1 \le j \le N$ and $1 \le m \le N$. The nonlinear coefficients in Equations (25) are identical to those in Equations (22) and are given by Equations (C-8) through (C-11).

$$C_o(j,m) = \int_0^1 X_m X_j^*\,dx \qquad \text{(C-12)}$$

$$C_1(j,m) = -\int_0^1 \frac{d^2X_m}{dx^2}\,X_j^*\,dx - K^2\bar{\rho}_p\int_0^1 X_m X_j^*\,dx$$

$$- K(\gamma-1)\bar{\rho}_p\int_0^1 \bar{u}_p(x)\,\frac{dX_m}{dx}\,X_j^*\,dx + \frac{dX_m}{dx}(1)X_j^*(1) \qquad \text{(C-13)}$$

$$C_2(j,m) = 2\int_0^1 \bar{u}(x)\,\frac{dX_m}{dx}\,X_j^*\,dx + (\gamma+1)\int_0^1 \frac{d\bar{u}}{dx}\,X_m X_j^*\,dx$$

$$+ K\bar{\rho}_p\int_0^1 X_m X_j^*\,dx + \gamma Y X_m(1)X_j^*(1) \qquad \text{(C-14)}$$

$$C_3(j,m) = K^3\bar{\rho}_p \int_o^1 X_m X_j^* \, dx + (\gamma-1) K^2 \bar{\rho}_p \int_o^1 \bar{u}_p(x) \frac{dX_m}{dx} X_j^* \, dx \qquad \text{(C-15)}$$

$$C_4(j,m) = -\gamma \int_o^1 \frac{d\bar{u}}{dx} X_m X_j^* \, dx \qquad \text{(C-16)}$$

C-3. Methodology for Calculating Coefficients in Equations (39).

Separation of Real and Imaginary Parts. Equations (39) were derived by applying the Method of Averaging (MOA) to Equations (25). This procedure requires that Equations (25) be separated into their real and imaginary components. Assuming that $A_j(t) = F_j(t) + iG_j(t)$, substituting into Equations (25), and separating real and imaginary parts yields:

$$\sum_{m=1}^{2N} \left\{ C_o'(j,m) \frac{d^2B_m}{dt^2} + C_1'(j,m)B_m + \left[C_2'(j,m) + h_c \Re_m^r E_1'(j,m) + h_c \Re_m^i E_2'(j,m) \right] \frac{dB_m}{dt} \right.$$

$$\left. + C_3'(j,m) e^{-Kt} \int_o^t B_m(t') e^{Kt'} dt' \right\} + \sum_{m=1}^{2N} \sum_{n=1}^{2N} \left\{ D'(j,m,n) B_m \frac{dB_n}{dt} \right\} = 0$$

$$j = 1,2,3 \ldots 2N \qquad \text{(C-17)}$$

where the B_m's are related to the F_m's and G_m's by Equations (33) of Section 2.4. The real coefficients C_o', C_1', C_2', C_3', E_1', E_2' and D' in Equation (C-17) are related to the original complex coefficients (i.e., $C_o, \ldots C_4$, $D_1, \ldots D_4$) appearing in Equations (25) as follows:

$$\begin{aligned} C_k'(2j-1,\ 2m-1) &= \mathrm{Re}\left[C_k(j,m)\right] \\ C_k'(2j-1,\ 2m) &= -\mathrm{Im}\left[C_k(j,m)\right] \\ C_k'(2j,\ 2m-1) &= \mathrm{Im}\left[C_k(j,m)\right] \\ C_k'(2j,\ 2m) &= \mathrm{Re}\left[C_k(j,m)\right] \end{aligned} \qquad \text{(C-18)}$$

for k = 0,1,2,3, j = 1,2,... N, m = 1,2,... N,

$$E_1'(2j-1,\ 2m-1) = \mathrm{Re}\left[C_4(j,m)\right]$$

$$E_1'(2j-1,\ 2m) = -\mathrm{Im}\left[C_4(j,m)\right]$$

$$E_1'(2j,\ 2m-1) = \mathrm{Im}\left[C_4(j,m)\right]$$

$$E_1'(2j,\ 2m) = \mathrm{Re}\left[C_4(j,m)\right]$$

$$E_2'(2j-1,\ 2m-1) = -\mathrm{Im}\left[C_4(j,m)\right]$$

$$E_2'(2j-1,\ 2m) = -\mathrm{Re}\left[C_4(j,m)\right]$$

$$E_2'(2j,\ 2m-1) = \mathrm{Re}\left[C_4(j,m)\right]$$

$$E_2'(2j,\ 2m) = -\mathrm{Im}\left[C_4(j,m)\right] \qquad \text{(C-19)}$$

for j = 1,2... N, m = 1,2,... N, and:

$$D'(2j-1,\ 2m-1,\ 2n-1) = \mathrm{Re}\left[D_1(j,m,n) + D_2(j,m,n) + D_3(j,m,n) + D_4(j,m,n)\right]$$

$$D'(2j-1,\ 2m-1,\ 2n) = \mathrm{Im}\left[-D_1(j,m,n) + D_2(j,m,n) - D_3(j,m,n) + D_4(j,m,n)\right]$$

$$D'(2j-1,\ 2m,\ 2n-1) = \mathrm{Im}\left[-D_1(j,m,n) - D_2(j,m,n) + D_3(j,m,n) + D_4(j,m,n)\right]$$

$$D'(2j-1,\ 2m,\ 2n) = \mathrm{Re}\left[-D_1(j,m,n) + D_2(j,m,n) + D_3(j,m,n) - D_4(j,m,n)\right]$$

$$D'(2j,\ 2m-1,\ 2n-1) = \mathrm{Im}\left[D_1(j,m,n) + D_2(j,m,n) + D_3(j,m,n) + D_4(j,m,n)\right]$$

$$D'(2j,\ 2m-1,\ 2n) = \mathrm{Re}\left[D_1(j,m,n) - D_2(j,m,n) + D_3(j,m,n) - D_4(j,m,n)\right]$$

$$D'(2j,\ 2m,\ 2n-1) = \mathrm{Re}\left[D_1(j,m,n) + D_2(j,m,n) - D_3(j,m,n) - D_4(j,m,n)\right]$$

$$D'(2j,\ 2m,\ 2n) = \mathrm{Im}\left[-D_1(j,m,n) + D_2(j,m,n) + D_3(j,m,n) - D_4(j,m,n)\right]$$

(C-20)

for $j = 1,2,\ldots N$, $m = 1,2,\ldots N$, $n = 1,2\ldots N$.

Transformation to Uncoupled Form. Equations (C-17) are coupled in the second derivatives; that is, there are two or more C_o' terms in each equation. This coupling results from the non-orthogonality of the axial eigenfunctions. In order to apply the MOA to Equations (C-17), they must be decoupled to the form:

$$\frac{d^2B_j}{dt^2} = f_j\left(B_1, B_2,\ldots B_{2N}, \frac{dB_1}{dt}, \frac{dB_2}{dt}, \ldots \frac{dB_{2N}}{dt}\right) \qquad \text{(C-21)}$$

in which only one second derivative appears in each equation. Using Equation (C-21), it is seen that Equation (34) (or Equation (C-17)) can be expressed as

$$C_o' f = g \qquad \text{(C-22)}$$

where C_o' is the 2N x 2N matrix of coefficients of the coupled system, f is the column matrix corresponding to the right-hand-side of the decoupled system, and g is the column matrix corresponding to the right-hand-side of the coupled system. To decouple Equations (C-17), therefore, Equation (C-22) is solved for f, thus

$$f = C_o^{-1} g \qquad \text{(C-23)}$$

where C_o^{-1} is the inverse of the matrix C_o'. Performing these operations and equating the coefficients of like terms in f and C_o^{-1} g gives the following relations:

$$\mathfrak{C}_i(j,m) = \sum_{k=1}^{2N} C_o^{-1}(j,k)\ C_i'(k,m) \qquad i = 1,2,3$$

$$\mathfrak{E}_i(j,m) = \sum_{k=1}^{2N} C_o^{-1}(j,k)\ E_i'(k,m) \qquad i = 1,2$$

(C-24)

$$\tilde{D}(j,m,n) = \sum_{k=1}^{2N} C_o^{-1}(j,k)\, D'(k,m,n)$$

where $\tilde{C}_i$, $\tilde{E}_i$, and $\tilde{D}$ are the corresponding coefficients of the decoupled system.

Due to the complicated nature of the relationships given by Equations (C-24), explicit expressions for the coefficients $\tilde{C}_i$, $\tilde{E}_i$, and $\tilde{D}$ in terms of the spatial integrals can not be given. The coefficients must be calculated numerically by first computing the complex coefficients using Equations (C-12) through (C-16) and Equations (C-8) through (C-11), next calculating the coefficients of the equivalent coupled real system using Equations (C-18), (C-19), and (C-20), and finally computing the coefficients of the decoupled system using Equations (C-24). A similar procedure is used in the numerical solution of the equations obtained using the Galerkin method without averaging (i.e., Equations (22) and (23) or Equations (25)).

Application of MQA. The MQA procedure is described in Section 2.4 which results in Equations (39). In performing the time integrations indicated by Equations (32), two integrals of the products of three trigonometric functions arise. These appear in Equations (39) and are defined by:

$$\beta_1(p,q,\ell) = \omega_1 \int_0^{2\pi/\omega_1} \cos(\omega_p t)\cos(\omega_q t)\cos(\omega_\ell t)\, dt$$

$$= \pi/2 \quad \text{if} \quad p = q + \ell$$

$$\text{or} \quad q = p + \ell$$

$$\text{or} \quad \ell = p + q$$

$$= 0 \quad \text{for all other integer values of } p,q,\ell \qquad \text{(C-25)}$$

$$\beta_2(p,q,\ell) = \omega_1 \int_0^{2\pi/\omega_1} \cos(\omega_p t)\sin(\omega_q t)\sin(\omega_\ell t)\, dt$$

$$= \pi/2 \quad \text{if} \quad \ell = p + q$$

$$\text{or} \quad q = p + \ell$$

$$= -\pi/2 \quad \text{if} \quad p = q + \ell$$

$$= 0 \quad \text{for all other integer values of } p,q,\ell \qquad \text{(C-26)}$$

C-4. Mode-Amplitude Equations for T-Burners.

The mode-amplitude equations for T-burners are similar to Equations (22) and (23) with an additional equation for u_n' (Equation (76)). The T-burner equations are:

$$\sum_{m=1}^{2N} \left\{ C_o(j,m) \frac{d^2 A_m}{dt^2} + C_1(j,m) A_m + \left[C_2(j,m) + KC_3(j,m) + h_c \Re_m C_4(j,m) \right] \frac{dA_m}{dt} \right\} + \frac{A_v h_c}{\beta_v} C_7(j) u_n' + \sum_{m=1}^{2N} \sum_{n=1}^{2N} \left\{ D_1(j,m,n) \left[A_m \frac{dA_n}{dt} + A_m^* \frac{dA_n^*}{dt} \right] + D_2(j,m,n) \left[A_m \frac{dA_n^*}{dt} + A_m^* \frac{dA_n}{dt} \right] \right\} = 0$$

$$j = 1,2 \ldots N \qquad \text{(C-27)}$$

$$\sum_{m=1}^{2N} \left\{ C_5(j,m) \frac{dA_m}{dt} + C_6(j,m) A_m \right\} = 0$$

$$j = 1,2,\ldots N \qquad \text{(C-28)}$$

$$\frac{du_n'}{dt} + (\bar{u}_n / L_{eff}) u_n' = (\gamma / L_{eff}) \sum_{m=1}^{N} C_7(m) \frac{dA_m}{dt} \qquad \text{(C-29)}$$

The linear coefficients appearing in Equations (C-27) are:

$$C_o(j,m) = \int_o^1 X_m X_j \, dx \qquad \text{for } 1 \le m \le N$$

(C-30)

$$C_o(j,m) = 0 \qquad \text{for } N+1 \le m \le 2N$$

$$C_1(j,m) = -\int_0^1 \frac{d^2X_m}{dx^2} X_j \, dx \qquad \text{for } 1 \le m \le N$$

(C-31)

$$C_1(j,m) = 0 \qquad \text{for } N+1 \le m \le 2N$$

$$C_2(j,m) = 2\int_0^1 \bar{u}(x) \frac{dX_m}{dx} X_j \, dx + (\gamma+1) \int_0^1 \frac{d\bar{u}}{dx} X_m X_j \, dx - V_\ell \int_{(1-\beta_v)/2}^{(1+\beta_v)/2} d\bar{u}/dx \, X_m X_j \, dx + \gamma \bar{u}_b \left[1 + X_m(1) X_j(1)\right] \qquad \text{for } 1 \le m \le N$$

(C-32)

$$C_2(j,m) = -(\gamma-1) \int_0^1 \bar{u}_p \bar{\rho}_p \frac{dX_m}{dx} X_j \, dx \qquad \text{for } N+1 \le m \le 2N$$

$$C_3(j,m) = \int_0^1 \bar{\rho}_p X_m X_j \, dx \qquad \text{for } 1 \le m \le N$$

(C-33)

$$C_3(j,m) = -\int_0^1 \bar{\rho}_p X_m X_j \, dx \qquad \text{for } N+1 \le m \le 2N$$

$$C_4(j,m) = -\gamma \left[\int_0^{\beta/2} \frac{d\bar{u}}{dx} X_m X_j \, dx + \int_{1-\beta/2}^1 \frac{d\bar{u}}{dx} X_m X_j \, dx \right] - \gamma \bar{u}_b \left[1 + X_m(1) X_j(1)\right] \qquad \text{for } 1 \le m \le N$$

(C-34)

$$C_4(j,m) = 0 \qquad \text{for } N+1 \le m \le 2N$$

$$C_7(j) = \frac{1}{j\pi}\left\{\sin\left[j\pi\left(\frac{1+\beta_v}{2}\right)\right] - \sin\left[j\pi\left(\frac{1-\beta_v}{2}\right)\right]\right\} \qquad \text{(C-35)}$$

The coefficients of the linear terms in Equations (C-28) are:

$$C_5(j,m) = 0 \qquad \text{for } 1 \le m \le N$$

$$C_5(j,m) = \int_0^1 X_m X_j \, dx \qquad \text{for } N+1 \le m \le 2N \qquad \text{(C-36)}$$

$$C_6(j,m) = -K\int_0^1 X_m X_j \, dx \qquad \text{for } 1 \le m \le N$$

$$C_6(j,m) = \int_0^1 \bar{u}_p(x) \frac{dX_m}{dx} X_j \, dx + \int_0^1 \frac{d\bar{u}_p}{dx} X_m X_j \, dx$$
$$- v_\ell \int_{(1-\beta_v)/2}^{(1+\beta_v)/2} \frac{d\bar{u}_p}{dx} X_m X_j \, dx + K\int_0^1 X_m X_j \, dx \qquad \text{(C-37)}$$

$$\text{for } N+1 \le m \le 2N$$

The nonlinear coefficients appearing in Equations (C-27) are similar to those appearing in Equations (22) and are given by:

$$D_1(j,m,n) = \frac{(1-i)}{2}\int_0^1 \frac{dX_m}{dx}\frac{dX_n}{dx} X_j \, dx + \frac{(\gamma-1)(1-i)}{4}\int_0^1 \frac{d^2X_m}{dx^2} X_n X_j \, dx \qquad \text{(C-38)}$$

$$D_2(j,m,n) = \frac{1+i}{2}\int_0^1 \frac{dX_m}{dx}\frac{dX_n}{dx} X_j \, dx + \frac{(\gamma-1)(1+i)}{4}\int_0^1 \frac{d^2X_m}{dx^2} X_n X_j \, dx \qquad \text{(C-39)}$$

$$\text{for } 1 \le j \le N, \quad 1 \le m \le N, \quad 1 \le n \le N$$

The axial eigenfunctions $X_j(x)$ appearing in the above expressions are given by:

$$X_j(x) = \cosh(ij\pi x) = \cos j\pi x \tag{C-40}$$

thus

$$\frac{dX_j}{dx} = - j\pi \sin j\pi x \tag{C-41}$$

and

$$\frac{d^2X_j}{dx^2} = - j^2\pi^2 \cos j\pi x \tag{C-42}$$

APPENDIX D

DERIVATION OF STEADY-STATE SOLUTIONS

D-1. Steady-State Solutions for Motors.

The steady-state solutions for gas and particle velocity and particle density for motors with full-length, cylindrically perforated grains (i.e., Equations (40), (41), and (42) of Section 2.5) will now be derived. For small steady-state Mach numbers the gas density and mass burning rate are assumed to be constant (the variation in $\bar{\rho}$ and $\dot{\bar{m}}_g$ is of $O(\bar{M}_e^2)$); thus for $\bar{\rho}(x) = 1$ the steady-state continuity equation becomes:

$$\frac{d\bar{u}}{dx} = \frac{2\dot{\bar{m}}_g}{R} \tag{D-1}$$

Integrating Equation (D-1) and using the head-end boundary condition $\bar{u}(0) = 0$ gives:

$$\bar{u}(x) = \left(\frac{2\dot{\bar{m}}_g}{R}\right) x = \bar{u}_e x \tag{D-2}$$

which is Equation (40) of Section 2.5.

The steady-state particle density and velocity are obtained from the steady-state particle continuity and momentum equations. Neglecting variations of $\bar{\rho}_p$ with x as being of $O(\bar{M}_e^2)$, $\partial\bar{\rho}_p/\partial x \approx 0$ and Equations (2) and (4) of Section 2.1 become:

$$\frac{d\bar{u}_p}{dx} = \frac{2}{\bar{\rho}_p R}\,\dot{\bar{m}}_p \tag{D-3}$$

$$\bar{\rho}_p\,\bar{u}_p\,\frac{d\bar{u}_p}{dx} = \bar{\rho}_p\,K(\bar{u} - \bar{u}_p) - \frac{2}{R}\,\dot{\bar{m}}_p\,\bar{u}_p \tag{D-4}$$

Integrating Equation (D-3) with $\bar{u}_p(0) = 0$ gives:

$$\bar{u}_p(x) = \left(\frac{2\dot{\bar{m}}_p}{\bar{\rho}_p R}\right) x \tag{D-5}$$

To determine $\bar{\rho}_p$, Equations (D-2), (D-3) and (D-5) are substituted into Equation (D-4) to obtain the following quadratic equation for $\bar{\rho}_p$:

$$\bar{\rho}_p^2 - \left(\frac{\dot{\bar{m}}_p}{\dot{\bar{m}}_g}\right)\bar{\rho}_p - 2\left(\frac{\dot{\bar{m}}_p}{\dot{\bar{m}}_g}\right)^2 \frac{\bar{u}_e}{K} = 0 \qquad \text{(D-6)}$$

which is independent of x. Solving Equation (D-6) and taking the positive root yields:

$$\bar{\rho}_p = \frac{\dot{\bar{m}}_p}{2\dot{\bar{m}}_g}\left[1 + \sqrt{1 + \frac{8\bar{u}_e}{K}}\right] \qquad \text{(D-7)}$$

which is Equation (42) of Section 2.5. The particle velocity is then obtained by substituting Equation (D-7) for $\bar{\rho}_p$ in Equation (D-5) to obtain:

$$\bar{u}_p(x) = \frac{2\bar{u}_e x}{1 + \sqrt{1 + \frac{8\bar{u}_e}{K}}} \qquad \text{(D-8)}$$

which is Equation (41) of Section 2.5.

D-2. Steady-State Solutions for T-Burners.

The steady-state solutions for gas and particle velocities and particle density for a cup-grain T-burner will now be derived. Solutions are obtained for Regions 1,2, and 3; the solutions in Regions 4 and 5 are readily obtained by symmetry.

Region 1. The steady-state solutions in the region of lateral surface burning (i.e., $0 \leq x \leq \beta/2$) for the T-burner differ from the solutions given previously in Section D-1 for motors only if end-burning is present. For this case the steady-state velocity of the gases leaving both the lateral propellant surfaces and the end surfaces is denoted by $\bar{u}_b$; hence, $\dot{\bar{m}}_g = \bar{u}_b$ for $\bar{\rho} = 1$. Integrating the steady-state continuity equation (i.e., Equation (D-1)) and using the boundary condition $\bar{u}(0) = \bar{u}_b$ gives:

$$\bar{u}(x) = \bar{u}_b\left(1 + \frac{2}{R}x\right) \qquad (0 \leq x \leq \beta/2) \qquad \text{(D-9)}$$

which is Equation (48) of Section 2.6.

As before, the particle properties are obtained by solving the steady-state particle continuity and momentum equations. If the approach used in Section D-1 is

employed, the resulting solution for $\bar{\rho}_p$ is dependent on x which violates the assumption that $\bar{\rho}_p$ is constant. Furthermore $\bar{\rho}_p \to \infty$ as $x \to 0$ which is physically meaningless. Thus for the case of end burning, the assumption of a uniform particle density is inconsistent with the particle continuity and momentum equations.

To obtain solutions for $\bar{\rho}_p(x)$ and $\bar{u}_p(x)$ an alternative solution procedure is used. Allowing $\bar{\rho}_p$ to vary but assuming that $\dot{\bar{m}}_p$ is a constant, the particle continuity equation becomes:

$$\frac{d}{dx}\left(\bar{\rho}_p \bar{u}_p\right) = \frac{2\dot{\bar{m}}_p}{R} \qquad \text{(D-10)}$$

Using the boundary condition, $\bar{\rho}_p(0)\,\bar{u}_p(0) = \dot{\bar{m}}_p$, Equation (D-10) is integrated to obtain:

$$\bar{\rho}_p \bar{u}_p = \dot{\bar{m}}_p\left(1 + \frac{2}{R}x\right) \qquad \text{(D-11)}$$

The steady-state particle velocity is then obtained from Equation (D-4) by substituting Equation (D-11) for $\bar{\rho}_p \bar{u}_p$, substituting Equation (D-9) for $\bar{u}$, and approximating $\bar{\rho}_p$ in the particle drag term by $C_m = \dot{\bar{m}}_p / \dot{\bar{m}}_g$. Simplifying the resulting expression yields a linear first order differential equation of the form:

$$\frac{d\bar{u}_p}{dx} + \frac{B}{1+Ax}\bar{u}_p = K \qquad \text{(D-12)}$$

where $B = K/\bar{u}_b + 2/R$ and $A = 2/R$. This equation has the general solution:

$$\bar{u}_p(x) = C_2\,(1 + Ax)^{-B/A} + \frac{K}{A+B}\,(1 + Ax) \qquad \text{(D-13)}$$

Using the boundary condition $\bar{u}_p(0) = \bar{u}_b$ (the particles and gas are assumed to leave the propellant surface with the same velocity), introducing the expressions for A and B, and introducing $\eta = 4\bar{u}_b/RK$, Equation (D-13) becomes:

$$\bar{u}_p(x) = \frac{\bar{u}_b}{1+\eta}\left\{1 + \frac{2}{R}x + \eta\left[1 + \frac{2}{R}x\right]^{-\frac{\eta+2}{\eta}}\right\} \qquad \text{(D-14)}$$

The steady-state solution for particle density is obtained by substituting

Equation (D-14) into Equation (D-11) and solving for $\bar{\rho}_p$, thus:

$$\bar{\rho}_p(x) = \left\{ \frac{1+\eta}{1+\eta\left[1+\frac{2}{R}x\right]^{-(2\eta+2)/\eta}} \right\} C_m \qquad \text{(D-15)}$$

Equations (D-14) and (D-15) correspond to Equations (49) and (50) of Section 2.6 respectively

Region 2. In Region 2 the source terms $\dot{\bar{m}}_g$ and $\dot{\bar{m}}_p$ vanish and the steady-state continuity equation for the gas phase becomes:

$$\frac{d}{dx}(\bar{\rho}\bar{u}) = 0 \qquad \text{(D-16)}$$

which is integrated to obtain $\bar{\rho}\bar{u}$ = constant. The constant is obtained by matching the solutions at the boundary between Regions 1 and 2. Evaluating Equation (D-9) at $x = \beta/2$ yields the constant value of $\bar{u}$ in Region 2, thus:

$$\bar{u}(x) = \bar{u}_b(1+\beta/R) \qquad (\beta/2 \le x \le (1-\beta_v)/2) \qquad \text{(D-17)}$$

which is Equation (55) of Section 2.6.

The particle conservation equations in Region 2 become:

$$\frac{d}{dx}(\bar{\rho}_p\bar{u}_p) = 0 \qquad \text{(D-18)}$$

$$\bar{\rho}_p\bar{u}_p\frac{d\bar{u}_p}{dx} = \bar{\rho}_p K(\bar{u}-\bar{u}_p) \qquad \text{(D-19)}$$

Integrating Equation (D-18) and matching solutions at the boundary between Regions 1 and 2 gives:

$$\bar{\rho}_p\bar{u}_p = \bar{\rho}_p(\beta/2)\,\bar{u}_p(\beta/2) \qquad \text{(D-20)}$$

Substituting Equation (D-20) into Equation (D-19), approximating $\bar{\rho}_p$ by C_m in the right-hand-side of Equation (D-19), and substituting $\bar{u} = \bar{u}(\beta/2)$ yields a linear first order differential equation of the form:

$$\frac{d\bar{u}_p}{dx} + A\bar{u}_p = Q \qquad \text{(D-21)}$$

where $$A = C_m K/[\bar{\rho}_p(\beta/2)\ \bar{u}_p(\beta/2)]$$

and $$Q = C_m K\bar{u}(\beta/2)/[\bar{\rho}_p(\beta/2)\ \bar{u}_p(\beta/2)]$$

Equation (D-21) has the general solution given by:

$$\bar{u}_p(x) = R/A + C_1\, e^{-Ax} \qquad \text{(D-22)}$$

Matching particle velocities at the boundary between Regions 1 and 2 gives the constant C_1. Introducing the values of C_1, A, and Q into Equation (D-22) gives the desired steady-state solution for the particle velocity in Region 2:

$$\bar{u}_p(x) = \bar{u}\ (\beta/2)\left\{1 - \frac{\eta}{1+\eta}\ e^{-\alpha(x-\beta/2)}\right\} \qquad \text{(D-23)}$$

$$(\beta/2 \le x \le (1-\beta_v)/2)$$

where $\alpha = K/\bar{u}(\beta/2)$ and η is the same as in Region 1. Equation (D-23) corresponds to Equation (56) of Section 2.6.

Substituting Equation (D-23) for $\bar{u}_p$ in Equation (D-20) and solving for $\bar{\bar{\rho}}_p$ yields:

$$\bar{\bar{\rho}}_p(x) = \frac{\bar{\rho}_p(\beta/2)\bar{u}_p(\beta/2)}{\bar{u}(\beta/2)}\left\{1 - \frac{\eta}{1+\eta}\ e^{-\alpha(x-\beta/2)}\right\}^{-1} \qquad \text{(D-24)}$$

$$(\beta/2 \le x \le (1-\beta_v)/2)$$

Region 3. In the vent region the source terms appearing in the continuity and momentum equations are determined by the flow out the vent. Assuming uniform flow across the vent, the steady-state continuity equation for the gas phase becomes:

$$\frac{d}{dx}(\bar{\bar{\rho}}\bar{\bar{u}}) = -2\bar{\bar{\rho}}\bar{\bar{u}}_b(1 + \beta/R)/\beta_v \qquad \text{(D-25)}$$

Again assuming that $\bar{\rho} = 1$ Equation (D-25) is integrated to obtain

$$\bar{u}(x) = \bar{u}_b(1 + \beta/R)(1 - 2x)/\beta_v \qquad ((1-\beta_v)/2 \leq x \leq (1+\beta_v)/2) \tag{D-26}$$

where the constant of integration was obtained by matching the solutions at the boundary between Regions 2 and 3. Equation (D-26) is the same as Equation (70) of Section 2.6.

Assuming that the particle sink at the vent is simply the product of C_m and the gas sink, the particle conservation equations become:

$$\frac{d}{dx}(\bar{\rho}_p \bar{u}_p) = -2 C_m \bar{u}_b(1 + \beta/R)/\beta_v \tag{D-27}$$

$$\bar{\rho}_p \bar{u}_p \frac{d\bar{u}_p}{dx} = \bar{\rho}_p K(\bar{u}-\bar{u}_p) + 2 C_m \bar{u}_b(1+\beta/R)(1-V_\ell)\bar{u}_p/\beta_v \tag{D-28}$$

Following the method used in Region 1, Equation (D-27) is integrated to obtain:

$$\bar{\rho}_p \bar{u}_p = C_m \bar{u}_b(1 + \beta/R)(1 - 2x)/\beta_v \tag{D-29}$$

which is substituted into Equation (D-28) to obtain a linear first order differential equation of the same form as Equation (D-12) where A = -2 and:

$$B = \frac{K\beta_v}{\bar{u}_b(1+\beta/R)} - 2(1-V_\ell)$$

Substituting these values of A and B into the general solution given by Equation (D-13) and matching solutions at $x = (1-\beta_v)/2$ gives the desired solution for $\bar{u}_p$:

$$\bar{u}_p(x) = \frac{\bar{u}_b(1+\beta/R)}{1-\eta_v}\left\{\frac{1-2x}{\beta_v} - \eta_v\left[\frac{1-2x}{\beta_v}\right]^q\right\} \tag{D-30}$$

$$(1-\beta_v)/2 \leq x \leq 1/2$$

where $$\eta_v = \frac{(4 - 2V_\ell)}{K\beta_v}\bar{u}_b(1+\beta/R)$$

and $q = 2/\eta_v + (V_\ell - 1)$

Substituting Equation (D-30) into Equation (D-29) and solving for $\bar{\rho}_p$ gives:

$$\bar{\rho}_p(x) = \left\{ \frac{1 - \eta_v}{1 - \eta_v \left[\frac{1 - 2x}{\beta_v} \right]^{q-1}} \right\} C_m \qquad \text{(D-31)}$$

$$(1 - \beta_v)/2 \leq x \leq 1/2$$

Equations (D-30) and (D-31) correspond to Equations (71) and (72) of Section 2.6 These equations are valid only in the left half of the vent region ($(1 - \beta_v)/2 \leq x \leq 1/2$), while the corresponding values in the right half of Region 3 are obtained by symmetry.